Nanostructure Science and Technology
Series Editor: David J. Lockwood

Kazuo Kondo
Rohan N. Akolkar
Dale P. Barkey
Masayuki Yokoi *Editors*

Copper Electrodeposition for Nanofabrication of Electronics Devices

Springer

Nanostructure Science and Technology

Volume 171

Series editor

David J. Lockwood, Ottawa, Canada

For further volumes:
http://www.springer.com/series/6331

Kazuo Kondo · Rohan N. Akolkar
Dale P. Barkey · Masayuki Yokoi
Editors

Copper Electrodeposition for Nanofabrication of Electronics Devices

Editors
Kazuo Kondo
Department of Chemical Engineering
Osaka Prefecture University
Osaka
Japan

Dale P. Barkey
Department of Chemical Engineering
University of New Hampshire
Durham, NH
USA

Rohan N. Akolkar
Intel Corporation
Hillsboro, OR
USA

Masayuki Yokoi
Industrial Technology Support Institute
Osaka
Japan

ISSN 1571-5744 ISSN 2197-7976 (electronic)
ISBN 978-1-4614-9175-0 ISBN 978-1-4614-9176-7 (eBook)
DOI 10.1007/978-1-4614-9176-7
Springer New York Heidelberg Dordrecht London

Library of Congress Control Number: 2013954032

© Springer Science+Business Media New York 2014
This work is subject to copyright. All rights are reserved by the Publisher, whether the whole or part of the material is concerned, specifically the rights of translation, reprinting, reuse of illustrations, recitation, broadcasting, reproduction on microfilms or in any other physical way, and transmission or information storage and retrieval, electronic adaptation, computer software, or by similar or dissimilar methodology now known or hereafter developed. Exempted from this legal reservation are brief excerpts in connection with reviews or scholarly analysis or material supplied specifically for the purpose of being entered and executed on a computer system, for exclusive use by the purchaser of the work. Duplication of this publication or parts thereof is permitted only under the provisions of the Copyright Law of the Publisher's location, in its current version, and permission for use must always be obtained from Springer. Permissions for use may be obtained through RightsLink at the Copyright Clearance Center. Violations are liable to prosecution under the respective Copyright Law.
The use of general descriptive names, registered names, trademarks, service marks, etc. in this publication does not imply, even in the absence of a specific statement, that such names are exempt from the relevant protective laws and regulations and therefore free for general use.
While the advice and information in this book are believed to be true and accurate at the date of publication, neither the authors nor the editors nor the publisher can accept any legal responsibility for any errors or omissions that may be made. The publisher makes no warranty, express or implied, with respect to the material contained herein.

Printed on acid-free paper

Springer is part of Springer Science+Business Media (www.springer.com)

Preface

Copper has lower resistivity than aluminum and can be electrodeposited easily. Hence, copper can be used for chip wiring. In 1998, the copper damascene on-chip interconnect process was introduced commercially and became the first industrial nanofabrication process. This nanofabrication technology relies on electrodeposition of copper to fill cavities or vias of diameters less than 0.1 μm. This process has now been adopted worldwide for advanced semiconductor manufacturing and has branched into several industrial applications: Damascene metallization, through-silicon via metallization, interstitial via hole build-up in printed wiring boards, and both sides smooth Cu foils for collectors in Li-ion batteries.

However, no comprehensive books have been published on Copper Electrodeposition for Nanofabrication. The Part I of present book introduces the reader to fundamental aspects of copper electrodeposition. This is followed by details of additive chemistry, suppression effects (due to PEG additive), and acceleration effects (due to SPS additive), leading to filling mechanisms. Mathematical models for superfilling, continuum models for nucleation and growth, Kinetic Monte Carlo simulations, and shape evolution are then reviewed.

The Part II of the book covers two specific challenges facing nano-interconnect fabrication in the coming decade, i.e., direct electrodeposition on noble metal barriers and liners and microstructure evolution in electrodeposited Cu nanowires and its impact on Cu resistivity. The part starts with a critical overview of the specific scaling challenges foreseen in damascene interconnect fabrication. It also outlines the current challenges to the two technologies, such as direct plating, electroless deposition, and theory-guided molecular design of additives in electrochemical systems. This introductory chapter is followed by a comprehensive study that discusses the evolution of microstructure in electrodeposited Cu nano-interconnects. A hallmark of this study is the development of metrology techniques (SIMS) to probe patterned metal lines. Finally, the part ends with a contribution documenting mechanisms involved in direct plating of Cu on noble metals such as ruthenium (Ru).

In Part III of this book, emerging applications of electrodeposition are outlined: through-silicon vias (TSVs), printed wiring boards, copper foils for Li-ion battery current collectors, and through-hole filling. TSVs are used for fast conduction of digital signals from one chip to another chip in advanced packaging solutions in smart phones, high speed image processing, and capsule endoscopes. In interstitial

via hole build-up printed wiring boards, the interstitial via holes are filled by copper electrodeposition. Then, the individual board layers are piled up so that the via holes interstitially connect the wiring in the vertical direction. The primary application of this technology recently has been in smart phones. Smooth copper foils serve as electric collectors for the anode of Li-ion batteries. In order to coat the carbon on both sides of the copper foil, the foil must be smooth and thus coated with electrodeposited copper. Through-hole plating is an emerging technology in printed wiring board manufacturing.

Kazuo Kondo was very much astonished when he visited the IBM Watson Research Center in 1999 and Drs. M. Datta and J. Dukovic kindly showed him their lab and red copper wafer electrodeposited by copper. Drs. Datta and Dukovic are team members for the development of the damascene on-chip semiconductor wiring process. This experience gave Kazuo Kondo the initial motivation to start research in copper electrodeposition.

We hope that this book benefits scientists, engineers, and academicians working in the field of copper electrodeposition. We are grateful to all the contributors for their time, commitment, patience, and feedback. Through our interactions with the contributors, we have learned a great deal. We sincerely hope the readers enjoy the chapters. Finally, we would like to acknowledge the opportunity given to us by K. Howell of Springer to edit this book.

Kazuo Kondo
Rohan N. Akolkar
Dale P. Barkey
Masayuki Yokoi

Contents

Part I Copper Electrodepositon and Additive Chemistry

1 **Copper Electrodepositon** 3
Masayuki Yokoi

2 **Supression Effect and Additive Chemistry** 27
Masayuki Yokoi

3 **Acceleration Effect** 45
Dale P. Barkey

4 **Modeling and Simulation** 63
Yutaka Kaneko

Part II Copper on Chip Metallization

5 **Frontiers of Cu Electrodeposition and Electroless Plating for On-chip Interconnects** 99
James F. Rohan and Damien Thompson

6 **Microstructure Evolution of Copper in Nanoscale Interconnect Features** 115
James Kelly, Christopher Parks, James Demarest, Juntao Li and Christopher Penny

7 **Direct Copper Plating** 131
Aleksandar Radisic and Philippe M. Vereecken

Part III Through Silicon Via and Other Methods

8 **Through Silicon Via** 177
Kazuo Kondo

9 Build-up Printed Wiring Boards (Build-up PWBs) 193
Kiyoshi Takagi and Toshikazu Okubo

10 Copper Foil Smooth on Both Sides for Lithium-Ion Battery 229
Akitoshi Suzuki and Jun Shinozaki

11 Through Hole Plating 267
Wei-Ping Dow

Eratum to: Acceleration Effect E1
Dale P. Barkey

Part I
Copper Electrodepositon and Additive Chemistry

Chapter 1
Copper Electrodepositon

Masayuki Yokoi

1.1 Functions of Primary Constituents

Copper sulfate ($CuSO_4 \cdot 5H_2O$) and sulfuric acid (H_2SO_4) are the primary constituents of the acid copper sulfate bath [1]. The formulation of the bath is adjusted depending on the intended use, as given in Table 1.1.

For conventional copper deposition such as decorative plating, electroforming, copper refining, high copper sulfate concentration, and low sulfuric acid concentration baths have long been adopted. Their formulations are determined on the basis of whether the bath voltage is low and the current efficiency of copper deposition is high, in terms of energy cost, important in large-scale copper deposition manufacturing such as electroforming, refining, decorative plating for automobiles, and so on. For printed wiring board and through-hole plating, a low copper-high sulfuric acid baths were developed for high macro-throwing power bath in the 1980s, and were used widely for achieving uniform copper deposition on large area circuit boards and inside the through-holes sub-mm order in size. In recent years, since the Copper damascene process was created in 1997, both constituent concentrations are adjusted to relatively low copper sulfate-high sulfuric acid bath for the purpose of bottom-up filling of via/trench of nanometer size in semiconductor interconnect technology.

In printed wiring board and through-hole plating, macro-throwing power, the most important property to be expected, is drastically improved by decreasing copper concentration and increasing sulfuric acid concentration. As is well known, macro-throwing power was defined as the product of specific conductivity of the solution (κ) and the derivative of surface overpotential with respect to current density $(\mathrm{d}\eta/\mathrm{di})$ by Carl Wagner [2].

M. Yokoi (✉)
Osaka Prefecture University, Osaka, Japan
e-mail: masayuki_yokoi@hotmail.com

K. Kondo et al. (eds.), *Copper Electrodeposition for Nanofabrication of Electronics Devices*, Nanostructure Science and Technology 171, DOI: 10.1007/978-1-4614-9176-7_1,

© Springer Science+Business Media New York 2014

Table 1.1 Formulations of acid copper sulfate baths

Baths	Primary constituents (g/L)	Applications
Conventional bath	$CuSO_4 \cdot 5H_2O$ 180–250 H_2SO_4 60–40	Decorative plating Copper refining Electroforming, etc
High-through bath	$CuSO_4 \cdot 5H_2O$ 60–100 H_2SO_4 250–200	Printed wiring board plating Through-hole plating
Via filling bath	$CuSO_4 \cdot 5H_2O$ 150–230 H_2SO_4 15–50	Build-up PWB plating
Nano-plating bath	$CuSO_4 \cdot 5H_2O$ 60–100 H_2SO_4 200–10	LSI trench/via filling

$$\text{Macro - throwing power} \ \alpha \ (k) \ \times \ (\mathrm{d}\eta/\mathrm{di})$$

High sulfuric acid concentration increases κ, and low copper concentration increases surface resistance $\mathrm{d}\eta/\mathrm{di}$, resulting in a high-throwing power plating bath. Figure 1.1 shows how specific conductivity depends on copper sulfate and sulfuric acid concentration [3]. Specific conductivity increases in almost direct proportion to the sulfuric acid concentration, while, changing little with increase in copper sulfate concentration. The proportional increase in conductivity with increase in sulfuric acid is achieved by a particular kind of H^+ ionic transport in the solution, named Grotthuss mechanism as shown at the bottom of Fig. 1.1. Ionic conduction in acidic solution is caused by the consecutive H^+ ion movement between hydronium ions, in which H^+ ion on a water molecule transfers to the next molecule, and H^+ ion on the second molecule moves to a neighbor. For via/trench filling plating in tens of micrometer scale depth, it is important to furnish enough copper ions continuously into the concave region, rather than to the convex region of the surface. In concavities of such size, copper ions are supplied to the surface almost entirely by diffusion alone and not by convection. Further, the diffusion coefficient of Cu^{2+} is as low as about 5.0×10^{-10} [m^2/s]. So, it may be a preferred condition that the copper concentration in the bath is high. However, high Cu^{2+} concentration alone is not enough to fill the via/trench. Organic additive constituents added in small amounts play special roles to accelerate copper deposition in the concave region and suppress it on the convex region. The PEG-SPS-JGB additive system developed for decorative bright copper plating in the 1960s is applied to the via/trench filling accordingly. Even now, development of new additive system having the same characters and also the investigation of action mechanism is still an active research area. The details will be described in the following Sect. 1.2 additive chemistry. While, for the via/trench filling copper for on-chip wiring on the sub-μm scale, known as copper damascene interconnect, high concentration of copper ions has no point because of the smaller size scale. On the contrary, high Cu^{2+} concentration causes non-negligible dissolution of copper seed layer in nanometer thickness. So, relatively low copper concentration baths are used typically.

In every acid copper plating bath, small amounts of Cl^- ions are added as indispensable components in addition to the principal components of $CuSO_4$ and

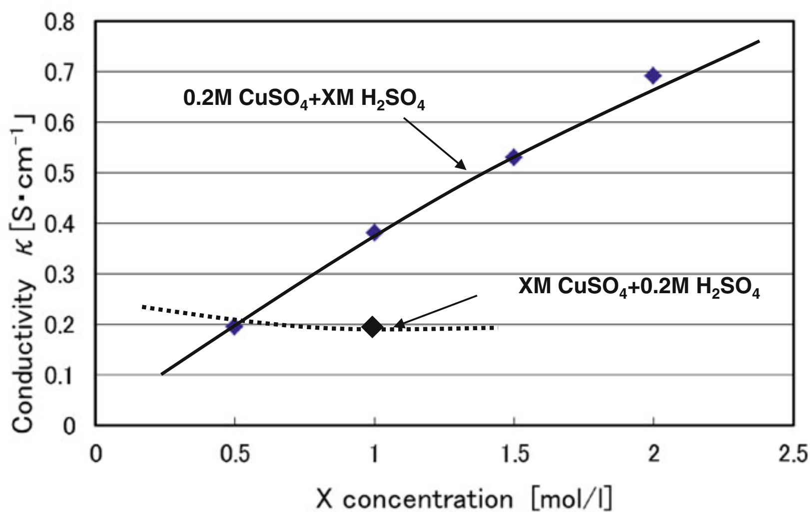

Fig. 1.1 Conductivity of acid copper sulfate bath changing with sulfuric acid and copper sulfate concentration. ※ Electric conduction mechanism of acidic solution; Grotthuss mechanism

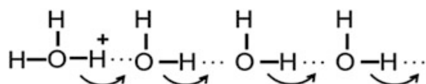

H_2SO_4. The Cl^- concentration is strictly controlled in a narrow range from about 1–2 mM. The presence of Cl^- ions at conentrations higher than the upper limit of about 2 mM raises copper anode passivation by precipitation of CuCl on the surface. On the other hand, below the lower limit of 1 mM, copper deposits with excellent properties cannot be obtained because of unequal action of organic additives on the copper deposition reaction. With the development of surface analysis/observation methods like as STM, AFM, and etc., the roles of the addition agents in copper plating are becoming clear.

1.2 Electrochemical Kinetics of Copper Deposition and Dissolution

(1) Consecutive reaction mechanism of copper deposition and dissolution

The overall reaction of copper deposition and dissolution is described simply as follows: a cupric ion is reduced with two electrons to form copper, and vice versa.

$$Cu^{2+} + 2e \Leftrightarrow Cu$$

However, the real aspect of the reaction was unclear for a long time. From the end of the 1950s, an abundance of information on the Cu^{2+}/Cu system in sulfuric acid bath started to be found by electrochemical methods Mattson et al. [4–6]. Suggested the two-step reduction/oxidation reaction and crystallization/decrystallization process for the Cu^{2+}/Cu system by means of galvanostatic measurements, as shown below. Similar reaction kinetics were proposed by Fisher et al. [4].

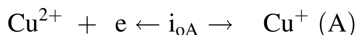

$$Cu^{2+} + e \leftarrow i_{oA} \rightarrow Cu^{+} \quad (A)$$

$$Cu^{+} + e \leftarrow i_{oB} \rightarrow Cu_{ad} \quad (B)$$

$$Cu_{ad} \longleftrightarrow Cu_{lattice} \quad (C)$$

Bockris et al. showed that the redox process between Cu^{2+} and Cu^{+} (A) is rate-controlling, while Cu^{+} exists in a reversible equilibrium with Cu at the electrode surface. And in the case of a copper surface prepared by melting in Helium (with low dislocation density of the surface), surface diffusion of Cu_{ad} to $Cu_{lattice}$, reaction (C) is rate-determining. And further, by observing the extremely low increase in the potential at the early stage of potential-time transients they found that the reaction (B) was a very fast reaction and the exchange current density (i_{0B}) of the reaction was larger than 30 mA/cm^2. For the reaction (A), an i_{0A} of around 3 mA/cm^2 was estimated by extrapolation of Tafel lines on potential-current curves with 0.1 M $CuSO_4$ + 0.5 M H_2SO_4 bath at 30 °C. Figure 1.2 shows the schematic view of the consecutive reaction stages involved in the copper deposition and dissolution reactions.

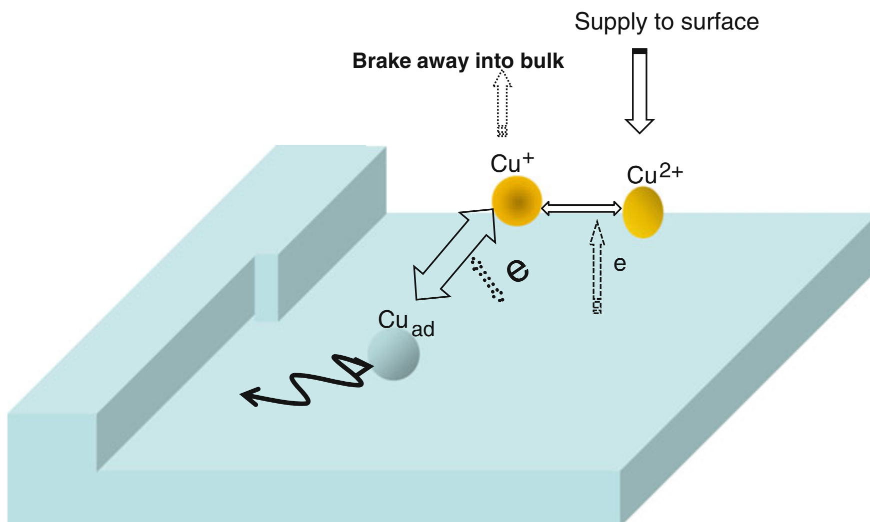

Fig. 1.2 Consecutive reaction stages involved in the copper deposition and dissolution reaction. The reaction, $Cu^{+} + e \Leftrightarrow Cu_{ad}$, is fast to be in quasi equilibrium state over wide cathodic and anodic polarization region

Later in the 1970s, Molodov and co-workers [7, 8] investigated the theoretical relationship between the electrode potential and intermediate concentration for the consecutive electrochemical reaction system involving low valence intermediate on the basis of Butler-Volmer equations for each elementary reaction.

For copper deposition and dissolution reactions, they indicated that the Cu^+ ion concentration at the surface changes depending on the electrode potential (E). In detail, in the low polarization region where the reaction (B) is so fast compared with reaction (A) as to be in a reversible state, the Cu^+ concentration changes with E in accordance with the Nernst equation.

$$E = E_o + (RF/F)\ \mathrm{In}\ [(Cu^+/Cu)] \tag{1.1}$$

While, in the highly polarized region where both reactions are in irreversible states, the relationship between E and Cu^+ concentration obeys the following equations.

For anodic polarization,

$$E = K_1 + RT/(F(\alpha_B - \alpha_A)) \cdot \mathrm{In}\ [(Cu^+)/(Cu)] \tag{1.2}$$

For cathodic polarization,

$$E = K_2 + RT/F(\beta_B - \beta_A) \cdot \ln\left[(Cu^+)/\left(Cu^{2+}\right)\right] \tag{1.3}$$

$\alpha_{A,}$ $\beta_{A,}$ $\alpha_{B,}$ β_B are transfer coefficients of the elementary reactions (A) and (B), respectively. K_1 and K_2 are constants determined with transfer coefficients and reaction constants of the elementary reactions.

Equation (1.2) indicates that E changes depending on Cu^+ concentration and electrode activity, Eq. (1.3) depending on Cu^+ concentration as well as Cu^{2+} concentration. The relationship between E and Cu^+ expressed by Eqs. (1.1), (1.2), and (1.3) is shown schematically in Fig. 1.3. When the relationship between reaction intermediate Cu^+ concentration and E is possibly obtained as well as the exchange current and transfer coefficients of reaction (A), the exchange current density and also the transfer coefficients of reaction (B) can be obtained.

Molodov et al. [8] confirmed experimentally the relationship between Cu^+ concentration and electrode potential during copper deposition and dissolution, expected by Eq. (1.1). They found that Cu^+ ions diffuse away from the copper electrode electrolyzed in a perchlorate bath of 14 mM Cu^{2+} + 5 $NHClO_4$ by using a platinum indicator and that the Cu^+ concentration change with the electrode potential obeys Nernst's equation. Also, they confirmed the clear potential shift of ca. 30 mV in the relationship around at the equilibrium potential, which was caused by the change in electrode activity (Cu_{ad}), indicating an accumulation of adatoms on the electrode surface in the cathodic polarization region.

It is important to note that the results clearly show the reversible reaction (B) in the deposition or dissolution potential, even though they did not get to observe the relationships of Eqs. (2) and (3) because of the still very small polarization potential.

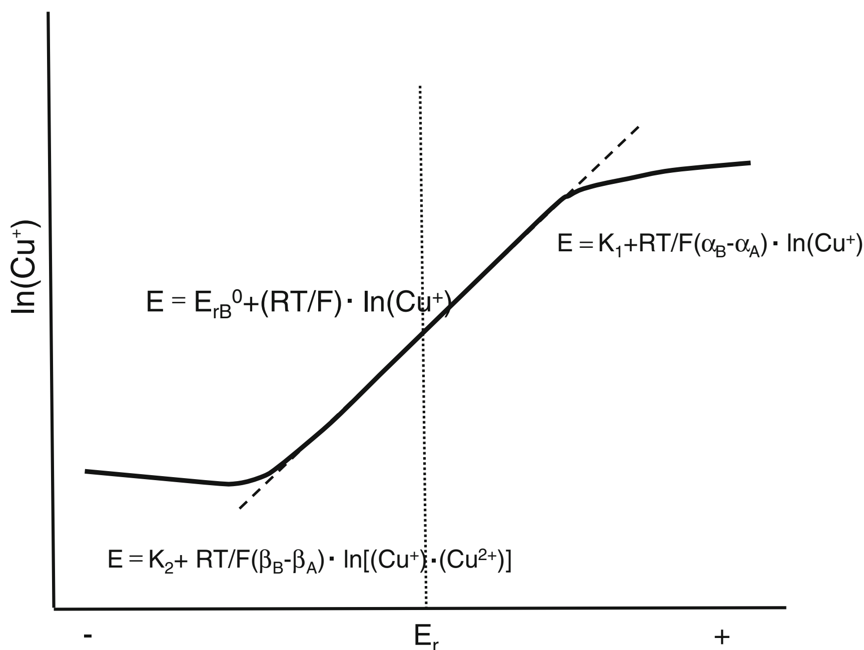

Fig. 1.3 Schematic relationship between reaction intermediate and electrode potential for consecutive copper deposition and dissolution reaction model, assuming $i_{0A} \ll i_{0B}$ and $(Cu_{ad}) =$ constant, by Molodov et al. [7]. The intermediate concentration changes with the potential obeying Nernst's equation in the low overpotential region

Other authors [9–14] also confirmed the two-step reduction mechanism in the Cu^{2+}/Cu system. Peter and Cruser [9] confirmed the two-step reduction mechanism in the kinetics of Cu^{2+}/Cu in a chloride solution using a chrono-potentiometric method. Applying a mathematical model based on the two-step reaction mechanism coupled with the disproportionation reaction of cuprous ions in a $Cu/CuSO_4$ system under pulse current conditions, Wan [10] evaluated the exchange current densities of the consecutive two charge transfer steps of copper reduction. By using a potentiostatic pulse, rotating disk electrodes, and EIS techniques in the analysis of copper deposition on a real surface, Harrison and co-workers [11–13] confirmed the two-step reduction mechanism for the electron transfer reaction and suggested that adatoms need not be invoked to explain the experiments. Glarum and Marshall [14] analyzed the admittance of rotating disk copper electrodes in $CuSO_4$-H_2SO_4 system as a function of frequency, potential, and concentration on the basis of the two-step reduction model. Although the basic electrode model provided an adequate explanation for the results at the equilibrium potential, substantial deviations occur at anodic potentials due to disproportionation.

(2) Kinetic analysis by the rotating ring-disk electrode system, RRDE

In an acid copper sulfate bath, the intermediate Cu^{+} ions of the copper deposition and dissolution reactions are stable enough in the solution to be detected by the rotating ring disk electrode system [15–17]. As indicated in the paper by Moldov et al. [7], if a concentration change of an intermediate such as Cu^{+} and Cu_{ad} on a copper surface are measurable over the wide potential range of copper electrode, details of the deposition and dissolution mechanism including exchange current densities of the elementary reactions can be cleared up.

Figure 1.4 shows the concentration change of the Cu^{+} ions (given in i_R) and the polarization current i_D of the disk electrode over the wide potential range for the copper deposition and dissolution in baths of various Cu^{2+} concentration, measured using the rotating ring-disk electrode system (RRDE) [18]. In the anodic dissolution of copper, i_R increased linearly and reached a limiting value independent of Cu^{2+} concentration with an increase in anodic over-potential up to 100 mV. In the cathodic deposition of copper, an increase in i_R was observed with small polarization up to about 10 mV, followed by a linear decrease with increase in the cathodic polarization potential. The slight i_R increase corresponds to the Cu^{+} ion's increase caused by the accumulation of Cu_{ad} in the surface diffusion reaction (C). In both polarization regions, the slope of the linear part of the log iR-E curves was about 60 mV/decade, obeying the Nernst equation, indicating that reaction (B) is in a quasi equilibrium state in the polarization regions. Further, the log i_R-E relation deviates from the linear line around a cathodic over-potential of about 150 mV, and reaches minimum values that depend on Cu^{2+} concentration with increasing over-potential, as expected from Eq. (3). In the potential region more negative than about 0.1 V versus SHE, the reaction (B) becomes a rate-determining step and is no longer in a quasi reversible state. That is, the copper deposition reaction is under the mixed control of reaction (A) and (B). Tindall et al. [16] pointed out that the potential region where no Cu^{+} ions were detected in copper deposition is more negative than 0.09 V versus SHE. The region corresponds to the mixed controlled reaction region.

In Table 1.2, the characteristics of the log i_R-E and log i_D-E relations in Fig. 1.4 are summarized. The exchange current densities and transfer coefficients are estimated from the Tafel lines observed under cathodic polarization. In this table, data obtained with log i_R-E and log i_D-E curves for copper deposition and dissolution reactions at various bath temperatures are also listed.

The limiting value of i_R observed in the anodic polarization region is attributable to the disproportionation reaction of the Cu^{+} ions. When the Cu^{+} ion concentration reached a certain concentration level, the Cu^{+} ions broke down to Cu^{2+} ions and Cu particles according to the following reaction, called the disproportionation reaction.

$$2Cu+ \rightarrow Cu^{2+} + Cu \downarrow$$

The Cu particles precipitated in the vicinity of the copper anode are sometimes so large so as to be visible in practical plating line. Once small metallic particles

Table 1.2 Electrochemical characteristics of i_R –E and i_D–E curves measured by RRDE system in acid copper sulfate baths of various bath temperature and $CuSO_4$ concentration

$CuSO_4$ XM H_2SO_4 0.5 M 30 °C	E eq (mV) versus SHE	iR.eq (μA)	iR.min (μA)	Exchange current density (mA cm^{-2}) io_c	Transfer coefficient β
X = 1.0 M	300	88	0.55	3.6	0.6
X = 1.4 M	288	58	0.34	2.3	0.6
X = 1.2 M	279	42	0.26	1.7	0.6
X = 1.1 M	270	33	0.21	1.2	0.6
$CuSO_4$ $_{xM}$ H_2SO_4 0.5 M					
t = 20 °C	302	32	0.4	1.7	0.59
t = 30 °C	300	88	0.55	3.6	0.6
t = 40 °C	296	140	0.94	7.3	0.6
t = 50 °C	294	280	2.6	12.1	0.61

produced from some kind of cause in the solution, Cu^+ reduction and Cu^+ oxidation reaction may proceed concurrently in equal rate on the particles to grow them larger and larger.

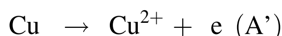

$$Cu \rightarrow Cu^{2+} + e \quad (A')$$

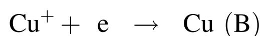

$$Cu^{+} + e \rightarrow Cu \quad (B)$$

On the other hand, copper particles dipped into the Cu^{2+} solution dissolve to Cu^+ ions accompanying reduction of Cu^{2+} to Cu^+ ions, and copper dissolution reaches the equilibrium state [19]. Continuous O_2 provided to the solution oxydizes the Cu^+ ions to Cu^{2+} ions, therefore, converting the copper metal into Cu^{2+} ions. The reaction is known and described as a comproportionation reaction, relative to disproportionation reaction. It is reported that copper dissolves in the same manner in the presence of chloride ions [20].

(c) Indirect proof for consecutive reactions of copper deposition by pulse plating

In order to improve the physical properties of copper deposits, pulsed current electrolysis has been studied. It has been found that the current efficiency of copper deposition and the surface morphology of the copper deposits are remarkably affected by the pulse parameters [21–23]. These phenomena are closely related to the deposition mechanism and the behavior of intermediate, Cu^+, in the electrodeposition of copper.

Figure 1.5 shows a schematic illustration of square-wave pulsed current and resulting electrode potential of the pulsed current electrolysis in the millisecond range. The duty factor of the pulse plating is defined as the ratio of Pulse-on time to 1 cycle of Pulse-on and off time. In this pulsed plating, even if the average current density is not changed, the current efficiency of copper deposition decreased with decrease in the duty factor, and also epitaxial growth of copper deposits is observed at relatively high average current density.

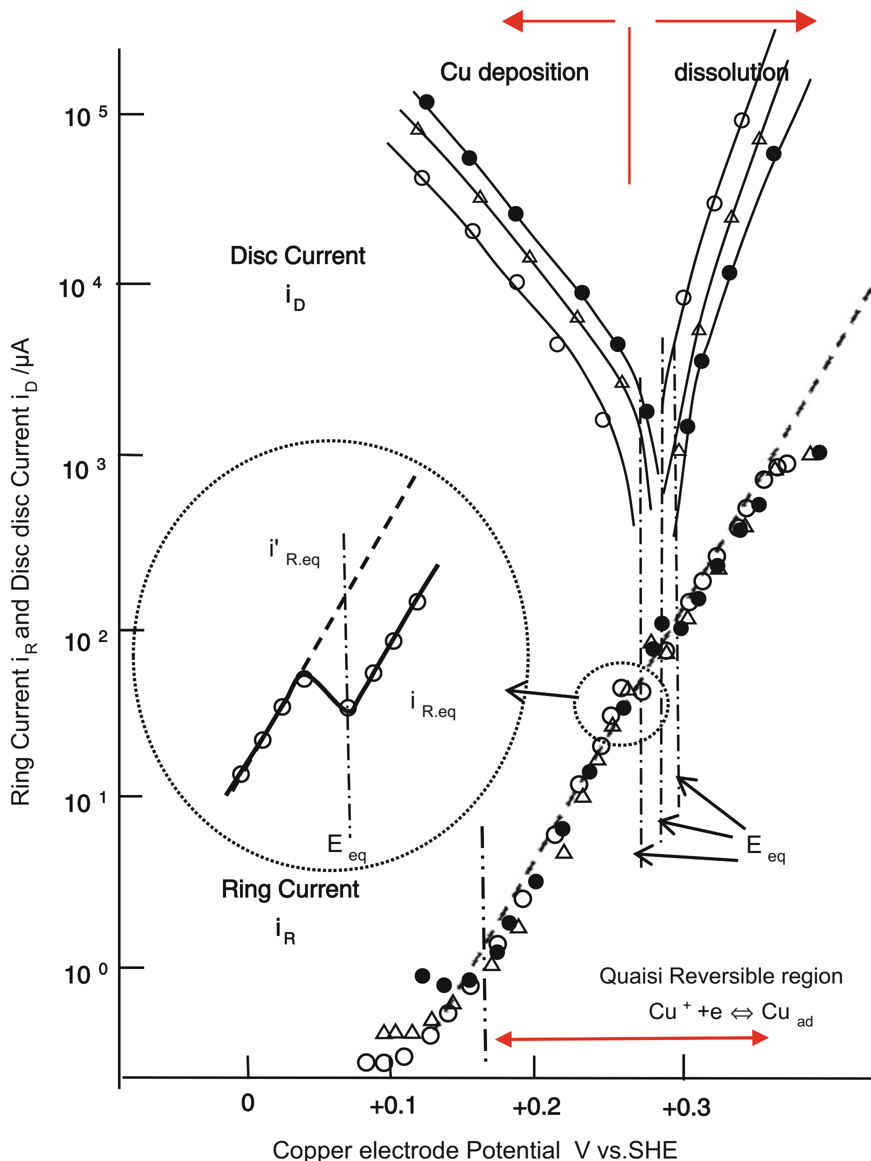

Fig. 1.4 Changes in reaction intermediate (Cu^+) concentration and copper deposition and dissolution currents depending on copper electrode potential, measured by Rotating Ring Disk Electrode system in acid copper sulfate baths ($CuSO_4$ (x) M + H_2SO_4 0.5 M). $CuSO_4$; ●; 1 M, △; 0.4 M, ○; 0.1 M

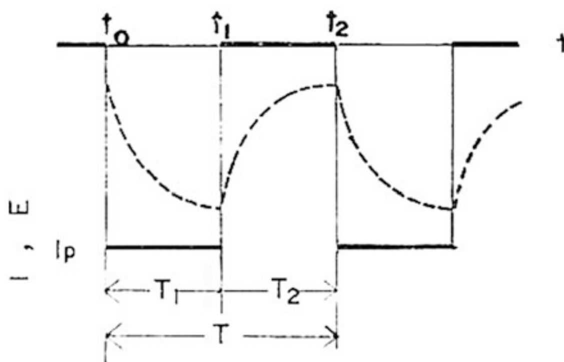

Fig. 1.5 Schematic diagram of square-wave pulsed current and resulting electrode potential.: Pulsed current,: Electrode potential T: Pulse repetition time, T1: Pulse-on time, T2: Pulse-off time, Ip: Pulsed current, Pulse duty factor = T_1/T, Average current = $I_p \times T_1/T$

Figure 1.6 shows the changes in current efficiency of copper deposition with average current densities as a function of pulsed current density in copper sulfate bath. The larger the pulsed current density is, id est, the longer the pulse-off time is, the lower the current efficiency is.

Figure 1.7 shows surface morphology of copper deposits 2 μm in thickness obtained on the (111) plane of a copper single crystal at an average current density of 75 mA/cm^2 under direct current electrolysis and pulsed current electrolysis. The current efficiencies of copper deposition at the average current density are almost 100 %. Whereas a large amount of small pyramidal growth caused by nucleation is observed with direct current electrolysis, distinct layer growth and also sharply defined spiral growth, characteristic of epitaxial growth, are observed with pulsed current electrolysis.

Both phenomena reflect the step-wise copper deposition mechanism, in which the elementary reaction (B) is so fast as to be in quasi equilibrium. Figure 1.8 shows the changes in Cu^+ concentration (i_R) with average pulsed current as a function of pulsed current density in acid copper sulfate bath, measured with a RRDE. For comparison, Cu^+ concentration changed with direct current electrolysis is plotted together. When the pulsed current electrolysis is applied, clearly seen

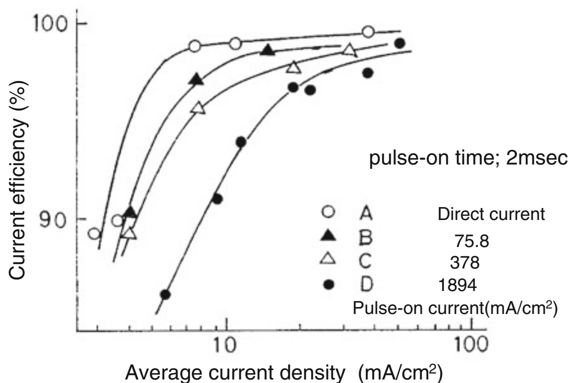

Fig. 1.6 Changes in current efficiency of copper deposition with average current densities as a function of pulsed current density in copper sulfate bath ($CuSO_4$ 0.8 M + H_2SO_4 0.5 M) at 30 °C

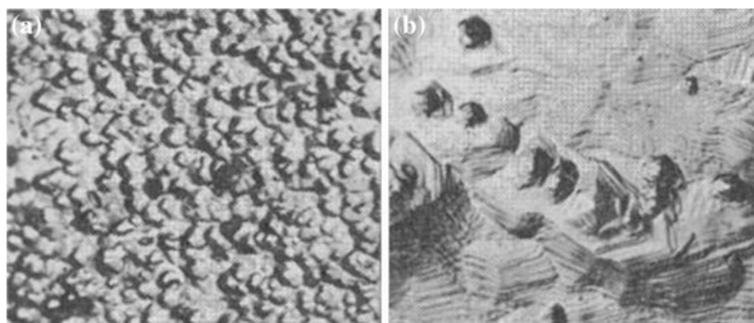

Fig. 1.7 Surface morphology of copper deposits on (111) plane of copper single crystal under the direct current electrolysis and pulsed current electrolysis. **a** direct current 75 mA/cm^2, **b** pulsed current 750 mA/cm^2, pulse-on time 1 ms, duty factor 10 %

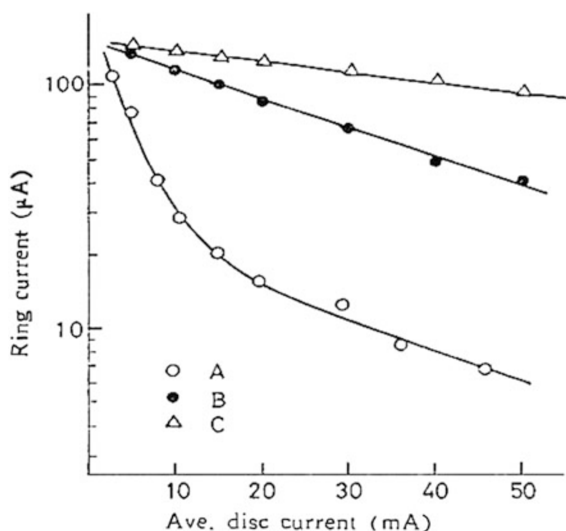

Fig. 1.8 Changes in Cu^+ concentration (i_R) with average pulsed current under the pulsed current electrolysis of copper deposition in acid copper sulfate bath ($CuSO_4$ 0.8 M + H_2SO_4 0.5 M) at 30 °C. Collection efficiency; 0.32, Surface area of disk electrode; 0.785 cm^2, Pulse-on time; 1.0 ms, Rotation speed; 1000 RPM, Ring potential = + 0.64 V versus SHE, Pulsed current density: A; D.C., B; 130 mA/cm^2, C; 380 mA/cm^2

Cu^+ concentration is kept high, and further, the higher the pulsed current density is, the higher the Cu^+ concentration is.

It would appear that the current efficiency decrease is due to "diffusion away" of the reaction intermediate, Cu^+, from the copper surface and the epitaxial growth is caused by hindering of nucleation with the buffering action of the reaction (B) and also by the dissolution and reconfiguration of unstable copper atoms on the copper surface during the pulse off-time. Tantavichet et al. [24] investigated a model for galvanostatic pulse plating via pulse current and pulse reverse modes and compared with experimentally obtained electrode responses during copper deposition, indicating the appropriate model incorporates capacitance effects due to double-layer charging and adsorption of an intermediate, in which arises a series connection between the adsorption pseudocapacitance and faradaic reaction (B).

1.3 Role of Chloride Ions in Copper Deposition and Dissolution

As an indispensable component for copper plating, a small amount of Cl^- ions is added to the acid copper sulfate bath at 1−2 mM concentration. The acceleration of copper deposition and dissolution, synergetic effects on copper deposition with organic additives, copper anode passivation are well-known actions.

(a) Cl^- adsorption and copper deposition/dissolution reaction depending on copper electrode potential

In acid copper sulfate bath, zero charge potential (pzc) of the copper is −0.26 to −0.61 V versus SHE [25], and Cl^- ions are adsorbed on the copper surface to different extents depending on the electrode potential. Since the beginning of 1990s, the adsorption state of Cl^- was investigated using Advanced surface analysis method such as Auger spectroscopy, low-energy electron diffraction (LEED) , scanning tunneling microscopy (STM) , atomic force microscope (AFM) [26–29], and found information on Cl^- adsorption behavior on copper surfaces.

Figure 1.9 shows Cl^- adsorption states and the changes of copper deposition/dissolution reaction states depending on copper electrode potentials. The cyclic voltamogram was obtained in 0.01 M $HClO_4$ + 1 m MKCl at 0.1 V/S, showing Cl^- desorption and adsorption in the potential region of −0.1 to −0.5 V versus SHE. The Cl^- on the copper surface in the potential region moves too fast to be observed with STM, and is considered to be in a disordered adsorption state. While

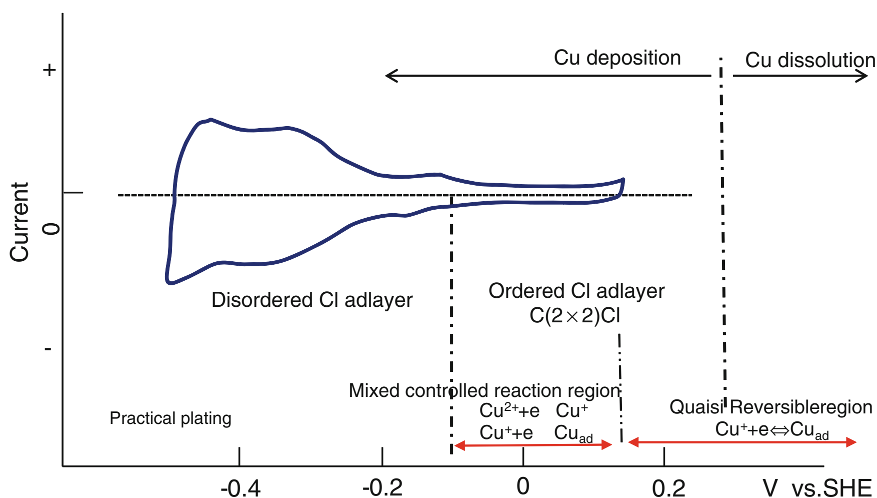

Fig. 1.9 Adsorption behavior of Cl^- on copper surface depending on electrode potential. Cyclic voltamogram inserted inside was obtained with 0.01 $MHClO_4$ + 1 m MKCl at 0.1 V/s by T.P. Moffat et al. showing Cl^- desorption and adsorption

in the potential region more positive than − 0.1 V, for example on the Cu (100) plane, an ordered adsorbed layer of c (2 × 2) Cl and distinct steps of [101] and [001] directions were formed on the copper surface [27]. The c (2 × 2) Cl is an adlayer with a Cl coverage of 1/2, formed by allocating one Cl^- atom to a hole site formed with four nearest neighbor copper atoms on a copper surface. The Cl atoms of the c (2 × 2) Cl adlayer have a high degree of freedom to be exchanged with Cl^- in the solution. Thus, if there exists no Cl^- in the solution, the adlayer would disappear in a moment. Even in the potential region more positive than + 0.1 V versus SHE where copper dissolves, the c (2 × 2) Cl adlayer is found to be maintained in the Cl^- containing solution.

Figure 1.10 shows in situ STM images of a c (2 × 2) Cl^- adlayer formed on Cu (100) in a 1 mM HCl + 0.01 M $HClO_4$ electrolyte. In the left image, straight steps of [100] orientation are observed, in the top-right image appears the phase shift of the c(2 × 2)Cl^- lattice associated with surface steps, while a screw dislocation is evident in the bottom-right image 28.

In Figure 1.9 is indicated the potential regions where copper deposition and dissolution occurs in the presence of Cu^{2+} ions in the solution. As described in the previous section, the equilibrium potential of copper deposition and dissolution in 0.5 M $CuSO_4$ sulfate bath is about 0.30 V versus SHE, and the reaction (B), the second discharge reaction between Cu_{ad} and Cu^+, is in quasi equilibrium state in the

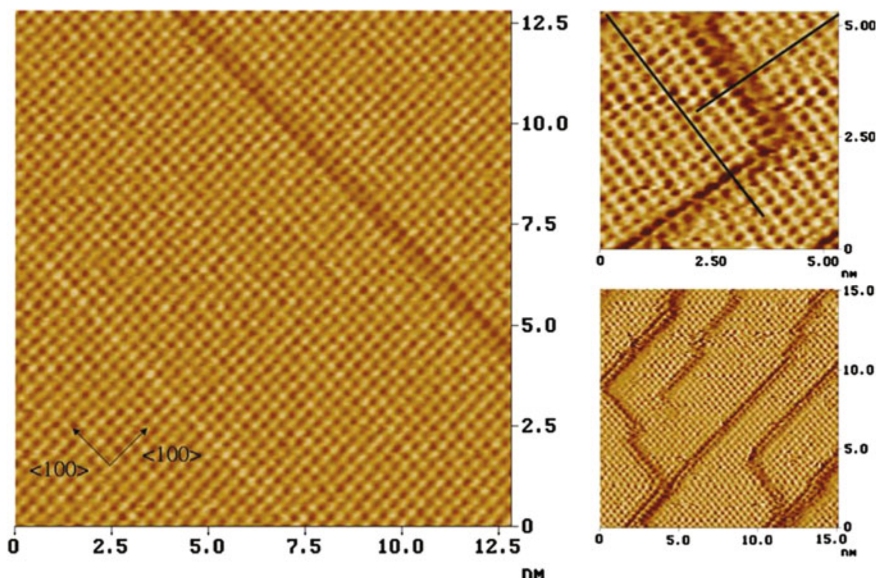

Fig. 1.10 In situ STM images of c (2 × 2) Cl^- adlayer formed on Cu (100) in a 1 mM HCl + 0.01 M $HClO_4$ electrolyte by Moffat et al. [28]

potential region more positive than 0.15 V. It is noteworthy that in practical plating such as decorative bright copper plating, through-hole plating is conducted in the potential range more negative than 0.15 V versus SHE, where no Cu^{+} ions exist in reversible state. The negative potential shift of the practical copper plating is a result of suppression of the copper deposition reaction, achieved by the synergetic effect of Cl^{-} adlayers and polymeric additives such as PEG, PPG, and so on.

(b) Effect of Cl^{-} on the copper deposition and dissolution reaction
Figure 1.11 shows the effect of Cl^{-} addition on log i_R-E and log i_D-E curves in an acid copper sulfate bath measured on a RRDE. On the disk electrode, copper deposition and dissolution was performed potentiostatically to obtain log i_D-E curves. Cu^{+} ions produced on the disk electrode were oxidized concurrently on the ring electrode, being measured as ring current i_R. By addition of 3 mM Cl^{-}, both deposition and dissolution currents increase, and i_R (Cu^{+}) increases correspondingly. The ring current increases linearly with a slope of about 60 mV/decade depending on the copper disk electrode in the low polarization region. The graphical form of the log i_R-E and log i_D-E curves are similar to the ones obtained with no Cl^{-} bath. With 9 mM Cl^{-} addition, the deposition current and corresponding i_R increase with increasing potential in the positive direction. However, near the equilibrium potential both i_R and i_D slow down to steady values, the former to 2 mA, the latter to 100 μA, respectively. The phenomena of reaching the plateau in i_D and i_R are caused by precipitation of CuCl on the copper disk electrode.

It is well known that Cl^{-} ions adsorb specifically on copper surfaces to accelerate the copper deposition and dissolution reaction via an electron-bridge mechanism [30]. That is, Cu^{2+} ions coordinate to Cl^{-} ions adsorbed on the copper surface, and are then reduced to Cu^{+} ions at a higher rate than ions without Cl^{-} coordination. For example, Fig. 1.12 shows changes in copper deposition current on a rotating disk electrode at various polarization potentials versus Cl^{-} concentration in acid copper sulfate baths of 0.2, and 1.0 M $CuSO_4$. The set potentials are within the Tafel region of log i_D-E curves in Fig. 1.13, in which reaction (B) is in a quasi equilibrium state. The acceleration rate is normalized with reference to the current with no Cl^{-} addition, $i_{Cl-=0}$ at each set potential. The currents are inside the figure. In the early stage of Cl^{-} addition, every rate increases drastically, and then moderately increases to reach a constant rate depending on the set potential and Cu^{2+} concentration. The Langmuir plots of the acceleration curves provide straight lines for each curve as shown in Fig. 1.13, and confirm Langmuir adsorption of Cl^{-} ions on copper surface. The saturation currents from the slopes of the straight lines plotted against the reference currents (at set potentials) in Fig. 1.14 indicate that the saturation currents are almost twice the reference current in the low current region. The decrease in the saturation current, deviating lower from the dotted line in the high current region would be due to the effect of the diffusion retardation of Cu^{2+} ions. The adsorbed Cl^{-} is envisaged as the Cl^{-} adlayer described in the former section, and the coverage rate of Cl^{-} on copper surface at the Cl^{-} concentration range of from 1–2 mM can be seen to be 70–80 % from the acceleration curves in Fig. 1.12 with the plating condition.

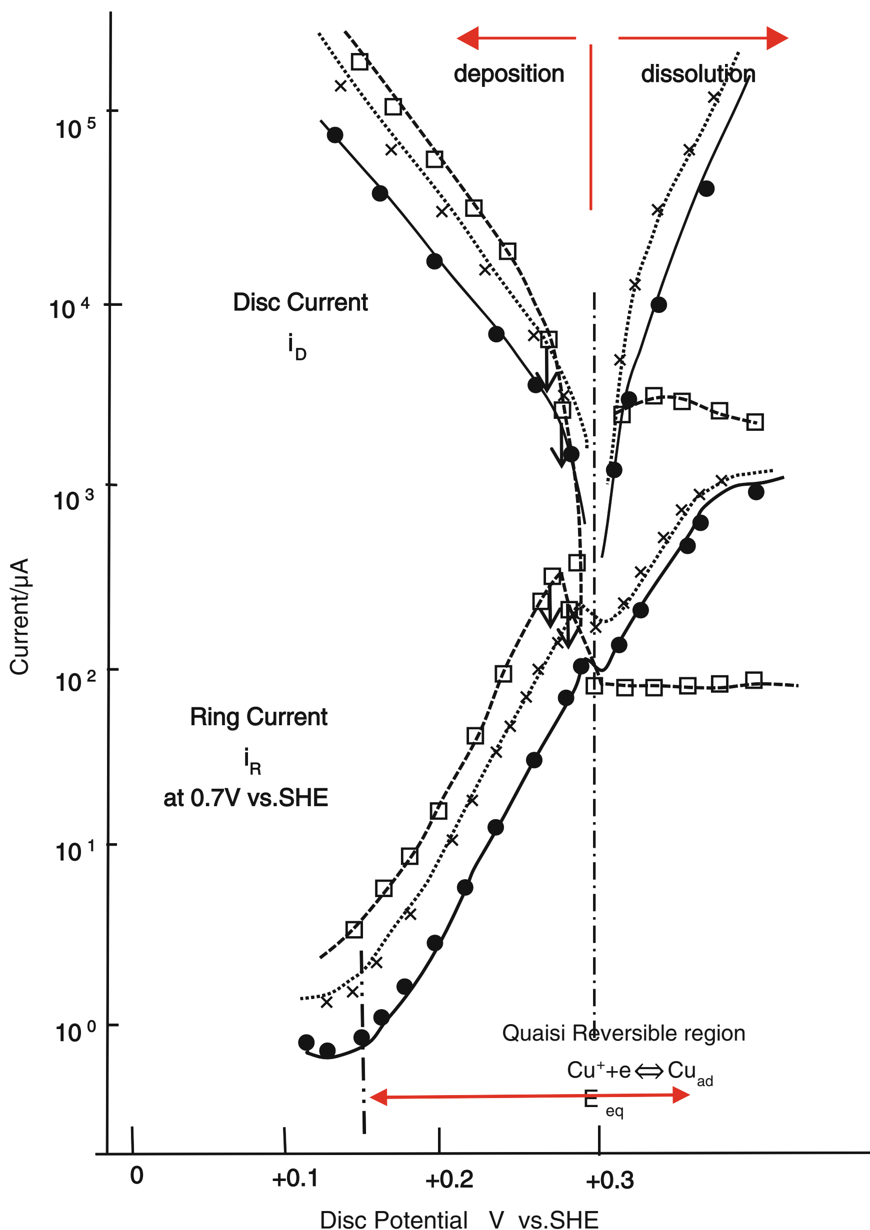

Fig. 1.11 Effect of Cl^- concentration on logi_R-V and log i_D-V curves in an acid copper sulfate bath of $CuSO_4$ 1.0 M + H_2SO_4 0.5 M HCl: ●; 0 mM, × ; 3 mM; 9 mM

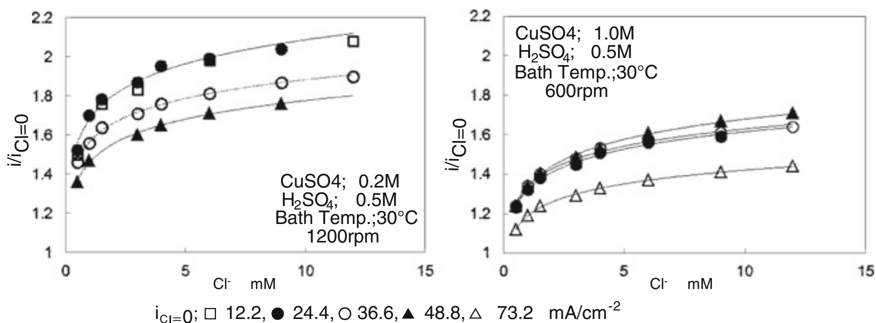

Fig. 1.12 Changes in acceleration rate of copper deposition reaction on rotating disk electrode at various polarization potential with changing Cl^- concentration in acid copper sulfate baths. The acceleration rate is normalized with reference to the current with no Cl^- addition, $i_{Cl-\ =\ 0}$ at each set potential

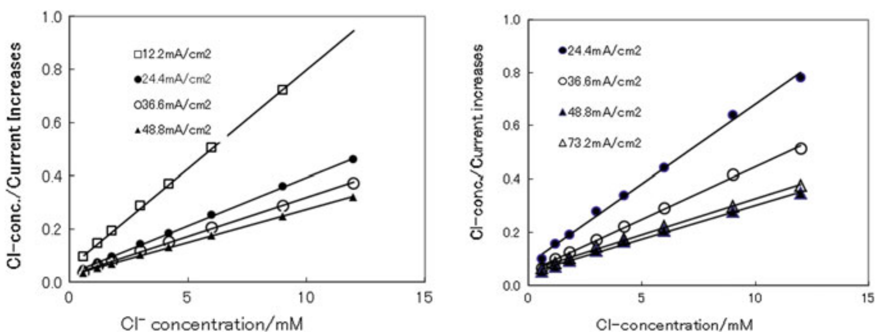

Fig. 1.13 Langmuir's plot of Copper deposition current change with Cl^- concentration at various polarization potential in acid copper sulfate baths. A; 0.2 M $CuSO_4$ + 0.5 M H_2SO_4, B; 1.0 M $CuSO_4$ + 0.5 M H_2SO_4 Inside figures are reference currents at no Cl^- in each set potential

Fig. 1.14 Saturation current from the Langmuir's plot of Copper deposition current change with Cl^- concentration at various reference currents in acid copper sulfate baths of 0.2 M $CuSO_4$ + 0.5 M H_2SO_4 and 1.0 M $CuSO_4$ + 0.5 M H_2SO_4

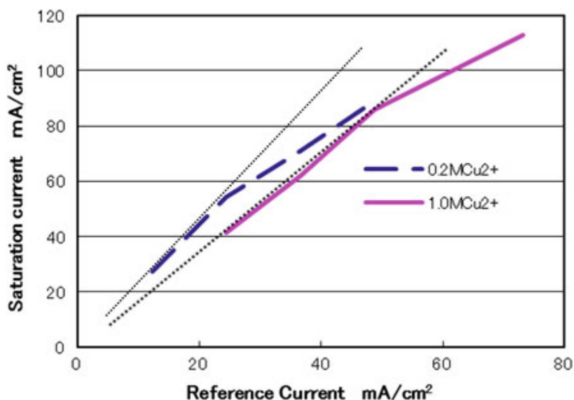

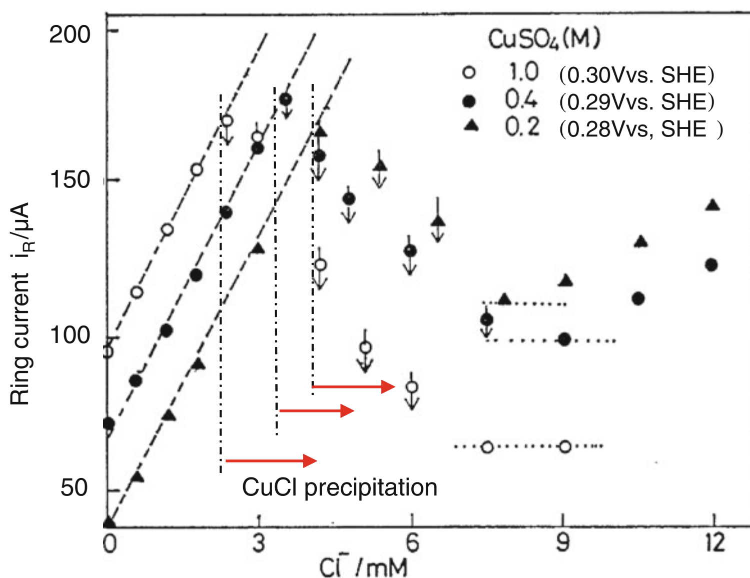

Fig. 1.15 Changes in intermediate concentration (Ring current i_R) with Cl^- concentration at the rest potential (Er) of copper in acid copper sulfate baths. Straight section; $i_R \propto 7.9 \times 10^{-4} \sqrt{[Cu^{2+}]}\,(1 + 7 \times 10^2\,[Cl^-])$

(c) Reaction intermediate increase with Cl^- addition

The increase in reaction intermediates on copper surface with Cl^- addition shown in Fig. 1.11 will be discussed in more detail. Figure 1.15 shows changes in intermediate concentration (Ring current i_R) with Cl^- concentration at the rest potential (E_r) of copper in acid copper sulfate baths of various Cu^{2+} concentrations. For all solutions, i_R increases linearly with Cl^- concentration up to a specific concentration that depends on the Cu^{2+} concentration. These specific values are 2.0, 3.0, and 4.0 mM for the 1.0, 0.4, and 0.2 M Cu^{2+}, respectively. Above the specific Cl^- concentration, i_R decrease slowly down to each unique value, and then increased again with increasing Cl^- concentration. While, the rest potential of the copper disk electrode, E_r remained constant until the Cl^- concentration increased to a specific value, beyond which the E_r temporarily shifts about 10 mV in the cathodic direction. In the concentration region where the second increase of i_R is observed, the E_r tends to be the initial potential. The i_R decreases and E_r cathodic shifts are attributable to the formation of insoluble CuCl on copper surfaces. The copper disk is apparently covered with a white semi-transparent product at these Cl^- concentrations.

Itagaki et al. [20, 31] reported that the disproportional reaction of copper in Cl^- containing acid Cu^{2+} solution is composed of the following anodic and cathodic reactions involving the intermediate CuCl using the channel flow double electrodes. Cu metal is oxidized by Cu^{2+} ions reduction on copper surface to form Cu^+ species in the solution.

Cathodic Reactions

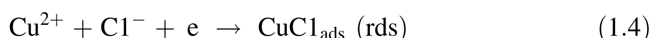

$$Cu^{2+} + Cl^- + e \rightarrow CuCl_{ads}\ (rds) \quad (1.4)$$

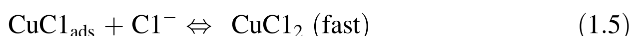

$$CuCl_{ads} + Cl^- \Leftrightarrow CuCl_2\ (fast) \quad (1.5)$$

Anodic Reactions

$$Cu + Cl^- \Leftrightarrow CuCl_{ads} + e\ (fast) \quad (1.6)$$

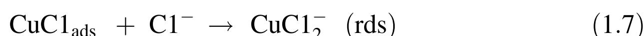

$$CuCl_{ads} + Cl^- \rightarrow CuCl_2^-\ (rds) \quad (1.7)$$

They proposed the reaction by observing the behavior of intermediate production and polarization current with the wide concentration range of Cl^- and Cu^{2+}. The anodic reaction was proposed by Lee et al. [32] for the anodic copper dissolution in acid copper chloride solution to explain the production behavior of $CuCl_2^-$.

According to the reaction scheme for the disproportionation reaction, the first step reaction (1) of the cathodic reaction is rate-determining (rds) and the reaction order of Cl^- and Cu^{2+} are 1. The linear increase in Cu^+ species with Cl^- concentration observed in Fig. 1.17 is understandable from the scheme.

Figure 1.16 shows changes in intermediate concentration (ring current i_R) at various copper deposition potentials with changing Cl^- concentrations in acid copper sulfate bath of 0.2 M $CuSO_4$ + 0.5 M H_2SO_4. Even under copper deposition conditions, every i_R increases in proportion to Cl^- concentration. As described in

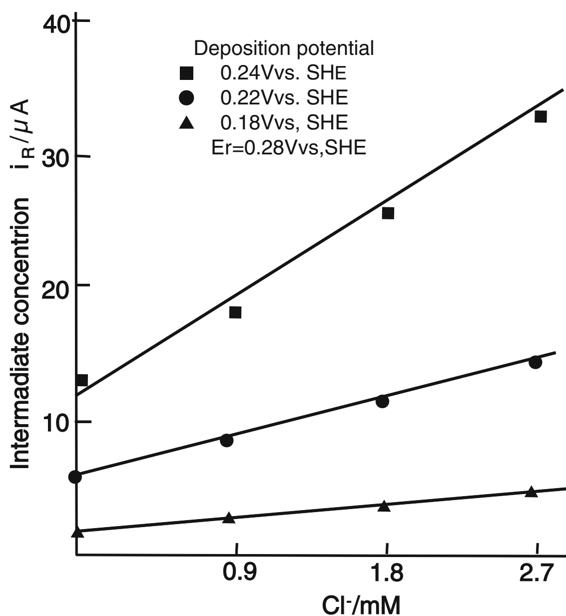

Fig. 1.16 Changes in intermediate concentration (Ring current i_R) at various copper deposition potentials with changing Cl^- concentrations in acid copper sulfate bath of 0.2 M $CuSO_4$ + 0.5 M H_2SO_4

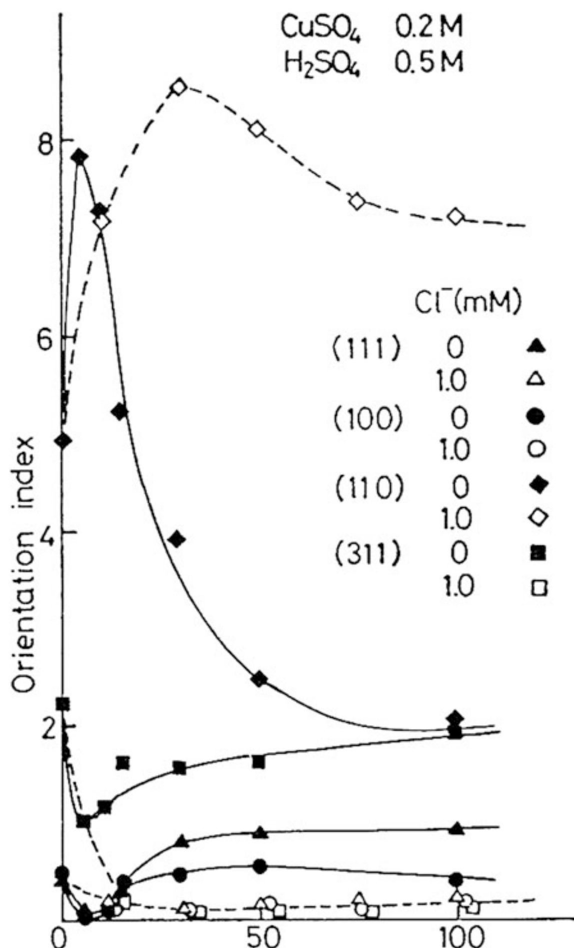

Fig. 1.17 Effect of current density and Cl^- ions on the orientation indexes of various Cu crystal facets of the copper deposits (40 μm). Substrate copper has (100) preferred orientation

Fig. 1.11, the reaction (3) is maintained still in a quasi equilibrium state under the deposition potential. Envisaging the disproportionation reaction during copper deposition, the linear increase in Cu^+ species is understood (Fig. 1.18).

(d) Epitaxial growth of copper deposits by Cl^-.

As the copper deposition and dissolution reaction in acid copper sulfate bath is accelerated and the reaction intermediate increased by Cl^- addition in small amounts, the structure of copper deposit is also affected strongly. By the addition of Cl^- ions, if the copper crystal nucleation in the course of copper deposition is suppressed, epitaxial growth of deposits should be accelerated.

As is well known, the activation overpotential of copper deposition on various crystal facets increases in the following order.

$$\eta\,(110) < \eta\,(311) < \eta\,(100) < \eta\,(111)$$

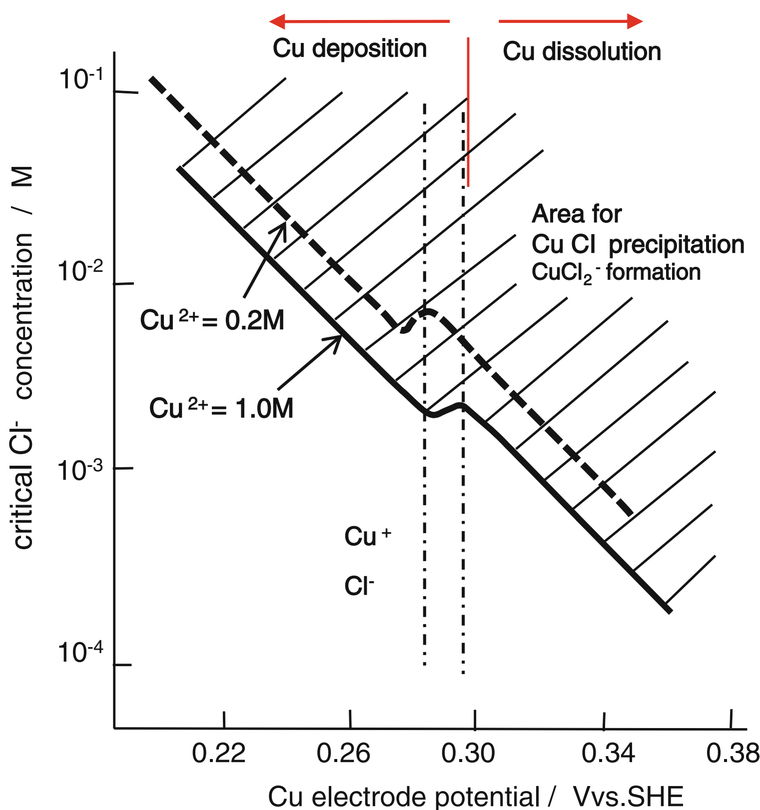

Fig. 1.18 Dependence of critical Cl^- concentration for CuCl formation on the copper electrode potential as a function of Cu^{2+} concentration—; 1.0 M Cu^{2+}, ———; 0.2 M Cu^{2+}

On the other hand, nucleation overpotential for two-dimensional crystallite increase in the following order [33–36].

$$\eta\ (111) < \eta\ (100)\ \eta\ (311) << \eta\ (110)$$

In the case of copper deposition on polycrystalline copper surfaces, if the nucleation reactions are suppressed, crystal facets with high growth rates (110) are expected to appear as a predominating facets, while other crystal facets with slower growth rates would disappear. Figure 1.17 shows the effect of current density and Cl^- ions on the orientation indexes of various Cu crystal facets of the copper deposits (40 μm thickness). Substrate copper is polycrystalline having (100) preferred orientation. The orientation indexes are defined following Wilson's method [37, 38].

In the absence of Cl^- ions, the preferred orientation of (110) characteristic of the deposit at low current density decreases with increase in deposition current density. While, in the presence of 1 mM Cl^- crystal facets except (110) almost

completely disappear, and strong (110) preferred orientation dominated even at high current density region. These results demonstrate the nucleation reaction is strongly suppressed and epitaxial growth is accelerated by Cl^-.

(e) CuCl precipitation on copper surfaces

As a large amount of Cu^+ ions produced on copper surface during anodic copper dissolution and Cl^- ions are indispensable constituent in the copper plating bath, copper anodes are sometimes passivated by CuCl precipitation on the copper surface. Also in cathodes there may be some inclusion of CuCl in the copper deposit when the copper deposition is conducted at a low current density, or on passivated substrates such as Ti, stainless steel, and so on. That is to say, the Cl^- concentration has a permissible upper limit, and so it is important to know the true Cu^+ concentration on copper surface.

The Cu^+ concentration can be calculated from the equilibrium constant for the disproportination reaction of Cu^+ in an acid copper sulfate solution. Bruckenstein et al. [17] determined the constant K to be 5.6×10^{-7} using the rotating ring-disk electrode system.

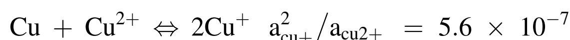

$$Cu + Cu^{2+} \Leftrightarrow 2Cu^{+} \quad a_{cu+}^{2}/a_{cu2+} = 5.6 \times 10^{-7}$$

For example, the activity of Cu^{2+}, a_{Cu2}^{+} in acid copper sulfate bath of 0.4 M $CuSO_4$ + 0.5 M H_2SO_4 is determined to be 0.022 from the rest potential of copper electrode, E_r listed in Tabel 1.2, and a_{Cu}^{+} to be 1.5×10^{-4}. While the solubility product of CuCl ($Ksp = a_{Cu}^{+} \times a_{Cl}^{-}$) is 1.72×10^{-7} [39]. Using these values the critical Cl^- concentration to begin CuCl precipitation on a copper surface, that is the upper limit of Cl^- concentration of the plating bath, is obtained to be 1.55×10^{-3}.

Soares et al. [40] investigated the mass change of copper electrodes by changing the Cl^- concentration from 1 to 8 mM in the acid copper sulfate bath of $CuSO_4$ 0.3 M + H_2SO_4 2.2 M using Electrochemical quartz crystal microbalance (EQCM) and cyclic voltamometry (CV), and found that CuCl precipitation occurs with Cl^- addition above 1 mM concentration and at low cathodic polarization region even under the copper deposition. As already described above in Fig. 1.15, the authors confirmed CuCl precipitation on copper surface by detecting the change in reaction intermediates concentration, Cu^+ or $CuCl_2^-$, with changing Cl^- concentration in the plating bath of various Cu^{2+} concentrations using RRDE. The critical Cl^- concentrations for CuCl precipitations are found to be 2, 3, and 4 mM for the baths of 1.0, 0.4, and 0.2 M Cu^{2+} concentrations, respectively. Considering the high concentration of the plating bath, those critical Cl^- concentrations would be reasonable.

As shown in Fig. 1.4 of the preceding section, Cu^+ concentration on copper surface changes depending on the electrode potential obeying the Nernst equation in the Cu plating bath. Therefore, the critical Cl^- concentration to begin CuCl precipitation in the copper plating bath should change with electrode potential [41]. Figure 1.17 illustrated the CuCl precipitation area expected on Cl^- concentration-potential diagram. This figure shows the Cl^- critical concentration

increase with the electrode potential decrease, resulting in no inclusion in the copper deposits under the usual plating conditions. On the contrary, the more noble the electrode potential, the smaller the critical concentration is. In the conventional copper plating bath, phosphorized copper anode is used to suppress the Cu^+ increase in the anodic copper dissolution. Recently, a new plating process using dimensionally stable anode (DSA) was developed to avoid the problems caused by Cu^+ accumulation, and was widely used.

References

1. Dini JW, snyder DD (2010) Electrodeposition of copper in modern electroplating. In: Schlesinger M, Paunovic M (ed) Wiley, NewYork
2. Wagner C (1951) Theoretical analysis of the current density distribution in electrolytic cells. J Electrochem Soc 98:116–128
3. Conway BE, Bockris J.O'M, Linton Ü (1956) Proton conductance and the existence of the H_3 ion. J Chem Phys 24:834–850
4. Seiter H, Fischer H, Albert L (1960) Elektrochemish-morphologische studien zur erforschung des mechanismus der elektrokristallisation, fern vom anfangszustand. Electrochim Acta 2:97–120
5. Mattsson E, O' J, Bockris M (1959) Galvanostatic studies of the kinetics of deposition and dissolution in the copper + copper sulfate system. Trans Faraday Soc 55:1586–1601
6. O' J, Bockris M, Enyo M (1962) Mechanism of electrodeposition and dissolution processes of copper in aqueous solutions. Trans Faraday Soc 58:1187–1202
7. Molodov AI, Markosyan GN, Losev VV (1972) Regularities of low-valency inter mediate accumulation during a step-wise electrode process. Electrochim Acta 17:701–721
8. Molodov AI, Yanov LA, Markosyan GN, Losev VV (1977) Surface effects during cathodic copper deposition from methanolic and aqeous solutions. Extend abstracts of I.S.E meeting, Vazna 69:313
9. Peters D, Cruser S (1965) Cathodic chronopotentiometry of copper (I) and copper (II) in chloride media. J Electroanal Chem 9:27–40
10. Wan CC (1974) A study of electrochemical kinetics of copper deposition under pulsed current conditions. Columbia University, Dissertation
11. Burrows IR, Harrison JA, Thompson J (1975) The deposition of copper. Electroanal Chem 58:241–249
12. Harrison JA, Sandbah DR, Stronach PJ (1979) The rate of deposition of copper, Zinc and Cadmium. Electrochim Acta 24:179–189
13. Burrows IR, Dick KL, Harrison JA (1976) A comparison of the rate of copper deposition at mercury copper amalgam and copper metal. Electrochim Acta 21:81–84
14. Glarum SH, Marshall JH (1981) An admittance study of the copper electrode. J Electrochem Soc 128:968–979
15. Tindall GW, Bruckenstein S (1968) A ring-disk electrode study of the deposition and stripping of thin copper films at platinum in sulfuric acid. Anal Chem 40:1637–1640
16. Tindall GW, Bruckenstein S (1968) A ring-disk electrode study of the electrochemical reduction of copper (II) in 0.2 M sulfuric acid on platinum. Anal Chem 40:1051–1054
17. Tindall GW, Bruckenstein S (1968) Determination of heterogeneous equilibrium constants by chemical stripping at a ring disk electrode. Anal Chem 40:1402–1404
18. Yokoi M, Konishi S, Hayashi T (1983) Mechanism of the electrodeposition and dissolution of copper in an acid copper sulfate bath. Denki Kagaku 51:310–315

19. Jenkins LH, Bertocci U (1965) On the equilibrium properties of single crystalline copper electrodes. J Electrochem Soc 112(5):517–520
20. Itagaki M, Yamamoto H, Watanabe K (2000) Disproportional reaction of copper in chloride solution investigated by channel flow double. Zairyo-to-Kankyo (in Japanese) 49:546–552
21. Lamb VA (1969) Electroplating with current pulses in the microsecond range. Plating 56:909–913
22. Cheh HY, Linford HB, Wan CC (1977) A pplication of pulsed plating techniques to metal deposition—2 pulsed plating of copper. Plating 64:66–67
23. Hayashi T, Yokoi M (1979) The role of intermediate (Cu +) in the electrodeposition of copper from an acid copper sulfate bath under pulsed current electrolysis. Denki Kagaku 47(11):654–658
24. Tantavichet N, Pritzker MD (2003) Low- and high-frequency pulse current and pulse reverse plating of copper. J Electrochem Soc 150:C665–C677
25. Trasatti S (1992) Electrified interfaces in physics, chemistry and biology. In Guidelli R (ed) Kluwer Academic Publishers, Dordrecht, p 245
26. Ehlers CB, Villegas I, Stickeny JL (1990) The surface chemistry of Cu (100) in HCl solutions as a function of potential: a study by LEED, Auger spectroscopy and depth profiling. J Electroanal Chem 284:403–412
27. Vogt MR, Lachenwitzer A, Magnussen OM, Behm RJ (1998) In-situ STM study of the initial stages of corrosion of Cu (100) electrodes in sulfuric and hydrochloric acid solution. Surf Sci 399:49–69
28. Moffat TP, Ou Yang LY (2010) Accelerator surface phase associated with super conformal Cu electrodeposition. J Electrochem Soc 157(4):D228–D241
29. Li WH, Wang Y, Ye JH, Li SFY (2001) In situ STM study of chloride adsorption on Cu (110) electrode in hydrochloric acid aqueous solution. J Phys Chem B 105:1829–1833
30. Nagy Z, Blaudeau JP, Hung NC, Curtiss LA, Zurawski DJ (1995) Chloride ion catalysis of the copper deposition reaction. J Electrochem Soc 142(6):L87–L89
31. Itagaki M, Tagaki M, Watanabe K (1996) Study of dissolution mechanism of copper in perchloric acid solution containing NaCl by channel flow double electrode and electrochemical quartz crystal microbalance. Corros Sci 38:1109–1125
32. Lee HP, Nobe K (1986) Kinetics and mechanisms of Cu electrodissolution in chloride media. J Electrochem Soc 133:2035–2043
33. Pangarov NA (1965) Preferred orientations in electro-deposited metals. J Electroanal Chem 9:70–85
34. Itoh S, Yamazoe N, Seiyama T (1977) Electrocrystalization of various metals onto copper single crystal substrates. Surf Techn 5:27–42
35. Damjanovic A, Setty TC, Bockris JO'M (1966) Effect of crystal plane on the mechanism and the kinetics of copper electrocrystallization. J Electrochem Soc 113:429–440
36. Okada G, Yamazoe N, Seiyama T (1976) Polarization measurement of copper deposition on copper single crystal electrodes by the galvanostatic double pulse method, Denki Kagaku (in Japanese) 44:413–417
37. Wilson KS, Rogers JA (1996). Tec Proc Amer Electroplaters Soc 51:92–95
38. Yokoi M, Konishi S, Hayashi T (1983) Effect of Cl^{-} ions on the crystallization process in acid copper sulfate baths. Denki Kagaku 51:416
39. 74th CRC Handbook of Chemistry and Physics (1992) Solubility product constants. CRC Press Inc., Boca Raton 8–49
40. Soares DM, Wasle S, Weil KG, Doblhofer K (2002) Copper ion reduction catalyzed by chloride ions. J Electroanal Chem 532:353–358
41. Yokoi M, Konishi S, Hayashi T (1983) Mechanism of the electrodeposition and dissolution of copper in an acid copper sulfate bath IV. Acceleration mechanism in the presence of Cl^{-} ions, Denki Kagaku 51(6):460–464

Chapter 2
Supression Effect and Additive Chemistry

Masayuki Yokoi

2.1 Additive Chemistry

The excellent additive systems for acid copper sulfate bath developed in the 1960s successfully produce bright copper deposits with smooth surfaces and high ductility. Since then, many applications of copper plating were developed for electronic device and through-hole plating for PCBs as well as conventional decorative plating on steel, electroforming, etc. In 1997, the Copper Damascene Process was developed in improved interconnect material fabrication of ULSIs by IBM. With this turning point, the role of addition agents came under further study using advanced analytical techniques such as Enhanced Raman Spectrometry, QCM, AFM, TEM, EIS, in addition to conventional electrochemical plating research methods.

Addition agents in acid copper sulfate bath consist of suppressors, levelers, and accelerators. The former suppress copper deposition on convex regions, and the latter catalyze copper deposition on concave regions in the presence of a small amount of Cl^{-} ions [1–4], resulting in via/trench copper. In the following sections, the roles of the addition agents will be described on the basis of knowledge accumulated by many researchers.

2.2 Role of Suppressors

PEG or PEG/PPG copolymers of nonionic surfactants and cationic dyes such as JGB containing nitrogen atoms are widely used as representative suppressors and levelers, respectively. Both of them exert a strong suppression effect on copper deposition reactions in the presence of Cl^{-} ions. The suppressor acts in a relatively

M. Yokoi (✉)
Osaka Prefecture University, 8-15 Taishi-Cho, 586-0041 Kawachi Nagano Shi, Japan
e-mail: masayuki_yokoi@hotmail.com

K. Kondo et al. (eds.), *Copper Electrodeposition for Nanofabrication of Electronics Devices*, Nanostructure Science and Technology 171, DOI: 10.1007/978-1-4614-9176-7_2,

© Springer Science+Business Media New York 2014

wide copper deposition current region, the leveler plays the role of a surface leveling agent in the low deposition current region, less than a few mA/cm^2 [5]. For the suppression mechanism by surfactants of the PEG family, many researchers have studied it in detail since the mid-1980s, and it has basically become clear [6–29]. The action of levelers on copper deposition is under fundamental study for application to via/trench or through-hole copper filling [30–36].

2.2.1 *The Role of Peg in Bright Copper Plating by the Hull-Cell Test*

The Polyoxyethylene family of surface active agents, used as indispensable additives in various metal plating baths, play a decisive role in bright copper plating, through-hole plating, and on-chip wiring copper plating. Kardos [1] indicated in his patent drawing that the appropriate combination of three components, S containing compound, N containing compound, and ethylene oxide polymer give good bright copper plating in the presence of Cl^- ions. Mirkova et al. [4] reported that PEG or PPG have a central function in leveling during bright copper plating. In addition, the authors [5] presented evidence that the suppression action of PEG on the copper deposition reaction emerges only in the presence of Cl^-. Both PEG and Cl^- are basic components of plating baths for bright copper plating as confirmed by Hull-Cell patterns and potential-current curve measurements. That is, bright copper plating can be obtained over the entire region of deposition current density by addition of appropriate amounts of sulfur compounds and N containing compounds only in the presence of both PEG and Cl^-.

A Hull-Cell test is the practical method for control of plating baths, by which the surface appearance of plating over the wide current density region can be observed in a single plating operation with suitable cell current and plating time [37, 38]. A Hull-Cell is a trapezoidal cell in which a diagonal cathode substrate is placed opposite the anode as shown in Fig. 2.1. Plating conditions and addition agents used in the Hull-Cell experiments are noted in this figure.

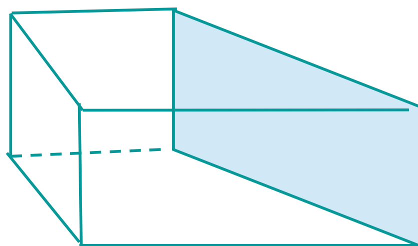

Fig. 2.1 Hull Cell for visual evaluation of copper plating over the wide range of deposition current. Cell volume; 267 mL, Temp; 30 °C, Electric quantity; 2A × 8 min. Bath composition; $0.4 M CuSO_4 + 0.5 M H_2SO_4$ Brightener components; PEG (M.W.: 3,300 suppressor); 1.6 μM ~ 1.0 mM 2-Mercaptobenzothiazole-S-Propanesulfonic acid (accelerator); ~2.0 mM Janus Green B (a derivative of safronic dye) (leveler); ~80 μM Cl^- ; ~16 mM

Figure 2.2 shows the changes in Hull Cell patterns of copper plating with POE/POP (P) and JGB (J), in the presence of S and Cl^- with constant concentrations. These patterns are found to have a tendency to widen the nodule (patchy) area with increasing J component, while having the tendency to narrow the nodule area into the high current density region with increasing P concentration. Finally, when P is 0.026 mM, and J is 0.004 mM, the total area of the Hull Cell panel came to have a bright copper surface. It is interesting to know that nodule formation behavior is controlled by the concentration ratio of P–J.

Figure 2.3 shows the changes in Hull Cell patterns with Changing Cl^- concentration in baths which contain either P alone or P + S + J as additives in, respectively. In both baths, the nodule area in the current density region of 10–40 mA/cm^2 at low Cl^- concentration is narrowed into a high current density region with increasing Cl^-. Although the patterns from the plating bath with only P are not brightened, the fundamental characteristics of changes in nodule formation patterns with Cl^- concentration are very similar to the ones with three components, P + S + J. By observing the Hull Cell pattern changes carefully, it is found that P and Cl^- are required to obtain bright copper plating, and S and J seem to contribute to brightening of the surface in the presence of P and Cl^-.

Figure 2.4 shows SEM images of the surface morphology obtained at 20 mA/cm^2 with varying Cl^- concentration. Nodules as large as sub-mm meter size are observed at 0.5 mM Cl^-. It is important to note that such nodules deposited at high current density can exist together with a relatively smooth surface at low current density on the same substrate. Similar surface morphologies were observed for the solution with PEG and nonionic surfactants of the PEG family such as PEG-PPG (polyoxyethylene-polyoxypropylene glycol), PNPE (Polyoxyethylen-nonylphenilether), POE (polyoxyethylene-oreilether), and so on [8]. In recent years, it has been reported that copper filling of via/trench in nanometer to micrometer size can be achieved by copper plating with a single PEG or Diallylamine-Type polymer Additive [30–35].

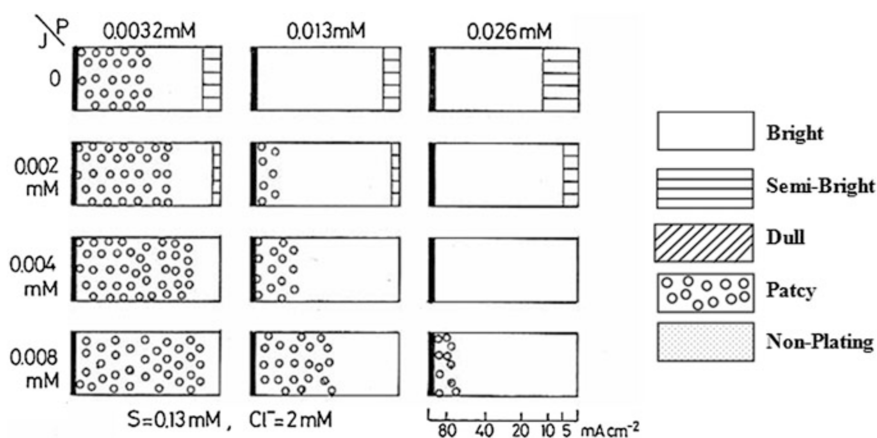

Fig. 2.2 Changes in Hull Cell patterns with P and J concentrations in the presence of S and Cl^-

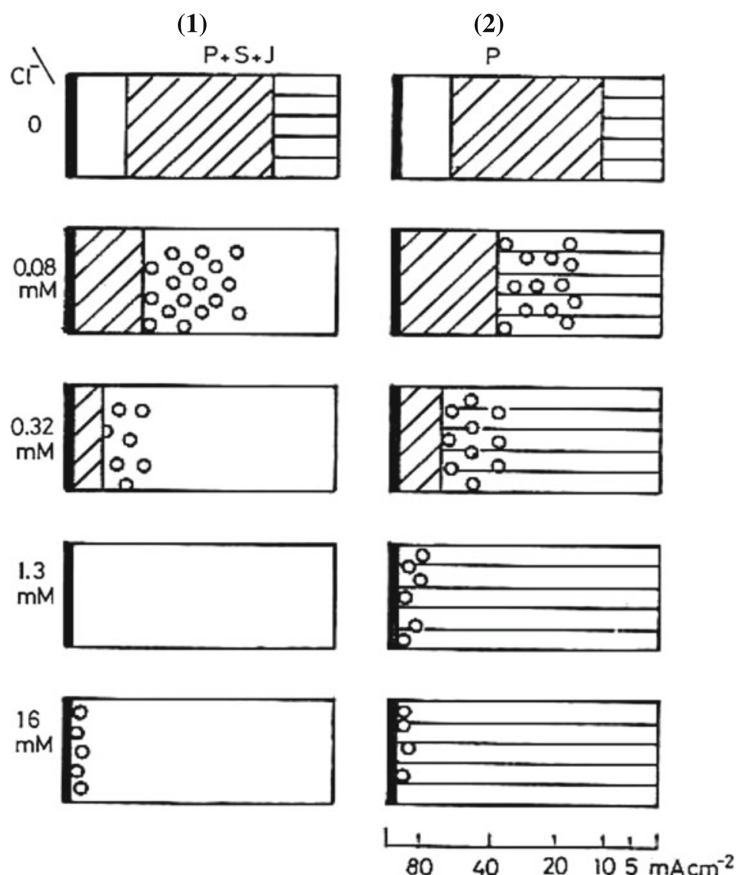

Fig. 2.3 Changes in Hull Cell patterns with Cl^- concentration in the presence of P + S + J (*left column*) or P (*right column*) in acid copper sulfate bath

The filling is considered to be caused by the emergence of "two stable states" for copper deposition on the same surface [36]. It would be a closely linked phenomenon to nodule formation in Hull-Cells as described above.

2.2.2 Suppression Behavior of Copper Deposition and Dissolution by PEG

Many researchers have confirmed the suppression behavior of PEG in copper deposition and dissolution reactions by electrochemical methods [6–15]. To determine the effect of PEG on the cupper deposition and dissolution reactions in an acid copper sulfate bath, potential-current curves were measured for various

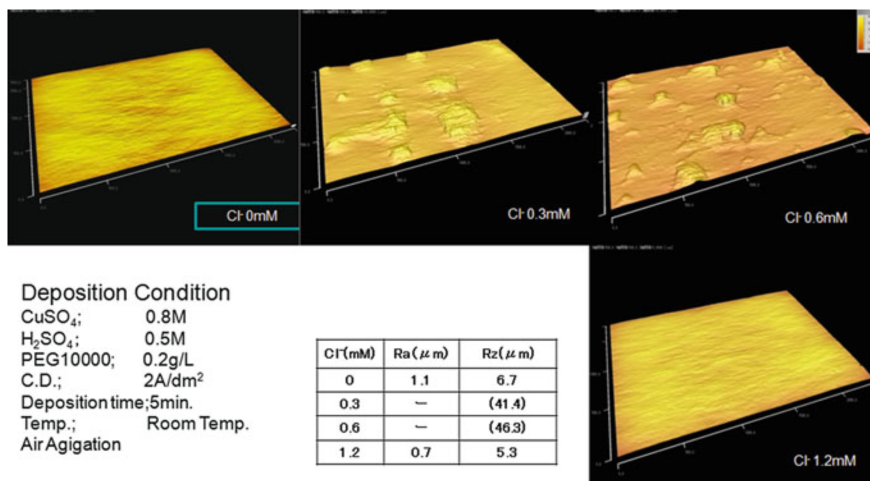

Cl⁻(mM)	Ra(μm)	Rz(μm)
0	1.1	6.7
0.3	–	(41.4)
0.6	–	(46.3)
1.2	0.7	5.3

Fig. 2.4 Changes in surface appearance of copper deposits with Cl^- in the presence of P

PEG of different molecular weights in the absence or presence of Cl^- ions [7]. Figure 2.5 shows a typical result for PEG of Mn = 20,000. For the solution without Cl^-, shown as a dotted line, an abrupt increase in deposition current is observed at a potential of about 0.15 V versus SHE in the sweep direction from anodic to cathodic potential. The sudden decrease in the current was also found at ca. +0.17 V versus SHE in a reverse direction sweep. In the anodic polarization region no abrupt change appeared with a potential sweep, although the anodic current was suppressed.

While, for the Cl^- containing solution, the reaction currents were suppressed over the entire potential range measured in this experiment. Even in a potential range more negative than ca. 0.15 V versus SHE, the suppression of copper deposition was maintained, and the Tafel relationship is observed in the polarization-current curves. The potential region where the reaction (B) Cu + ⇔Cu_{ad} is kept in a quasi reversible state, is also demonstrated in Fig. 2.5. Interestingly, it coincides nearly with the potential region where deposition current is suppressed considerably.

The characteristics of potential-current curves for the other PEGs were almost the same as the ones observed in Fig. 2.5 with the exception that lower molecular-weight PEG gave rise to weaker suppression. Also, similar polarization behavior was observed with solutions containing PPG or triblock copolymers of PEG-PPG [29].

The rest of the potentials (Er) of the copper electrode, obtained immediately after cut-off of the potentiostatic electrolysis, were plotted against the set potentials as in Fig. 2.6. For the plating bath without Cl^-, Er shifted gradually in the cathodic direction to give the most negative value of ca. +0.23 V versus SHE (−65 mV versus Cu^{2+}/Cu) with variation of the set potentials in the cathodic direction from 0.36 V to 0.15 V versus SHE (+60 to −150 mV versus Cu^{2+}/Cu), and abruptly shifted back to the potential of about 0.29 V, nearly equilibrium potential of Cu^{2+}/Cu, at set

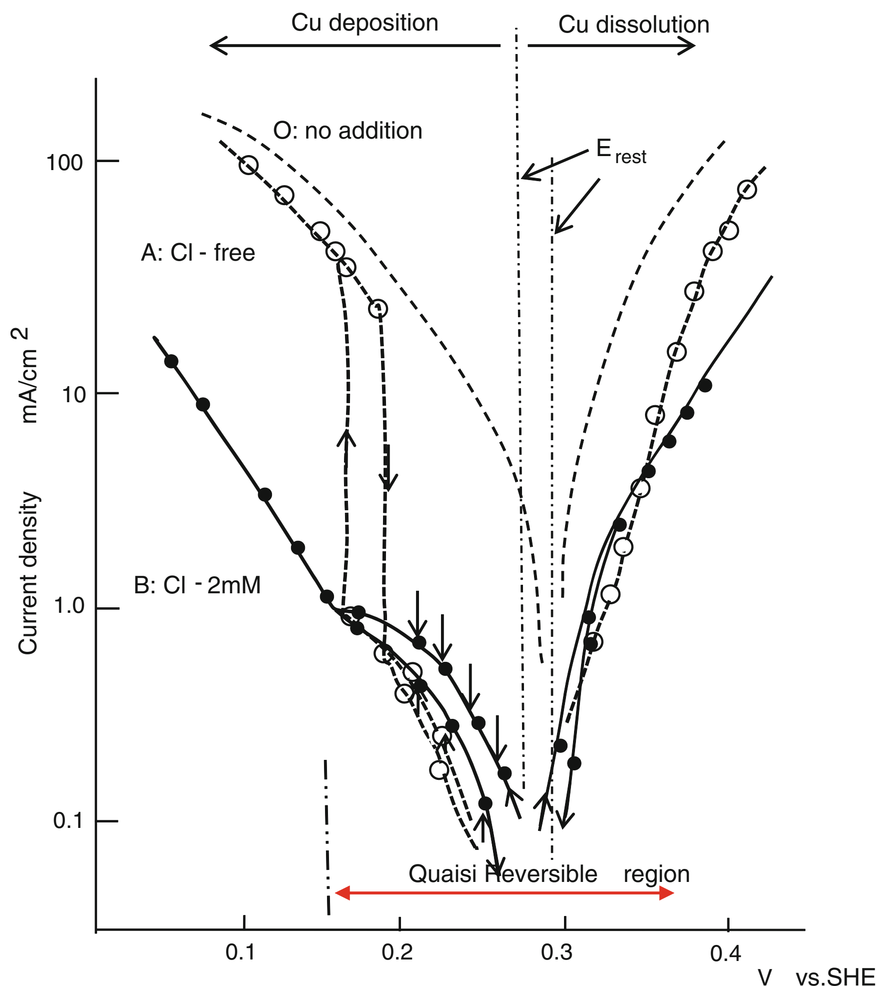

Fig. 2.5 Effect of Polyoxyethylene glycol on potential-current curves for the copper deposition and dissolution reaction in acid copper sulfate baths in the presence or absence of Cl^- ions. PEG (MW = 20,000); 0.02 g/l$^-$, *A* Cl^- free, *B* Cl^- 2 mM, O: no addition

potentials more negative than +0.15 V versus SHE. In the opposite direction, cathodic to anodic, a sudden change in Er was observed at ca. +0.18 V versus SHE. For the copper plating bath containing Cl^-, no abrupt change in Er was observed.

Comparing the curves in Figs. 2.5 and 2.6, the change in currents representing copper deposition and dissolution suppression corresponds to the changes in Er with the electrode potential change. The larger the suppression rate, the more negative the Er was. The Er observed after cutoff of electrolysis reflects the situation of copper surface adsorbed by PEG under electrolysis.

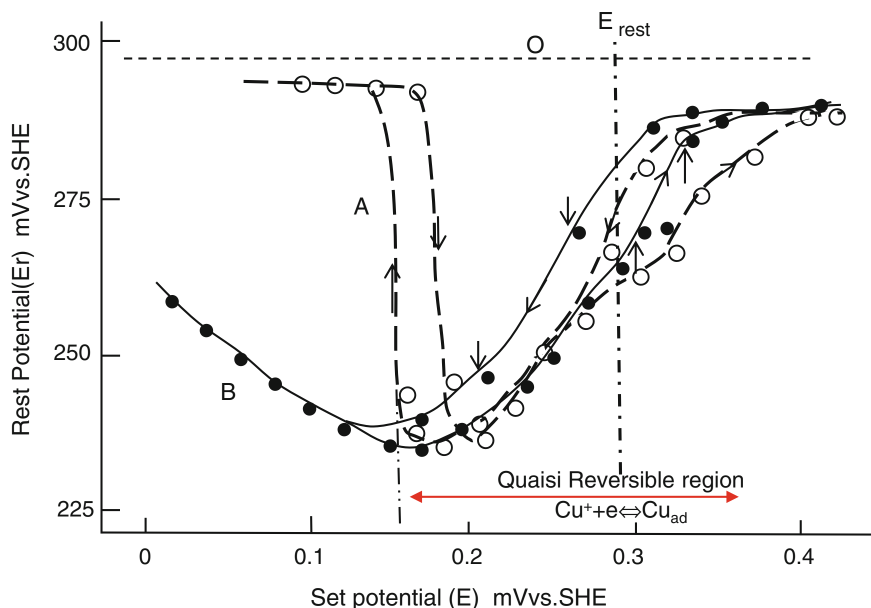

Fig. 2.6 Variation of the rest potentials of copper electrode with changing the set potentials in acid copper sulfate baths containing 0.02 g/l PEG (MW = 20,000) in the presence or absence of Cl^- ions. *O* no addition, *A* PEG, *B* PEG + Cl^- 2 mM

To determine the PEG adsorption behavior on copper surface depending on electrode potential, double-step electrolysis was conducted with two consecutive plating baths. Figure 2.7 shows the current–time curves measured with the copper electrode at various set potentials of 0.14, 0.2, and 0.35 V versus SHE in the second $CuSO_4 + H_2SO_4$ bath free of PEG, which had been electrolyzed in the first $CuSO_4 + H_2SO_4$ bath containing PEG and Cl^-. With the second bath containing Cl^-, the reaction current at +0.14 V versus SCE increased slowly in the early stage of the electrolysis, reaching the value with a PEG free bath. At +0.2 V versus SHE, the current remained constant at a small value specific to the PEG containing bath. The current at +0.35 V was also maintained at the suppressed value, even though the current increased gradually with time.

With the Cl^- free second bath, PEG has no suppression effect on the reaction current at +0.14 V versus SHE, while the current at +0.2 V and +0.35 V versus SHE increased drastically in the early stage of electrolysis and the suppression effect disappeared.

The changes in curves suggest that PEG molecules adsorb strongly on the copper surface in the potential range more positive than +0.15 V in the presence of Cl^-, where the reaction (B) Cu + ⇔Cu_{ad} is kept in a quasi-reversible state. Cu^+ ions of the reaction (B) are expected to play an important role in PEG adsorption on the copper surface.

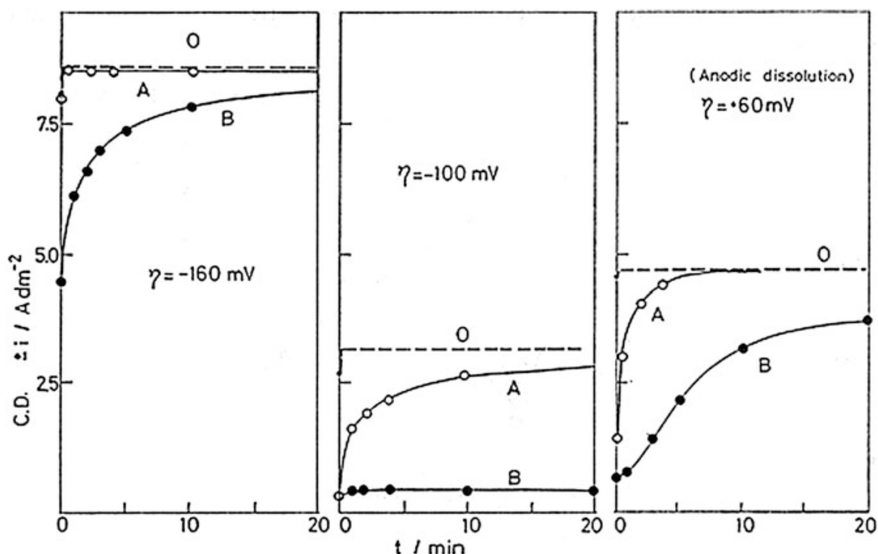

Fig. 2.7 Changes in deposition and dissolution current with time at fixed overpotential in the second electrolysis for the copper electrolyzed in the first baths in advance

Similar experiments were conducted in more detail by Kelly et al. [14], Willey et al. [27], Huerta et al. [28]. Strong suppression of copper deposition was observed in the presence of Cl^- and Cu^{2+} together and they pointed out that adsorbed Cl^- ions on copper surfaces have high freedom of desorption and adsorption.

2.2.3 Effect of PEG Concentration and Molecular Weight on Copper Deposition and Dissolution

Figure 2.8 shows the effect of PEG concentration on the copper deposition and dissolution currents at an electrode potential of ca 0.13 V versus SHE ($\eta = -160$ mV) and 0.35 V versus SHE ($\eta = +60$ mV) as a function of PEG molecular weight, which changed from 200 to 20,000. Regardless of the direction of the reaction current, currents were suppressed gradually by increasing the concentration, the higher the molecular weight, the greater the suppression.

Deposition and dissolution currents at a PEG concentration of 0.02 g/l were plotted against the PEG molecular weight, i.e., polymerization degree, as in Fig. 2.9. In both cases, the reaction currents measured at $\eta = -160$ mV, and $\eta = +60$ mV decreased drastically at the polymerization degree of 7–10, and to reach the critical minimum values with increasing polymerization degree.

Figure 2.10 shows the rest potentials (Er) of the copper electrode immediately after cutoff of electrolysis plotted against the polarization current, which were obtained with copper plating baths containing PEG of various molecular weight

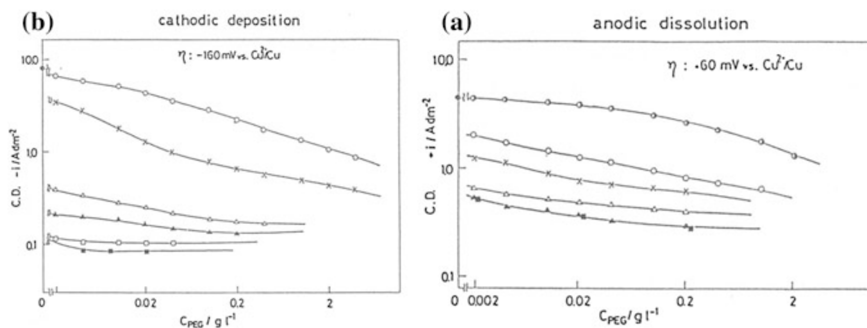

Fig. 2.8 Effect of PEG concentration on copper deposition and dissolution current at −160 mV and +60 mV versus Cu^{2+}/Cu as a function of PEG molecular weight. Mn: 200 (●), 400 (○), 600 (×), 1,000 (△), 2,000 (▲), 6,000 (□), 20,000 (■)

and in different concentrations. In the case of copper deposition at $\eta = -160$ mV, a linear relationship with a slope of 30 mV/decade between the Er and deposition current was obtained independent of the molecular weight of PEG. The results indicate that the polymerization degree and the concentration of PEG do not affect the copper deposition mechanism, but reduces the Cu^{2+} activity in the vicinity of the copper surface. From the most negative value of Er, the Cu^{2+} activity is expected to become as small as a hundredth part. In the case of copper dissolution,

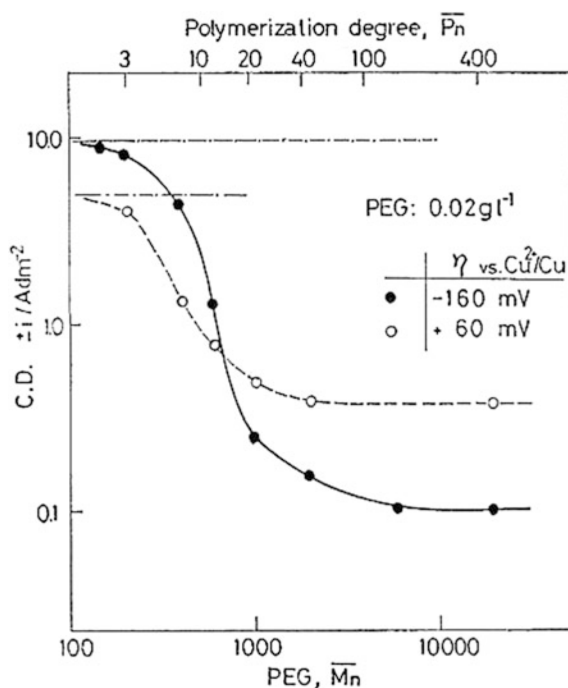

Fig. 2.9 Effect of polymerization degree of PEG on copper deposition and dissolution current at −160 and +60 mV versus Cu^{2+}/Cu in acid copper sulfate bath at a given PEG concentration of 0.02 g/l

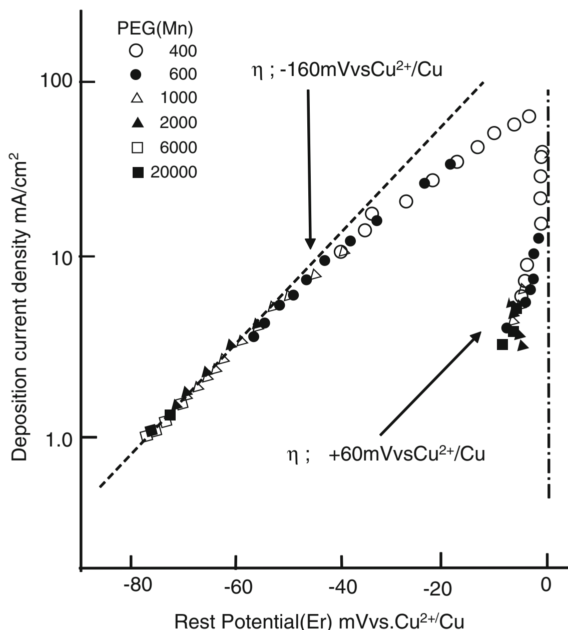

Fig. 2.10 The relationship between the copper deposition and dissolution current and the rest potentials observed after cut-off of loaded potential in acid copper sulfate baths

the changes in Er are very small comparing with those observed in copper deposition. This would be caused by the one-sided flow of reaction species and the loosely adsorbed PEG film on the copper surface.

Based on the experimental results, the authors developed a hypothesis for current suppression by PEG in terms of cation seizing by the PEG molecule [7]. That is, PEG having enough ether oxygen to form a pseudo crown would grasp the copper ions inside and adsorb on the copper surface electrostatically as a poly-cation, resulting in suppression of copper deposition and dissolution. Papke et al. [39] had reported that linear polyether has a helical conformation with a 0.26 nm inside diameter to react with alkali metals. The molecular model is one where the tunnel is lined with oxygen atoms with the proper orientation for coordination to cations inside the helix. Crown ethers had also been found to complex with alkaline cations [40].

2.2.4 Adsorption and Suppression Mechanism

Figure 2.11 shows a PEG adsorption model depending on electrode potential in the absence and presence of Cl^- proposed by the authors. The PEG grasping Cu^{2+} or Cu^+ ions with the formation of pseudo-crown moieties, positively charged, are attracted to the copper surface and/or coordinated to the negatively charged chloride ions adsorbed on the copper surface. In the potential region more positive than +150 mV versus SHE, where reaction (B) $Cu + \Leftrightarrow Cu_{ad}$ is in a reversible state, Cu^+ ions existing in a large amount keep the PEG positively charged by being wrapped in it. While, in the potential region more negative than the definite

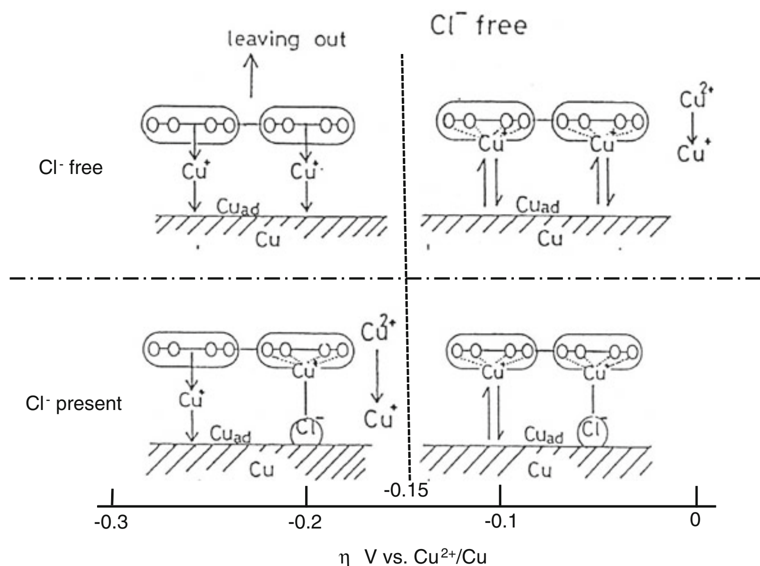

Fig. 2.11 Mechanism of PEG adsorption on copper surface changing with the electrode potential in the absence and presence of Cl^- in acid copper sulfate bath

potential values, the Cu^+ in PEG is reduced to Cu in one direction to liberate the PEG into the electrolyte. In the presence of Cl^-, Cu^+ ions grasped in PEG moieties coordinate to Cl^- ions on the copper surface, and keep the PEG in the adsorbed state. Cu^{2+} ions wrapped in PEG would be reduced to Cu^+ by chloride bridging to the copper surface.

In this model, when the Cl^- concentration is less than about 1 mM, too low to form a Cl^- adsorbed monolayer, c (2×2) Cl, uneven suppression of copper deposition is expected [25] resulting in nodule formation [8].

Since then, many researchers have studied PEG adsorption on copper by various research methods, and presented experimental evidence for the chemical identity of the adsorbed species and for the PEG adsorption model.

Kang et al. [23] reported no inclusion of C and Cl^- in deposits from PEG and Cl^- bath by SIMS analysis. They also observed formation of big pyramidal features in deposits by AFM, and stated that deposition occurs under the organic layer which must float above the growing substrate.

Kelly et al. [14, 15], who studied the adsorption behavior of PEGs in the presence of Cl^- by LSV, QCM, and EIS measurements, reported that adsorbed PEG forms nearly a monolayer in the presence of chloride ions, and competes for adsorption sites with Cu^{2+} ions on the copper surface. Further the introduction of PEG and $C1^-$ does not necessitate modifying kinetic parameters from values observed in the presence of Cl^- alone.

For the hypothesis of "pseudo-crown ether complex" grasping Cu^+ ions inside the ring, Stoychev et al. [9] studied the interaction of poly (ethylene glycol)

Mn = 3000 with Cu^+ and Cu^{2+} ions in aqueous-acidic media by measuring specific electrical conductivity, optical density, and the cyclic voltammetric curves in Cu^+ and Cu^{2+} solutions, and suggested the formation of complexes of the {Cu + $(–EO–)_3$·(x − 1)H_2O} and {$Cu_{2+}$$(–EO–)_4$·(y − 1)$(H_2O)_2$} types. In view of the considerable differences in the conformation interactions of PEG units in water and nonwater media, they considered another scheme suggested by Suryanarayana et al. [40] According to which, the copper ion coordinates just a single oxygen atom of the PEG unit, while the remaining coordinations are occupied by already situated water molecules. The stoichiometry –EO–/Cu^+ = 3 and –EO–/Cu^{2+} = 4 indicates the –EO– segment length including both the EO-unit coordinated with Cu ions, and its neighbors.

The form and the structure of the ethylene oxide units are strongly influenced by the nature of the solvent [39], and the pseudo-crown helix structures formed between PEG and alkaline metals are established in nonaqueous media and in the solid phase [41]. However, high coordination numbers are not typically found in aqueous Cu(I) chemistry. So, the complete pseudo-crown grasping Cu ions inside the ring proposed by the authors might be unlikely to exist in the plating solution.

Noma et al. [42] detected Cu^+-PEG complexes with different chain lengths of n PEG segments from n = 4 to 43 in a copper plating solution in factory operation using Matrix-Assisted Laser Desorption/Ionization-Mass Spectroscopy (MALDI-MS) and showed that Cu^+ ions exist in the solution as small complexes and large complexes with PEG. And the latter ones are more stable than the former ones to prevent chelating reactions of Cu^+ with BCS (Bathocuroinedisulfonic acid disodium salt).

Further, Feng et al. [22] examined PEG complexes on copper surfaces in an acidic solution containing PEG and Cl^- by Surface enhanced Raman spectroscopy (SERS) measurements, and confirmed the formation of a PEG–Cu–Cl species at the surface. On the basis of the spectroscopic data, two models of a three-coordinated Cu center associated with two oxygen atoms one chloride ligand are constructed with the help of calculations as shown in Fig. 2.12.

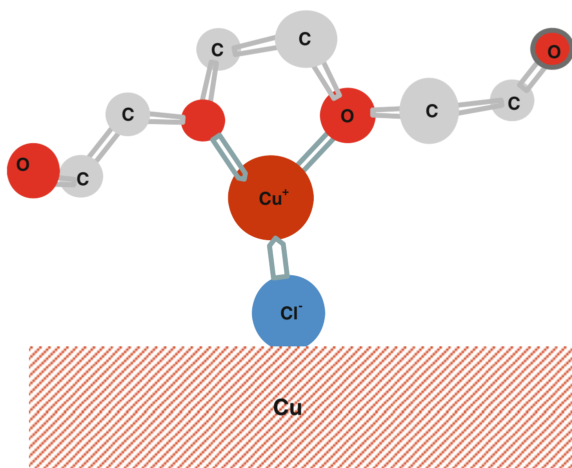

Fig. 2.12 Structural Model of PEG-Cu^+–Cl^- complex with reference to the model by Feng et al. [22]. Cu^+ ion is associated with two ether oxygen atoms and one Cl^- ion adsorbed on copper surface

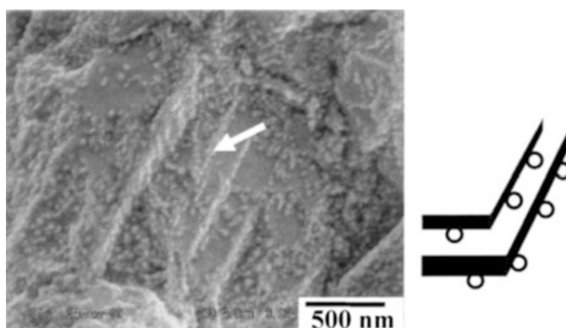

Fig. 2.13 Field-emission SEM micrograph of the deposited copper surface. Additives are Cl^- and PEG. (by Kondo et al. [18])

As stated above, the existence of PEG-Cu^+ complexes in the solution and adsorbed PEG–Cu^+–Cl^- on copper surfaces are deduced from the electrochemical behavior of copper deposition and dissolution reactions, changes in electric conductivity and optical density of the solution, SERS, QCM measurements, and etc. Kondo et al. [18, 19] directly observed PEG adsorbed on copper electrodeposit by scanning electron microscopy (SEM) as shown in Fig. 2.13. The SEM images show the PEG molecules of about 30 nm in diameter absorbed preferentially at the edges of copper macrosteps and inhibiting the lateral growth of copper electrodeposits [16, 42]. The direct observation is a significant result, even though those images were not obtained in situ observation in the plating solution. Jin et al. [17] further investigated the dissolution/deposition of the intermediate complex of copper (PEG–Cu^+) by detecting the simultaneous mass change of the electrode during cyclic voltammetric (CV) measurement by using EQCM. They observed two current peaks in the CV curves corresponding to the mass changes, illustrating the generation and consumption of intermediate complex PEG–Cu^+–Cl^- on the copper electrode. Mass changes depending on the electrode potential are shown in Fig. 2.14.

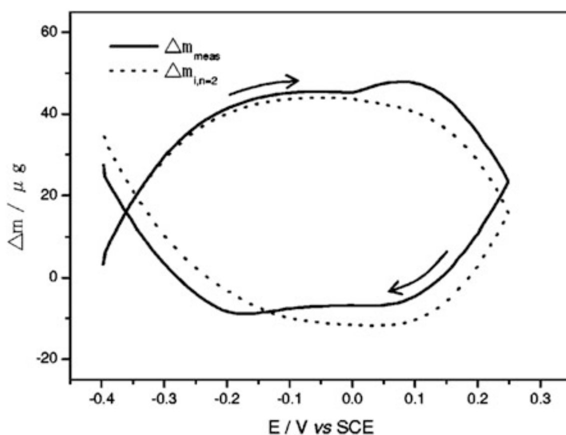

Fig. 2.14 Measured and calculated (n = 2, reaction Cu/Cu^{2+}) voltmassogram obtained at sweep rate 10 mV/s. in $CuSO_4$ +H_2SO_4 + PEG + HCl electrolyte. (by Jin et al. [20])

2.2.5 PEG Adsorption on Coinage Metals

PEG form PEG-Cu^+ complex and adsorb on copper surface in the presence of Cl^-. However, PEG can adsorb on copper surfaces without Cu^+ ions as long as Cl^- ions are present in the solution.

Walker et al. [24] examined the adsorption of PEG and Cl^- on polycrystalline Cu, Ag, and Au electrodes in the solution of 1.8 M H_2SO_4 + 88 μM PEG3400 + 1 mM Cl^- by in-situ Ellipsometry. They found that PEG adsorption is clearly evident at potentials near or positive of the pzc for all metals only in the presence of Cl^-. The thicknesses of the adsorbed PEGs are reported to be 1.30 nm at 0.35 V and 1.21 nm at 0.5 V for Au, 1.6 nm at 0.5 V for Ag, and 0.98 nm at 0 V and 0.85 nm at −0.2 V for Cu. The potential of zero charge (pzc) of Au, Ag, and Cu is 0.25 V, −0.68 V, and −0.35 V, respectively. All the potentials are referred to SHE. They concluded that the presence of Cl^- is a necessary and sufficient condition for PEG adsorption, and univalent ions such as Cu^+ and Ag^+ are unnecessary.

Kelly et al. [14] also confirmed PEG adsorption on Au and Cu in 0.24 M Cu^{2+} +1.8 M H_2SO_4 solution by QCM measurement. Doblhofer et al. [21] further demonstrated CuCl formation and dissolution in acid copper sulfate solution with a Cl^- concentration of more than 2 mM by EQCM measurement, and showed that the inhibiting layer forms by reaction between the adsorbate-covered copper electrode and PEG. Neither Cu^+ nor Cu^{2+} from the electrolyte are required. Jin et al. [20], by using AFM, confirmed PEG adsorbed in a flat-cone shape with a bottom radius of 15–25 nm and a height of 2–4 nm on polished Cu surfaces after being dipped into the solution of H_2SO_4 + PEG + HCl at −0.01 V versus SHE for 2000s, as shown in Fig. 2.15.

It has been shown that univalent metal ions, Cu^+, are not necessary for PEG adsorption on copper surface, by QCM measurement, Ellipsometric study, and etc., as stated above. However, Huerta et al. [28] obtained interesting results about

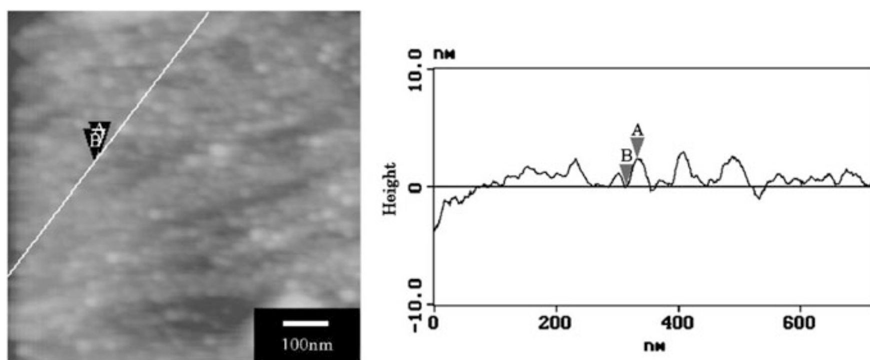

Fig. 2.15 AFM top view image and section analysis of polished Cu surface after being dipped into H_2SO_4 + PEG + HCl at −0.01 V versus SHE for 2000s. (by Jin et al. [20])

the character of the adsorption films formed on copper surfaces by conducting systematic double-step electrolysis with two consecutive plating baths. They found that PEG can adsorb in the presence of Cl^{-} in a Cu^{2+}-free solution, but does not strongly inhibit deposition when subsequently immersed in a $CuSO_4$ solution. Only when Cl^{-} and PEGs are present in the solution where Cu^{2+} is being reduced is strong inhibition observed.

The film adsorbed on copper surfaces in the solution without Cu^{2+} would be evidently different in structure from the film formed during copper deposition. PEG is expected to be positively charged by H^{+} ions in acid solution, and adsorbed on negatively charged copper surface by Cl^{-} adsorption.

References

1. Kardos O, Durham HB, Tomson AJ, Arcilesi DA (1970) Electrodeposition of copper. USP 3542655
2. Stoychev DS, Vitanova I, Vitanov T Rashkov St (1978) Adsorption of substances acting as brighteners in the electrolytic deposition of copper. Surf Tech 7:427–432
3. Konishi S, Yokoi M, Goto S, Itabashi S (1978) Effects of bath composition and brightener on leveling of bright copper plating from copper sulfate baths. J Surf Finish Soc Jpn (in Japanese) 29:339
4. Mirkova L, Rashkov St, Nanev Chr (1982) The levelling mechanism during bright acid copper plating. Surf Tech 15:181–190
5. Yokoi M, Konishi S (1983) Interactions of Cl^{-} and brightener-components in copper plating from an acid sulfate bath. J Surf Finish Soc Jpn (in Japanese) 34: 434–439
6. Hill MRH, Rogers GT (1978) Polyethylene glycol in copper electrodeposition on to a rotating disc electrode. J Electroanal Chem 86:179–188
7. Yokoi M, Konishi S, Hayashi T (1984) Adsorption behavior of polyoxyethyleneglycole on the copper surface in an acid copper sulfate bath. Denki Kagaku 52:218–223
8. Yokoi M, Konishi S (1984) Effect of polyoxyethylene surfactants on the hardness of copper electrodeposited from an acid copper sulfate bath, J Surf finish Soc Jpn (in Japanese) 35:421–427
9. White JR (1987) Reverse pulse plating of copper from acid electrolyte; a rotating ring disc electrode study. J Appl Electrochem 17:977–982
10. Reid JD, David AP (1987) Impedance behavior of a sulfuric acid-cupric sulfate/copper cathode interface. J Electrochem Soc 134:1389–1394
11. Healy JP, Pletcher D, Goodenough M (1992) The chemistry of the additives in an acid copper electroplating bath: part I. Polyethylene glycol and chloride ion. J Electroanal Chem 338:155–165
12. Stoychev DS, Tsvetanov C (1996) Behaviour of poly (ethylene glycol) during electrodeposition of bright copper coatings in sulfuric acid electrolytes. J Appl Electrochem 26:741–749
13. Stoychev DS (1998) On the role of poly (ethylene glycol) in deposition of galvanic copper coatings. Trans Inst Met Finish 76:73–80
14. Kelly JJ, West AC (1998) Copper deposition in the presence of polyethylene glycol; I. Quartz crystal microbalance study. J Electrochem Soc 145:3472–3476
15. Kelly JJ, West AC (1998) Copper deposition in the presence of polyethylene glycol; II. Electrochemical impedance specfroscopy. J Electrochem Soc 145:3477–3481
16. Kelly JJ, Tian C, West AC (1999) Leveling and microstructural effects of additives for copper electrodeposition. J Electrochem Soc 146:2540–2545

17. Kondo K, Yamakawa N, Hayashi K (2000) Role of damascene via filling additive-morphology evolution, ECS meeting abstracts of toronto meeting No. 358
18. Kondo K, Yamakawa N, Tanaka Z, Hayashi K (2003) Copper damascene electrodeposition and additives. J Electroanal Chem 559:137–142
19. Kondo K, Matsumoto T, Watanabe K (2004) Role of additives for copper damascene electrodeposition; experimental study on inhibition and acceleration effects. J Electrochem Soc 151:C250–C255
20. Jin Y, Kondo K, Suzuki Y, Matsumoto T, Barkey DP (2005) Surface adsorption of PEG and Cl additives for copper damascene electrodeposition. Electrochem Solid-State Lett 8:C6–C8
21. Doblhofer K, Wasle S, Soares DM, Weil KG, Ertl G (2003) An EQCM study of the electrochemical Copper(II)/Copper(I)/Copper System in the presence of PEG and Chloride ions. J Electrochem Soc 150:C657–C664
22. Feng ZV, Li X, Gewirth AA (2003) Inhibition due to the interaction of polyethylene glycol, chloride, and copper in plating baths: a surface-enhanced raman study. J Phys Chem B 107:9415–9423
23. Kang M, Gewirth AA (2003) Influence of additives on copper electrodeposition on physical vapor deposited (PVD) copper substrates. J Electrochem Soc 150:C426–C434
24. Walker ML, Richter LJ, Moffat TP (2005) *In Situ* ellipsometric study of PEG/Cl-Coadsorption on Cu, Ag, and Au, J Electrochem Soc 152:C403–C407
25. Hebert KR (2005) Role of chloride ions in suppression of copper electrodeposition by polyethyleneglycol. J Electrochem Soc 152(5):C283–C287
26. Ding R, Zhang X, Evans JW, Doyle FM (2006) EQCM study of the influence of copper ions on the adsorption of polyethyleneglycol and bis (sodiumsulfopropyl) disulfide at a copper cathode. ECS Trans 2(3):281–292
27. Willey MJ, West AC (2006) Microfluidic studies of adsorption and desorption of polyethylene glycol during copper electrodeposition. J Electrochem Soc 153(10):C728–C734
28. Huerta Garrido ME, Pritzker MD (2008) Voltammetric study of the inhibition effect of polyethylene glycol and chloride ions on copper deposition. J Electrochem Soc 155(4):D332–D339
29. Gallaway JW, West AC (2008) PEG, PPG, and their triblock copolymers as suppressors in copper electroplating. J Electrochem Soc 155(10):D632–D639
30. Hayase M, Taketani M, Aizawa K, Hatsuzawa T, Hayabusa K (2002) Copper bottom-up deposition by breakdown of PEG-Cl inhibition. Electrochem Solid-State Lett 5(10):C98–C101
31. Hayase M, Taketani M, Hatsuzawa T, Hayabusa K (2003) Trenches by consumption of halide ion preferential copper electrodeposition at submicrometer. Electrochem Solid-State Lett 6(6):C92–C95
32. Dow Wei-Ping, Liu De-Huei, Chun-Wei Lu, Chen Chien-Hung, Yan Jhih-Jyun, Huangb Su-Mei (2011) Through-hole filling by copper electroplating using a single organic additive. Electrochem Solid-State Lett 14:D13–D15
33. Takeuchi M, Kondo K, Kuri H, Bunya M, Okamoto N, Saito T (2012) Single Diallylamine-Type Copolymer Additive Which Perfectly Bottom-Up Fills Cu Electrodeposition. J Electrochem Soc 159:D230
34. Hayashi T, Kondo K, Saito T, Takeuchi M, Okamoto N (2011) High-speed through silicon via (TSV) filling using diallylamine additive II. Optimization of diallylamine concentration. J Electrochem Soc 158:D715–D718
35. Moffat TP, Josell D (2012) Extreme bottom-up superfilling of through-silicon-vias by damascene processing: suppressor disruption, positive feedback and turing patterns. J Electrochem Soc 159(4):D208–D216
36. Mac Intyre F, Hull RO (1943) Plating test control of plating baths. Proc Am Electroplater's Soc 30:95
37. Terakado R, Nagasaka H, Finishing M (1976) A Study of The Electric Current Distribution in Hull Cell, J Surf finish Soc Jpn (in Japanese) 27:676–680

38. Papke BL, Ratner MA, Shriver DF (1982) Conformation and ion-transport models for the structure and ionic conductivity in complexes of polyethers with alkali metal salts. J Electrochem Soc 129(8):1694–1701
39. Yanagida S, Takahashi K, Okamura M (1977) Metal-ion complexation of noncyclic poly (oxyethylene) derivatives. I solvent extraction of alkali and alkaline earth metal thiocyanates and iodides. Bull Chem Soc Jpn 50:1386–1390
40. Suryanarayana D, Narayana PA, Kevan L (1983) Effect of molecular cage size on the motion and coordination of copper (2+) in cross-linked poly (vinyl alcohol) and poly (ethyleneoxide) gels: electron spin echo and electron spin resonance studies. Inorg Chem 2:474–478
41. Noma H, Koga T, Hirakawa C, Nonaka K, Kaibuki T, Moriyama S (2012) Analysis of Cu(I) in copper sulfate electroplating solution. J Surf Finish Soc Jpn (in Japanese) 63:124–128
42. Vogt MR, Lachenwitzer A, Magnussen OM, Behm RJ (1998) In-situ STM study of the initial stages of corrosion of Cu (100) electrodes in sulfuric and hydrochloric acid solution. Surf Sci 399:49–69

Chapter 3
Acceleration Effect

Dale P. Barkey

3.1 Introduction

Fabrication of microscale and nanoscale structures can be implemented by electrodeposition of copper onto conductive templates that contain recesses in form of the desired structure. The current distribution that results from deposition from a simple acid copper solution is concentrated near the upper corners of recesses and results in incomplete filling, formation of voids, and a substantial overburden of nonfunctional material. In industrial practice, effective filling of features such as trenches and vias by copper electrodeposition relies on additive ensembles that promote bottom-up filling, uniform current macrodistribution and minimal overburden.

The components of these additive systems include suppressors, accelerants, and levelers. Suppressors and levelers both inhibit electrodeposition. For our purposes, a suppressor is an inhibitor that can be deactivated by an accelerant. Suppressors include polyalkyl glycols (PAG) such as polyethylene glycol (PEG). They are weakly adsorbed on the surface in combination with chloride and are not consumed or chemically transformed on the metal surface. Levelers, such as Janus Green B, are inhibitors that are not deactivated by accelerants. They are strongly adsorbed and are consumed on the metal surface. Filling of microscale and nanoscale features is achieved through one of two broad categories of mechanism [1]. One of these is the diffusion-limited consumption of leveler. This mechanism has been understood for decades and is the basis for leveling on many different physical scales. Since it does not involve an accelerant, it will not be considered further. The other mechanism relies on the combination of suppressor and accelerant. In this latter type of mechanism, the accelerant is concentrated at the bottom of features and deactivates or excludes the suppressor there. Accelerants have been postulated to lift or displace adsorbed suppressors from the surface and restore the

D. P. Barkey (✉)
Department of Chemical Engineering, College of Engineering and Physical Science,
Kingsbury Hall, Room W305, Durham, NH 03824, USA
e-mail: dpb@cisunix.unh.edu

K. Kondo et al. (eds.), *Copper Electrodeposition for Nanofabrication of Electronics Devices*,
Nanostructure Science and Technology 171, DOI: 10.1007/978-1-4614-9176-7_3,
© Springer Science+Business Media New York 2014

higher rate of deposition observed on the suppressor-free surface. While the application considered here is the filling of trenches, vias, or other substrate features that act as templates for fabrication of microscale and nanoscale structures, the principle is the same as that which produces bright deposits in more conventional plating, and the accelerant is sometimes referred to as a brightener.

While many suppressors and levelers can be found in the literature, few effective accelerants are known. In the open literature, most reports concern bis(3-sulfopropyl) disulfide (SPS) or its reduced monomer, 3-mercaptopropylsulfonate (MPS) (see, Fig. 3.1). The solution and surface chemistries of this compound in acid-sulfate copper-plating solutions are more complicated than those of either suppressors or levelers. Both the sulfate functional group and the sulfur–sulfur bond (in SPS) or thiolate (formed by MPS) appear to play critical roles in the accelerant mechanism. In contrast to suppressors, these molecules are consumed at a high rate in plating operations, and the rate of consumption is sensitive to the cell configuration and applied current waveform.

What follows is a review of chemical and electrochemical studies of these accelerant compounds as well as mechanistic models of their role in filling processes. We begin with a consideration of the homogeneous solution chemistry of SPS and MPS and their interactions with other components of the bath. These interactions include transformations of the molecules into the effective accelerant as well as their degradation and deactivation. We then turn to their adsorption on copper and to the effect of applied potential on their surface chemistry. Finally, we consider the models that have been proposed to describe the role played by accelerants in the filling of features on various spatial and temporal scales.

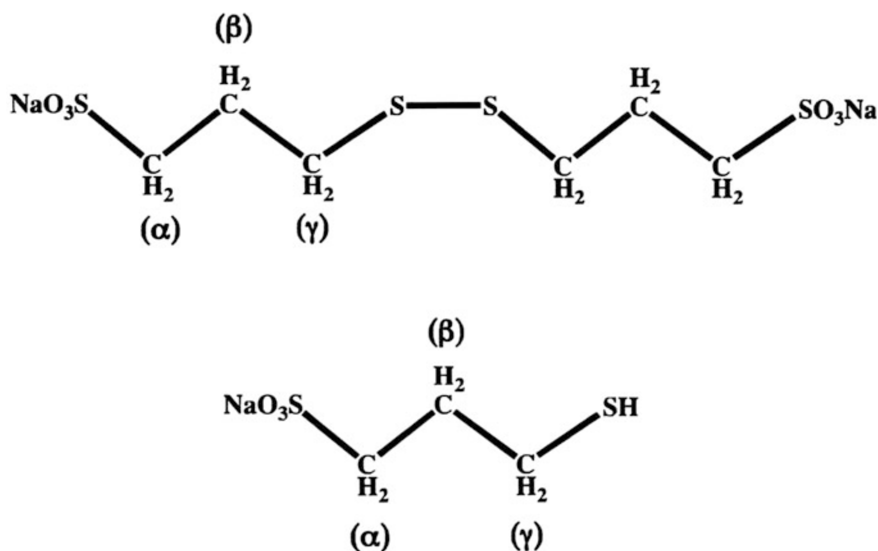

Fig. 3.1 The SPS and MPS molecules, shown here as sodium salts. Reproduced with permission from Garcia-Cardona et al. [9], their Fig. 3.1

3.2 Solution Chemistry

SPS and MPS are added in parts per million (ppm) concentrations to acid-sulfate copper plating baths. These baths also contain chloride in concentrations in the tens of ppm range. Chloride is known to play a role in both copper deposition and in the function of the accelerant. There is considerable evidence that Cu(I) interacts with SPS and MPS as well. An important feature of acid-sulfate copper plating baths is the fact that the reduction potential of Cu(I) is substantially positive of the reduction potential of Cu(II), the main form of copper in solution. In equilibrium with the metal, the concentration of Cu(I) is therefore much lower than the concentration of Cu(II). Moreover, in practical plating operations, the metal and solution are not in equilibrium at open circuit. Dissolved oxygen oxidizes Cu(I) to Cu(II), so that the bulk aerated solution contains a concentration of Cu(I) that is lower than the equilibrium value. Under this condition, the metal corrodes by proportionation,

$$\mathrm{Cu(II)} + \mathrm{Cu} = 2\mathrm{Cu(I)} \tag{3.1}$$

and Cu(I) is generated at the metal-solution interface. Chloride, on the other hand, stabilizes Cu(I) through formation of CuCl and $CuCl_2^-$. For these reasons, the interactions in solution among SPS, MPS, Cu(I), chloride, and oxygen are of interest.

The role of chloride in accelerant function was demonstrated by Tan et al. [2]. They conducted galvanostatic copper deposition experiments and showed that, in the absence of chloride ion, either SPS or MPS added to the plating solution inhibited copper deposition. Upon the addition of Cl^-, a transition from inhibition to acceleration was observed for both additives. They also found that the effectiveness of SPS is more dependent on potential than that of MPS, an observation that would suggest a role for faradaic reduction of SPS to MPS.

In the presence of cuprous chloride, both SPS and MPS appear to form complexes with Cu(I), and it has been proposed by a number of investigators that one of these complexes is the effective accelerant. Reduction of SPS to MPS is probably a key initial step in the process, and Vereecken et al. presented rotating ring-disk data indicating that this reduction takes place by homogeneous reaction of SPS with Cu(I) rather than by an interfacial faradaic process [1].

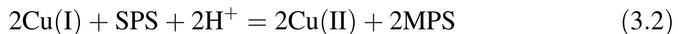

$$2\mathrm{Cu(I)} + \mathrm{SPS} + 2\mathrm{H}^+ = 2\mathrm{Cu(II)} + 2\mathrm{MPS} \tag{3.2}$$

They point out that in a aerated solution, significant amounts of Cu(I) appear only near the copper metal. As a result, the effective accelerant is formed there and not elsewhere in the plating cell.

The reduction of SPS to MPS can also be driven by the deliberate inclusion of another reducing agent in place of Cu(I). So, for example, Volov and West showed that the ferrous/ferric couple can reduce SPS to MPS and hence increase accelerant efficiency [2].

$$2\text{Fe(II)} + \text{SPS} + 2\text{H}^+ = 2\text{Fe(III)} + 2\text{MPS} \tag{3.3}$$

A number of investigators have presented evidence for formation of Cu(I) thiolates by reaction of copper ions with SPS or MPS. Healy et al. found that SPS forms a Cu(I) thiolate and that Cu(II) and MPS react to form a Cu(I) thiolate [3]. They suggested the mechanism

$$4\text{Cu(I)} + \text{SPS} = 2\text{Cu(II)} + 2\text{Cu(I)thiolate} \tag{3.4}$$

Survila et al. proposed the mechanism,

$$2\text{Cu(II)} + 4\text{MPS} = 2\text{Cu(I)thiolate} + \text{SPS} + 4\text{H}^+ \tag{3.5}$$

and they determined an equilibrium K_1 of $10^{3.3}$ for this reaction [4]. Frank and Bard observed a Cu(I)-MPS thiolate by UV–visible spectroscopy and electron paramagnetic resonance spectroscopy [5]. Pasquale et al. reported reaction of Cu(II) with MPS to produce a Cu(I) thiolate product that they confirmed by UV–visible spectroscopy [6]. Okubo, Watanabe, and Kondo, based on rotating ring-disk electrode experiments, suggested formation of two distinct Cu(I)-additive complexes, one from MPS (CuCl-thiolate), the other from SPS [7]. Chen et al., based on electrochemical impedance spectroscopy and linear sweep voltammetry experiments, proposed the formation of a CuCl-MPS complex [8]. Garcia-Cardona et al. used NMR to study reactions of SPS and MPS with Cu(I) and Cu(II) chlorides [9]. In addition to Reaction (3.5), they considered two additional reactions.

$$4\text{Cu(I)} + \text{SPS} = 2\text{Cu(II)} + 2\text{Cu(I)thiolate} \tag{3.6}$$

$$\text{Cu(I)} + \text{nMPS} = [\text{Cu(I)thiolate}_n]^{(n-1)} + \text{nH}^+ \tag{3.7}$$

They found that SPS reacts directly with CuCl to give a Cu(I) thiolate product and Cu(II) with an equilibrium constant K_2 of 5.2×10^{-3} M^{-1}. No evidence for formation of a Cu(I)-SPS or CuCl-SPS complex was found.

Thiolates are not the only products reported in interactions of SPS and copper species. Frank and Bard reported a SPS-Cu(I) complex which retained the disulfide bond, suggesting a sulfonate complex [5]. Schultz and coworkers also proposed formation of a CuCl-SPS complex with sulfonate coordination based on vibrational spectroscopic as well as mass spectral data and density functional theory calculations (see Fig. 3.2) [10]. Tan et al. hypothesized that a MPS thiol acts as an inhibitor while the accelerant effect is due to the MPS sulfonate group [11].

The accelerant function of SPS is known to be affected by aging of the plating solution. Aging may have both positive and negative effects on the accelerant. In commercial plating of interconnects onto wafers, for instance, plating baths may be preconditioned by deposition onto dummy wafers. Depletion of accelerant in plating operations is often a significant factor and may be particularly rapid in pulse-reverse deposition or in the presence of partially submerged anodes. Pulse-reverse plating may completely exhaust the plating bath after just one wafer. At the

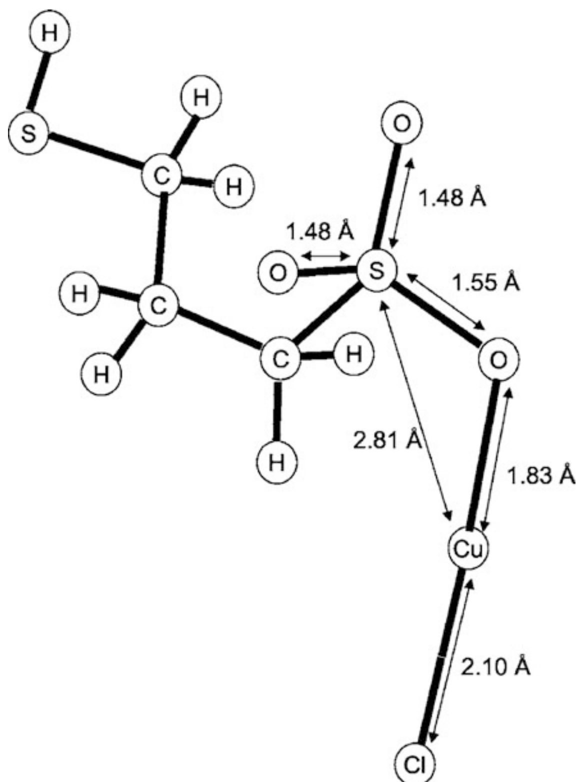

Fig. 3.2 Sulfonate-CuCl complex structure proposed by Schulz et al. Reproduced with permission from Schulz et al. [10]

same time, some transformation of the accelerant additive is essential. Hence, the consumption of accelerant may be integral to its operation or it may result from extraneous processes that could be eliminated through careful design.

A possible pathway for decomposition of SPS to propane disulfonic acid (PDS) is oxidation at the disulfide S–S bond by molecular oxygen or reactive oxygen species.

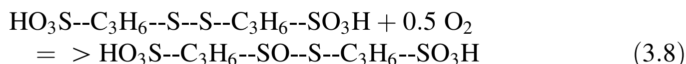

$$\begin{aligned} &HO_3S\text{--}C_3H_6\text{--}S\text{--}S\text{--}C_3H_6\text{--}SO_3H + 0.5\ O_2 \\ &\quad = > HO_3S\text{--}C_3H_6\text{--}SO\text{--}S\text{--}C_3H_6\text{--}SO_3H \end{aligned} \tag{3.8}$$

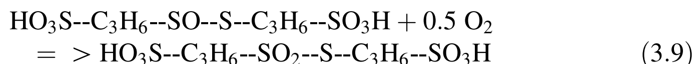

$$\begin{aligned} &HO_3S\text{--}C_3H_6\text{--}SO\text{--}S\text{--}C_3H_6\text{--}SO_3H + 0.5\ O_2 \\ &\quad = > HO_3S\text{--}C_3H_6\text{--}SO_2\text{--}S\text{--}C_3H_6\text{--}SO_3H \end{aligned} \tag{3.9}$$

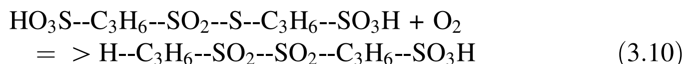

$$\begin{aligned} &HO_3S\text{--}C_3H_6\text{--}SO_2\text{--}S\text{--}C_3H_6\text{--}SO_3H + O_2 \\ &\quad = > H\text{--}C_3H_6\text{--}SO_2\text{--}SO_2\text{--}C_3H_6\text{--}SO_3H \end{aligned} \tag{3.10}$$

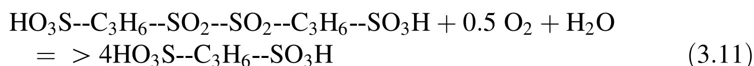

$$\begin{aligned} &HO_3S\text{--}C_3H_6\text{--}SO_2\text{--}SO_2\text{--}C_3H_6\text{--}SO_3H + 0.5\ O_2 + H_2O \\ &\quad = > 4HO_3S\text{--}C_3H_6\text{--}SO_3H \end{aligned} \tag{3.11}$$

A heterogeneous faradaic process can also be considered.

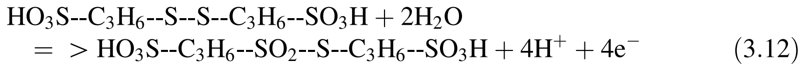

$$\mathrm{HO_3S\text{--}C_3H_6\text{--}S\text{--}S\text{--}C_3H_6\text{--}SO_3H + 2H_2O = > HO_3S\text{--}C_3H_6\text{--}SO_2\text{--}S\text{--}C_3H_6\text{--}SO_3H + 4H^+ + 4e^-} \tag{3.12}$$

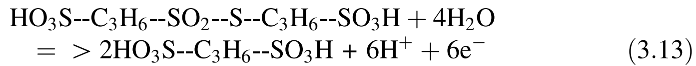

$$\mathrm{HO_3S\text{--}C_3H_6\text{--}SO_2\text{--}S\text{--}C_3H_6\text{--}SO_3H + 4H_2O = > 2HO_3S\text{--}C_3H_6\text{--}SO_3H + 6H^+ + 6e^-} \tag{3.13}$$

Hung et al. investigated the products of SPS oxidation in plating solutions by mass spectroscopy [12]. They observed that PDS was the main product of SPS decomposition. Using ion chromatography and electrospray ionization mass spectroscopy, Brennan et al. found that PDS is the most prevalent impurity in commercial SPS and that it is a product of the oxidation of SPS [13]. However, they observed that SPS is stable in air-saturated solution except in the presence of Cu(I). This result is consistent with the fact that Cu(I) is a good catalyst for generation of reactive oxygen species in solution. Gabrielli et al. investigated the influence of soluble and insoluble anodes on accelerant performance. They found that degradation of SPS is more rapid at insoluble anodes due to their higher surface overpotential [14]. Lee et al. also examined the effects of current density and anodic processes of the decomposition of SPS to PDS in plating solutions [15].

3.3 Surface Processes

The presumed mechanism by which the accelerant reactivates a surface that has been inhibited by a suppressor is through removal of the suppressor from the surface either by displacement (competitive adsorption) or by disruption of the suppressor-surface bond. Hence, the affinity of SPS, MPS, or their complexes for adsorption onto the copper surface is central to an understanding of the accelerant mechanism. Tan et al. studied the PEG/Cl^-/SPS system by transient electrochemical methods including voltammetry and accelerant injection [11, 16]. They concluded that the filling effect depends on both a competitive adsorption mechanism as well as consumption of accelerant on the surface. They also found that the presence of chloride is required for strong adsorption of the accelerant. Basol and West used a plating cell equipped with sweeping pad to demonstrate inhibition by adsorbed inhibitor followed by reactivation by the accelerant [17]. Each sweep disproportionately removed the accelerant while leaving a relatively large amount of suppressor on the surface. Within a characteristic time, the accelerant re-adsorbed and restored a higher deposition rate. Bozzini et al. found evidence by Raman spectroscopy for adsorption of SPS in the presence of chloride [18]. Walker et al. found evidence of MPS and SPS adsorption by spectroscopic ellipsometry [19]. Both Taubert et al. [20] and Tu et al. [21] observed similar adsorption by STM. Pasquale reported an adsorbed SPS-Cu species by Raman and IR spectroscopy [6]. Kinetics of suppressor displacement were measured for

several suppressors by Willey and West with a microfluidic cell [22]. By contrast Bae and Gewirth, using cyclic voltammetry, capacitance, and electrochemical scanning tunneling microscopy, concluded that neither SPS nor MPS was strongly adsorbed even in the presence of chloride [23].Walker et al. found that at lower negative overpotential, adsorption of MPS is slower and less potential-dependent than is adsorption of SPS [24]. At higher overpotential the adsorption rate of SPS is more comparable to that of MPS and this is reflected in the potential dependence of the SPS accelerant effect.

Broekmann's group has proposed a detailed mechanism of accelerant action that entails adsorption and dissociation of SPS to MPS followed by deactivation of the suppressor. [25–27] Their data indicate that suppression is due to formation of a branched polymeric complex with Cu(I) on top of a halide adlayer (see Fig. 3.3). This complex is broken up and dissolved by MPS which competes with the complex for Cu(I). Under this hypothesis, the accelerant is generated on the surface, and its generation is promoted by the copper deposition reaction. MPS accumulates on the surface and prevents the formation of the suppressor complex through rupture of the surface-suppressor coordination bond. At the same time, free MPS in the near surface solution may dissolve the suppressor complex through competition for Cu(I). This latter mechanism involves a free MPS accelerant that is not adsorbed.

3.4 Filling Mechanism

The literature presents two types of models to account for filling by suppressor-accelerant additive ensembles. The first is based on concentration of surface-confined accelerant by elimination of surface area during growth in recesses (see Fig. 3.4) [28, 29]. This model was developed to simulate filling of submicron features on short time scales. The second type of model is based on a favorable distribution of suppressor and accelerant within a feature that is a result of both mass transfer and competitive adsorption. It was developed to account for filling of larger features, such as through-silicon vias (TSV) over much longer periods of time (see Fig. 3.5) [30–33]. This latter type may incorporate features of both mechanisms [33]. However, bottom-up filling in features of this scale has been demonstrated in the absence of curvature [34, 35]. In addition, some attention has been given to the effect of a transport-limited oxidizer [36, 37].

Moffat et al. introduced a model based on local accumulation of accelerant on the surface [28]. The increase in local surface concentration is due to the decrease in surface area during growth on a concave surface. This model provides a mechanism for bottom-up fill in submicrometer trenches (see Fig. 3.6). In an initially square trench, the points of highest curvature, and hence most rapid acceleration in growth rate, are the bottom corners. As these fill in, the maximum curvature shifts toward the bottom of the trench. Hence, after a short time, the highest deposition rate prevails at the bottom, resulting in bottom-up fill.

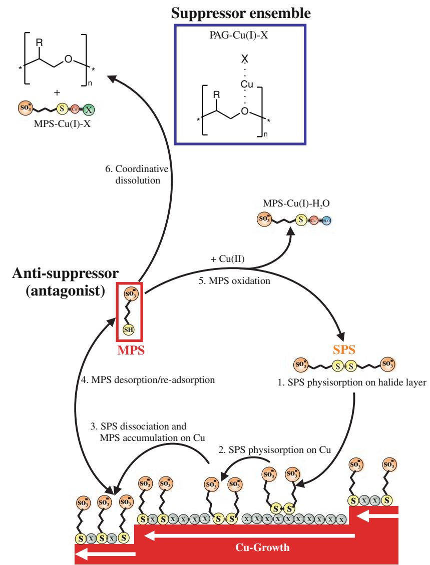

Fig. 3.3 Displacement of suppressor by accelerant. Reproduced with permission from Huynh et al. [27], their Fig. 3.1

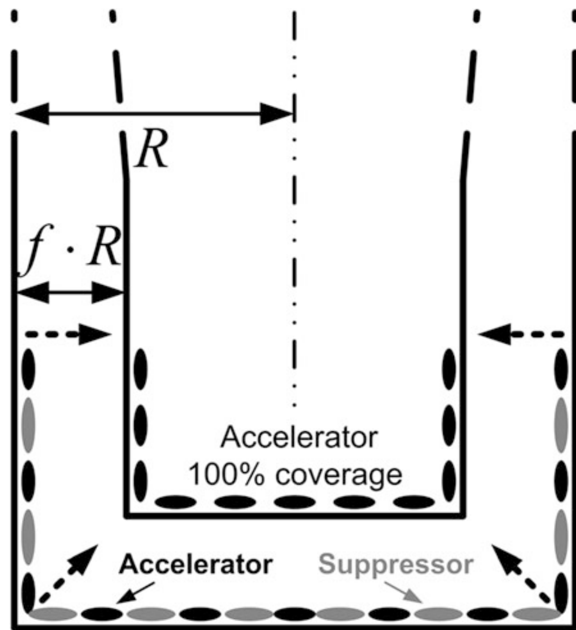

Fig. 3.4 Schematic of superfilling mechanism based on the surface-contraction model. Reproduced with permission from Adolf and Landau [33] (their Fig. 3.2)

The mechanism also accounts for the lag between the beginning of deposition and the onset of bottom-up fill, since the accelerant is only concentrated at points of high curvature after some shape change has occurred. Finally, it accounts for the overburden or bump above the filled trench. Bump formation is driven by the fact

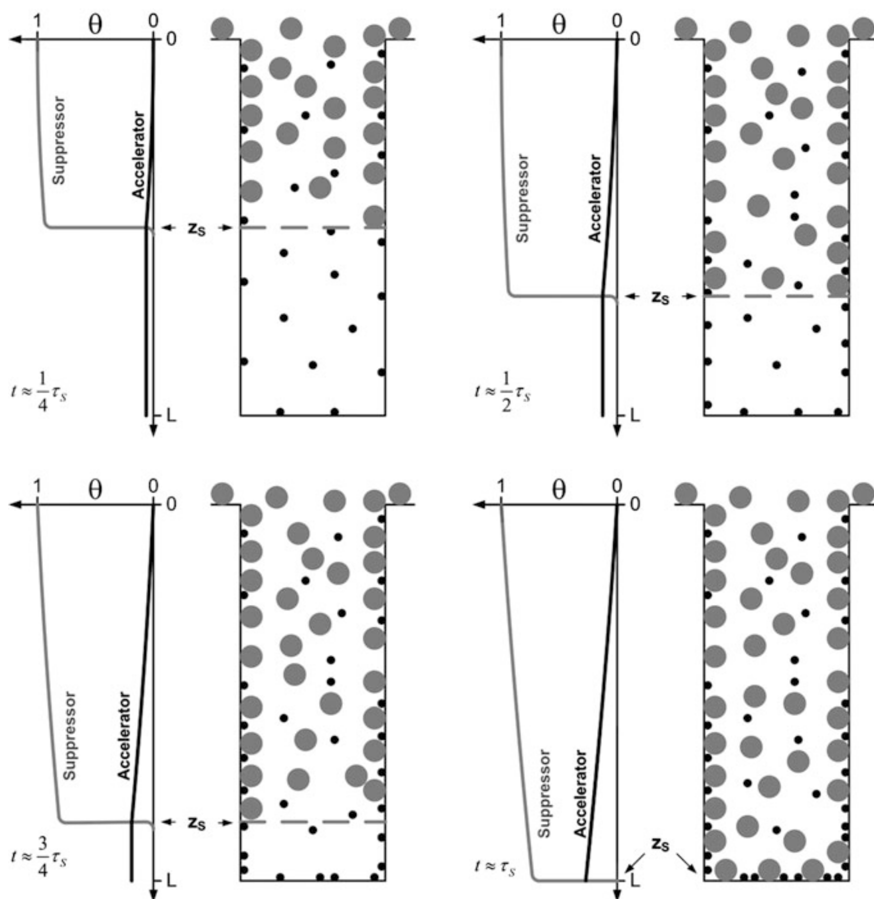

Fig. 3.5 Schematic of superfilling based on the transport model. Reproduced with permission from Adolf and Landau [33] (their Fig. 3.1)

that the high concentration of accelerant at the bottom of the feature carries over to the wafer plane after the feature is filled.

West, Mayer, and Reid independently formulated a similar model at the same time [29]. They also emphasized that the model provides a mechanism for bottom-up fill and accounts for bump formation after feature filling. Their discussion addresses the fact that this type of model introduces dynamic surface phenomena into leveling models that had previously considered only bulk transport. Both groups showed that hysteretic cyclic voltammetry curves, in which the current on a return sweep is higher than current on a cathodic sweep, is a characteristic of super filling plating baths (see Fig. 3.7). This hysteresis is the result of reactivation of the suppressed surface by adsorbed accelerant.

Akolkar and Landau presented a suppressor-accelerant model that emphasizes time-dependent transport of additives coupled with adsorption in filling of larger

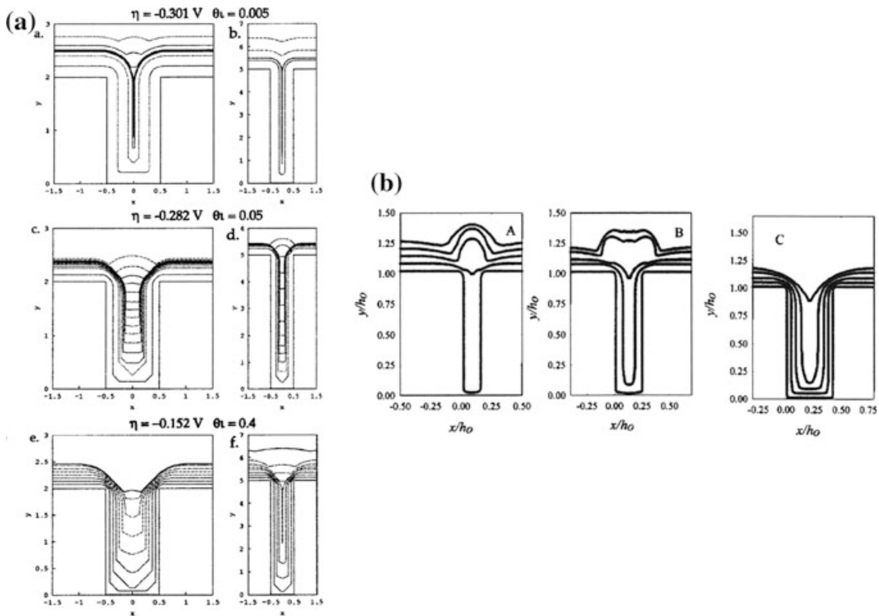

Fig. 3.6 Simulations of trench filling by the surface-contraction model. **a** Reproduced with permission from Moffat et al. [28], their Fig. 3.2 and **b** Reproduced with permission from West et al. [29], their Fig. 3.1

scale features such as through-silicon vias (see Fig. 3.5) [31, 32]. This model includes the instantaneous initial depletion of suppressor within the via by kinetically fast adsorption on the side walls and bottom, followed by diffusion of suppressor from the via exterior to the via bottom. The slow transport of suppressor is due to both its relative low diffusivity compared with the accelerant and to the fact that its transport down the via is hindered by adsorption on the via sidewalls. Adsorption of the accelerant by contrast is not transport limited. Rather its rate is controlled by adsorption kinetics. Bottom-up filling is thus promoted by two distinct competitions between suppressor and accelerant. The first is adsorption of accelerant near the via bottom where the suppressor concentration is low, preventing suppressor adsorption. The second is adsorptive displacement of suppressor by accelerant further up the via at longer times. Each of these steps is characterized by a time constant. The mechanism is effective in high aspect ratio vias where the initial depletion of suppressor is rapid.

Transient bulk-diffusion phenomena are most important in filling of large features because the dimensions of these features produce sufficiently long diffusion times. In filling of submicrometer features, bulk diffusion reaches a steady state before the onset of bottom-up filling. The transport-diffusion model on larger scales does not require curvature to predict bottom-up fill. This fact has been demonstrated experimentally by Kondo and coworkers deposition into holes in

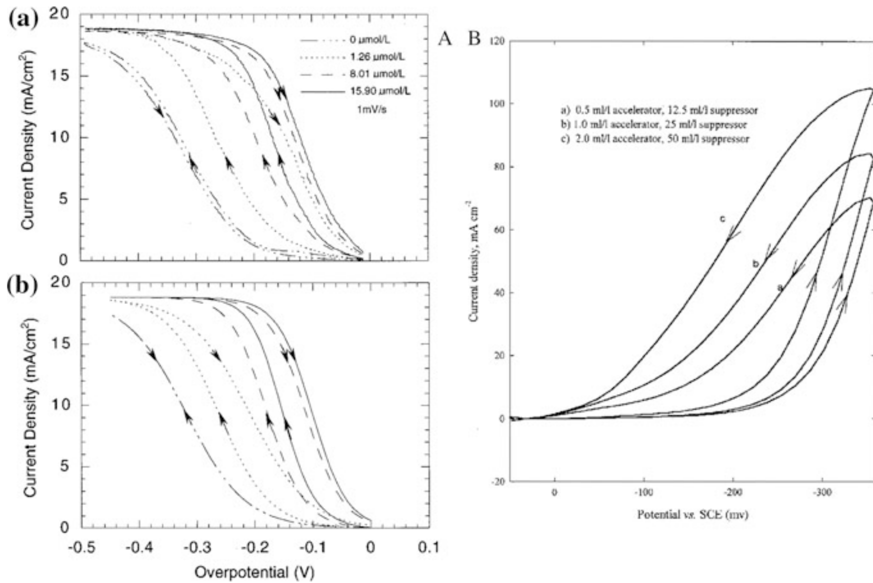

Fig. 3.7 Hysteresis loop **a** Reproduced with permission from Moffat et al. [28], their Fig. 3.2 and **b** Reproduced with permission from West et al. [29], their Fig. 3.1

insulating masks on copper foil [34, 35]. In this configuration, the problem is nearly one dimensional, and the growing surface remains flat throughout. Yet, thicker masks result in more rapid growth. The result can be understood by application of the transport-adsorption mechanism, although it differs in some detail due to the absence of side walls, and the more rapid diffusion of accelerant compared with that of suppressor is consistent with the experimental observation in these experiments. (see Fig. 3.8). As in TSV filling, the suppressor is adsorbed at a rate controlled by diffusion to the via bottom. The accelerant wins the race to the via bottom because of its higher diffusion constant and eventually displaces the suppressor altogether.

The effects of competitive diffusion phenomena, where the accelerant arrives more rapidly at a feature bottom than does the suppressor, can be amplified by addition of oxidizers to the bulk solution (see Fig. 3.8). Examples include ozone [36] and oxygen [37]. Because formation of the effective accelerant proceeds through reduction of SPS to MPS by Cu(I), an oxidizing environment can inhibit accelerant production either by oxidation of MPS or oxidation of Cu(I). In this instance, it is the diffusion limitation on the oxidizer that promotes filling. The oxidizer deactivates the accelerant near the tops of features. Because it is consumed in the process, it does not penetrate deeply into the via and cannot deactivate the accelerant near the bottom of features. This effect appears to connect the various filling models with the accelerant chemistry because the oxidizers act by destruction of the Cu(I)thiolate.

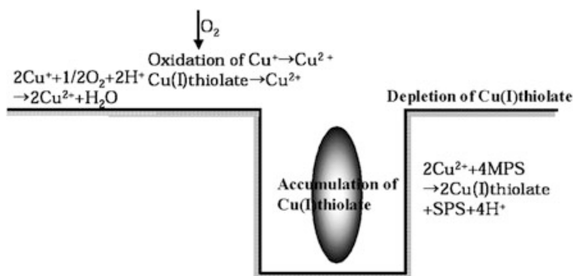

Fig. 3.8 Schematic of super filling based on the free accelerant model with oxidative destruction of accelerant. Reproduced with permission from Kondo et al. [35]

The formation of cuprous is a crucial intermediate and the cuprous intermediate is always produced during the electrodepositon process.

$$Cu^{2+} + e^- \underset{k_{-1}}{\overset{k_1}{\rightleftarrows}} Cu^+ \tag{3.14}$$

$$Cu^{2+} + e^- \underset{k_{-1}}{\overset{k_2}{\rightleftarrows}} Cu^+ \tag{3.15}$$

These reactions are reversible processes. The reaction constant k_1 for the cupric ions to cuprous ions is $2\text{x}10^{-4}$ mol·m^{-2}s^{-1}and k_{-1} for the cuprous to cupric ions is 8×10^{-3} mol·m^{-2}s^{-1}. k_2 for the cuprous ions to metallic copper is 130 mol·m^{-2}s^{-1} and k_{-2} for the metallic copper to cuprous ions is $3.9\text{x}10^{-7}$ mol·m^{-2}s^{-1}. Large value of k_2 for 130 mol.m^{-2}s^{-1} means that once the cuprous ions is formed, the reaction to reduce it to metallic copper is extremely rapid [38]. Furthermore, the cuprous ions are transparent and odorless. Hence it is extremely difficult to detect the cuprous ions and accordingly few studies exist which are related to the acceleration effect of cuprous ions.

On the other hand, a rotating ring disk electrode (RRDE) has been used to detect the cuprous ions. The cuprous ions detected at the ring of the RRDE is 1,000 times higher for the copper dissolution, if it is compared to the cuprous ions for the electrodeposition [39]. Hence, we formed a large amount of cuprous ions within the confined area of the trench in the trench bottom electrodes and experimentally verify the relation between the cuprous ions and acceleration. The trench bottom electrodes have been photo-lithographed on the copper foil with OFPR-800-(Tokyo-oka) photoresist. The trench widths are 3, 5, and 10 μm.

This work is from Kondo and coworker's recent researches [40, 41]. The effect of the O_2 bubbling and N_2 bubbling has been initially tested in the nonstirred bath. The bath consists of the basic bath and 1ppm SPS, 400 ppm PEG and 50 ppm Cl^-. Prior to the LSVs, the cuprous ions were formed by dissolving the copper electrode at the trench bottom for 12s at 10 mA/cm^2. Figure 3.9a shows the LSV result with N_2 bubbling. The potential and current density are illustrated for the trench bottom electrode widths of 3, 5, and 10 μms. Drastic increases in the current densities due to the acceleration effect are observed and the current density increased up to

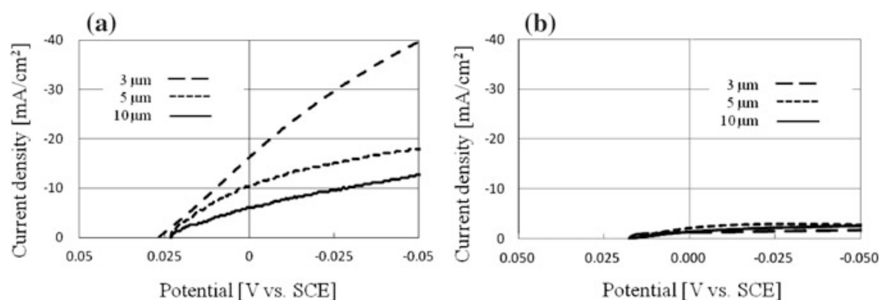

Fig. 3.9 **a** Result of LSV measurements with N_2 bubbling. **b** Result of LSV measurements with O_2 bubbling. SPS:1 ppm, Cl^-:50 ppm, PEG:400 ppm

-40 mA/cm^2 for the 3 μm trench bottom electrode width at -0.05V vs. SCE. Furthermore, the current densities increase with the narrower trench bottom electrode width. On the contrary, the currents show a very low value of -1.0mA/cm^2 for the LSV result with O_2 bubbling Fig. 3.9b. The current densities are same with the trench bottom electrode widths of 3, 5, and 10 μms. The drastic difference in the current densities with the O_2 gas concentration in the electrolyte must be caused by the cuprous complex formed in the trench of the trench bottom electrode. The increase in the current densities for the narrower trench of the trench bottom electrode must be caused by the accumulation of a cuprous complex in the trench.

In order to prove that this cuprous complex is free, floating in the electrolyte, and not adsorbing on the electrode, forced convection has been applied by the stirrer at 600 rpm. The current densities have been then measured by LSV by initially dissolving the copper electrode at the trench bottom. The LSV measurements are shown in Fig. 3.10a. The current densities decrease to a few mA/cm^2 and almost no difference in the current densities for the trench widths of 3, 5, and 10 μm. The acceleration effect has deceased. This is because the free cuprous complex flows out of the trenches due to the stirring at 600 rpm.

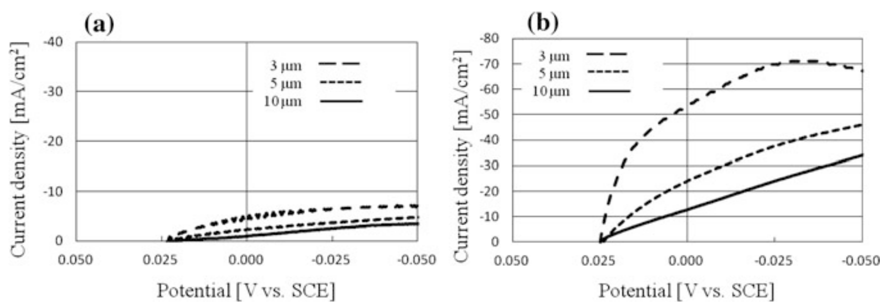

Fig. 3.10 **a** Result of LSV measurements with N_2.Stirring rate of stirrer is 600 rpm. SPS:1 ppm, Cl^-:50 ppm, PEG:400 ppm.**b** Result of LSV measurements with N_2 bubbling. Cl^-:50 ppm

Next, in order to investigate the cuprous ions and the additives, we have eliminated the additives and the LSVs have been measured. We then have eliminated PEG and SPS and only the Cl^- has added. The current shows a marked increase for −70mA/cm^2 for 3 μm at −0.05V vs. SCE Fig. 3.10b. The narrower the trench is the current densities increase. Cl^- is an important additive for the acceleration, and the acceleration must be related to the free cuprous complex and electron bridge formation of Cl^- [42], which may be enlarging reaction constant of k_1 in eq. (1) through the electron bridge formation.

Without dissolving copper at the trench bottom electrodes, the current densities have been measured at the constant potential of −0.15V vs. SCE. This is because we want to prove that the cuprous forming through the electrodeposition process is an accelerator. With O_2 bubbling, the current densities are low values of about 1.0 mA/cm^2. However, the current densities markedly increase with the N_2 bubbling. With the narrower trenches, the current densities increase and −23mA/cm^2 has been measured for the 3 μm trench width. These constant potential measurements without dissolving the copper electrode also show that the free cuprous complex formed through electrodeposition is the accelerant.

3.5 Summary

Investigations over the last two decades have produced considerable insight into the nature and mechanism of copper-plating accelerants. Nevertheless, there remain disagreements and uncertainties over the configuration of the accelerant and its mechanism of action. It appears that there are substantial constraints on the molecular structure of accelerants, and as a result suitable molecules are few. This review has focused on SPS/MPS. The mechanism of action of the accelerant SPS/MPS is complicated in comparison to that of suppressors and levelers. It involves reversible transformations of the additive through interactions with at least two other species in solution and with the metal. Chloride is essential to formation of the accelerant complex. In addition, Cu(I) must be present or be formed at the metal-solution interface as well. The transformations among SPS, MPS, and accelerant complex are probably reversible and may run through a cycle. In addition, there are irreversible transformations that may take place in the presence of oxidizers or at the anode, and these can result in rapid consumption of the accelerant in practical operations.

The most widely held view is that SPS/MPS forms a Cu(I) thiolate that deactivates suppressors such as PEG, although it is not settled whether the complex is formed in solution or on the metal surface. Deactivation of the suppressor may proceed by competitive adsorption and displacement or by disruption of the suppressor-surface bond either by a free accelerant or an adsorbed accelerant. It is possible that either mechanism may be important depending on the character of the suppressor, and the literature demonstrates that the interaction between suppressor and accelerant is complicated, involving complexes of both components with

Cu(I) and Cl^-. The mechanism by which suppressor-accelerant combinations produce filling is complicated as well. The role of accelerants in filling may be controlled by surface processes or by bulk-diffusion processes depending on the feature scale and filling time. Their effectiveness may also be enhanced by the use of reducing agents.

This review has highlighted a relatively small part of the literature. The number of publications on the topic is large. More attention has been paid to solution chemistry and to accelerant-suppressor interactions and less to the very large literature on super filling. These topics are addressed in detail elsewhere in this volume.

Acknowledgments The author acknowledges many helpful suggestions provided by Professor Edward H. Wong.

References

1. Vereecken PM, Binstead RA, Deligianni H, Andricacos PC (2005) The chemistry of additives in copper Damascene plating. IBM J Res Dev 49:3–19
2. Tan M, Guymon C, Wheeler DR, Harb JN (2007) The role of SPS, MPSA, and chloride in additive systems for copper electrodeposition. J Electrochem Soc 154:D78–D81
3. Healy JP, Pletcher D (1992) The chemistry of additives in an acid copper electroplating bath. J Electroanal Chem 338:167–177
4. Survila A, Kanapeckaite S, Pauliukaite R (1998) Polaragraphic behavior of Cu(II) solutions involving 3-Mercapto-1-Propanosulphonic Acid. Chemija 1:21–26
5. Frank A, Bard AJ (2003) The decomposition of the sulfonate additive sulfopropyl sulfonate in acid copper electroplating chemistries. J Electrochem Soc 150:C244–C250
6. Pasquale MA, Bolzan AE, Guida JA, Piatti RCV, Arvia AJ, Piro OE, Castellano EE (2007) A new polymeric [Cu(SO3(CH2)3SeS(CH2)3SO3)(H2O)4]n complex molecule produced from constituents of a super-conformational copper plating bath: Crystal structure, infrared and Raman spectra and thermal behavior. Solid State Sci 9:862–868
7. Okubu T, Watanabe K, Kondo K (2007) Analytical study of the characteristics of Cu(I) species for the via-filling electroplating using a RRDE. J Electrochem Soc 154:C181–C187
8. Chen H-M, Parulekar SJ, Zdunek A (2008) Interactions of chloride and 3-Mercapto-1-Propane sulfonic acid in acidic copper sulfate electrolyte. J Electrochem Soc 155:D349–D356
9. Garcia-Cardona E, Wong EH, Barkey DP (2011) NMR spectral studies of interactions between the accelerants SPS and MPS and copper chlorides. J Electrochem Soc 158:D143–D148
10. Schultz ZD, Feng ZV, Biggin ME, Gewirth AA (2006) Vibrational spectroscopic and mass spectrometric studies of the interaction of Bis(3-sulfopropyl)-disulfide with Cu surfaces. J Electrochem Soc 153:C97–C107
11. Volov I, West AC (2011) Interaction between SPS and MPS in the presence of ferrous and ferric ions. J Electrochem Soc 158:D456–D461
12. Hung C-C, Lee W-H, Hu S-Y, Chang S-C, Chen K-W, Wang Y-L (2008) Investigation of Bis-(3-sodiumsulfopropyl disulfide) (SPS) decomposition in a copper-electroplating bath using mass spectroscopy. J Electrochem Soc 155:H329–H333
13. Brennan, RG, Philips, MM, Ou Yang, L-Y, Moffat, TP (2011) Characterization and purification of commercial SPS and MPS by ion chromatography and mass spectrometry. J Electrochem Soc 158:D178–D186

14. Gabrielli C, Mocoteguy P, Perrot H, Zdunek A, Nieto-Sanz D (2007) Influence of the anode on the degradation of the additives in the Damascene process for copper deposition. J Electrochem Soc 154:D163–D169
15. Lee W-H, Hung C-C, Chang S-C, Wang Y-L (2010) Bis-(3-sodiumsulfopropyl disulfide) decomposition with cathodic current flowing in a copper-electroplating bath. J Electrochem Soc 157:H131–H135
16. Tan M, Harb JN (2003) Additive behavior during copper electrodeposition in solutions containing Cl^{-}, PEG, and SPS. J Electrochem Soc 150:C420–C425
17. Başol BM, West AC (2006) Study on mechanically induced current suppression and super filling mechanisms. Electrochem Solid-State Lett 9:C77–C80
18. Bozzini B, D'Urzo L, Romanello V, Mele C (2006) Electrodeposition of Cu from acidic sulfate solutions in the presence of Bis-(3-sulfopropyl)-disulfide (SPS) and chloride ions. J Electrochem Soc 153:C254–C257
19. Walker ML, Richter LJ, Moffat TP (2006) Competitive adsorption of PEG, Cl^{-}, and SPS/MPS on Cu: an in situ ellipsometric study. J Electrochem Soc 153:C557–C561
20. Täubert CE, Kolb DM, Memmert U, Meyer H (2007) Adsorption of the additives MPA, MPSA, and SPS onto Cu(111) from sulfuric acid solutions. J Electrochem Soc 154:D293–D299
21. Tu H-L, Yen P-Y, Chen S, Yau S-L, Dow W-P, Lee Y-L (2011) In situ imaging of Bis-3-sodiumsulfopropyl-disulfide molecules adsorbed on copper film electrodeposited on Pt(111) single crystal electrode. Langmuir 27:6801–6807
22. Willey MJ, West AC (2007) SPS adsorption and desorption during copper electrodeposition and its impact on PEG adsorption. J Electrochem Soc 154:D156–D162
23. Bae S-E, Gewirth AA (2006) In situ EC-STM studies of MPS, SPS, and chloride on Cu(100): structural studies of accelerators for dual Damascene electrodeposition. Langmuir 22:10315–10321
24. Walker ML, Richter LJ, Moffat TP (2007) Potential dependence of competitive adsorption of PEG, Ci- and SPS/MPS on Cu: an in situ ellipsometric study. J Electrochem Soc 154:D277–D282
25. Hai NTM, Kramer KW, Fluegel A, Arnold M, Mayer D, Broekmann P (2012) Beyond interfacial anion/cation pairing: the role of Cu(I) coordination chemistry in additive-controlled copper plating. Electrochim Acta 83:367–375
26. Hai NTM, Huynh TMT, Fluegel A, Arnold M, Mayer D, Reckien W, Broekmann P (2012) Competitive anion/anion interactions on copper surfaces relevant for Damascene electroplating. Electrochim Acta 70:286–295
27. Huynh TMT, Weiss F, Hai NTM, Reckien W, Bredow T, Fluegel A, Arnold M, Mayer D, Keller H, Broekmann P (2013) On the role of halides and thiols in additive-assisted copper electroplating. Electrochim Acta 89:537–548
28. Moffat TP, Wheeler D, Huber WH, Jossell D (2001) Superconformal electrodeposition of copper. Electrochem Solid-State Lett 4:C26
29. West AC, Mayer S, Reid J (2001) A superfilling model that predicts bump formation. Electrochem Solid-State Lett 2001(4):C50–C53
30. Chalupa R, Cao Y, West AC (2002) Unsteady diffusion effects on electrodeposition into a submicron trench. J Appl Electrochem 32:135–143
31. Akolkar R, Landau U (2004) A time-dependent transport-kinetics model for additive interactions in copper interconnect metallization. J Electrochem Soc 151:C702–C711
32. Akolkar R, Landau U (2009) Mechanistic analysis of the 'bottom-up' fill in copper interconnect metallization. J Electrochem Soc 156:D351–D359
33. Adolf J, Landau U (2011) Predictive analytical fill model of interconnect metallization providing optimal additives concentrations. J Electrochem Soc 158:D469–D476
34. Kondo K, Yamakawa N, Tanaka Z, Hayashi K (2003) Copper Damascene electrodeposition and additives. J. Electroanalytical Chem. 559:137–142

35. Kondo K, Matsumoto T, Watanabe K (2004) Experimental study on inhibition and acceleration effects role of additives for copper Damascene electrodeposition. J Electrochem Soc 151:C250–C255
36. Mazur S, Jackson CE Jr (2008) Enhanced electrodeposition of Cu into recessed features via topographically selective ozonolysis of adsorbed accelerator. J Electrochem Soc 155:D608–D613
37. Kondo K, Yonezawa T, Mikami D, Okubo T, Taguchi Y, Takahashi K, Barkey DP (2005) High-aspect-ratio copper-via-filling for three-dimensional chip stacking; II. reduced electrodeposition process. J Electrochem Soc 152:H173–H177
38. Tantavishet N, Pritzker M (2003) Low- and high-frequency pulse current and pulse reverse plating of copper. J Electrochem Soc 150:C665–C670
39. White JR (1987) Reverse pulse plating of copper from acid electrolyte; a rotating ring disk electrode study. J Applied Electrochem 17:977–982
40. Kondo K, Hamazaki K, Yokoi M, Okamoto N, Saito T (2013, in present) Behavior of cuprous intermediate in copper damascene electrodeposition. ECS Electrochem. Lett.,In course of publication
41. Kondo K, Hamazaki K, Yokoi M, Okamoto N, Saito T (2013, in present) Behavior of cuprous intermediate in copper damascene electrodeposition. ECS 2013 Fall Meeting in SanFransisco, Abstract 2086
42. Nagy Z, Blaudeau JP, Hung NC, Curtiss LA, Zurawski DJ (1995) Chloride ion catalysis of the copper deposition reaction. J.Electrochem Soc 142:L87–L92

Chapter 4
Modeling and Simulation

Yutaka Kaneko

This chapter is devoted to recent developments in mathematical modeling and computer simulation of copper electrodeposition. We focus our attention on continuum models and kinetic Monte Carlo simulations for shape evolution and the effects of additives on copper deposition, especially the filling of small features in microelectronics. The modeling, mathematical treatments, and simulation results are reviewed with brief summaries of efficient numerical algorithms. Fast computing and prospects of simulation research are also discussed.

4.1 Introduction

Copper electrodeposition has attracted a great deal of attention since IBM announced the replacement of conventional vapor deposition of aluminum with copper electrodeposition for the production of LSI interconnects [1]. The dual damascene process is now a central technique for the fabrication of three-dimensional (3D) LSI circuits. An important requirement for the success of this process is the capacity to fill submicron features such as via holes and trenches completely without voids or seams. This process is called "superfilling" or "superconformal filling." It has been found experimentally that superfilling is achieved by the synergistic effects of different kinds of additives, and the optimal deposition conditions have been explored.

Mathematical modeling and numerical simulations are indispensable means of research to understand the underlying chemistry from a microscopic point of view and to determine the optimal conditions for practical applications. There are two types of modeling for copper electrodeposition. The first type is based on

Y. Kaneko (✉)
Department of Applied Analysis and Complex Dynamical Systems Graduate School of Informatics, Kyoto University, Yoshida-Honmachi, Sakyo-ku, Kyoto 606-8501, Japan
e-mail: kaneko@acs.i.kyoto-u.ac.jp

K. Kondo et al. (eds.), *Copper Electrodeposition for Nanofabrication of Electronics Devices*, Nanostructure Science and Technology 171, DOI: 10.1007/978-1-4614-9176-7_4,
© Springer Science+Business Media New York 2014

"continuum models" in which the physical quantities are expressed in terms of continuous variables. The basic equations are partial differential equations. The second type is "molecular simulation" such as Monte Carlo (MC) and molecular dynamics (MD) computations in which ions and molecules are treated as particles. In this chapter, we overview the recent developments of these two types of simulation for copper electrodeposition to understand the present status of sophistication.

This chapter is organized as follows. The next section is the brief review of the numerical simulations based on continuum models. Section 4.2.1 is devoted to the mathematical models for superfilling. The basic ideas and mathematical formulas of the diffusion-consumption theory [1–5], the recent theory of curvature enhanced accelerator coverage [6–14], and the theory based on time-dependent transport [15, 16] are described. We then review the nucleation theory in terms of the continuum equations in Sect. 4.2.2. Diffusion-limited [17–22] and kinetically limited [23, 24] nucleation and growth are discussed. The fluid mechanical approach to copper electrodeposition is presented in Sect. 4.2.3 for the example of copper bump formation in microelectronics [25–32].

Since the size of recent LSI chips is as small as nanoscale, molecular simulations are important tools for microscopic analyses. The kinetic Monte Carlo (KMC) simulation is a promising technique with a wide range of applications. We discuss the KMC simulation and multiscale modeling in Sects. 4.3 and 4.4. The basic concept of the KMC method, the combination of the KMC method and continuum models, the multiscale modeling, and application to 3D device fabrication are presented [33–50]. Further developments of fast computing are discussed in Sect. 4.5 [51–56]. A summary and a brief comment on MD simulation [57, 58] are given in Sect. 4.6.

Since the purpose of the present article is to describe the mathematical frameworks and numerical methods, the parameter-setting in individual models is not stated although it is an important step in performing the simulations. We refer to the literature for setting parameters. Some details of the numerical algorithms which are important for simulation are summarized in Appendices.

Since this chapter is a review of more than 50 articles, some of the nomenclatures of variables and formulas are different from those in the original articles.

4.2 Mathematical Models for Copper Electrodeposition

The conventional mathematical models of electrodeposition are essentially boundary problems of the Laplace equation for current distribution and the diffusion equation for mass transport in solution. The deposition reactions and additive effects are incorporated in the boundary conditions. Since the electrode surface moves toward the solution as a result of electrodeposition, the technique to track the moving boundary is required for numerical calculations. In this section,

we overview the mathematical models for copper electrodeposition based on continuum models.

4.2.1 Mathematical Models for Superfilling

The success of the damascene process has accelerated the theoretical approach to copper electrodeposition. It has been shown experimentally that void-free filling of high-aspect ratio via holes and trenches can be obtained by the combination of suppressors (polyethylene glycol, PEG), halide ions (Cl^-), accelerators (bis 3-sulfopropyl disulfide, SPS), and levelers (Janus Green B, etc.). This section is concerned with an overview of recent theories to explain the additive effects, which are essential for superfilling within the framework of continuum models.

4.2.1.1 Diffusion-Consumption Model

The diffusion-consumption model is a traditional theory for leveling by suppressors [2, 3]. In this theory, the distribution of suppressors is assumed to be transport-limited, adsorbed on the surface where it inhibits metal deposition, and then consumed (annihilated from the surface). Figure 4.1a shows a schematic picture of the theory. Since the flux of suppressor comes from the solution far from the electrode, more suppressors are deposited around the opening of the hole than at the bottom. As a result, the metal deposition rate becomes higher at the bottom than at the top, resulting in bottom-up filling. Superfilling in the damascene process was first explained by this type of model [1, 4, 5]. The mathematical formulas used in the original paper of Andricacos et al. [1] are as follows:

The mass transport of metal ions and additives (suppressors) in the concentration boundary layer is assumed to occur only by diffusion. Assuming a stationary state, the concentrations of metal ions C, additives C_{ad} and the potential Φ obey the Laplace equations,

$$\nabla^2 C = 0, \nabla^2 C_{ad} = 0, \nabla^2 \Phi = 0, \tag{4.1}$$

C, C_{ad} and Φ are assumed to be independent in solution and are coupled only at the electrode surface. The boundary conditions at the electrode surface are

$$2FD\nabla C \cdot \mathbf{n} = \kappa_c \nabla \Phi \cdot \mathbf{n}, \tag{4.2}$$

$$C_{ad} = 0, \tag{4.3}$$

where F is Faraday's constant and κ_C is the electrical conductivity. $\mathbf{n}$ is the unit vector normal to the surface. Equation (4.2) arises from the balance of the current density and the flux of metal ions on the surface, where D is the diffusion constant

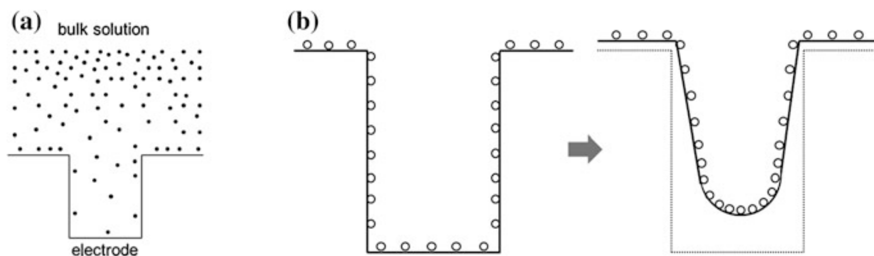

Fig. 4.1 **a** Image of the diffusion-consumption model. Suppressors (*solid circles*) diffuse from bulk solution to the electrode and annihilated. The concentration of suppressors is higher around the via top than at the bottom. **b** Image of the area change. Accelerators (*open circles*) are condensed as the bottom area is reduced

of metal ions. The condition (4.3) represents consumption of the additives on the surface. The current density at the electrode surface is given by the Tafel equation

$$i = i_0^{\infty} \psi \left(\frac{C}{C^{\infty}} \right)^{\gamma + \alpha / n} e^{\alpha F \Phi / RT}. \tag{4.4}$$

Here i_0^{∞} is the exchange current density of the additive-free bulk solution, ψ includes the suppressing effect of additives depending upon the spatial distribution of additive flux. α is a transfer coefficient and γ, n are constants. At the upper boundary in solution (the edge of the boundary layer), C and C_{ad} take the constant bulk values, C^{∞}, C_{ad}^{∞}, and $\nabla\Phi$ is calculated from the bulk current density. Equation (4.1) with the conditions Eqs.(4.2)–(4.4) has been solved using the moving boundary method [2]. The numerical simulations of this type of model showed that the diffusion-consumption theory can realize the bottom-up filling [1, 4, 5].

4.2.1.2 Curvature Enhanced Accelerator Coverage

The important characteristics of superfilling are (1) incubation period (conformal filling in the early stage), (2) bottom-up, and (3) overfilling and bump formation in the late stage. The diffusion-consumption theory can realize (2) bottom-up filling. However, it cannot explain the conditions (1) and (3). Also, in most of the experiments on superfilling, multiple additives (suppressor, accelerator, leveler) are required, while the diffusion-consumption model considers only suppressors. This means that an additional mechanism must be identified to explain the overall feature of superfilling.

A new theory has been proposed in terms of accelerators, which is known as the curvature enhanced accelerator coverage (CEAC) mechanism [6–8]. The key factor of this theory is the coverage of the accelerators on the electrode and the change in the surface area during the deposition process. Figure 4.1b is a

schematic picture of the idea of the CEAC mechanism. Assume that the accelerators are uniformly distributed on the feature surface. When the surface grows as a result of copper deposition, the surface of the bottom moves upward and the area becomes smaller. If the consumption of the accelerators is negligible, the surface coverage (concentration per unit area) of accelerators at the bottom increases. As a result, the deposition rate at the bottom becomes larger than that around the opening of the hole, which leads to bottom-up filling. A lot of papers have been published about the mathematical modeling and numerical simulations of the CEAC model. In the following, the basic formulas of the CEAC are summarized following the papers of Moffat et al. [6, 7, 9–14].

The system considered is copper electrodeposition with suppressors and accelerators. Assume that suppressors are quickly adsorbed on the surface and are soon replaced by the accelerators. Therefore, only the effect of accelerators is considered on the feature surface. The current density is assumed to be a function of the coverage θ_A of the accelerators and the overpotential η;

$$i = i(\theta_A, \eta). \tag{4.5}$$

Adsorbed accelerators float upon the growing metal surface, and their rate of consumption is assumed to be small. The time evolution of the coverage θ_A is represented by:

$$\frac{\partial \theta_A}{\partial t} = v\kappa\theta_A + R(\theta_A) + k_A\theta_A^q. \tag{4.6}$$

The local surface velocity v is given by $v = i\Omega/zF$, where Ω is the atomic volume and z is the valence of copper ions ($z = 2$ for Cu^{2+}). The reaction term $R(\theta_A)$ corresponds to the production rate of accelerants on the surface. The first term on the right-hand side of Eq. (4.6) represents the influence of the area change, where κ is the local curvature of the surface. This term means that the coverage θ_A depends on the sign of κ, i.e., θ_A will increase for the concave surface and decrease for the convex surface. Therefore, the growth rate of a concave surface becomes larger than that of flat or convex surfaces. The last term on the right-hand side of Eq. (4.6) shows the power law consumption of accelerants due to the incorporation. Equation (4.6) is solved with the equations representing the shape evolution of the electrode surface.

In the early works of Josell et al. [6], $k_A = 0$ and the following expressions were assumed,

$$i(\theta_A, \eta) = i_0(\theta_A)\left(1 - \frac{i}{i_L}\right)\exp\left(-\frac{\alpha(\theta_A)F}{RT}\eta\right), \tag{4.7}$$

$$R(\theta_A) = k^* C_A^i(1 - \theta_A), \tag{4.8}$$

where i_L is the transport-limited current density, C_A^i is the concentration of accelerators at the interface and k^* is the reaction rate. The exchange current density $i_0(\theta_A)$ and the transfer coefficient $\alpha(\theta_A)$ are obtained from independent

experiments on copper electrodeposition on a flat surface as a function of the accelerator coverageθ_A. The depletion of copper ions in solution was accounted for by the diffusion equation for copper ion density. The moving boundary has been treated by the level set method (LSM) [9].[1] Numerical calculations showed that the initial conformal deposition and bottom-up fill can be realized by this model depending upon the parameters. If the accelerators remain until the end of the filling, the accelerator concentration is large around the middle of the via, which leads to bump formation after filling is completed. Therefore, the CEAC is a model which reproduces the superfilling conditions.

The CEAC mechanism is regarded as a leveling theory in terms of the accelerators to control the roughness evolution of the surface [10]. The model has been modified to include the mass transport of accelerators in solution [9] and the surface diffusion of adsorbed accelerators [11]. It has also been extended to the multiple-additive system; PEG-SPS [12], PEG-SPS-Leveler [13, 14] to include the deactivation of accelerators by levelers. A summary of these works is found in Refs. [12, 14]. The idea of area change is quite general and has been incorporated in other mathematical forms as described in the following sections.

4.2.1.3 Time-dependent transport kinetics of additives

In the diffusion–consumption models in Refs. [1–5], a stationary state is assumed for the diffusion of suppressors. In the CEAC models cited in this section, time-dependent mass transport is taken into account for copper ions and accelerators, but not for suppressors. Akolkar and Landau pointed out that different mechanisms appear in the early stage and the late stage of the filling process due to the time-dependent transport and interactions between additives [15, 16]. They observed in their experiments [15] that PEG adsorbs on the copper surface almost instantaneously, while the diffusion of the PEG in solution is slow. SPS, on the other hand, diffuses rapidly in solution and adsorbs on copper surface moderately fast. The replacement of the adsorbed PEG by SPS is rather slow compared to the adsorption of PEG and SPS on the additive-free surface.

Taking into account these differences in the time scales, Akolkar and Landau developed a one-dimensional transport–adsorption model [16]. For a high-aspect ratio via (the radius R_V and the depth L_V), the radial variation of concentration is negligible and the time and space variation of the PEG concentration C_I in the axial direction (z-direction) parallel to the via sidewall is considered. The mass balance in the via hole leads to the following diffusion–reaction equation for C_I.

$$\frac{\partial C_I}{\partial t} = D_I \frac{\partial^2 C_I}{\partial z^2} - \frac{2}{R_V} \left[k_I C_I (1 - \theta_I - \theta_A) - k C_A^b \theta_A \right] \tag{4.9}$$

[1] LSM is a feasible method to track the moving boundary. The formulas are given in Appendix A.

The first term on the right-hand side is the diffusion term, where D_I is the PEG diffusion constant. The second term represents the reactions on the surface, where k_I is the adsorption rate constant, and θ_I and θ_A are the surface coverages of PEG and SPS, respectively. The second term in the square brackets represents the displacement of PEG by SPS, where k is the reaction rate. The concentration of SPS in the via is assumed to be the same as the bulk value C_A^b due to the rapid diffusion.

The time variations of the coverages θ_I and θ_A are represented by the balance of the reactions as

$$\frac{\partial \theta_I}{\partial t} = \frac{1}{\Gamma_I}\left[k_I C_I (1 - \theta_I - \theta_A) - kC_A^b \theta_A\right] \tag{4.10}$$

$$\frac{\partial \theta_A}{\partial t} = \frac{1}{\Gamma_A} kC_A^b (1 - \theta_I - \theta_A) + \frac{1}{\Gamma_I} kC_A^b \theta_I \tag{4.11}$$

The difference in the molecular size of PEG and SPS is taken into account by Γ_I and Γ_A, where $\Gamma_A/\Gamma_I \cong 13.33$. Equation (4.10) indicates that the coverage of PEG increases rapidly (first term) and is slowly replaced by SPS (second term). At the via bottom, however, PEG deposition is hindered by slow diffusion. The first and second terms on the right-hand side of Eq. (4.11) show the rapid adsorption of PEG on additive-free surface and the slow displacement of PEG, respectively. The total current density arises from the sum of the current densities of PEG-covered area, SPS-covered area, and additive-free copper surface, which are represented by

$$\begin{aligned} i_{tot} = {} & i_{0,I}\theta_I \exp\left(\frac{\alpha_I F\eta}{RT}\right) + i_{0,A}\theta_A \exp\left(\frac{\alpha_A F\eta}{RT}\right) \\ & + i_{0,Cu}(1 - \theta_I - \theta_A)\exp\left(\frac{\alpha F\eta}{RT}\right), \end{aligned} \tag{4.12}$$

where $i_{0,I}, i_{0,A}, i_{0,Cu}$ are exchange current densities and $\alpha_I, \alpha_A, \alpha$ are transfer coefficients corresponding to the three areas mentioned above. Equations (4.9–4.12) constitute the coupled equations for the transport–deposition process of PEG-SPS system.

The area reduction in the late stage, especially at the via bottom, is incorporated in the model in the form

$$\theta_A^{new}(t) = \left(\frac{A_{init}}{A(t)}\right)\theta_A^{TA}(t), \tag{4.13}$$

where $\theta_A^{TA}(t)$ is the time and area dependent surface coverage of SPS, and A_{init} and $A(t)$ are the initial area and the area at time t, respectively. The above equations are solved numerically using the moving boundary method.

Figures 4.2 and 4.3 show the time variations of surface coverage θ_I and θ_A at the via bottom ($z = L_V$) and via top ($z = 0$) produced by the simulation of the filling process (L_V/R_V = 5). Two distinct time regions are clearly observed.

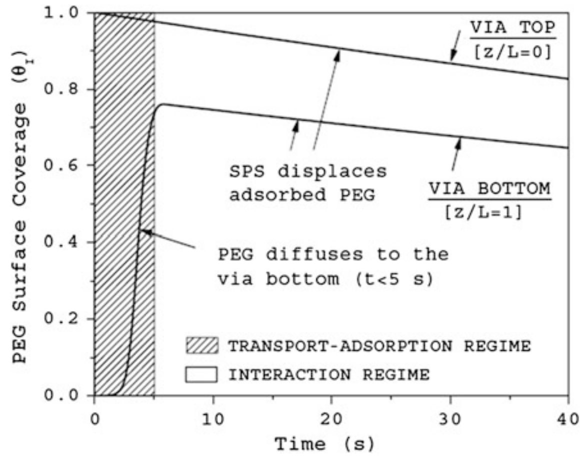

Fig. 4.2 The time-dependent PEG surface coverage at the via top and at the via bottom. The cross-hatched region ($t < 5$ [s]) is the transport-adsorption regime and unmarked ($t > 5$ [s]) is the interaction regime. The *upper line* shows the via *top* and the *lower line* via *bottom*. The kinetics parameters are listed in Table 4.1 in Ref. [16]. (Reproduced from Fig. 4.5 of Ref. [16] by the permission of The Electrochemical Society)

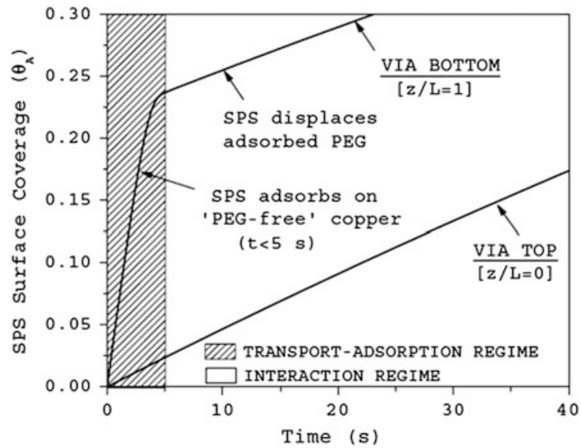

Fig. 4.3 The time-dependent SPS surface coverage at the via top and at the via bottom. The cross-hatched region ($t < 5$ [s]) is the transport-adsorption regime and unmarked ($t > 5$ [s]) is the interaction regime. The *upper line* shows the via *bottom* and the *lower line* via *top*. The kinetics parameters are listed in Table 4.1 in Ref. [16]. (Reproduced from Fig. 4.6 of Ref. [16] by the permission of The Electrochemical Society)

At $t = 0 \sim 5$ [s] the transport of additives is important, i.e., PEG adsorbs around the via top rapidly, while the via bottom is not covered with PEG due to the slow diffusion. The via bottom is covered with SPS which is expected to initiate the initial bottom-up fill. At $t \gtrsim 5$ [s], the interaction between additives becomes dominant and SPS displaces the PEG on the sidewall. The growth of the via bottom is even more accelerated by the effect of area reduction Eq. (4.13), which results in the bottom-up filling as shown in Fig. 4.4. The details of the simulation are described in Ref. [16].

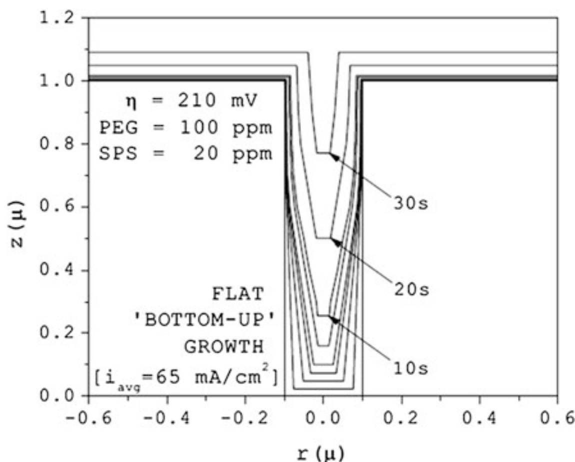

Fig. 4.4 Deposit growth simulation during bottom-up fill in a via with $R = 0.1[\mu\text{m}]$ and $L = 1[\mu\text{m}]$ at an overpotential of 120 [mV] in the presence of 20 [ppm] SPS and 100 [ppm] PEG. The kinetics parameters are listed in Table 4.1 in Ref. [16]. (Reproduced from Fig. 4.8 of Ref. [16] by the permission of The Electrochemical Society)

4.2.2 Continuum Models for Nucleation and Growth

Continuum models have been applied not only to macroscopic shape evolution but also to microscopic nucleation process. In dual damascene technology, direct electrodeposition of copper on barrier layers other than copper (e.g., ruthenium or titanium) has attracted attention to circumvent the limitations of plating copper seed layer on submicron vias and trenches. The key issue is to control the nucleation density in the early stage of electrodeposition to plate a continuous copper film which will lead to void-free filling. There has been a lot of work on nucleation and growth in copper electrodeposition on foreign substrates. Following is an overview of two models for nucleation and growth in different regimes.

4.2.2.1 Diffusion-Limited Growth

A simulation model for nucleation and growth under diffusion control has been developed by West et al. [17–19]. They considered the growth of hemispherical nuclei on a foreign substrate. The main focus is on mass transport in solution. The time dependence of the number of nuclei on the surface, $N(t)$, is

$$\frac{dN}{dt} = k_n \left(\frac{C}{C^\infty}\right)^n (N_0 - N) \qquad (4.14)$$

where k_n is the nucleation rate constant, C and C^∞ are the concentration of metal ions and that of the bulk, respectively. For instantaneous nucleation $N(t)$ is equal to the number of nucleation sites N_0. Once the number of nuclei is determined, nuclei are added to the surface stochastically by the MC method.

Nucleation is followed by the growth of nuclei. The concentration is governed by the diffusion equation

$$\frac{\partial C}{\partial t} = D\nabla^2 C \tag{4.15}$$

with the initial and boundary conditions

$$C = C^{\infty} \text{ at } t = 0 \tag{4.16}$$

$$C = C^{\infty} \text{ far from the electrode} \tag{4.17}$$

On the electrode surface, copper deposition occurs on the surface of the copper nuclei, but not on the foreign substrate. The flux normal to the surface is:

$$f = -D\frac{dC}{dn} = 0 \text{ at non-nucleated site} \tag{4.18}$$

$$f = -D\frac{dC}{dn} = k_G C, r = r_m(t) \text{ at a nucleus} \tag{4.19}$$

where k_{G} is the deposition rate constant. The growth is diffusion-limited when $C \to 0$ and $k_{\mathrm{G}} \to \infty$. $r_{\mathrm{m}}(t)$ is the radius of the nucleated hemispherical particle evaluated from the mass balance equation

$$\frac{dr_{\mathrm{m}}}{dt} = V_{\mathrm{M}} f \tag{4.20}$$

V_{M} is the molar volume of deposited species. These equations are coupled with the current density

$$i(t) = nFN(t)\left[f(t)2\pi r^2(t)\right]_{\mathrm{avg}} \tag{4.21}$$

$[\,]_{\mathrm{avg}}$ is the average over the existing nuclei. West et al. studied diffusion-limited growth ($k_{\mathrm{G}} = 0$) [17], deviation from the diffusion control due to $k_{\mathrm{G}} > 0$ [18] and the dependence of $N(t)$ on the concentration C [19]. Emekli and West [20–22] extended the theory to include additives and studied the influence of suppressors on nucleation using the same model.

4.2.2.2 Kinetically Limited Growth

Under the condition where the concentration of copper ions near the electrode can be assumed to be constant ($C = C^{\infty}$), nucleation and growth become kinetically limited. In this regime, the basic processes are the reduction of copper ions, surface diffusion of adatoms, and crystallization (nucleation and incorporation of adatoms into nuclei). The crucial point in the modeling is the accurate treatment of surface diffusion, which is much faster than the other surface processes. Stephens and

Alkire applied the “island dynamics” method to study the nucleation of copper with additives onto foreign substrates [23, 24].

The key variable in the theory is the adatom density $c_{\mathrm{ad}}(x, y)$ on the electrode surface ((x, y)-plane). The nucleation rate is given by the average adatom density

$$\frac{dN}{dt} = D_{\mathrm{s}}\sigma\langle c_{\mathrm{ad}}(x, y)\rangle, \tag{4.22}$$

where D_{s} is the surface diffusion constant of adatoms and σ is the reaction rate constant. The growth of the nuclei occurs when adatoms are incorporated into the island edge after surface diffusion. The edge velocity of a nucleus is evaluated by:

$$v(x, y) = D_{\mathrm{s}}(x, y)A_{\mathrm{m}}[\mathbf{n}\cdot\nabla c_{\mathrm{ad}}(x, y)|_{\mathrm{inside}} - \mathbf{n}\cdot\nabla c_{\mathrm{ad}}(x, y)|_{\mathrm{outside}}] \tag{4.23}$$

In Eq. (4.23), “inside” refers to the attachment of an adatom to the edge boundary from the top of the island (i.e., incorporation of an adatom deposited on the island) and “outside” refers to the attachment of an adatom from the lateral plane outside the island. The velocity $v(x, y)$ is used to track the moving boundary of the island by the LSM ((A.1) in Appendix A). When additives are deposited on the surface, they block the surface diffusion and the available area for adatom diffusion is less than the total area of the electrode surface. This is taken into account by defining the effective surface diffusion constant which is proportional to the fraction of available sites $\theta_{\mathrm{available\ site}}$ as

$$D_{\mathrm{effective}}(x, y) = \theta_{\mathrm{availablesite}}D_{\mathrm{s}}(x, y) \tag{4.24}$$

Using this approximation, the concentration field of adatoms $c_{\mathrm{ad}}(x, y)$ is simulated by the extended diffusion equation

$$\frac{\partial c_{\mathrm{ad}}(x, y)}{\partial t} - D_{\mathrm{effective}}(x, y)\nabla^2 c_{\mathrm{ad}}(x, y) = F \tag{4.25}$$

where F is the flux of adatoms onto the surface. Stephens et al. [23, 24] studied the influence of multiple additives (PEG, SPS) on the nucleation and growth process of copper on Cu and Au using the reaction models, which are the same as those used in the KMC simulations [38–40].

4.2.3 Fluid Mechanical Approach

In damascene electroplating and the nucleation problem presented in the previous sections, the effect of convection is not included in the modeling. The main driving force for mass transport is diffusion. When the feature size becomes $10 \sim 100 \mu$m or larger, on the other hand, the fluid mechanical flow and vortex formation will play an important role in the electrodeposition process. The flow patterns around the electrode with cavities have been widely studied by numerical simulations. The role of mass transport in etching of rectangular cavities has been studied by many

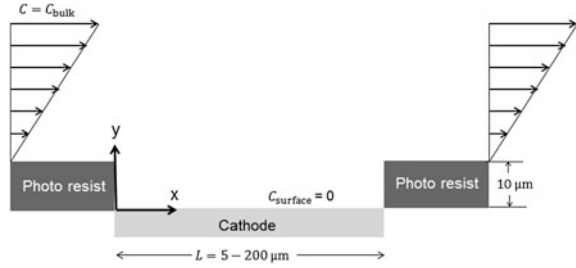

Fig. 4.5 Illustration of two-dimensional cross section of photoresist and cathode. (Width : L, height : h)

authors using the numerical fluid dynamics computations. Alkire et al. developed two-dimensional numerical fluid dynamics computation to study the etching of copper [25–27]. Shin and Economou studied electrolytic etching at a moving boundary for forced and natural convection [28].

The influence of fluid mechanical flow on the shape evolution of electrodeposited copper bumps has been studied by Kondo et al. using numerical fluid dynamics computation [29–32]. Electrodeposited bumps are important micro-connectors for high density interconnection between microprocessors, random access memories, the connection between liquid crystal display and driver chips, and so on. The bumps are electrodeposited on a dot-shaped cathode $10 \sim 200 \mu m$ in diameter. Kondo et al. showed that the influence of macroscopic flow and vortex formation is important for the control of electrodeposited bump shape and uniformity in height [29, 30].

The key parameter in the theory is the Peclet number P_e which represents the ratio of the flow speed to that of diffusion. Figure 4.5 illustrates the model system of two-dimensional cross section of photoresist and cathode with the boundary conditions. The Peclet number for this system is

$$P_e = \frac{hu_{y=2h}}{D}, \tag{4.26}$$

where h is the height of the resist, u is the flow velocity and D is the diffusion constant. The basic equations are the equation of continuity, Navier–Stokes equations and mass transfer equation

$$\frac{\partial u}{\partial x} + \frac{\partial u}{\partial y} = 0 \tag{4.27}$$

$$\rho\left(u\frac{\partial u}{\partial x} + v\frac{\partial u}{\partial y}\right) = -\frac{\partial P}{\partial x} + \mu\left(\frac{\partial^2 u}{\partial x^2} + \frac{\partial^2 u}{\partial y^2}\right) \tag{4.28}$$

$$\rho\left(u\frac{\partial v}{\partial x} + v\frac{\partial v}{\partial y}\right) = -\frac{\partial P}{\partial x} + \mu\left(\frac{\partial^2 v}{\partial x^2} + \frac{\partial^2 v}{\partial y^2}\right) \tag{4.29}$$

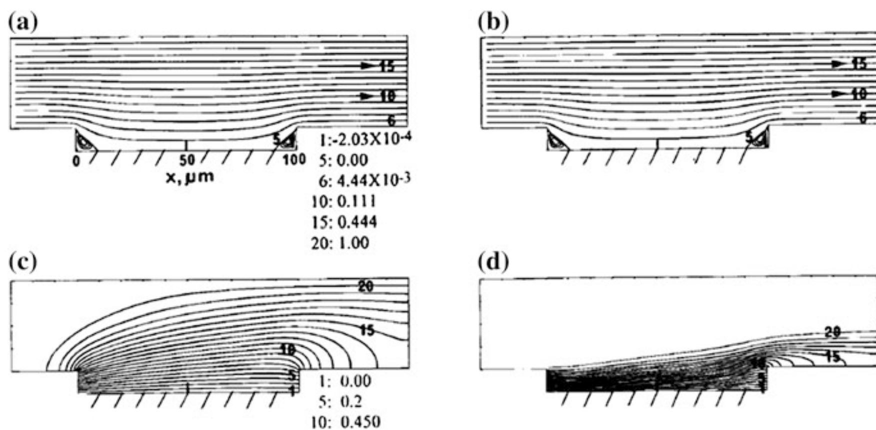

Fig. 4.6 Effects of Peclet numbers on streamlines and isoconcentration contours. The cavity width is100[μm]. Streamlines for $P_e = 1.31$ (**a**) and 41.6 (**c**). Isoconcentration contours for $P_e =$ 1.31 (**b**) and 41.6 (**d**). (Reproduced from Fig. 4.4 of Ref. [29] by the permission of The Electrochemical Society)

$$u\frac{\partial C}{\partial x} + v\frac{\partial C}{\partial y} = D\left(\frac{\partial^2 C}{\partial x^2} + \frac{\partial^2 C}{\partial y^2}\right) \tag{4.30}$$

where ρ, P, μ and C are the density, static pressure, viscosity, and the concentration, respectively.

Figure 4.6 shows examples of the normalized stream functions and isoconcentration contours for $P_e = 1.31$(a,c) and 41.6 (b,d). The solution flow is from left to right and the streamline labeled 6 is the penetration flow. Vortices are observed at the corners both at up and downstream sides. In the isoconcentration contours the difference in the thickness of the concentration boundary layers is observed for $P_e = 1.31$ and 41.6. The local copper deposition rate on the cathode depends on the dimensionless Sherwood number,

$$Sh = \frac{L}{\Delta C}\left(\frac{\mathrm{d}C}{\mathrm{d}y}\right)_{y=0} \tag{4.31}$$

which shows the ionic transport due to the concentration gradient.(Fig. 4.7) Sh shows the maximum at $x = 0\mu$m for $P_e = 1.3$, gradually decreases toward the downstream side and slightly increases at $x \gtrsim 90\mu$m. The maximum height at around $x = 0\mu$m is due to the vortex which captures copper ions and enhances the local mass transport to the cathode. The vortex at the downstream side also enhances the local mass transport of copper to the cathode, which leads to a slight increase in Sh. For $P_e = 41.6$, on the other hand, mass transport is mainly controlled by convection due to the penetrating flow and vortex rather than diffusion. The vortex on the upstream side does not provide ions to the cathode and local

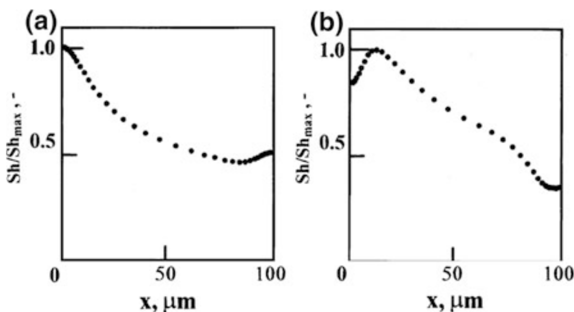

Fig. 4.7 Effects on Peclet numbers on flux (normalized Sherwood number). $P_e =$ 1.31 (**a**) and 41.6 (**b**). (Reproduced from Fig. 4.5 of Ref. [29] by the permission of The Electrochemical Society)

resistance arises. This leads to a slight shift of the maximum flux to $x \cong 10\mu$m. These flux profiles coincide with the bump shape observed in experiments as shown in Ref. [29]. Kondo et al. also studied the flow patterns for higher Peclet numbers [31] and the current distribution on copper bumps with photoresist sidewall angle by numerical simulation and experiments [32]. These works show that the interplay between the convection and diffusion is the key factor for control of bump formation.

4.3 Kinetic Monte Carlo Simulation and Multiscale Modeling

In the previous section, the recent theories based on continuum models have been presented. This and the following sections are devoted to molecular simulations of copper electrodeposition, in which ions and additive molecules are treated as particles. The KMC simulation is a stochastic method to simulate the time evolution of many-particle systems using rate constants and random numbers [33]. Since the KMC method is based on statistical mechanics and the mathematical theory of stochastic process, it has a wide range of application. In electrochemistry, the KMC method has been used as a feasible tool for simulations taking into account the microscopic process of nucleation and growth.

One of the characteristics of electrodeposition which makes the molecular simulation approach difficult is the multiscale aspect in time and space. For example, the microscopic surface reactions (of the order of nanometer and nanosecond) are dependent upon the concentrations of ions which are controlled by the macroscopic mass transport in the diffusion layer (micrometer and millisecond or larger scales). Since the KMC method is essentially an atomic-scale method, it has been extended to combination with some tools which deal with large-scale and long-time quantities in the application to electrochemical systems. Therefore, a hybridized method of KMC and continuum models have been developed for the unified simulation from micro to macro scales. In this section, we first describe the basic concept and modeling of the KMC simulation for crystal

growth, and then the recent sophistications of the multiscale KMC-continuum simulation for copper electrodeposition are reviewed referring to the works of Alkire et al. [34–40].

4.3.1 Solid-on-Solid Model

Solid-on-Solid (SOS) model is a basic model for crystal growth, which is widely used in theoretical and numerical studies [41, 42]. The system is a square (2D) or a cubic (3D) lattice as shown in Fig. 4.8. Each lattice site represents a solid atom, a liquid atom, or a vacancy. (In a coarse-grained system a site represents a group of atoms.) We first consider the additive-free case and assume three events such as adsorption, desorption, and surface diffusion to change the state of the sites. The rate constants are defined for these three events such as adsorption rate k_n^+, desorption rate k_n and surface diffusion rate k_{nm}. The suffix n represents the characteristics of the site on which the event occurs. (e.g., the number of nearest neighbor atoms) In k_{nm}, n and m represent the information before and after the movement, respectively. These rates are the functions of the binding energy, activation energy for surface diffusion, ionic concentration, and so on. The definitions of these rate constants characterize the model.

In the SOS model, adsorption occurs only “on” the surface sites, i.e., at the nearest neighbor vacant sites in the y-direction (Fig. 4.8). As a result, vacancy formation is inhibited in the SOS model. Also, overhang and shadowing are not allowed to occur during the growth. Therefore, the SOS model is appropriate for describing layer-by-layer growth, but is not suitable for rough surface and dendrites.

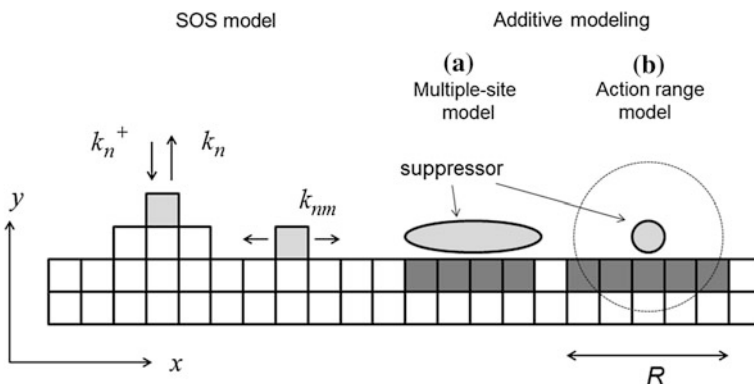

Fig. 4.8 *Left* Schematic picture of the SOS model. *Squares* denote solid atoms and *gray squares* are adatoms. *Right* Two types of additive modeling. **a** Multiple-site model and **b** Action range model. (R: action range)

Additives are incorporated in the SOS model as follows. Additives occupy lattice sites in the same way as metal atoms, and the adsorption and desorption rates of additives are given as input parameters. The adsorbed additives have suppressing or accelerating effects on metal deposition at the surrounding sites. In the case of polymer suppressors (such as PEG in copper electrodeposition), the molecular volume is much larger than that of metal atoms. There are two methods to take into account the size difference. One way is to assume that an additive occupies more than one lattice site and deposition of metal atoms on the sites covered by the additive is inhibited (multisite model) as illustrated in Fig. 4.8a [38]. An alternative method is shown in Fig. 4.8b. The additive occupies one lattice site and an action range R is defined around it. Metal deposition on the sites within the action range is inhibited. The range R is chosen to reflect the effective size of the polymer (e.g., Flory radius of a polymer chain). The latter model can be applied to the accelerators, i.e., the deposition rate of copper within the action range is assumed to be larger than that on the sites outside the action range.

In the KMC simulation, the state of each site is changed sequentially by using random numbers. There are two types of algorithm for KMC simulations. The simple algorithm is the rejection method. The procedure is to choose a site and an event randomly and decide if the event is realized or not by using random numbers. Although the coding of the rejection method is simple, it is not efficient in a situation where a lot of rejections are selected. The second type of algorithm is a rejection-free algorithm which was proposed for the simulation of Ising spin systems by Boltz et al. (BKL method) [43]. The general form for this type of algorithm is given by Gillespie [44]. The procedure is to tabulate the candidate atoms (or sites) and the reaction rates, decide the events using the rates and the random numbers, and renew the table after the event.[2] This method is efficient because rejection does not occur in the sequence. The point for the efficiency of the rejection method is how to reduce the number of rejections. The efficiency of the rejection-free method depends on the algorithm used to search and revise the tables. A comparison of the efficiencies of these methods is given in Ref. [33].

4.3.2 KMC-Continuum Combination

The rate constants k_n^+, k_n and k_{nm} depend not only on the physical quantities which can be assumed to be constant (such as the binding energy) but also on the quantities which change during the deposition (such as the ionic concentration in solution). Therefore, in most applications, the SOS model is combined with the continuum models which represent the time dependence of the quantities in the solution. The program consists of the KMC code and the continuum code [34]. The continuum code calculates the quantities in solution (concentration, potential, etc.)

[2] The BKL algorithm for crystal growth is given in Appendix B.

by solving the partial differential equations. It gives the information necessary for determining the rate constants for the KMC code. The KMC code simulates the crystal growth using the rate constants and gives the renewed surface information (the change in the concentration and the surface structure) back to the continuum code. The continuum code simulates the solution quantities using the renewed information as the boundary conditions. Since the surface moves into the solution as a result of crystal growth, the numerical treatment of moving boundaries is required.

The combination of the KMC method and continuum models is a general framework of the microscopic simulation of electrodeposition. Pricer et al. combined the (2 + 1)D SOS model with 1D diffusion equation for copper ions to simulate the surface morphology in copper electrodeposition [35]. Here (2 + 1)D means the two-dimensional substrate surface (2) and one layer of deposited atoms (+1). Drews et al. studied the effect of additives (PEG, Cl^-, MPSA) on the surface morphology [36]. Drews et al. extended the SOS model to represent the fcc (111) surface and studied the nucleation process by using the KMC simulation [37].

4.3.3 Multiscale KMC-Continuum Hybrid Simulation for Trench Filling

An extensive multiscale KMC-continuum simulation of trench filling by copper electrodeposition has been developed by Alkire et al. [38–40]. In their model, four kinds of additives (PEG, SPS, Cl^-, 1-2-hydroxyethyl-2-imidazolidinethione (HIT)), 14 surface reactions, and three homogeneous reactions in solution are taken into account. The system consists of three parts; (1) mass transport and reactions in solution, (2) surface shape evolution, and (3) crystal growth on the surface. Mass transport in solution is represented by the mass balance equation

$$\frac{\partial C_i}{\partial t} = D_i \nabla^2 C_i + z_i F u_i \nabla \cdot (C_i \nabla \Phi) + A_i, \tag{4.32}$$

where D_i, C_i, z_i and u_i are the diffusion constant, the concentration, the valence, and the mobility of species i, respectively. Φ is the potential and A_i is the production rate of species i due to the homogeneous reaction in solution. Equation (4.32) represents the overall material conservation in solution. The flux of species i is given by

$$\mathbf{N}_i = D_i \nabla C_i + z_i F u_i C_i \nabla \Phi. \tag{4.33}$$

The boundary conditions on the top bulk boundary are the bulk values

$$C_i = C_i^{\infty}, \Phi = \Phi^{\infty}. \tag{4.34}$$

The boundary conditions on the nonactive boundary and the active boundary (electrode surface) are:

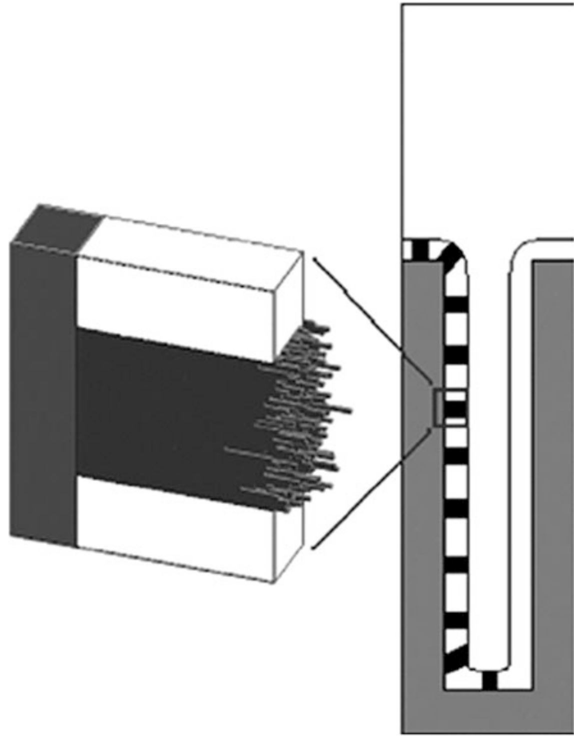

Fig. 4.9 The relation between the KMC code and the continuum code. *Right* Ten individual KMC domains along the wall of a trench. *Left* The enlarged image is one of the KMC domains. (Reproduced from Fig. 4.3 of Ref. [38] by the permission of The Electrochemical Society)

$$\mathbf{N}_i \cdot \mathbf{n} = 0, \tag{4.35}$$

$$\mathbf{N}_i \cdot \mathbf{n} = J_i, \tag{4.36}$$

respectively, where J_i is the flux of species i computed by the KMC code. These equations are solved by the finite volume (FV) method using the data from the KMC code as the boundary conditions.

The shape evolution of the growing trench surface as a result of the deposition reactions is tracked by LSM (Appendix A). The FV code and the LSM code are coupled to form the moving boundary which is also coupled with the KMC code. The relation between the KMC code and the moving boundary is illustrated in Fig. 4.9. There are 10 KMC simulation domains along the surface. In these domains, the crystal growth is simulated by the KMC code of the SOS model. The result of the KMC simulation in each domain is passed to the computation of the moving boundary. The results of the LSM code and the FV code are reflected in turn in the KMC code.

The reactions included in the model are summarized in Table 4.1. The copper ions are reduced in two steps, $Cu^{2+} + e^- \rightarrow Cu^+$, $Cu^+ + e^- \rightarrow Cu$. Four kinds of additives are included; PEG, SPS, Cl^-, and HIT. Chloride ions are combined with Cu^+ to produce CuCl on the surface (reaction 5). PEG is adsorbed on the surface as

Table 4.1 Species and chemical reactions in copper electrodeposition used in the simulations [38–40, 49, 50]

Reaction no.	Species and reactions
	Surface reactions
1	$Cu^{2+} + e^- \rightarrow Cu^+$
2	$Cu^+ + e^- \rightarrow Cu$
3	$Cu \rightarrow Cu^+ + e^-$
4	$Cu \rightarrow Cu(\text{surface diffusion})$
5	$Cu^+ + Cl^- \rightarrow CuCl$
6	$CuCl \rightarrow Cu^+ + Cl^-$
7	$CuCl + e^- \rightarrow Cu + Cl^-$
8	$CuCl + PEG \rightarrow CuClPEG$
9	$CuClPEG \rightarrow CuCl + PEG$
10	$SPS + 2e^- + 2H^+ \rightarrow 2MPS$
11	$Cu^+ + MPS \rightarrow Cu(I)thiolate + H^+$
12	$Cu(I)thiolate + H^+ \rightarrow Cu^+ + MPS$
13	$Cu^+ + Cu(I)thiolate + e^- \rightarrow Cu(I)thiolate + Cu$
14	$Cu(I)thiolate + HIT \rightarrow Cu(I)HIT + MPS$
15	$Cu(I)HIT + H^+ + Cu(I) \rightarrow HIT + Cu_2$
	Homogeneous reactions in solution
16	$MPS \leftrightarrow H^+ + thiolate^-$
17	$H_2SO_4 \leftrightarrow HSO_4^- + H^+$
18	$HSO_4^- \leftrightarrow SO_4^{2-} + H^+$

CuClPEG (reaction 8). The suppressing effect of CuClPEG is expressed by the multiple-site model (Fig. 4.8a). SPS produces two MPS molecules which create Cu(I)thiolate (reactions 10, 11, and 16). Cu(I)thiolate has a catalytic effect on the reduction of Cu^+ to Cu (reaction 13). The leveler HIT deactivates the Cu(I)thiolate (reaction 14) and lowers the copper deposition rate.

In the KMC code, one lattice site is assumed to represent a mesoparticle which contains a group of particles. This is to track a larger scale shape evolution. The area change is calculated from the local curvature by the LSM code and sent to the KMC codes at the different trench surface location. The KMC code calculates the changes of the surface coverage of Cu(I)thiolate at different locations. The concentrations of the Cu(I)thiolate are corrected by inserting additional Cu(I)thiolate so that the total mass of the chemical species is conserved.

Figure 4.10 shows the results of the simulation corresponding to the experimental condition; 0.3 M $CuSO_4$, 125 g/L H_2SO_4, 0.3 g/L PEG, 50 ppm Cl^- and 10 ppm SPS. The trench is 0.2 μm wide and is 1 μm high. The rate constants for the reactions in Table 4.1 are given in Refs. [38, 39]. Figure 4.10a shows the shape evolution pattern, b shows the time and space dependences of the surface coverage of Cu, CuCl, CuClPEG, and Cu(I)thiolate. In each figure, the position "0" corresponds to the trench opening and "0.5" is the center of the trench. Figure 4.10c shows the time and space dependencies of the reaction rates of reactions 2, 7, and 13 evaluated in the simulation. Figure 4.10a clearly shows the characteristics of superfilling; (i) initial incubation period, (ii) bottom-up, and (iii) overfill after the

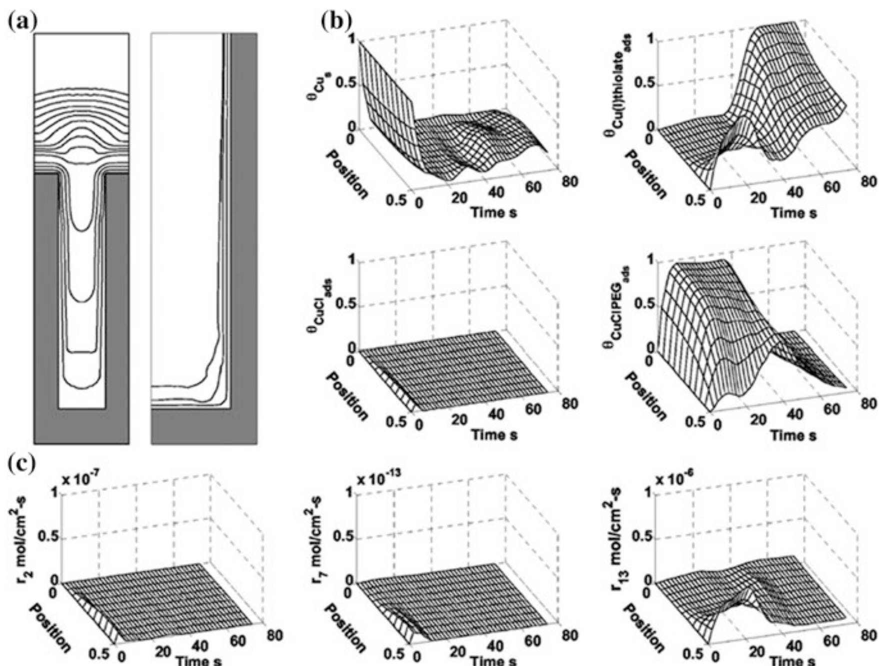

Fig. 4.10 Simulation of trench filling. **a** Two trench cross-sections showing the shape evolution. *Left* every 5 s for 0–70 s and *right* every 1 s for 0–3 s. **b** The surface coverage versus time and position for four surface species during the trench infill. **c** The time-dependent reaction rate distribution for the three reactions associated with copper electrodeposition (reactions 2, 7, and 13). The positions 0 and 0.5 correspond to the trench opening and the center of the trench, respectively. (Reproduced from Fig. 4.1 of Ref. [40] by the permission of The Electrochemical Society)

filling. Figures 4.10b, c shows that CuClPEG is distributed in the upper half of the trench and Cu(I)thiolate in the lower half of the trench. From the spatial distribution of r_{13} (the rate of reaction 13), the bottom-up fill is mainly due to the accelerating effect of Cu(I)thiolate. These results show that the combination of the KMC code, LSM code, and the FV code can perform the overall simulation of trench filling taking into account the slow mass transport represented by the mass balance equation (4.9) and the microscopic reactions listed in Table 4.1.

4.4 Solid-by-Solid Model and 3D Shape Evolution

The SOS model represents an ideal situation in which a new atom is deposited on a surface solid atom only in the vertical direction, and no vacancy is formed in the deposited films. In real deposition, lattice defects such as vacancies and

dislocations, which are created during electrodeposition, play an important role in determining the physical properties of the film. The SOS approach has been extended to a model, which includes void formation by Kaneko et al. [45, 46]. The new model is called the Solid-by-Solid (SBS) model. This section is concerned with the basic properties of the SBS model and its application to the 3D shape evolution of via and trench fillings.

4.4.1 Solid-by-Solid Model

We consider a 2D square lattice each site of which is occupied by either a liquid atom or a solid atom, otherwise vacant. The schematic picture of the model is shown in Fig. 4.11. Growth is in the y-direction and a periodic boundary condition is used in the x-direction. Surface solid atoms are denoted by bright gray squares which are distinguished from the solid atoms embedded in the film (dark gray squares). Empty sites surrounded by solid atoms with no contact with the liquid are defined as vacancies. Three events are assumed to occur to change the state of each site: adsorption, desorption, and surface diffusion. As for adsorption, the SOS criterion is removed, that is, a new atom is deposited on any nearest neighbor sites of the surface solid atom (as indicated by the arrows in Fig. 4.11). In order to allow this deposition, the surface solid atoms must be defined even when the surface has a rough structure. An accurate algorithm to search the surface solid atoms is a key factor for extension of the SOS model to the SBS model. The searching algorithm is given in Appendix C.

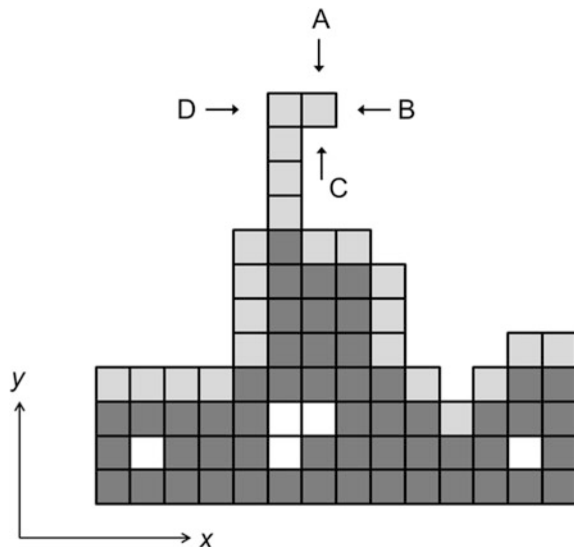

Fig. 4.11 Illustration of the SBS model. *Dark gray squares* are solid atoms and *bright gray squares* are surface solid atoms. *White squares* are vacancies. The adsorption of new atoms occurs from any directions indicated by *arrows* A, B, C, D

The rate constants for adsorption k_n^+, desorption k_n and surface diffusion k_{nm} are assumed to have the following relations; [41, 42]

$$\frac{k_n}{k_n^+} = \exp\left[(n_k - n)\frac{\varphi}{k_B T} - \frac{\mu}{k_B T}\right], \tag{4.37}$$

$$k_{nm} = \frac{k_n k_m^+}{k_1^+} \exp\left[\frac{\varphi - E_d}{k_B T}\right], \tag{4.38}$$

where φ is the binding energy between solid atoms, μ is the electrochemical potential and E_d is the activation energy for the surface diffusion. n_k is the number of bonds at a kink site. ($n_k = 2$ for 2D lattice and 3 for 3D lattice) k_B is Boltzmann constant and T is the temperature. The relation (4.37) is derived from the microscopic detailed balance at a kink site [42]. This model is called the SBS basic model hereafter.

The advantage of the SBS model is that one can perform the simulation of crystal growth on complex nonflat surfaces which accompanies void formation. The shape evolution can be simulated without using any additional algorithm to track the moving boundary. Therefore, it is suitable for the simulation of filling small features such as damascene electroplating. The effects of suppressors, accelerators, and levelers have been studied by the KMC simulations of 2D SBS model and the condition for void-free filling has been discussed. [47, 48]

It is straightforward to extend the SBS model to a 3D system. Figure 4.12 shows the simulation of dual damascene using the 3D SBS basic model without additives. The initial surface has a trench with a cylindrical via hole at the bottom. The aspect ratio of the trench and the via is unity. Periodic boundary conditions are used in the lateral directions. It is observed that the via hole is first filled with deposited atoms forming voids in the hole. Then the trench is filled forming seams which are elongated in the growth direction in the middle of the trench. Since ionic transport is not included in the SBS basic model, the filling is almost conformal. The surface is clearly defined at every KMC step by the searching algorithm given in Appendix C.

4.4.2 Multiscale SBS Model for 3D Shape Evolution

The 3D SBS model has been extended to include the solution with diffusion layer for the simulation of 3D device fabrications [49, 50]. Figure 4.13 illustrates the extended system which consists of three parts. The lowest part is the electrode with a small feature on the surface. The adsorption, desorption, surface diffusion, and the shape evolution are simulated by the KMC method of the SBS model. The additive reactions occur on the surface.

The solution is located above the electrode, which is also simulated by the KMC method. The solution is divided into a Cartesian grid which is the same as

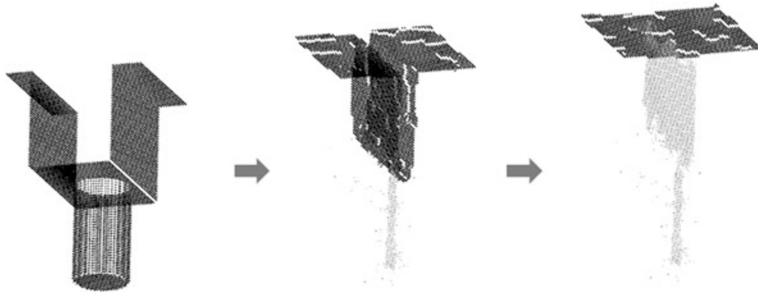

Fig. 4.12 KMC simulation of dual damascene (trench and via) using the 3D SBS basic model. *Gray dots* denote vacancies. The via is filled forming voids in the middle and then the trench is filled forming seams

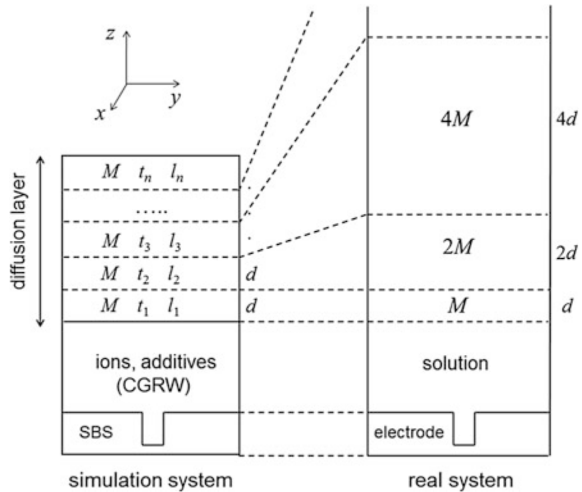

Fig. 4.13 The illustration of the multiscale modeling for electrode-solution interface. The simulation system and the corresponding real system are plotted. The system consists of the electrode, solution, and diffusion layer from the *bottom*. Multiscale method is used to simulate the diffusion layer

the cubic lattice of the SBS model for the electrode. The particles representing copper ions or additives are distributed on the grid points. The diffusion of ions and additives in solution is simulated by the coarse-grained random walk (CGRW). Ions and additives jump to one of the neighboring grid points with equal probability (1/6 for cubic lattice). Since the elementary process of ionic migration (jump diffusion) is the fastest process in the system, coarse-graining is applied, i.e., the jump distance per one KMC step is larger than the unit space of the grid.

The upper part of the solution is the diffusion layer which contains ions and additives. The migration of these particles is simulated by CGRW. Figure 4.13 shows the relation between the simulation system and the corresponding real system. The simulation system is divided into layers with the thickness d and each layer has different units of time t_j and length l_j, where j denotes the layer number. These units are scaled so that each layer corresponds to the real system which has a

larger volume with the same concentration. For example, layer 2 represents a portion of the solution with thickness 2*d* (i.e., the volume is twice as large as that of layer 1). The units t_j and l_j are scaled so that each layer has the same diffusion constant for each species. It is also assumed that each layer in the simulation system has M particles and a particle in the upper layer $j+1$ represents two particles in the lower layer j. The rate constants of the random walk of these particles at the boundary are scaled so that the microscopic detailed balance is satisfied between the layers. The whole system is simulated by the combined algorithm of the BKL method and CGRW.

The reactions in Table 4.1 have been incorporated in the 3D SBS model for copper electrodeposition. The solution contains three kinds of ion (Cu^{2+}, Cu^{+}, Cl^{-}), PEG and SPS. The reduction of Cu^{2+} occurs in two steps (reactions 1 and 2). The additive reactions 5–13 are assumed to occur on the electrode surface. Levelers are not included. The initial concentrations of ions and additives are Cu^{2+}; 2 M, Cl^{-}; 1.5×10^{-3} M, PEG; 8.8^{-5} M and SPS; 2.0^{-5} M. Surface sites are either of Cu (adatom), Cu (crystal), CuCl, CuClPEG, or Cu(I)thiolate. The inhibiting effect of PEG is simulated by the action range model in Fig. 4.8b. The catalytic effect of Cu(I)thiolate is reaction 13, which enhances copper deposition. The rate constants are taken from Refs. [38, 39]. In the simulation, the superparticle assumption is used, i.e., one lattice site represents a group of 10,648 atoms, and the rate constants are rescaled for superparticles. In this system, since the number of particles is conserved including incorporation and desorption, the effect of area change at the bottom of the trench is included. Therefore, no additional assumption is made to include the effect of area reduction.

Figure 4.14 shows the shape evolution during trench filling. The width of the trench is 132 [nm] and the aspect ratio is 2. The trench is filled from the bottom and a typical U-shape is observed during filling. As a result, only point defects appear in the film. Figure 4.15 shows the distribution of CuClPEG and Cu(I)thiolate within the trench averaged over the initial 30 % of the total filling time. $z = 0$ is the trench bottom and $z = 264$ [nm] is the initial trench top. It is clearly observed that CuClPEG is distributed at the upper half of the trench, preventing copper deposition around the opening of the trench. The accelerant Cu(I)thiolate is mainly distributed around the trench bottom. Such a heterogenous distribution of suppressors and accelerants initiates the U-shape of the surface, which leads to superfilling combined with area reduction at the bottom as observed in Fig. 4.14. These features agree with the results of the KMC-continuum simulation presented in Sect. 4.3.

4.5 Further Development of Efficient Algorithms

The numerical simulations of the continuum models and the KMC method are useful means to predict the optimal conditions in electrochemical engineering. However, accurate computation requires long computing time (more than days),

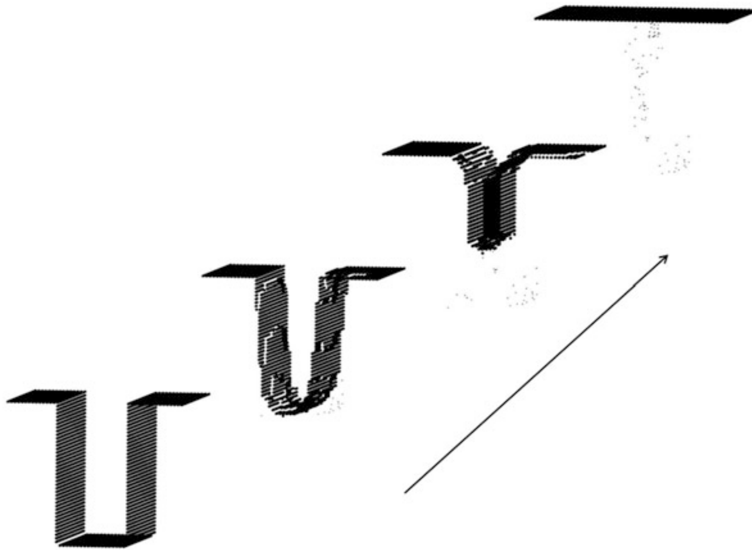

Fig. 4.14 Results of the simulation of trench filling with three additives (PEG, SPS, Cl^{-}). The trench is 132 [nm] wide and 264 [nm] deep. Only point defects appear in the film

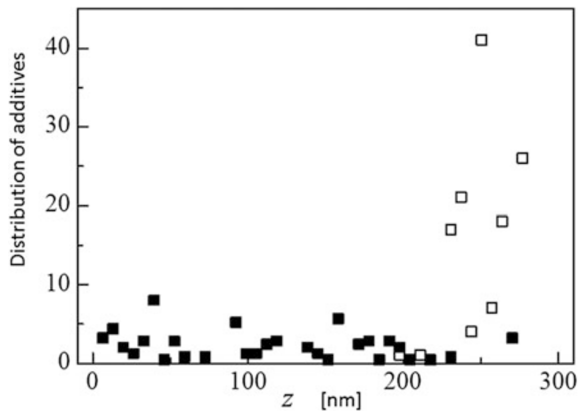

Fig. 4.15 Spatial distribution of additives averaged over the initial 30 % of the filling time (arbitrary unit). $z = 0$ is the trench bottom and $z = 264$ [nm] corresponds to the initial trench top. (*solid squares* : Cu(I)thiolate, *open squares* : CuClPEG)

especially for 3D systems, which will be the bottleneck for practical applications. Fast computing techniques have been developed for the simulations presented in the previous sections.

In the simulation of the continuum models, the large computing cost is in solving the mass balance equation (4.32) on irregular domains with moving boundaries. Buoni and Petzold [51] reported an efficient method to solve Eq. (4.32), which is an extension of the FV code. It uses FV spatial discretization including uniform small-cell region (around the feature and the electrode

boundary) and nonuniform large-cell region for the solution far from the electrode. The time integration is performed with a splitting technique. The right-hand side of Eq. (4.32) is split into three sets of terms; reaction terms, diffusion terms (plus boundary flux terms), and migration terms. The concentration field C_i is integrated in turn. It has been shown that the new algorithm is stable, scalable, and easy to parallelize. By using this method, Buoni and Petzold extended the combined system of the mass balance equation (4.32), LSM and the reaction-advection equation to a 3D system and performed the simulation of dual damascene with four kinds of additives [52].

In the KMC simulations of electrodeposition, a heavy computing cost arises when the rate of surface diffusion is much larger than the rates of other reactions. This is because numerous hops of adatoms must be computed before nucleation occurs in the ordinary KMC algorithm. The coarse-graining method (superparticles) allows us to perform the computation on large scales with the cost of losing the atomic-scale accuracy of the nucleation process. Several kinds of multiscale techniques have been developed to speed up the KMC code [33, 53].

A useful technique to overcome the problem of fast surface diffusion will be the first-passage kinetic Monte Carlo (FPKMC) method originally proposed as an efficient algorithm for the diffusion–reaction processes [54, 55]. Instead of simulating a lot of small hops, the FPKMC algorithm propagates the diffusing particles over a long distance sampled from the first-passage time distribution function which is a time-dependent Green's function of diffusion equation. The FPKMC method is an exact and efficient algorithm to skip the sampling of small hops to move the diffusing particles, which greatly reduces the computation time. Bezzola et al. applied the FPKMC method to the problem of nucleation and growth on the surface to study the presence of the exclusion zone in front of the growing step edge as a function of the surface diffusion/deposition rate ratio [56].

4.6 Summary

In this chapter, recent developments in the mathematical modeling and computer simulation of copper electrodeposition have been reviewed focusing attention on continuum models and KMC.

We first overviewed the numerical simulation of continuum models. As mathematical models for superfilling, we described the idea of the diffusion–consumption theory and the CEAC mechanism with the mathematical formulas. The CEAC is a model to realize superfilling and is regarded as a new type of leveling theory in view of accelerators. The numerical simulation of nucleation and growth and a fluid mechanical approach to copper electrodeposition are also overviewed. We then described the KMC method and the multiscale KMC-continuum simulation. The KMC-continuum hybrid method enables us to treat electrochemical phenomena ranging from microscopic surface reactions to large-scale mass transport in the diffusion layer. The recent development of the KMC method

is also presented from a "Solid-by-Solid" point of view. The extension from the SOS model to SBS model has led to a wide range of applications, especially, to the simulation of the 3D shape evolution for nanofabrication. Efficient algorithms for the fast computing of the above-mentioned simulations have also been overviewed.

Finally, let us comment on the molecular dynamics (MD) simulation which is not covered in this article. The MD method is a powerful tool to study the dynamical properties of condensed matter systems. The classical MD method, however, cannot be used for the electrochemical phenomena since the latter includes electron transfer reactions, which are essentially quantum mechanical processes. Recently a new method of molecular simulation of electrodeposition has been developed by combining the MD method with the KMC method [57, 58]. In the MD-KMC hybrid simulation, the whole dynamics of solution-electrode interface are simulated by the MD method and the reactions on the electrode are simulated by the KMC method. This method provides a direct dynamical simulation accompanying chemical reactions to study the correlation between the reaction rates and the surface morphology taking into account all the dynamics in solution and on the electrode.

The combination of efficient algorithms on different scales is the key factor in fast and accurate simulation. The simulations presented in this chapter and their hybridization will be promising tools for understanding the fundamental aspects of copper electrodeposition as well as their application to nanofabrication in electrochemical engineering.

A.1 Appendix A Level Set Method

LSM is a tracking method of moving boundaries, which is commonly used in recent numerical studies of electrodeposition. The level set function ϕ_L is a continuous function of space and time, defined in the whole area of liquid–solid interface. The surface is defined by $\phi_L = 0$, and the inner space (electrode) by $\phi_L < 0$ and the outer space (solution) by $\phi_L > 0$. The time derivative of ϕ_L is

$$\frac{\partial \phi_L}{\partial t} = \mathbf{v} \cdot \nabla \phi_L, \tag{A.1}$$

where $\mathbf{v}$ is the surface front velocity. The normal vector on the surface is:

$$\mathbf{n} = \frac{\nabla \phi_L}{|\nabla \phi_L|}, \tag{A.2}$$

and the normal velocity is defined as:

$$v = \mathbf{v} \cdot \mathbf{n}. \tag{A.3}$$

Using Eqs.(A.2) and (A.3), Eq.(A.1) becomes

$$\frac{\partial \phi_{\mathrm{L}}}{\partial t} = v|\nabla \phi_{\mathrm{L}}|. \tag{A.4}$$

The curvature of the surface in LSM is given by $\kappa = \nabla \cdot \mathbf{n}$. Equation (A.4) is the basic equation of LSM which should be solved numerically. Since v is defined not only at the interface but outside the interface, the extension velocity v_{ext} is defined by:

$$\nabla v_{\mathrm{ext}} \cdot \nabla \phi_{\mathrm{temp}} = 0, \tag{A.5}$$

where $v = v_{\mathrm{ext}}$ at $\phi_{\mathrm{L}} = 0$ and ϕ_{temp} is calculated by using the condition

$$|\nabla \phi_{\mathrm{L}}| = 1. \tag{A.6}$$

Using v_{ext} the LSM equation is written as:

$$\frac{\partial \phi_{\mathrm{L}}}{\partial t} = v_{\mathrm{ext}}|\nabla \phi_{\mathrm{L}}| \tag{A.7}$$

which is solved with the equations representing the electrodeposition reactions on the surface which give the boundary conditions. The equations are discretized and the quantities are evaluated on the grid points. The method of discretization and numerical procedures of LSM in combination with the FV code are found in the literature [9, 22].

A.2 **Appendix B** Rejection-Free Algorithm for KMC Simulation

Here we describe the application of the rejection-free algorithm to the 2D SOS and SBS models. Three events are assumed to occur on the surface. The rate constants for adsorption k_n^+, desorption k_n , and surface diffusion k_{nm} are dependent upon the number of nearest neighbor solid atoms n, m at the sites, where $1 \leq n, m \leq 4$. The rates of the creation (adsorption), annihilation (desorption), and surface diffusion are defined as

$$k_c = \sum_{n=1}^{3} k_n^+ N_{c(n)}, k_a = \sum_{n=1}^{3} k_n N_{a(n)}, k_d = \sum_{n,m=1}^{3} k_n N_{d(nm)}, \tag{B.1}$$

respectively, where $N_{c(n)}$, $N_{a(n)}$, $N_{d(nm)}$ are the numbers of candidate atoms (sites) for the events. The rate at which one of the three events occurs is given by

$$k_t = k_c + k_a + k_d. \tag{B.2}$$

The KMC algorithm for this model is as follows.

Search and tabulate the candidate surface atoms (sites) for the events.
Choose one of the events using a random number R on [0,1].

$$R < \frac{k_c}{k_t} \text{ : adsorption}$$

$$\frac{k_c}{k_t} \leq R < \frac{k_c + k_a}{k_t} \text{ : desorption}$$

$$\frac{k_c + k_a}{k_t} \leq R \text{ : surface diffusion}$$

Choose the type of events (the number of bonds) by generating another random number R'. In the case of adsorption,

$$R' < \frac{k_1^+ N_{c(1)}}{k_t} : n = 1$$

$$\frac{k_1^+ N_{c(1)}}{k_t} \leq R' < \frac{k_1^+ N_{c(1)} + k_2^+ N_{c(2)}}{k_c} : n = 2$$

$$\frac{k_1^+ N_{c(1)} + k_2^+ N_{c(2)}}{k_c} \leq R' : n = 3$$

Select one atom (site) from the table of the candidates for the event chosen in 2 and 3, and realize the reaction.
Renew the table and go to 2

This cycle defines one KMC step and the average time corresponding to this cycle is $1/k_t$. Additives and their reactions are incorporated in this algorithm as additional events. The numbers of the candidates for the reactions are calculated using the concentrations, which are passed from the continuum code or the results of CGRW in solution.

A.3 **Appendix C** Algorithm for Searching Surface Atoms

The crucial point in the extension of the SOS model to the SBS model is an efficient and accurate algorithm for searching surface atoms. Figure A.1 illustrates an example of the algorithm for a two-dimensional model. Black and white squares denote solid and liquid sites, respectively. Vacancies are denoted by white squares. The algorithm consists of successive numbering of the squares.

From the top of the liquid sites, put “1” to the white squares successively moving down in –y direction.

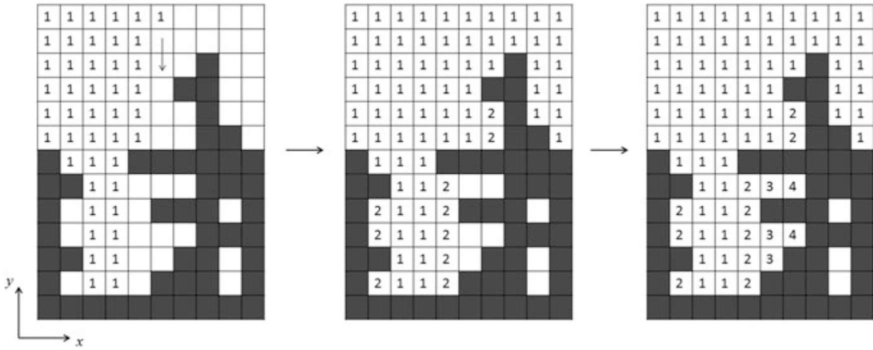

Fig. A.1 Searching algorithm of surface atoms. Successive numbering of the *squares* is illustrated. *Black squares* are solid atoms, *white squares* with numbers are liquid atoms, and *white squares* without numbers are vacancies. The surface solid atoms are the *black squares* adjacent to the numbered *white squares*

Then, put “2” to the white squares adjacent to the white squares numbered as “1”.
Put “3” to the white squares adjacent to the white squares numbered as “2”.
Repeat numbering the white squares adjacent to the already numbered squares.
Stop the numbering if there is no white square without numbers around the numbered white squares.
The solid squares adjacent to the “numbered” white squares are surface solid atoms. White squares adjacent to the surface solid squares are surface liquid sites.

Since the white squares surrounded by solid squares are not numbered, the liquid sites and vacancies are distinguished. It is straightforward to extend this method to a 3D model.

References

1. Andricacos PC, Uzoh C, Dukovic JO, Horkans J, Deligianni H (1998) Damascene copper electroplating for chip interconnects. IBM J Res Develop 42:567–574
2. Dukovic JO, Tobias CW (1990) Simulation of leveling in electrodeposition. J Electrochem Soc 137:3748–3755
3. Dukovic JO (1993) Feature-scale simulation of resist-patterned electrodeposition. IBM J Res Develop 37:125–141
4. West AC (2000) Theory of filling of high-aspect ratio trenches and vias in presence of additives. J Electrochem Soc 147:227–232
5. Georgiadou M, Veyret D, Sani RL, Alkire RC (2001) Simulation of shape evolution during electrodeposition of copper in the presence of additive. J Electrochem Soc 148:C54–C58
6. Josell D, Wheeler D, Huber WH, Moffat TP (2001) Superconformal electrodeposition in submicron features. Phys Rev Lett 87:016102-1–016102-4
7. Moffat TP, Wheeler D, Huber WH, Josell D (2001) Superconformal electrodeposition of copper. Electrochem Solid-State Lett 4:C26–C29

8. West AC, Mayer S, Reid J (2001) A superfilling model that predicts bump formation. Electrochem Solid-State Lett 4:C50–C53
9. Wheeler D, Josell D, Moffat TP (2003) Modeling superconformal eletrodeposition using the level set method. J Electrochem Soc 150:C302–C310
10. Wheeler D, Moffat TP, McFadden GB, Coriell S, Josell D (2004) Influence of a catalytic surfactant on roughness evolution during film growth. J Electrochem Soc 151:C538–C544
11. Josell D, Moffat TP, Wheeler D (2007) Superfilling when adsorbed accelerators are mobile. J Electrochem Soc 154:D208–D214
12. Moffat TP, Wheeler D, Edelstein MD, Josell D (2005) Superconformal film growth: mechanism and quantification. IBM J Res Develop 49:19–36
13. Moffat TP, Wheeler D, Kim SK, Josell D (2006) Curvature enhanced adsorbate coverage model for electrodeposition. J Electrochem Soc 153:C127–C132
14. Moffat TP, Wheeler D, Kim SK, Josell D (2007) Curvature enhanced adsorbate coverage mechanism for bottom-up superfilling and bump control in damascene processing. Electrochim Acta 53:145–154
15. Akolkar R, Landau U (2004) A time-dependent transport-kinetics model for additive interactions in copper interconnect metallization. J Electrochem Soc 151:C702–C711
16. Akolkar R, Landau U (2009) Mechanistic analysis of the “bottom-up” fill in copper interconnect metallization. J Electrochem Soc 156:D351–D359
17. Cao Y, Searson PC, West AC (2001) Direct numerical simulation of nucleation and three-dimensional, diffusion-controlled growth. J Electrochem Soc 148:C376–C382
18. Cao Y, West AC (2002) Nucleation and three-dimensional growth: deviation from diffusion control. J Electrochem Soc 149:C223–C228
19. Zheng M, West AC (2004) Simulation of the influence of reactant depletion on nucleation rate in electrodeposition. J Electrochem Soc 151:C502–C507
20. Emekli U, West AC (2010) Electrochemical nucleation of copper: the effect of Poly(ethylene glycol). J Electrochem Soc 157:D257–D263
21. Emekli U, West AC (2010) Simulation of the effect of additives on electrochemical nucleation. J Electrochem Soc 157:D479–D485
22. Emekli U, West AC (2010) Simulation of electrochemical nucleation in the presence of additives under galvanostatic and pulsed plating conditions. Electrochimca Acta 56:977–984
23. Stephens RM, Alkire RC (2009) Island dynamics algorithm for kinetically limited electrochemical nucleation of copper with additives onto a foreign substrate. J Electrochem Soc 156:D28–D35
24. Stephens RM, Willis M, Alkire RC (2009) Additive-assisted nucleation and growth by electrodeposition II. Mathematical model and comparison with experimental data. J Electrochem Soc 156:D28–D35
25. Alkire RC, Deligianni H (1988) The role of mass transport on anisotropic electrochemical pattern etching. J Electrochem Soc 135:1093–1100
26. Alkire RC, Deligianni H, Ju J-B (1990) Effect of fluid flow on convective transport in small cavities. J Electrochem Soc 137:818–824
27. Georgiadou M, Alkire RC (1994) Anisotropic chemical pattern etching of copper foil III. mathematical model. J Electrochem Soc 141:679–689
28. Shin CB, Economou DJ (1991) Forced and natural convection effects on the shape evolution of cavities during wet chemical etching. J Electrochem Soc 138:527–538
29. Kondo K, Fukui K, Uno K, Shinohara K (1996) Shape evolution of electrodeposited copper bumps. J Electrochem Soc 143:1880–1886
30. Kondo K, Shinohara K, Fukui K (1996) Shape evolution of higher density interconnection bumps used for microprocessor. Kagaku-kougaku Ronbunsyu 22:534–541 (in Japanese)
31. Kondo K, Fukui K, Yokoyama M, Shinohara K (1997) Shape evolution of electrodeposited copper bumps with high Peclet number. J Electrochem Soc 144:468–470
32. Kondo K, Fukui K (1998) Current evolution of electrodeposited copper bumps with photoresist angle. J Electrochem Soc 145:840–884

33. Chatterjee A, Vlachos DG (2007) An overview of spatial microscopic and accelerated kinetic Monte Carlo methods. J Computer-Aided Mater Des 14:253–308
34. Drews TO, Krishnan S, Alameda Jr JC, Gannon D, Braatz RD, Alkire RC (2005) Multiscale simulations of copper electrodeposition onto a resistive substrate. IBM J Res Develop 49:49–63
35. Pricer TJ, Kushner MJ, Alkire RC (2002) Monte Carlo simulation of the electrodeposition of copper I. Additive-free acidic sulfate solution. J Electrochem Soc 149:C396–C405
36. Drews TO, Ganley JC, Alkire RC (2003) Evolution of surface roughness during copper electrodeposition in the presence of additives—Comparison of experiments and Monte Carlo simulations. J Electrochem Soc 150:C325–C334
37. Drews TO, Radisic A, Erlebacher J, Braatz RD, Searson PC, Alkire RC (2006) Stochastic simulation of the early stages of kinetically limited electrodeposition. J Electrochem Soc 153:C434–C441
38. Li X, Drews TO, Rusli E, Xue F, He Y, Braatz RD, Alkire RC (2007) Effect of additives on shape evolution during electrodeposition I. Multiscale simulation with dynamically coupled kinetic Monte Carlo and moving-boundary finite-volume codes. J Electrochem Soc 154:D230–D240
39. Rusli E, Xue F, Drews TO, Vereecken PM, Andricacos P, Deligianni H, Braatz RD, Alkire RC (2007) Effect of additives on shape evolution during electrodeposition II. Parameter estimation from roughness evolution experiments. J Electrochem Soc 154:D584–D597
40. Qin Y, Li X, Xue F, Vereecken PM, Andricacos P, Deligianni H, Braatz RD, Alkire RC (2008) Effect of additives on shape evolution during electrodeposition III. Trench infill for on-chip interconnects. J Electrochem Soc 155:D223–D233
41. Gilmer GH, Bennema P (1972) Computer simulation of crystal surface structure and growth kinetics. J Cryst Growth 13(14):148–153
42. Gilmer GH, Bennema P (1972) Simulation of crystal growth with surface diffusion. J App Phys 43:1347–1360
43. Bortz AB, Kalos MH, Lebowitz JL (1975) A new algorithm for Monte Carlo simulation of Ising spin system. J Comp Phys 17:10–18
44. Gillespie DT (1976) A general method for numerically simulating the stochastic time evolution of couples chemical reactions. J Comp Phys 22:403–434
45. Kaneko Y, Hiwatari Y, Ohara K, Murakami T (2000) Monte Carlo simulation of thin film growth with lattice defects. J Phys Soc Jpn 69:3607–3613
46. Kaneko Y, Hiwatari Y (2002) The solid-by-solid model for crystal growth and electroplating: kinetic Monte Carlo simulation. In: Pandalai SG (ed) Recent research developments of physics and chemistry of solids, vol 1. Transworld Research Network, India p 47–64
47. Kaneko Y, Hiwatari Y, Ohara K (2004) Monte Carlo simulation of thin film growth with defect formation : application to via filling. Mol Sim 30:895–899
48. Kaneko Y, Hiwatari Y, Ohara K, Asa F (2006) Monte Carlo simulation of damascene electroplating: effects of additives. Mol Sim 32:1227–1232
49. Kaneko Y, Hiwatari Y, Ohara K, Asa F (2010) Simulation of three-dimensional solid-by-solid model and application to electrochemical engineering. ECS Trans 28(29):1–7
50. Kaneko Y, Hiwatari Y, Ohara K, Asa F (2011) Kinetic Monte Carlo approach to the effects of additives in electrodeposition. ECS Trans 35(27):7–12
51. Buoni M, Petzold L (2007) An efficient, scalable numerical algorithm for the simulation of electrochemical systems on irregular domains. J Comp Phys 225:2320–2332
52. Buoni M, Petzold L (2010) An algorithm for simulation of electrochemical systems with surface–bulk coupling strategies. J Comp Phys 229:379–398
53. Chatterjee A, Vlachos DG (2006) Multi-scale Monte Carlo simulations: multigriding, computational singular perturbation, and hierarchical stochastic closure. J Chem Phys 124:064110-1–064110-16
54. Oppelstrup T, Bulatov VV, Gilmer GH, Kalos MH, Sadigh B (2006) First-passage Monte Carlo algorithm: diffusion without all the hops. Phys Rev Lett 97:230602-1–230602-4

55. Oppelstrup T, Bulatov VV, Donev A, Kalos MH, Gilmer GH, Sadigh B (2009) First-passage kinetic Monte Carlo method. Phys Rev E 80:066701-1–066701-14
56. Bezzola A, Alkire RC, Petzold L (2012) Multiscale stochastic simulation of surface diffusion during early stages of electrodeposition, 221th ECS Meeting Abstract, **2012**., Abstract #1031
57. Hiwatari Y, Kaneko Y, Mikami T, Ohara K, Asa F (2007) Molecular dynamics-Monte Carlo hybrid simulation of thin film growth and void formation in electrodeposition process. Mol Sim 33:133–138
58. Kaneko Y, Nishimura S, Hiwatari Y, Ohara K, Asa F (2009) Monte Carlo and molecular dynamics studies of the effects of additives in electrodeposition. J Korean Phy Soc 54:1207–1211

Part II
Copper on Chip Metallization

Chapter 5
Frontiers of Cu Electrodeposition and Electroless Plating for On-chip Interconnects

James F. Rohan and Damien Thompson

5.1 Introduction

In the electronics industry, interconnect is defined as a conductive connection between two or more circuit elements. It interconnects elements (transistor, resistors, etc.) on an integrated circuit or components on a printed circuit board. The main function of the interconnect is to contact the junctions and gates between device cells and input/output (I/O) signal pads. These functions require specific material properties. For performance or speed, the metallization structure should have low resistance and capacitance. For reliability, it is important to have the capability of carrying high current density, stability against thermal annealing, resistance against corrosion and good mechanical properties.

Over the past 40 years, the continuous improvements in microcircuit density and performance predicted by Moore's Law has led to reduced interconnect dimensions. Until the mid-1990s, Al interconnect was sufficient for VLSI circuit processing [1]. Further developments in miniaturisation of IC interconnect required a more conductive material than Al to minimise the RC (resistance–capacitance) delay which is in effect a time-delay between the input and output for a signal or potential applied to a circuit. When coupled with the poor resistance to electromigration (transport of material caused by the gradual movement of the ions in a conductor due to the momentum transfer between conducting electrons and diffusing metal atoms) and poor mechanical properties for application in ultra large-scale integrated (ULSI) circuits, it was clear that an alternative to Al was required [2].

Only three metals, Ag, Au and Cu have lower resistivity than Al. For practical applications, it is clear that using Cu rather than Ag or Au is more realistic.

J. F. Rohan (✉) · D. Thompson
Tyndall National Institute, University College Cork, Lee Maltings, Cork, Ireland
e-mail: james.rohan@tyndall.ie

K. Kondo et al. (eds.), *Copper Electrodeposition for Nanofabrication of Electronics Devices*, Nanostructure Science and Technology 171, DOI: 10.1007/978-1-4614-9176-7_5,
© Springer Science+Business Media New York 2014

The resistivity of Cu is 1.67 μΩ cm, about 40 % lower than Al, which when coupled with the new low k dielectrics introduced for the processing led to significant improvement in the RC delay. Cu also has advantages of higher melting point 1083 °C by comparison with 660 °C for Al and higher barrier to migration of an atom from its lattice position in a crystal, Al (1.4 eV) and Cu (2.2 eV). Despite these advantages Cu had not been used for on-chip interconnect to that point because of device reliability concerns and processing difficulties. It can diffuse rapidly through SiO_2 in the presence of an electric field [3], decreasing transistor reliability. It also oxidises significantly at low temperatures but unlike Al it does not self-passivate [4]. However, one of the largest obstacles to its introduction was the fact that it cannot be etched readily in plasma. Therefore, an entirely new approach to interconnect processing had to be developed.

In 1997, IBM developed the electrodeposition technique for Cu metallisation [5]. The required breakthrough was damascene plating in which the dielectric is first patterned before infilling with the Cu conductor, which enabled Cu electrodeposition to be utilised for on-chip interconnect. It has since become the standard method for Cu metallisation with demonstrated wafer scale uniformity, high aspect ratio gap filling capability and low temperature processing. Semiconductor manufacturers have gradually adopted the electroplating technique for Cu interconnect deposition in electronic devices and continue to work on miniaturization of device and feature sizes. In the dual damascene technique, lines and vias can be filled with electrodeposited Cu at the same time. Figure 5.1 shows a schematic diagram of via filling with Cu and the requirement to achieve 'superfilling' or 'bottom-up fill' (BUF) deposition. This is achieved through the use of suitable additives in the plating bath [6–8], and is required because sub-conformal or conformal plating would lead to voids or seams in the Cu.

The additives typically required to achieve this superfilling are a suppressor such as polyethylene glycol (PEG) which in conjunction with chloride ion and an accelerator such as sulphopropyl disulphide (SPS) result in enhanced deposition within the feature while minimising overgrowth or a pinch off of the feature at the top surface. Detailed examinations of the mode of operation of the additives (discussed below in Sect. 5.3.2.1) and their interactions have been performed and has facilitated remarkable and predictable control of the deposition in sub 100 nm dimensions.

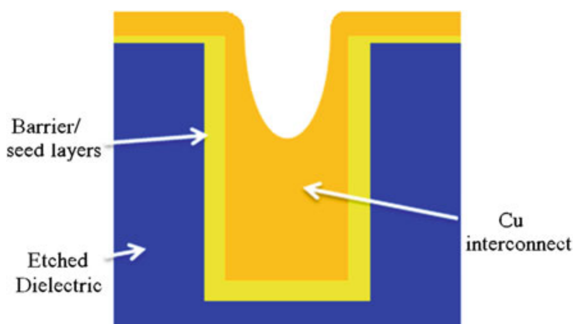

Fig. 5.1 Cross-section schematic of interconnect trench or via showing 'superfilling' or 'bottom-up filling' of features through the use of specific plating bath additives for optimum void-free profile evolution in damascene processing [5]

Improved barrier layers were also required and introduced with Cu in the damascene process. Refractory metals or their alloys such as TaN deposited by a standard physical vapour deposition (PVD) process have been sufficient to date. This layer covers the entire surface to act as a barrier to Cu diffusion. The low conductivity of TaN has required Cu seed layers for the subsequent electrodeposition, and these have also been processed by PVD [9]. However, PVD suffers from poor step coverage in deep sub-micrometer vias and trenches. An alternative process, chemical vapour deposition (CVD) remains a candidate for Cu deposition but requires the use of combustible precursors which has limited the implementation of Cu deposition by CVD [10] in IC processing to date. Once the barrier layer is in place, the active interconnect material can also be deposited by CVD and Moffat et al. have shown that a similar superfilling can be achieved using this approach [11]. For future device architectures, particularly at the lower metal layers of the interconnect, new processing routes must be established with even greater control over nucleation and layer growth to achieve the material dimensions required. This may necessitate a combination of new processing routes involving vacuum deposition techniques and wet chemistry processing.

5.2 Required Future Dimensions

The International Technology Roadmap for Semiconductors (ITRS) lists the dimensions for interconnect processing required over the next number of device generations [12]. Figure 5.2 has an illustrative cross-section from the ITRS of a typical microprocessor where the interconnect of different lines and vias between two adjacent layers are filled with Cu. The metal 1 pitch is also illustrated.

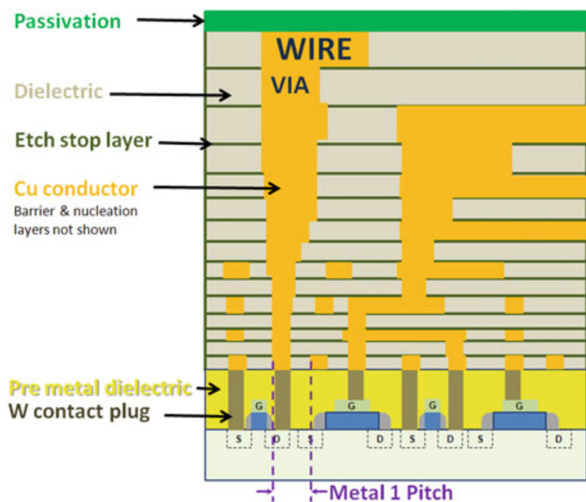

Fig. 5.2 Typical cross-section illustrating hierarchical scaling methodology [adapted from the ITRS technology roadmap, 2011 update for interconnect]

Table 5.1 Metal 1 (1/2 pitch) dimensions and barrier cladding thickness for metal 1 [ITRS technology roadmap, 2011 update for interconnect]

Year of production	2014	2016	2018	2020	2022	2024	2026
Metal 1 (1/2 pitch)/nm	24	19	15	12	10	8	6
Barrier cladding thickness for metal 1/nm	2.1	1.7	1.3	1.1	0.9	0.7	0.5

The microprocessor metal (1½ pitch) dimension in future device generations requirements is summarised in Table 5.1. It is clear that manufacturable processes are not yet known for metal 1 interconnect and barrier layer material past 2014 (highlighted in red squares). By 2020, IC interconnect at the smallest dimension will be 12 nm with an expected aspect ratio of 2 and barrier layer thickness of only 1.1 nm. The interconnect issues require urgent attention to enable further Cu scaling. This requires the combined assessment of novel barrier and seed layer processing and the active device interconnect material deposition.

As the feature sizes decrease and consequently the operating currents increase, electromigration becomes a serious issue once more [13], particularly where high direct current densities are used, such as in high performance processors. It has been reported that Cu vias are the weak link in the interconnect metallisation [14]. The Cu via connects directly to the Cu metal below. Consequently, if a void forms in the Cu underneath the via, there is no redundant layer available for current shunting. This is the primary cause of early failure in Cu interconnects. For the 22 nm technology node or below, the interconnect metal should have current carrying capability of more than 10^7 A/cm^2 to overcome the electromigration issue which is at the limit of pure Cu capability.

5.3 New Processing to Extend Cu

The decrease in cross-sectional area of the interconnect pushes the current density of the Cu wire towards the electromigration limit. To extend the use of Cu at the smaller dimensions, a decrease is required in the material stack that functions as barrier layer, in the adhesion or liner and/or in the conductive metal seed layer. This can be achieved through the use of more conductive and better adhered barrier layers and seed layers eventually possibly being thinned to a single plateable barrier. A graphical representation of the influence of the thickness of the barrier/adhesion/conductor seed stack on the percentage of available active Cu conductor cross-sectional area is shown in Fig. 5.3 for a simple 1:1 aspect ratio. It can be seen that a very significant proportion of the via or line will be consumed by low conductivity barrier stack materials unless the materials function can be optimised and decreased in dimension.

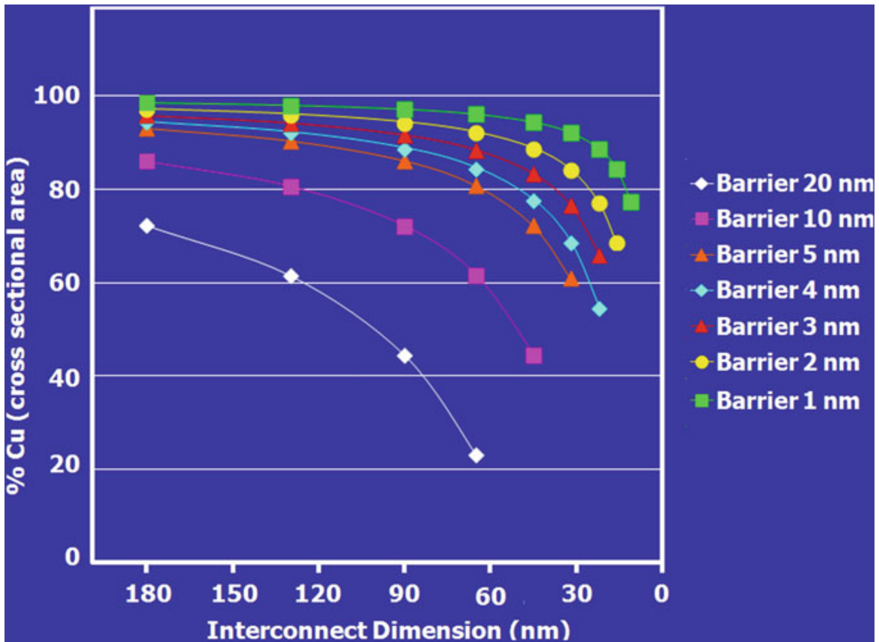

Fig. 5.3 The effect of thinning barrier/seed layer stacks for Cu interconnect based on the cross-sectional area of a 1:1 aspect ratio feature at decreasing interconnect dimensions

5.3.1 Barrier Layer Studies

Two potential solutions to the issue of decreasing the barrier/seed layer dimension have received the most attention to date. One is the use of higher conductivity 'plateable' barriers. The other is the use of self-forming barriers through the deposition of a Cu-based alloy. When the alloy is deposited, a stable nanoscale barrier forms between the alloying element and the low-k dielectric material upon heat treatment.

5.3.1.1 Plateable Barriers

Potential plateable barriers must fulfil a number of criteria to be considered as replacements for the current TaN barrier layer for Cu. The material must

- function as a barrier to Cu diffusion
- form a coherent, conformal nanoscale deposit
- have significantly better electronic conductivity to enable nanometre scale layer use at 300 mm and the future 450 mm diameter wafers without terminal effects [15] (where non-uniform Cu electrodeposition occurs across the wafer).

Lower conductivity plating solutions have also been introduced to minimise variation across the wafer by counteracting the resistive seed. The lower acid content of such solutions also enhances the Cu seed layer stability by reducing corrosion while improving the Cu solubility. Candidate barrier/seed materials are listed according to bulk resistivity in Table 5.2.

The materials must also

- be non-oxidising
- be competitive in cost
- be scalable to 1.7 nm by 2016, 1.1 nm by 2020 and 0.5 nm by 2026 in accordance with the ITRS roadmap.

Amorphous materials have in general been shown to function well as barrier layer materials and the introduction of nitrides or alloying elements has also been considered although high conductivity remains a concern when using an alloy or nitride.

Meeting each of the conditions listed above is a significant challenge and has resulted in the assessment of new and combined deposition techniques such as atomic layer deposition for the ultimate control over the barrier layer dimension. In atomic layer deposition, a cyclical process of metal precursor and reactant introduction to a vacuum chamber is performed to deposit materials atomically layer by layer. This is readily achieved for materials such as Al_2O_3 where first the Al precursor is introduced before the second active material pulse of water terminates the deposited Al with oxygen leading to a non catalytic surface for the next phase of deposition [16]. This process encourages the completion of the first atomic layer and minimises island or 3D growth. In the deposition of 'plateable' barrier layer metals the first pulse deposits material that is by design maintained conducting which leads to difficulties with the second phase of the process in which identical material is reacted on the deposit. This can lead to a catalytic process and the growth of islands or non-continuous layers.

Table 5.2 Bulk resistivity of candidate materials for Cu seed layers

Metal	Bulk resistivity/micro ohm cm
Rh	4.3
Ir	4.7
W	5.0
Co	6.0
Ni	6.8
Ru	7.1
Os	8.1
Pt	10.6
Ta	13.5
Ti	40
Mn	144
TaN	180

Detailed studies of Ru deposition demonstrate many of the challenges with the introduction of a plateable barrier. It can be deposited by PVD, CVD or ALD. However, as a pure material it generally deposits in a columnar arrangement with grain boundaries through which the Cu can readily diffuse and is thus a poor barrier layer material. It also experiences oxidation which requires additional processing prior to Cu nucleation and growth in subsequent stack depositions. To alleviate some of the issues multilayer solutions have been proposed such as layering Ru with TaN [17], the inclusion of phosphorus [18], nitrogen, boron and/or carbon [19] or forming alloys such as with tungsten [20]. Binary barrier layers prevent the columnar deposit while only marginally impacting the conductivity. Some of these layers have demonstrated sufficient barrier layer capability at 5 nm when deposited by PVD or CVD. Investigations will continue in this area targeting long-term barrier functionality of the layers, which would be deposited preferably through novel ALD processing capable of scaling the plateable seed layer to the dimensions that will be required for future device generations. The improved barrier materials may also be integrated further up the metal stack as improvements in the lower metal stack combinations are introduced.

5.3.1.2 Self-Forming Barriers

An alternative approach to future barrier layer processing is the use of self-forming barriers [21]. To realise a self-forming barrier, the alloying element must be in a simple solid solution phase with Cu. Elements that form intermetallics (such as Al, Mg, Sn and Ti) tend to remain in the Cu and result in increased resistivity. The diffusivity of the alloying element must also be faster than the self-diffusivity of Cu, so that the alloying element preferentially migrates to the dielectric interface. Ta, W and Mo which are slow diffusing cannot form a barrier layer before significant diffusion of Cu to the dielectric. The third requirement is that the standard free energy of oxide formation should be sufficiently large and negative but not much larger than SiO_2. The oxide formation energy provides a driving force for the element to migrate to the interface and ensures that SiO_2 is not strongly reduced. The activity coefficient of the element in a Cu solid solution should be close to or larger than unity. Elements of this type can be removed easily out of the Cu film, leading to a substantial decrease of resistivity.

Manganese has been shown to fulfil these criteria forming $MnSi_xO_y$ at the interface with the dielectric material. The manganese self forming barrier process is being investigated to more fully understand the mechanism and potential for use in future generations. Other issues being assessed are the scalability of the process, the uniformity, the barrier layer functionality with decreasing thickness and the interaction with current and future dielectric materials.

5.3.1.3 Self-Aligned Electroless Barrier/Capping Layers for On-Chip Interconnect

Electroless processing has already shown significant potential for IC interconnect applications in self-aligned capping layer deposition on Cu. Grain boundaries were the fastest diffusion path for electromigration in Al (activation energy 0.6 eV for grain boundary diffusion and 1.0 eV for interface diffusion). On the other hand, a metal/barrier layer interface is the fastest diffusion path for Cu (activation energy 1.2 eV for grain boundary diffusion and 0.7 eV for interface diffusion) [22, 23]. The interface electromigration mechanism placed a different focus for reliability improvement with Cu interconnect by comparison with the methods traditionally utilised for Al. In damascene processing, overdeposited Cu is removed by chemical mechanical polishing (CMP). The CMP produced top Cu surface is the fast Cu diffusion path which needs to be tightly capped. A non-conductive barrier layer is generally applied as the cap layer (e.g. silicon nitride, silicon carbide, nitride silicon carbide, etc.) to cover the Cu line top surface. However, there are some issues with using dielectric caps to passivate Cu. As devices become smaller, the current density through the interconnect increases leading to the requirement for better electromigration resistance. The dielectric cap generally also has a higher dielectric constant than the interlevel dielectric, resulting in an increase in line-to-line capacitance. Improved Cu electromigration resistance has been reported for Cu lines protected with thin conductive surface capping layers of self-aligned electrolessly deposited CoWP or CoSnP [24, 25].

5.3.2 Electroless On-Chip Interconnect Materials Deposition

Electroless plating has also been investigated as a means to deposit Cu for ULSI applications. Initial studies indicated that submicron features could be filled with electroless Cu from formaldehyde solutions with typical electroless Cu additives such as EDTA and wetting agents to remove hydrogen gas during deposition [26–28]. Alternative reducing agents have also been investigated such as glyoxylic acid [29, 30] and dimethyl amine borane [31]. Void free deposits were generally achieved although in the larger dimension features a more conformal deposit was observed than the superconformal deposits required for current and future device generations. An example of conformal deposition in a 0.36 μm trench is shown below in Fig. 5.4 for electroless Cu deposited on TaN from a DMAB-based bath.

5.3.2.1 Superconformal Electroless Cu Deposition

The achievement of BUF using similar additives to those used in electrolytic baths was reported by Shingubara et al. for 310 nm diameter openings [32]. They found that SPS concentration and PEG with a molecular weight in excess of 800 could be

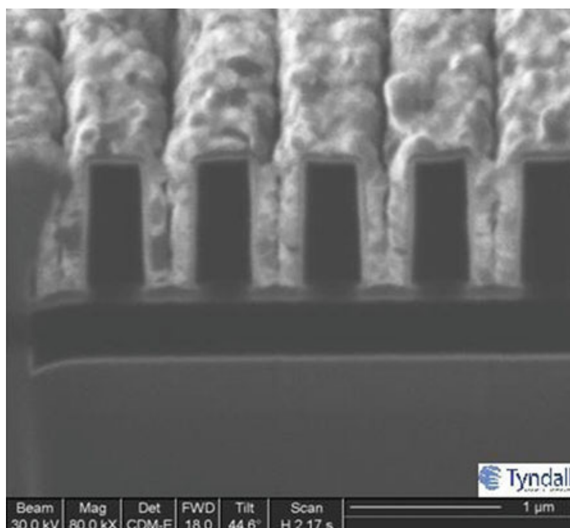

Fig. 5.4 Conformal electroless Cu from a DMAB bath deposited on TaN (0.36 μm trench)

used to encourage BUF even from this very different plating solution when compared to the electrolytic baths. They used glyoxylic acid at pH 12.5 (using tetra methyl ammonium hydroxide to modify pH) and common to all electroless baths no potential was imposed on the substrate. A 1 nm ICB deposited Pd layer was utilised to activate the substrate for electroless Cu deposition. Similar results were achieved in a formaldehyde bath for trench features with 400 nm openings [33] where lower concentrations of SPS (0.5 mg/L) gave BUF through an acceleration of the electroless deposition while for SPS concentrations in excess of 5 mg/L a suppression effect was observed which prevented BUF. PEG was not utilised in [33]. In a subsequent report [34] 2, 2 dipyridyl was added to enhance the deposition characteristics and BUF with 2 to 10 mg/L of SPS while above 25 mg/L a suppression of the electroless Cu deposition reaction was observed.

Similar baths using glyoxylic acid, 2, 2 dipyridine and sulphur containing organic acids with three different chain lengths were investigated [35]. The researchers concluded that enhanced diffusion of the lower molecular weight mercapto acids to the base of the etched structure promoted BUF. A study which assessed the effect of dilute 1 ppm PEG (MW 4000) on electroless Cu deposition from Glyoxylic acid also revealed BUF which they proposed was promoted within the etched structure (130 nm opening, 350 nm depth onto which a 35 nm PVD Ti/Cu seed layer was deposited) by the differences in PEG concentration that result from the diffusion characteristics and relatively slow diffusion for PEG by comparison with the ten times smaller EDTA complexed Cu ion [36]. Lee et al. [37] investigated the influence of 2-mercapto-5-benzimidazolesulfonic acid on BUF in a formaldehyde electroless Cu bath with 500 nm wide trenches. They also incorporated 2, 2 dipyridyl and PEG (MW 8000). Like their other studies the authors found an acceleration effect with low concentration of the sulphur

containing additive while at high concentration of the additive a suppressor effect was observed. Yang et al. [38] studied the synergistic effects of SPS and PEG (MW 4000) in a formaldehyde bath at pH 12.5 with trench openings of 150 nm and depth of 470 nm onto which Ti (10 nm) and Cu (40 nm) were sputtered. They found that inhibition by PEG at the top surface and acceleration by SPS within the trench promoted BUF in the feature sizes studied.

Each of these studies resulted in deposition similar to that observed in sulphuric acid electrolytic Cu deposition baths. The general characteristic of deposition suppression at the top surface by the adsorption of slower diffusing bulky species is common to deposition through both electrolytic and electroless means. In some cases, this appears to be assisted by an accelerator reaction within the trench though there is little evidence for the overfilled bump predicted by the curvature enhanced accelerator coverage model [39]. It should also be noticed that while chloride is always present in the electrolytic tests to enhance the functionality of the suppressor molecule, it is not used in the electroless studies. Healy et al. [40] showed the influence of chloride on the deposition from a typical strongly acidic sulphate electrolytic bath. At open circuit they suggested the adsorption of a Cu(I)-Cl complex with PEG as a ligand. They proposed that the complex forms a film at the Cu surface that hinders the Cu deposition rate. However, the potential region where Cu is deposited (typically in the range −0.5 to −0.6 V versus Hg/Hg_2SO_4 in such solutions) Cl^- no longer adsorbs and the PEG is adsorbed as a neutral molecule. In a formaldehyde electroless Cu bath operating in alkaline solution (pH 12.5) Cu has been shown to deposit in the region of −0.96 V versus Hg/Hg_2SO_4 [41]. It is also of interest to observe that the rest potential for a Cu electrode in the formaldehyde solution in the absence of added Cu ion is approximately −1.4 V versus Hg/Hg_2SO_4 [42]. Detailed analysis of each of the contributing bath additives and their interaction at the potential and pH of interest has not been performed to date for electroless Cu BUF.

Recent analysis of electroless Cu deposition from borane solutions [43] has shown the importance of designing cells that permit monitoring of the various components in the deposition process. The electroless plating baths are complex solutions typically involving multistep oxidation [44, 45] and metal reduction. To fully describe the reaction mechanism, more characterisation is required that will provide data on the individual components and their distributions in full cells. Complicating the analysis is the need to determine reactions at a single substrate. A further complicating factor is that the new phase deposited becomes the active electrode in electroless deposition experiments. It is also important to attempt to standardise the analysis to enable data comparison and mechanistic interpretations. Some of the variables that have hindered the derivation of mechanisms for electroless Cu deposition include bath pH, concentration of active materials, metal salts, additive types and concentration, substrate material, temperature, agitation, dissolved oxygen, impurity species and substrate to solution volume ratio.

5.3.2.2 Electrochemical Deposition for Future on Chip Interconnect

Electrolytic and electroless deposition have both been shown to fill structures with a required BUF mechanism. To date relatively few studies have been performed on electroless processing in the low nanometre range. Seed layers based on Pd or Cu have also been used and future interconnect architectures will not facilitate thick seed layers for initial nucleation and layer growth. Suitably activated electroless Cu deposition could be utilised on current TaN-based barrier layers given that a complete seed layer is not required and an electrical terminal effect will not influence the uniformity of the deposit. However, it is still unclear what the limits are for the seed layer required in electroless processing and what the capabilities of BUF are in sub 20 nm features. Plateable barriers based on more conductive materials may also be relevant for electroless processing and provide uniform seed layers for electroless Cu deposition. Electroless Cu for seed layer repair of PVD deposited seeds is currently under investigation and similar investigation may be required for CVD or ALD deposited barrier/seed layers as the achievement of ultrathin coherent conducting layers is not a trivial matter even with these vacuum-based high temperature processing routes.

More detailed analysis over the coming years is required to precisely control the electroless processing as has been achieved in the electrolytic case. The ability to then model and predict nucleation and growth mechanisms will greatly benefit future device fabrication. On non-conducting barrier layers existing electroless Cu baths require a catalyst deposition and this is typically achieved using a Sn-based sensitization step. In a recent study [46] an 18 nm coherent electroless Cu film was deposited from a formaldehyde-based solution. The limiting factor proposed for this film thickness was the need to achieve well-dispersed nuclei of Pd catalyst on the Sn sensitiser which were in turn on Ta on a TaN barrier layer. In that work Pd particle density was increased (to 6.8×10^{10} particles/cm^2) by the addition of PEG-3400 to the Sn sensitisation solution. They attributed this increase to PEG acting as a surfactant and stabilising agent for the Sn colloids. For electroless processing to be utilised in future on-chip interconnect even greater control of the nucleation density and layer growth dimension will be required, with the fundamental lower limit set by the Cu atom diameter of 0.245 nm.

Common to both electrolytic and electroless deposition for future Cu-based IC interconnect is the need to utilise additives to enhance the deposition characteristics. The additives typically employed in damascene plating are based on the interaction between PEG type materials and an accelerator. The size and shape of these additives will become more significant as the feature size for the structure decreases. A typical PEG material used in many of the studies reported has a molecular weight of 3350 based on 75 repeat units of the C–O–C unit. FE-SEM has been used to investigate PEG 7500 [47] in which particles 10 nm in diameter were attributed to PEG. Kondo et al. [48] using AFM observed adsorbed PEG (MW 7500) on Cu in the presence of Cl^- with a cone shape where the bottom radius was about 15–25 nm and the height was 2–4 nm. Kelly and West [49] had suggested a collapsed sphere 1.7 nm in diameter based on the molecular weight for

PEG 3350 and assuming no voids in the collapsed structure. Alternative polyethers have also been investigated [50] and shown to facilitate void free deposition in high aspect ratio features exhibiting superior BUF capability than PEG 1000 for example.

Molecular dynamics computer simulations can be used to calculate intra- and inter-molecular forces at the nanoscale and determine the structure, dynamics and energetics of macromolecules [51]. The computed structure of PEG (Fig. 5.5) [52] with MW 3362 (75 CH_2OCH_2 repeat units) shows that an estimated diameter of 1.7 nm [49] for a tightly folded PEG polymer of MW $\sim$3350 is reasonable. The structure was calculated using the NAMD programme [53] with the CHARMM force field [54] supplemented by literature data for PEG [55]. Four nanoseconds of room temperature Langevin molecular dynamics was performed in a NVT ensemble (constant number of particles, constant volume and constant temperature) using a two femtosecond time step for dynamics.

Such computed properties can be used to better understand and guide experiments in the development of functional nanomaterials for electronics [56–58]. Further models that include the Cu surface and water could be used to determine the size and structure of the polymer in Cu deposition experiments [49], including also the effect of ions [59] on the structure of the PEG (or similar functioning polyethers), to assist with prediction of the viability of materials processing for future electrolytic or electroless on-chip interconnect.

Electrochemical deposition for on-chip interconnect has over the past 15 years inspired many aspects of nanoscale electrochemical processing. The detailed analysis of the electrolytic route has resulted in a continuous scaling that has matched the requirements of the ITRS for sub 100 nm deposition. As the issues of

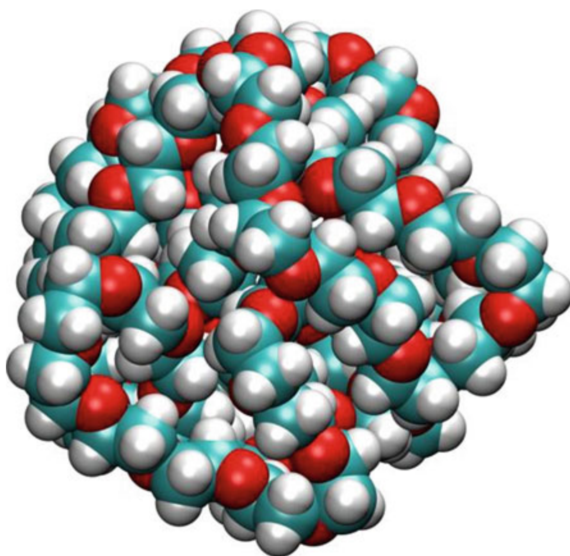

Fig. 5.5 Computed room temperature structure of $HOCH_2–(CH_2OCH_2)_{75}–CH_2OH$ (M. W. = 3362). Carbon, oxygen and hydrogen atoms are blue, red and white spheres. The computed PEG structure exhibits a radius of gyration of 0.86 ± 0.01 nm (averaging over 100 structures, sampling every ten picoseconds during the final nanosecond of dynamics), corresponding to a diameter of 1.72 nm

barrier/seed layers and nucleation become more critical electroless deposition must also be considered for future on-chip interconnect applications and combinations with ALD or CVD may be required to deliver the future scaling requirements. Novel electroless plating solutions and detailed electrochemical and microstructural characterisation are required. Computer simulations of bath constituents and interactions will assist greatly in the continued implementation of electrochemical solutions for applied nanotechnology.

Acknowledgments This work was part resourced by the Nano-EI project within CCAN—the Collaborative Centre for Applied Nanotechnology (www.ccan.ie), supported by Enterprise Ireland & IDA Ireland (grant no. CC/2009/0002). D. T. acknowledges financial support from Science Foundation Ireland (SFI; grant no. 11/SIRG/B2111).

References

1. Vadasz LL, Grove AS, Rowe TA, Moore GE (1969) Silicon gate technology. IEEE Spectrum 6:28
2. Solanki R, Pathangey B (2000) Atomic layer deposition of copper seed layers. Electrochem Solid State Lett 3:479
3. Wang MT, Lin YC, Chen MC (1998) Barrier properties of very thin Ta and TaN layers against copper diffusion. J Electrochem Soc 145(7):2538
4. Hu CK, Luther B, Kaufman FB, Hummel J, Uzoh C, Pearson DJ (1995) Copper interconnection integration and reliability. Thin Solid Films 262:84
5. Andricacos PC, Uzoh C, Dukovic JO, Horkans J, Deligianni H (1998) Damascene copper electroplating for chip interconnections. IBM J Res Dev 42:567
6. Kondo K, Hayashi K, Tanaka Z, Yamakawa N (2000) Role of damascene via filling additives—morphology evolution. ECS proceedings on electrochemical processing in ULSI fabrication 8:76
7. Kelly JJ, West AC (1999) Leveling of 200-nm features by organic additives. Electrochem Solid State Lett 2:561
8. Healy JP, Pletcher D, Goodenough M (1992) The chemistry of the additives in an acid copper electroplating bath: part III. The mechanism of brightening by 4,5-dithia-octane-1, 8-disulphonic acid. J Electroanal Chem 338:179
9. Abe K, Harada Y, Onoda H (1995) Sub-half micron copper interconnects using reflow of sputtered copper films. In: Proceedings of 13th Intern VLSI Multilevel Interconnect Conference, p 308
10. Cho JSH, Kang HK, Asano I, Wang SS (1992) CVD Cu interconnections for ULSI. In: IEDM Technical Digest, p 297
11. Josell D, Wheeler D, Moffat TP (2002) Superconformal Deposition by Surfactant-Catalyzed Chemical Vapor Deposition. Electrochem Solid State Lett 5:C44–C47
12. International Technology Roadmap for Semiconductors (2011) update, http://www.itrs.net/Links/2011Winter/11_Interconnect.pdf. Accessed 13 Jul 2012
13. Hu CK, Harper JME (1998) Copper interconnects and reliability. Mater Chem Phys 52:5
14. Li B, Sullivan T, Lee T, Badami D (2004) Reliability challenges for copper interconnects. Microelectron Reliab 44:365
15. Armini S, Vereecken PM (2010) Impact of 'Terminal Effect' on Cu plating: theory and experimental evidence. ECS Transactions 25(27):185–194
16. Groner MD, Fabreguette FH, Elam JW, George SM (2004) Low temperature Al_2O_3 atomic layer deposition. Chem Mater 16:639–645

17. Kumar S, Xin HL, Ercius P, Muller DA, Eisenbraun E (2008) ALD growth of a mixed-phase novel barrier for seedless copper electroplating applications. IEEE 2008 International Interconnect Technology Conference (IITC 2008), Proceedings, pp. 96–98
18. Shin J, Waheed A, Agapiou K, Winkenwerder WA, Kim H, Jones RA, Hwang GS, Ekerdt JG (2006) Growth of ultra-thin films of amorphous ruthenium-phosphorus alloys using a single source CVD precursor. J Am Chem Soc 128:16510–16511
19. Perng D-C, Yeh J-B, Hsu K-C, Wang Y-C (2010) 5 nm amorphous boron and carbon added Ru film as a highly reliable Cu diffusion barrier. Electrochem Solid State Lett 13(8):H290–H293
20. Yeh J-B, Perng D-C, Hsu K-C (2010) Amorphous RuW film as a diffusion barrier for advanced Cu metallization. J Electrochem Soc 157(8):H810–H814
21. Koike J, Wada M (2005) Self-forming diffusion barrier layer in Cu–Mn alloy metallization. Appl Phys Letts 87:041911
22. Li B, Sullivan T, Lee T, Badami D (2004) Reliability challenges for copper interconnects. Microelectron Reliab 44:365
23. Hu C, Gignac L, Rosenberg R (2006) Electromigration of Cu/low dielectric constant interconnects. Microelectron Reliab 46:213
24. Hu CK, Gignac L, Rosenberg R, Liniger E, Rubino J, Sambucetti C, Stamper A, Domenicucci A, Chen X (2003) Reduced Cu interface diffusion by CoWP surface coating. Microelectron Eng 70:406
25. Gambino J, Wynne J, Gill J, Mongeon S, Meatyard D, Lee B, Bamnolker H, Hall L, Li N, Hernandez M, Little P, Hamed M, Ivanov I, Gan C (2006) Self-aligned metal capping layers for copper interconnects using electroless plating. Microelectron Eng 83:2059
26. Shacham-Diamand Y, Dubin V, Angyal M (1995) Electroless copper deposition for ULSI. Thin Solid Films 262:93
27. Hsu H–H, Lin K-H, Lin S-J, Yeh J-W (2001) Electroless copper deposition for ultralarge-scale integration. J Electrochem Soc 148:C47
28. Dubin VM, Shacham-Diamand Y, Zhou B, Vasudev PK, Ting CH (1997) Selective and blanket electroless copper deposition for ultralarge scale integration. J Electrochem Soc 144:898
29. Shacham-Diamand YY (2000) Electroless copper deposition using glyoxylic acid as reducing agent for ultralarge scale integration metallization articles. Electrochem Solid State Lett 3:279
30. Wang Z, Yaegashi O, Sakaue H, Takahagi T, Shingubara S (2003) Suppression of native oxide growth in sputtered TaN films and its application to Cu electroless plating. J Appl Phys 94:4697
31. Patterson J, O'Reilly M, Crean GM, Barrett J (1997) Selective electroless copper metallization on a titanium nitride barrier layer. Microelectron Eng 33:65
32. Shingubara S, Wang Z, Yaegashi O, Obata R, Sakaue H, Takahagi T (2004) Bottom-up fill of copper in deep submicrometer holes by electroless plating. Electrochem Solid State Lett 7:C78
33. Lee C-H, Lee S-C, Kim J–J (2005) Bottom-up filling in Cu electroless deposition using bis-(3-sulfopropyl)-disulfide (SPS). Electrochim Acta 50:3563
34. Lee C-H, Lee S-C, Kim J–J (2005) Improvement of electrolessly gap-filled Cu using 2, 2'-Dipyridyl and Bis-(3-sulfopropyl)-disulfide (SPS). Electrochem Solid State Lett 8:C110
35. Wang Z, Obata R, Sakaue H, Takahagi T, Shingubara S (2006) Bottom-up copper fill with addition of mercapto alkyl carboxylic acid in electroless plating. Electrochim Acta 51:2442
36. Hasegawa M, Yamachika N, Shacham-Diamand Y, Okinaka Y, Osaka T (2007) Evidence for "superfilling" of submicrometer trenches with electroless copper deposit. Appl Phys Lett 90:101916
37. Lee C-H, Kim A-R, Koo H-C, Kim J-J (2009) Effect of 2-Mercapto-5-benzimidazolesulfonic acid in superconformal Cu electroless deposition. J Electrochem Soc 156:D207
38. Yang Z, Wang X, Li N, Wang Z, Wang Z (2011) Design and achievement of a complete bottom-up electroless copper filling for sub-micrometer trenches. Electrochim Acta 56:3317

39. Moffat TP, Wheeler D, Huber WH, Josell D (2001) Superconformal electrodeposition of copper. Electrochem Solid State Lett 4:C26
40. Healy JP, Pletcher D, Goodenough M (1992) The chemistry of the additives in an acid copper electroplating bath: part I. Polyethylene glycol and chloride ion. J Electroanal Chem 338:155
41. Paunovic M, Arndt R (1983) The effect of some additives on electroless copper deposition. J Electrochem Soc 130:794
42. Paunovic M (1977) Ligand effects in electroless copper deposition. J Electrochem Soc 124:349
43. Plana D, Campbell AI, Patole SN, Shul G, Dryfe RAW (2010) Kinetics of electroless deposition: the copper-dimethylamine borane system. Langmuir 26:10334
44. Nagle LC, Rohan JF (2005) Investigation of DMAB oxidation at a gold microelectrode in base. Electrochem Solid State 8:C77
45. Nagle LC, Rohan JF (2006) Ammonia borane oxidation at gold microelectrodes in alkaline solutions. J Electrochem Soc 153:C773
46. Lim T, Koo H-C, Park K-J, Kim M-J, Kim S-K, Kim J–J (2012) Optimization of catalyzing process on Ta substrate for copper electroless deposition using electrochemical method. J Electrochem Soc 159:D142
47. Kondo K, Matsumoto T, Watanabe K (2004) Role of additives for copper damascene electrodeposition: experimental study on inhibition and acceleration effects. J Electrochem Soc 151:C250
48. Jin Y, Kondo K, Suzuki Y, Matsumoto T, Barkey DP (2005) Surface adsorption of PEG and Cl^- additives for copper damascene electrodeposition. Electrochem Solid State Lett 8:C6
49. Kelly JJ, West AC (1998) Copper deposition in the presence of polyethylene glycol I. Quartz crystal microbalance study. J Electrochem Soc 145:3472
50. Akolkar R, Landau U (2009) Mechanistic analysis of the “Bottom-Up” fill in copper interconnect metallization. J Electrochem Soc 156:D351
51. Allen MP, Tildesley DJ (1989) Computer simulation of liquids. Oxford University Press, Oxford. ISBN 0-19-855645-4
52. Thompson D, unpublished results
53. Phillips JC, Braun R, Wang W, Gumbart J, Tajkhorshid E, Villa E, Chipot C, Skeel RD, Kale L, Schulten K (2005) Scalable molecular dynamics with NAMD. J Comput Chem 26:1781
54. MacKerell AD, Bashford D, Bellott M, Dunbrack RL, Evanseck JD, Field MJ, Fischer S, Gao J, Guo H, Ha S, Joseph-McCarthy D, Kuchnir L, Kuczera K, Lau FTK, Mattos C, Michnick S, Ngo T, Nguyen DT, Prodhom B, Reiher WE, Roux B, Schlenkrich M, Smith JC, Stote R, Straub J, Watanabe M, Wiorkiewicz-Kuczera J, Yin D, Karplus M (1998) All-atom empirical potential for molecular modeling and dynamics studies of proteins. J Phys Chem B 102:3586
55. Tasaki K (1996) Poly(oxyethylene)—water interactions: a molecular dynamics study. J Am Chem Soc 118:8459
56. Nerngchamnong N, Li Y, Qi D, Jian L, Thompson D, Nijhuis CA (2013) The role of van der Waals forces in the performance of molecular diodes. Nat Nanotechnol 8:113–118
57. Thompson D, Hermes JP, Quinn AJ, Mayor M (2012) Scanning the potential energy surface for synthesis of dendrimer-wrapped gold clusters: design rules for true single-molecule nanostructures. ACS Nano 6:3007
58. Gannon G, Larsson JA, Greer JC, Thompson D (2010) Molecular dynamics study of naturally occurring defects in self-assembled monolayer formation. ACS Nano 4:921
59. Vukovic L, Khatib FA, Drake SP, Madriaga A, Brandenburg KS, Kral P, Onyuksel H (2011) Structure and dynamics of highly PEG-ylated sterically stabilized micelles in aqueous media. J Am Chem Soc 133:13481 (For a recent example of computer simulations of highly PEG-ylated phospholipids in salt solutions)

Chapter 6
Microstructure Evolution of Copper in Nanoscale Interconnect Features

James Kelly, Christopher Parks, James Demarest, Juntao Li and Christopher Penny

6.1 Introduction

Ever since being implemented in manufacturing for the production of on-chip interconnect wiring in the late 1990s [1, 2], electrodeposition of copper has become a research topic of renewed technological importance. While the role of the various organic electrolyte additives commonly used in such processes has been a primary focus [3–8], the structure and recrystallization of the electrodeposited Cu have also attracted significant attention [9–21]. Since it is desirable to minimize interconnect resistance to improve overall system performance [1], much effort has been made to understand the various contributions to Cu line resistance and promote the full recrystallization of the electrodeposited Cu. These aspects become especially important as interconnect dimensions shrink to the nanoscale [22–26]. Josell et al. give a comprehensive review of much of this line resistance-related work [27].

Another important aspect of metal interconnect integration is electromigration performance. The microstructure of the Cu electrodeposited within the interconnection directly impacts its subsequent resistance to electromigration (EM); in general, a bamboo-like grain structure typically leads to good EM resistance [28, 29]. As interconnect dimensions shrink, relative line current densities and the number of atoms present at the interface increases, resulting in lower EM lifetimes. EM performance can be improved by incorporating an alloying element into the interconnect structure (e.g., Al and Mn have been described in some detail previously) [30, 31], or by using a metal capping layer (e.g, electrolessly deposited Co alloys) [32].

J. Kelly (✉) · J. Demarest · J. Li · C. Penny
IBM Research, Albany, NY 12203, USA
e-mail: mjklly@us.ibm.com

C. Parks
IBM Microelectronics, Hopewell Junction, NY 12533, USA

K. Kondo et al. (eds.), *Copper Electrodeposition for Nanofabrication of Electronics Devices*, Nanostructure Science and Technology 171, DOI: 10.1007/978-1-4614-9176-7_6,
© Springer Science+Business Media New York 2014

Although the efficacy of these approaches in extending EM lifetimes has been demonstrated, some complication is associated with each one; for the former, a resistivity penalty accompanies the EM improvement, while for the latter a new material and highly selective film deposition process step is required [32]. Promoting a bamboo, large-grained Cu interconnect structure by optimizing Cu microstructure is a straightforward way to improve reliability without the introduction of new materials and/or processes. In this chapter, we consider the microstructure evolution of Cu electrodeposited within Damascene features, along with the behavior of incorporated impurities.

6.2 Microstructure Evolution and Impurities in Nanoscale Interconnects

The challenge of attaining a stabilized microstructure for Cu electrodeposited in narrow interconnect lines is illustrated in Fig. 6.1. This figure, a version of which we have shown previously [33], has been updated with new data for 28-nm-wide metal lines. We characterize the extent of microstructure evolution in plated Cu interconnect features after planarization of the plated Cu overburden by chemical mechanical planarization (CMP) using a ratio of interconnect electrical resistances. The post-CMP, 8 h 350 °C anneal line resistance R is normalized with

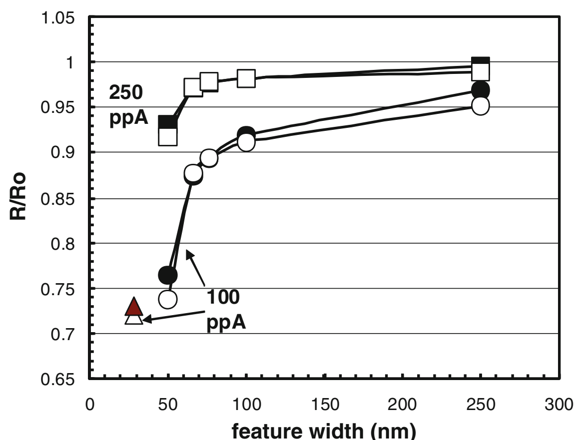

Fig. 6.1 Electrical resistance ratio R/R_o as a function of linewidth and post-plate anneal temperature for both "pure" and "doped" electrodeposited Cu (*hollow* and *solid points*, respectively). *Square symbols* indicate 250 °C post-plate anneal, while *circles* and *triangles* indicate 100 °C post-plate anneal. R/R_o values close to one suggest little post-CMP microstructure evolution takes place, while decreasing R/R_o values suggest increased post-CMP Cu microstructure refinement. (A portion of this figure reproduced with permission from [33]. Copyright 2012, The Electrochemical Society)

respect to the line resistance measured immediately after CMP, R_o. For R/R_o values that are close to one, we infer relatively little microstructure evolution takes place during the post-CMP 8 h 350 °C anneal, suggesting that the Cu microstructure is almost fully stabilized by the post-plate anneal process. A decreasing R/R_o ratio suggests the occurrence of more post-CMP microstructure evolution in the patterned Cu interconnect lines, i.e., the post-plate anneal process does not fully stabilize the Cu microstructure. The ratio R/R_o is shown as a function of linewidth for two chemistry types and two post-plate anneal temperatures. The chemistries have been described previously in [33]; one (a “doped” type) yields an electrodeposited Cu blanket film having total impurity levels (C, S, Cl, O) on the order of a few hundred ppm, while the other (a “pure” type) produces a Cu blanket film having a total impurity level <10 ppm.

Figure 6.1 clearly shows that as feature width decreases below about 100 nm, R/R_o values start to decrease, suggesting that the Cu in narrow lines is less stabilized than that in wider lines prior to CMP, particularly in the case of the 100 °C post-plate anneal (represented by circles in the plot). Chemistry type does not appear to strongly impact the R/R_o behavior; instead, the influence of linewidth and post-plate anneal temperature is much stronger. This is consistent with the finding that for narrow features, both chemistry types have similar impurity levels within the metal lines, as described previously [33]. The two 28 nm feature width data points represented by triangles do not seem to fall on the trend lines in the figure. This is not unexpected since a different patterning process and dielectric were employed in the fabrication of the 28-nm wide structures, leading to a somewhat different aspect ratio and profile for these smaller features. Consequently, these two data points do not represent a simple change in the feature width but a different overall geometry as compared to the wider lines. Apparently, geometric parameters other than the feature width (such as top opening and taper, aspect ratio, etc.) can influence the degree of microstructure evolution that occurs in the Cu interconnect.

The grain structure of Cu electrodeposited in various feature widths is qualitatively shown by a transmission electron microscopy (TEM) cross-section in Figs. 6.2 and 6.3, for samples having structures processed with both the “pure” and “doped” Cu chemistry, respectively. In these images, where the Cu overburden was left intact, the line structures are sectioned perpendicular to their length in order to view multiple feature widths in the same image. A room temperature anneal (over the course of several days) was experienced by the structures in both images. The coarse grain structure in the Cu overburden is clearly visible for both chemistry types, consistent with the high degree of recrystallization and grain growth expected for blanket electrodeposited Cu films [13–15]. It is possible that the “pure” Cu exhibits somewhat larger grains in the overburden with less microstructural detail visible within each as compared to the “doped” Cu. We did not attempt a detailed analysis. Although it might be expected that the chance of observing some finer grains within the wider Cu lines might be higher simply owing to their larger area, this does not appear to be the case. In fact, fine-grained regions are more evident within the narrow features (approximately 40 nm wide in

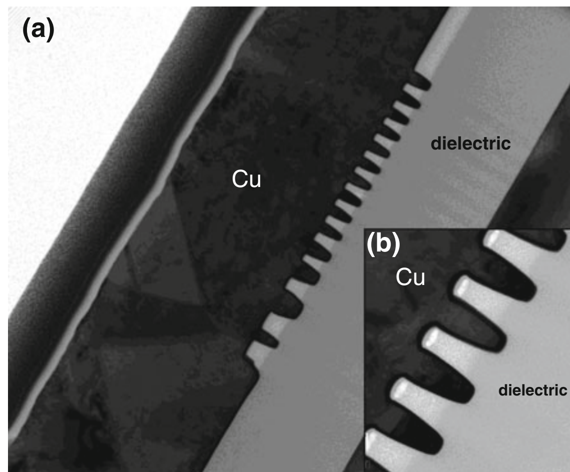

Fig. 6.2 **a** TEM micrograph of various linewidth features filled with electrodeposited Cu for a "pure" Cu chemistry with no post-plate anneal. The width of the *smallest patterned line* is approximately 40 nm. **b** higher magnification view of *narrow lines* in **a**. Large grains are evident in the overburden but less so within *narrow lines*

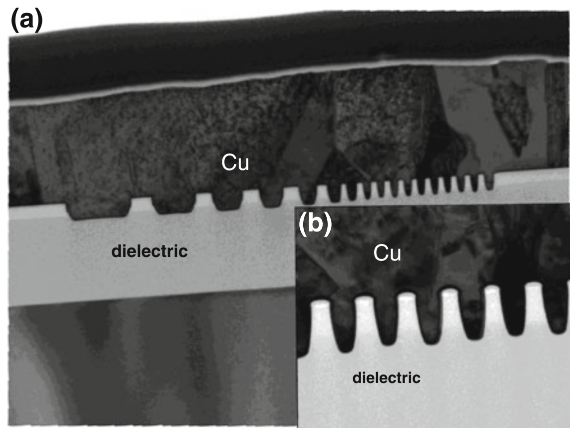

Fig. 6.3 **a** TEM micrograph of various linewidth features filled with electrodeposited Cu for a "doped" Cu chemistry with no post-plate anneal. The width of the *smallest patterned line* is approximately 40 nm, **b** higher magnification view of *narrow lines* in **a**. Large grains are evident in the overburden but less so within *narrow lines*

both figures, shown in higher magnification in the inset) as compared to the wider ones, for both chemistry types. This seems to be consistent with the line resistance behavior shown in Fig. 6.1, where stabilization of the Cu microstructure in wide lines is less difficult as compared to more narrow ones, and no strong difference with chemistry type was observed.

We have noted that Cu deposited in narrow features can exhibit higher levels of incorporated plating impurities, such as S and Cl, as compared to that found in wider features [33]. In wide lines, the electrodeposited Cu impurity content is governed by the choice of the additive chemistry and corresponds to that expected for a blanket film deposited from that chemistry (either "pure" or "doped"). This trend is shown in Fig. 6.4a, b for the case of Cu deposited in various linewidths from a "pure" chemistry. Secondary ion mass spectroscopy (SIMS) was used to

quantify the concentration of S and Cl for the Cu deposited within the patterned lines (experimental details are given in [33]. For the 40 nm line, the Cl signal increases substantially from that observed in the bulk overburden Cu, to a level on the order of a few hundred ppm. The S signal roughly tracks with the Cl signal and appears to be present at a somewhat lower concentration, on the order of tens of ppm for the 40-nm line. It should be noted that similarly high levels of impurities were found in narrow Cu lines when a "doped" chemistry was employed [33].

The incorporated S levels are consistent with those predicted by Moffat et al., based on experimentally measured accelerator consumption rates (the accelerator molecule contains S) [8, 34]. In this work, higher and lower accelerator consumption rates were observed for Cu electrodeposition at lower and higher overpotentials, respectively. Differences in local overpotential with feature width may be one way to interpret the observed incorporated S concentration dependency on line width. Another possible explanation is related to the fairly different time scales over which narrow and wider features are filled; it is likely that the dynamics of additive adsorption and incorporation into the electrodeposited Cu are simply quite different for a narrow feature (filled in a second or even less once the wafer is cathodically biased) and a wider feature (probably filled over a the course of several seconds or longer and likely under more quasi steady-state conditions).

A study of Cl incorporation in electrodeposited Cu by Hayase et al. employed SIMS to show relatively high Cl levels incorporated into the initially deposited Cu layers on a Pt substrate [35]. As they probed regions of the electrodeposited Cu farther from the Pt/Cu interface, measured Cl levels diminished, suggesting some Cl consumption during the growth of the Cu film (the incorporated Cl concentration was not quantified). Hebert developed a model for Cl incorporation based on this data to predict steady-state Cu deposition potential-current behavior for a bath having a suppressor and a range of Cl concentrations [36]. The increased Cl level observed for narrow lines in Fig. 6.4 is consistent with these data and model in that, for the initially deposited layers of Cu, the Cl at the interface has not yet been appreciably consumed, allowing for a high surface coverage of available Cl for incorporation within the Cu deposit. As narrow lines are filled more quickly than wide ones, a larger fraction of the Cu is deposited during this transient period of potentially high Cl surface coverage, possibly leading to higher incorporated Cl levels within narrow features.

One complication in attempting to experimentally determine nonmetallic impurity levels for Cu electrodeposited into patterned dielectric is the presence of the dielectric material itself. Since dielectrics typically used in industry may contain some C and O, it is not straightforward to determine the concentrations of these elements in Cu deposited in the patterned lines. This is the reason that S and Cl, which are not nominally present in the dielectric, are shown in Fig. 6.4. Nonetheless, the possibility of the presence of some S or Cl in the features as an unintentional impurity from some upstream patterning or clean process cannot be ruled out with absolute certainty. As a check on that possibility, features having only the Cu seed on the metal liner were analyzed with SIMS. Results from such samples are shown in Fig. 6.5 where 28 and 100 nm feature widths are considered.

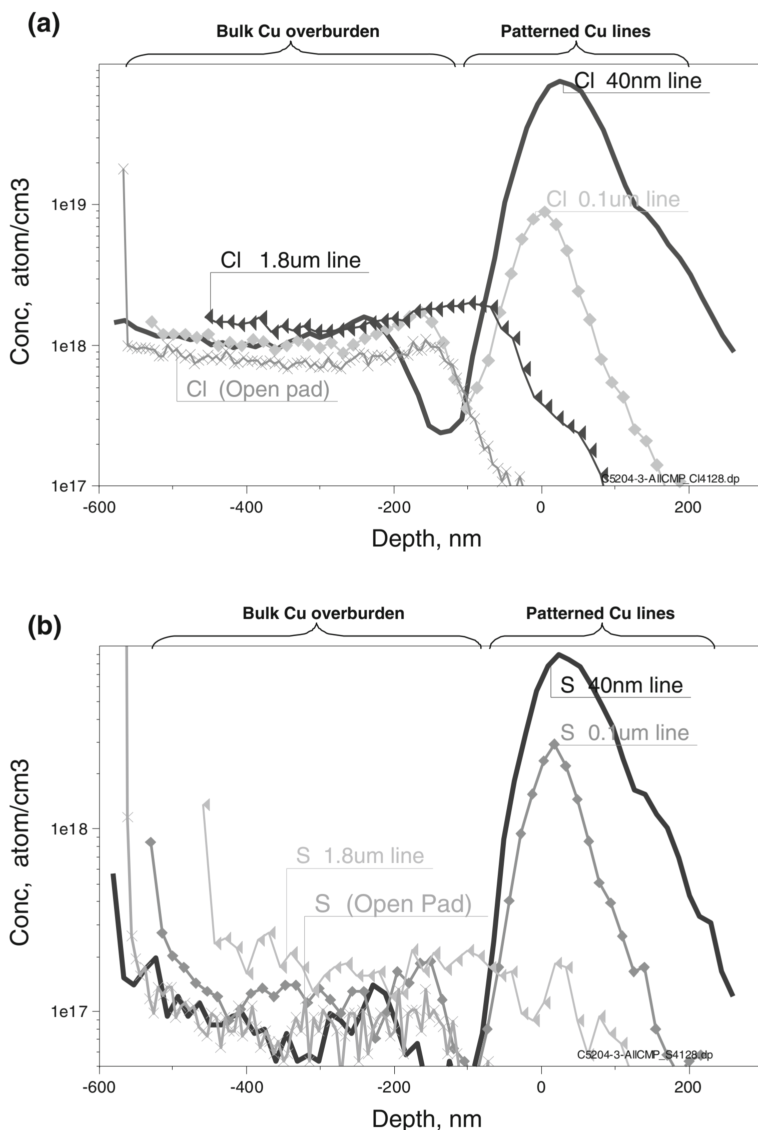

Fig. 6.4 **a** Concentration of Cl incorporated into electrodeposited Cu determined by SIMS for 40 nm, 0.1, and 1.8 μm linewidths as well as 200 μm *square open* pad, **b** same as (**a**) but for S. Both Cl and S increase as feature size decreases

Although some S and Cl are detected for the Cu seed-only sample, the levels are still much lower (~factor of 10 or more) compared to the concentrations measured in the most narrow features. From blanket wafer experiments, it is known that a certain quantity of S and Cl can be found on the PVD Cu seed

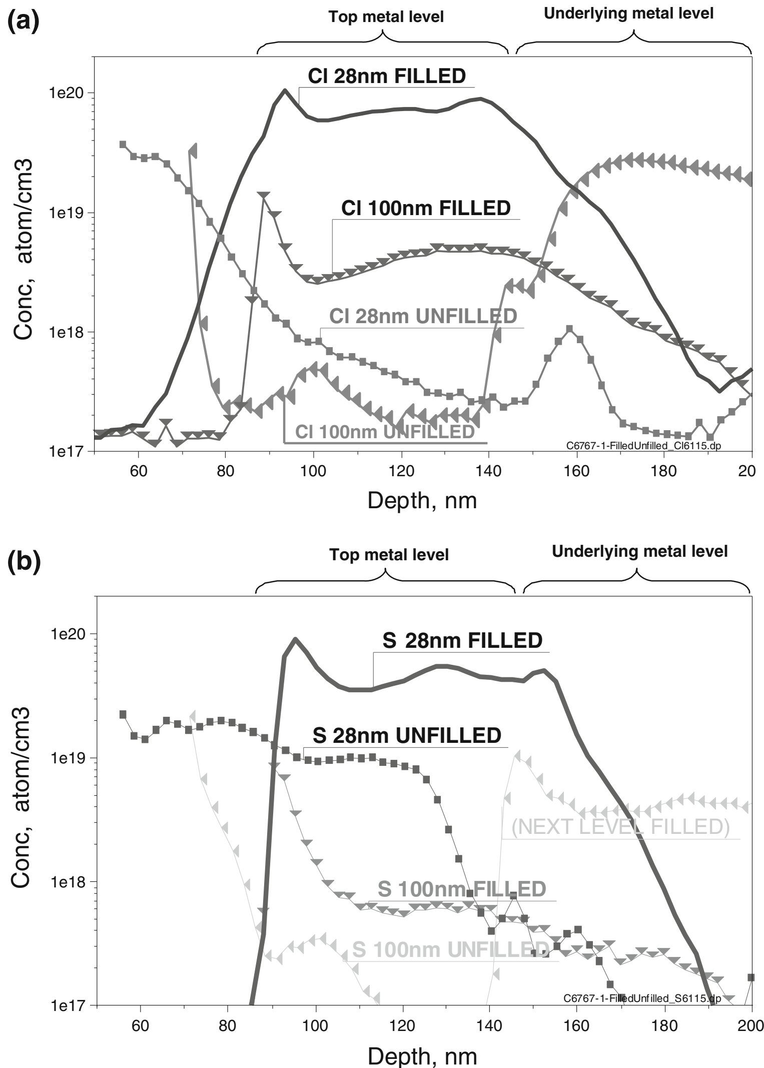

Fig. 6.5 **a** Comparison of measured Cl levels for Damascene lines, both unfilled (seed-only) and filled Cu, with linewidth as indicated. The Cl is higher for the filled samples for all linewidths, **b** same as (**a**) but for S. The low levels of S in widelines filled with plated Cu are similar to those measured for the seed-only sample. The S concentration measured in the filled *narrow lines* is higher than that measured for the seed-only sample. The underlying metal level is visible for the 100 nm but not 28 nm linewidth macro on the seed-only samples due to a difference in the *patterned line* orientation for the two macros

surface, likely due to the presence of surface contaminants. Though not shown here, our internal blanket wafer SIMS data suggest that this impurity layer adsorbed on the Cu seed is not significantly incorporated into the electroplated Cu.

This is presumably due to its dissolution/desorption upon exposure to the Cu electrolyte. It is likely that this contaminant layer contributes to some of the seed-only S and Cl signal seen in Fig. 6.5. We thus conclude the lower levels of S and Cl measured for wider lines (e.g., 0.1 micron and larger) may be impacted by background presence of these elements, but the high concentrations of S and Cl measured in narrow Cu interconnect lines is attributable to the electrodeposited Cu itself. It should also be noted that the impurity levels found in the filled 28-nm wide Cu line in Fig. 6.5 are somewhat higher than those found for the 40-nm wide Cu line, following the trend of increasing impurity incorporation for decreasing linewidth shown in Fig. 6.4.

6.3 Grain Structure in Nanoscale Interconnects

Cu grain structure is shown in Fig. 6.6 for a 40-nm wide interconnect line both before and after a post-CMP 8 h 350 °C anneal. In this case, the Cu was deposited from a "pure" Cu chemistry. The post-CMP microstructure shows a fair amount of defect detail within the Cu line. Grains are small and not clearly defined in some regions. After anneal, the grain structure is on average a little coarser compared to that of the pre-anneal case, though some small grains remain. Somewhat less

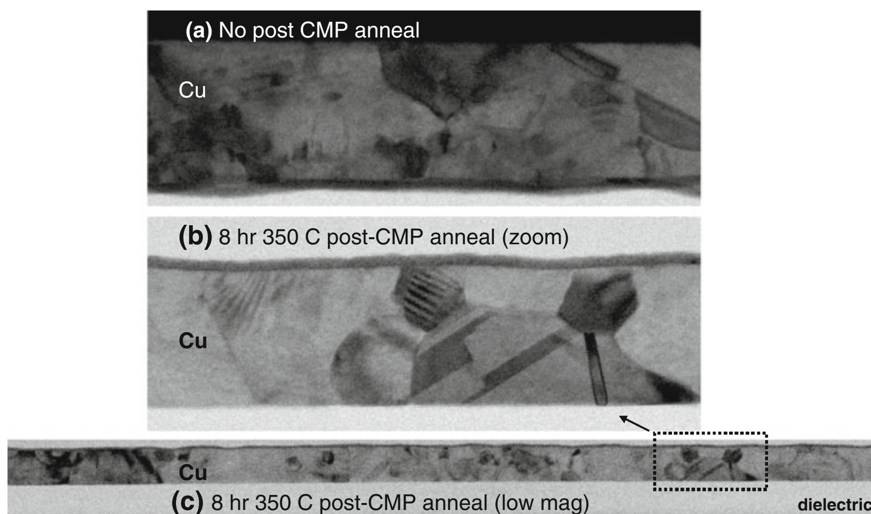

Fig. 6.6 **a** Longitudinal TEM micrograph of 40 nm wide line filled with Cu from a "pure" Cu chemistry (100 °C post-plate anneal, no post-CMP anneal). Many fine grains having much electron diffraction contrast are visible, **b** same as (**a**), but with 8 h 350 °C post-CMP anneal. A fair number of fine grains are still visible, but the interior grain electron diffraction contrast is greatly diminished compared to (**a**), **c** low magnification view of (**b**). (A portion of this figure reproduced with permission from [33]. Copyright 2012, The Electrochemical Society.)

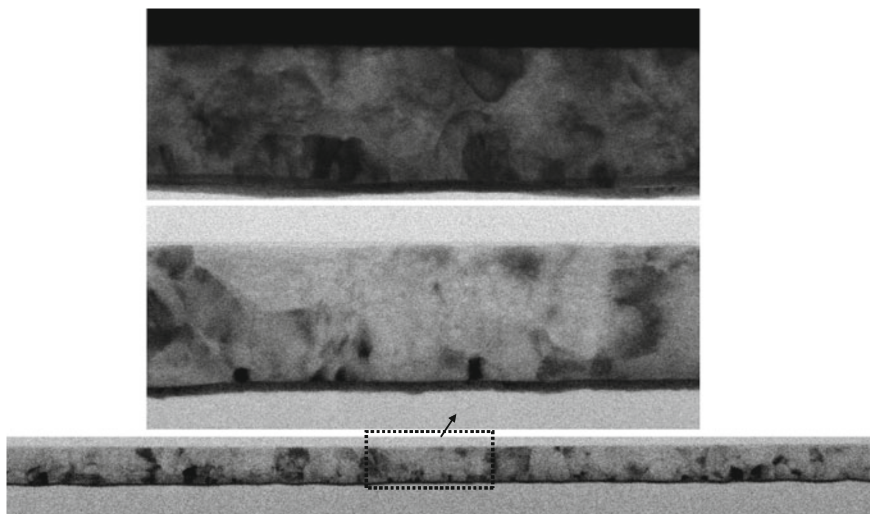

Fig. 6.7 **a** Longitudinal TEM micrograph of 40 nm wide line filled with Cu from a "doped" Cu chemistry (100 °C post-plate anneal, no post-CMP anneal). Many fine grains having much electron diffraction contrast are visible, **b** same as (**a**), but with 8 h 350 °C post-CMP anneal. As for the "pure" Cu chemistry, many fine grains are still visible after the high temperature anneal, but the electron diffraction contrast within each grain is much more uniform post-anneal. **c** low magnification view of (**b**). (A portion of this figure reproduced with permission from [33]. Copyright 2012, The Electrochemical Society.)

contrast is evident within each grain as compared to pre-anneal. Figure 6.7 shows a similar set of images for Cu deposited from a "doped" chemistry. The grain structure evolution with anneal roughly parallels that observed in Fig. 6.6, with the post-anneal structure appearing somewhat coarser. Given the degree of microstructure evolution suggested by line resistance change with annealing in Fig. 6.1, it is somewhat surprising that the change in Cu grain size is not more significant than observed. As is the case for the behavior shown in Fig. 6.1, the type of plating chemistry does not seem to significantly influence the observed Cu microstructure in narrow lines.

In Figs. 6.8 and 6.9, Cu grain structure is shown before and after a post-CMP 8 h 350 °C anneal for 80- and 120-nm wide Cu lines, respectively (for these figures, only Cu from a "doped" chemistry are shown). Since the lines are much wider and the degree of post-CMP microstructure evolution inferred by resistance change in Fig. 6.1 is much less compared to the 40 nm lines, it might be expected that the grains would have already coarsened somewhat immediately after CMP, with little additional change upon further annealing; but this is not observed in the TEM micrographs in Figs. 6.8 and 6.9. Instead, a number of small grains are evident in the post-CMP sections of both the 80 and even 120-nm wide lines. A fair degree of contrast variation is visible within each grain. This contrast variation is related to some physical feature that impacts the diffraction of

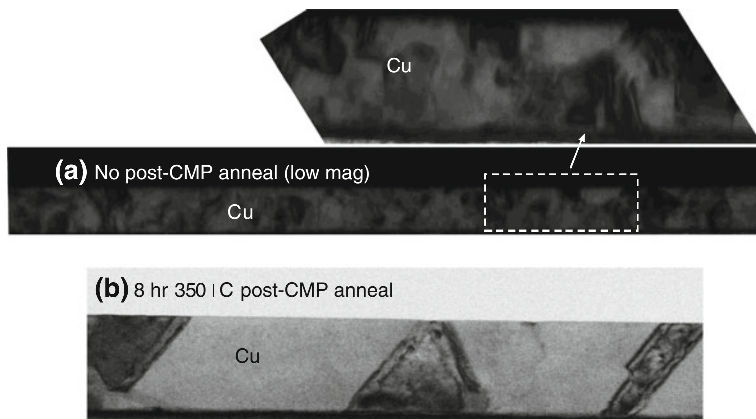

Fig. 6.8 **a** Longitudinal TEM micrograph of 80 nm wide line filled with Cu from a "doped" Cu chemistry (100 °C post-plate anneal, no post-CMP anneal). Many fine grains having much electron diffraction contrast are visible, **b** same as (**a**), but with 8 h 350 °C post-CMP anneal. Contrary to 40 nm wide line behavior, much grain growth along with a reduction of interior grain electron diffraction contrast is observed post-anneal

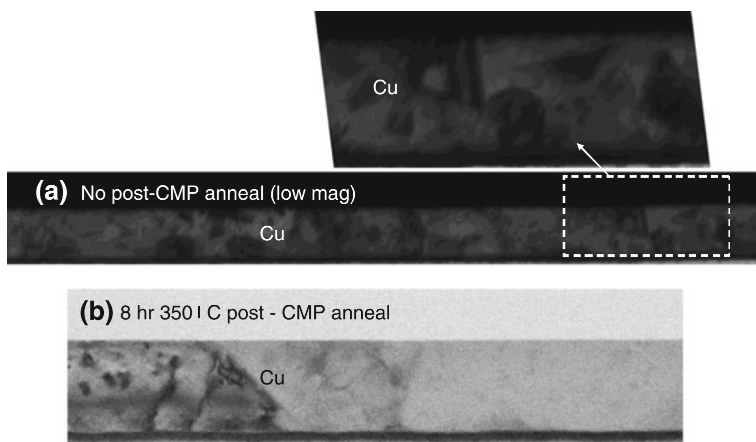

Fig. 6.9 **a** Longitudinal TEM micrograph of 120 nm wide line filled with Cu from a "doped" Cu chemistry (100 °C post-plate anneal, no post-CMP anneal). Even for this wider line, the grain size is fairly small with much electron diffraction contrast apparent, **b** same as (**a**), but with 8 h 350 °C post-CMP anneal. Similar to the 80 nm wide lines, much grain growth along with a reduction of interior grain electron diffraction contrast is observed post-anneal (the area shown in (**b**) has some visible features, but a large fraction of the TEM sample had little to no observable electron diffraction contrast within the line)

electrons as they interact with the sample composed predominantly of the Cu lattice, such as crystalline point and line defects, or strain, which could be relieved with higher temperature annealing due to thermally activated atomic movement

[37]. After anneal, both the 80 and 120-nm wide line microstructures undergo a transition to a very coarse grain structure. The pre-anneal microstructural detail visible in the grain interiors is greatly diminished.

Our results are consistent with those reported previously where trench width influenced the attainable grain size [16, 19, 29]. One recent study concluded differently, reporting that Cu grain growth was not limited by line geometry for linewidths between 25 and 45 nm based on top-down electron backscatter diffraction (EBSD) imaging [26]. As the grain structure may vary significantly through the depth of the Cu interconnect as shown in Figs. 6.6 and 6.7 as well as refs. [16, 19, 29], it is probable that finer grains within narrow lines may not be detected by topdown techniques like EBSD, especially for those at the trench bottom. The results in Figs. 6.7, 6.8, 6.9 are somewhat counterintuitive in that they suggest fairly large line resistance changes can occur with only relatively modest changes in grain size (observed for narrow lines), while a significant degree of grain growth may occur with relatively little change in line resistance (as is the case for wider lines). Since grain growth does not appear to easily explain the behavior of narrow lines in Fig. 6.1, the Cu interconnect impurity distribution response to annealing was studied in the next section.

6.4 Impurity Movement within Nanoscale Interconnects

The impact of the high temperature anneal described above on the S and Cl impurity distribution is shown in Figs. 6.10 and 6.11 for 40 nm and 1.8 micron wide lines, respectively. The Cu was deposited from a "doped" Cu chemistry in order to introduce impurities into the wide features. In the case of the 40 nm lines, annealing has little influence on the distribution of S and Cl within the Cu, while in the wide lines it appears to lower observed S and Cl levels toward the middle of the trench depth. Although not apparent in Fig. 6.11, based on work using other samples with a variety of wide lines and higher depth resolutions, we believe that upon annealing these dopants are moving toward the dielectric capping material deposited on top of the Cu line (the increased impurity levels at the very top of the patterned lines is sometimes difficult to capture for depth resolutions that allow for practical analysis, especially if the S and Cl are highly localized in a very thin layer). Impurity segregation data for 0.1 micron wide lines, similar to the dimensions for the lines considered in Figs. 6.8 and 6.9, are qualitatively similar to the behavior shown in Fig. 6.11 for the 1.8 micron wide line, but somewhat less pronounced.

The vertical movement of S and Cl in wider lines for higher anneal temperatures in this study is consistent with previous work where blanket electrodeposited Cu films were considered. Brongersma et al. studied the movement of impurities as a function of annealing temperature in plated Cu, noting that carbon was detected on the film surface starting at about 80 °C, with the signal vanishing before 150 °C was attained [14]. Sulfur, in contrast, did not start to be detected until 150 °C, with

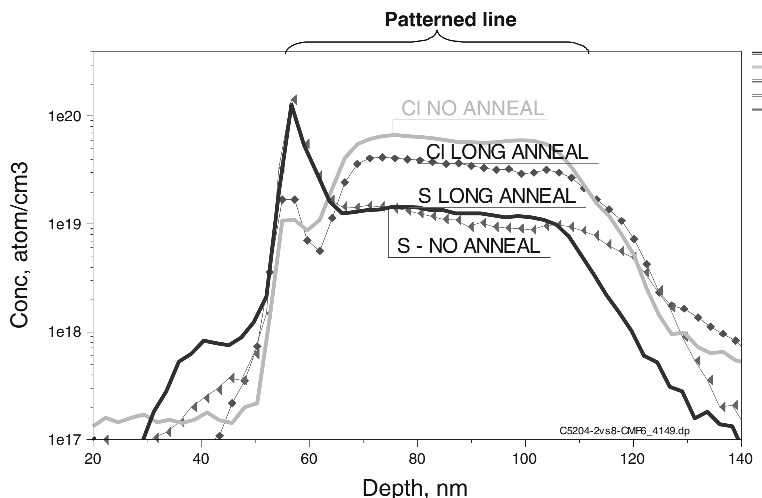

Fig. 6.10 Concentration of S and Cl within 40 nm wide Cu lines *with* and *without* 8 h 350 °C post-CMP anneal (Cu deposited from "doped" Cu chemistry, post-plate anneal temperature of 100 °C). Very little movement of the S and Cl is observed with anneal

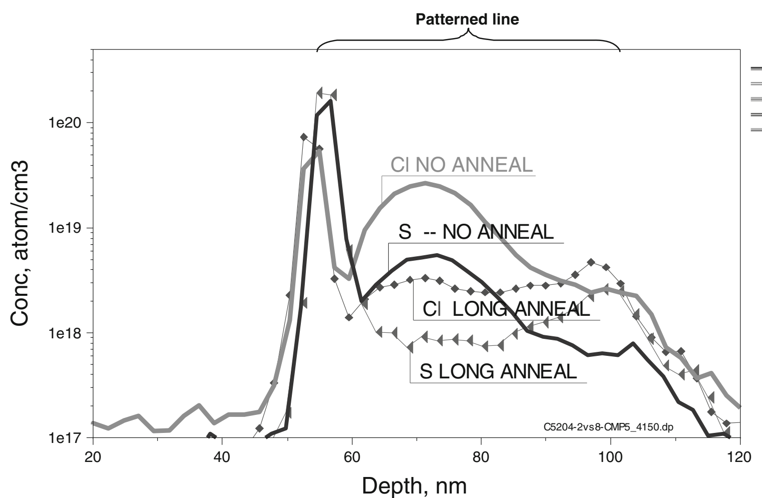

Fig. 6.11 Concentration of S and Cl within 1.8 micron wide Cu lines with and without 8 h 350 °C post-CMP anneal (Cu deposited from "doped" Cu chemistry, post-plate anneal temperature of 100 °C). The S and Cl levels in the *middle of trench* depth decrease significantly with annealing

an increase in signal occurring as the temperature was ramped to 400 °C; the movement of S with these higher anneal temperatures was accompanied by additional film grain growth as was observed in this study. Liu et al. using

somewhat lower annealing temperatures (<220 °C), found similar results, detecting C and O migration out of the electrodeposited Cu but no S or Cl movement at these temperatures [17]. It appears that the large degree of grain growth observed for wider lines at higher anneal temperatures is correlated with a redistribution of the S and Cl impurities within the Cu (Yoon et al. observed a similar effect for blanket plated Cu films) [13].

The 40-nm wide Cu lines considered in this study, which exhibit a lesser degree of grain growth with a high temperature anneal, also show little to no corresponding impurity movement. This seems to be consistent with the literature in that little impurity redistribution would be expected in the absence of significant grain growth; both the ability to migrate S and Cl out of the narrow lines and promote significant grain growth appear to be limited by the narrow feature geometry. However, we infer that some sort of physical change occurs within the narrow Cu lines when anneal at high temperature based on the behavior shown in Fig. 6.1. Brongersma et al. considered the reflectance of blanket plated Cu films as a function of temperature, noting a significant change occurring at about 350 °C that persisted upon cooling the sample down [14]. They also reported measuring large amounts of hydrogen leaving the Cu film at elevated temperatures (details were not given) employing a residual gas analyzer in a low-energy ion scattering experimental setup. It was postulated that hydrogen desorption in the sample was responsible for the reflectance change, presumably as it would eliminate contaminants adsorbed on the Cu surface. This is consistent with thermal desorption measurements made by Fukai et al., who found significant hydrogen escaping from electrodeposited Cu starting at about 300–350 °C [38]. They interpreted their data as evidence of the presence of lattice vacancy-hydrogen clusters in the electrodeposited Cu, with the sharpness of the desorption peak suggesting H atom-Cu vacancy pairing. Positron annihilation experiments also suggest a decrease in concentration of vacancy clusters starting at about 300 °C for electroplated Cu [39].

The elimination of such point defects at higher annealing temperatures could be one explanation for the high temperature resistance changes observed in narrow Cu interconnect lines. It would not easily explain why wide lines behave differently than narrow ones as shown in Fig. 6.1, since the high temperature anneal ought to eliminate vacancy defects in these features too. One possibility that would explain this apparent discrepancy would simply be a higher concentration of vacancy defects for narrow lines. While we have no experimental evidence for a higher concentration of lattice defects in narrow lines, the fact that they contain higher amounts of S and Cl (even for Cu deposited from a “pure” chemistry) compared to wide lines suggests something fundamentally different in the manner in which narrow and wide features are filled. Certainly, the difference in time scales over which Cu fill occurs for the two feature sizes would imply more of a transient, non-steady-state situation for narrow lines, while wider ones would be mostly filled after the initial adsorption of the additive molecules. It could be

argued that such a difference in the Cu fill process for narrow and wide lines would lead to a tendency for narrow lines to contain more lattice defects.

Another possible explanation for the difference in narrow and wide line resistance behavior could be the relative importance of grain boundary resistance with linewidth. Recent work has shown that high-angle, random grain boundaries in electroplated Cu scatter electrons much more strongly compared to ones exhibiting more structural symmetry across the boundary (known as “coincidence” grain boundaries) [40, 41]. As the grain boundary resistance contribution to overall line resistance is relatively more significant for narrow lines [27], a restructuring of the Cu lattice near the grain boundary at higher anneal temperatures would be more easily observed in narrow line electrical resistance, explaining the behavior shown in Fig. 6.1. The idea of grain boundary restructuring by a recovery process at higher anneal temperatures seems consistent with Figs. 6.6, 6.7, where some subtle microstructure evolution but limited grain growth was observed for annealed narrow Cu lines. Recovery processes (traditionally considered in metals having a high number of lattice defects induced by cold working) have been explained by the elimination of defects in a crystal lattice at relatively low temperatures, preceding recrystallization and grain growth [42–44]. This type of mechanism appears consistent with resistance changes observed in narrow Cu interconnects in this study, except that it is occurring at temperatures that would typically suffice to promote significant recrystallization and grain growth in a bulk material. It seems that though physical mechanisms by which the Cu interconnect crystal quality may be improved are limited at narrow dimensions, they are sufficient to induce appreciable resistance changes for nanoscale features.

6.5 Conclusions

The evolution of Cu microstructure and incorporated impurities was studied using TEM, SIMS, and electrical resistance measurements for Damascene features. As feature width drops below 100 nm, resistance measurements suggest an increasing degree of post-CMP microstructure evolution with anneal for Cu deposited from both “doped” and “pure” Cu plating chemistries. While little to no post-anneal grain growth and impurity movement occurs for narrow Cu lines, some subtle post-anneal microstructure evolution is visible. Post-anneal resistance changes in narrow features are consistent with recovery of the Cu lattice via elimination of crystal defects without significant grain growth.

Acknowledgments This work was performed by the Research Alliance Teams at various IBM Research and Development Facilities. We are grateful to Dan Edelstein of IBM for critically reviewing the original manuscript. We also acknowledge useful discussions with Dr. Dan Josell of NIST.

References

1. Edelstein D, Heidenreich J, Goldblatt R, Cote W, Uzoh C, Lustig N, Roper P, McDevitt T, Motsiff W, Simon A, Dukovic J, Wachnik J, Rathore H, Schulz R, Su L, Luce S, Slattery J (1997) Full copper wiring in a sub-0.25 mm cmos ulsi technology. In: Technical digest, IEEE international electron devices meeting, pp 773–776
2. Andricacos PC, Uzoh C, Duckovic JO, Horkans J, Deligianni H (1998) Damascene copper electroplating for chip interconnections. IBM J Res Dev 42(5):567
3. West AC, Mayer S, Reid J (2001) A superfilling model that predicts bump formation. Electrochem Solid State lett 4(7):C50
4. Moffat TP, Wheeler D, Huber WH, Josell D (2001) Superconformal electrodeposition of copper. Electrochem Solid State Lett 4(4):C26
5. Vivian Feng Z, Li X, Gewirth AA (2003) Inhibition due to the interaction of polyethylene glycol, chloride, and copper in plating baths: a surface-enhanced Raman study. J Phys Chem B 107:9415
6. Akolkar R, Landau U (2004) A time-dependent transport-kinetics model for additive interactions in copper interconnect metallization. J Electrochem Soc 151(11):C702
7. Vereecken PM, Binstead RA, Deligianni H, Andricacos PC (2005) The chemistry of additives in damascene copper plating. IBM J Res Dev 49(1):3
8. Moffat TP, Wheeler D, Edelstein MD, Josell D (2005) Superconformal film growth: mechanism and quantification. IBM J Res Dev 49(1):19
9. Harper JME, Cabral C Jr, Andricacos PC, Gignac L, Noyan IC, Rodbell KP, Hu CK (1999) Mechanisms for microstructure evolution in electroplated copper thin films near room temperature. J Appl Phys 86(5):2516
10. Ueno K, Ritzdorf T, Grace S (1999) Seed layer dependence of room-temperature recrystallization in electroplated copper films. J Appl Phys 86(9):4930
11. Hau-Riege SP, Thompson CV (2000) In situ transmission electron microscope studies of abnormal grain growth in electroplated copper films. Appl Phys Lett 76(3):309
12. Field DP, Dornisch D, Tong HH (2001) Investigating the microstructure-reliability relationship in cu damascene lines. Scripta Mater 45:1069
13. Yoon MS, Park YJ, Joo YC (2002) Impurity redistributions in electroplated Cu films during self-annealing. Thin Solid Films 408:230–235
14. Brongersma SH, Kerr E, Vervoort I, Saerens A, Maex K (2002) Grain growth, stress, and impurities in electroplated Cu. J Mater Res 17(3):582
15. Lee H, Wong SS, Dopatin SD (2003) Correlation of stress and texture evolution during self- and thermal annealing of electroplated Cu films. J Appl Phys 93(7):3796
16. Wu W, Ernur D, Brongersma SH, Van Hove M, Maex K (2004) Grain growth in copper interconnect lines. Microelectron Eng 76:190
17. Liu C-W, Wang Y-L, Tsai M-S, Feng H-P, Chang S-C, Hwang G-J (2005) Effect of plating current density and annealing on impurities in electroplated Cu film. J Vac Sci Technol A 23(4):658
18. Stangl M, Acker J, Dittel V, Gruner W, Hoffmann V, Wetzig K (2005) Characterization of electroplated copper self-annealing with investigations focused on incorporated impurities. Microelectron Eng 82:189
19. Zhang W, Brongersma SH, Heylen N, Beyer G, Vandervorst W, Maex K (2005) Geometry effect on impurity incorporation and grain growth in narrow copper lines. J Electrochem Soc 152(12):C832
20. Zhang W, Brogersma SH, Conard T, Wu W, Van Hove M, Vandervorst W, Maex K (2005) Impurity incorporation during copper electrodeposition in the curvature-enhanced accelerator coverage regime. Electrochem Solid-State Lett 8(7):C95
21. Stangl M, Acker J, Oswald S, Uhlemann M, Gemming T, Baunack S, Wetzig K (2007) Incorporation of sulfur, chlorine, and carbon into electroplated Cu thin films. Microelectron Eng 84:54

22. Steinlesberger G, Engelhardt M, Schindler G, Steinhoegl W, Von Glasow A, Mosig K, Bertagnolli E (2002) Electrical assessment of copper damascene interconnects down to sub-50 nm feature sizes. Microelectron Eng 64:409
23. Steinhoegl W, Schindler G, Steinlesberger G, Engelhardt M (2002) Size-dependent resistivity of metallic wires in the mesoscopic range. Phys Rev B 66:075414
24. Schindler G, Steinlesberger G, Engelhardt M, Steinhoegl W (2003) Electrical characterization of copper interconnects with end-of-roadmap feature sizes. Solid-State Electron 47:1233
25. Zhang W, Brongersma SH, Li Z, Li D, Richard O, Maex K (2007) Analysis of the size effect in electroplated fine wires and a realistic assessment to model copper resistivity. J Appl Phys 101:063703
26. Graham RL, Alers GB, Mountsier T, Shamma N, Dhuey S, Cabrini S, Geiss RH, Read DT, Peddeti S (2010) Resistivity dominated by surface scattering in sub-50 nm cu wires. Appl Phys Lett 96:042116
27. Josell D, Brongersma SH, Tokei Z (2009) Size-dependent resistivity in nanoscale interconnects. Annu Rev Mater Res 39:231
28. Li B, Sullivan TD, Lee TC, Badami D (2004) Reliability challenges for copper interconnects. Microelectron Reliab 44:365
29. Hu CK, Gignac L, Baker B et al (2007) Impact of Cu microstructure on electromigration reliability. In: International interconnect technology conference, p 93
30. Nogami T et al (2010) High reliability 32 nm Cu/ULK BEOL based on PVD CuMn seed and its extendibility. In: IEDM, pp 33.5.1–33.5.4
31. Maekawa K, Mori K, Suzumura N, Honda K, Hirose Y, Asai K, Uedono A, Kojima M (2008) Impact of Al in Cu alloy interconnects on electro and stress migration reliabilities. Microelectron Eng 85(10):2137
32. Yokogawa S, Kikuta K, Tsuchiya H, Takewaki T, Suzuki M, Toyoshima H, Kakuhara Y, Kawahara N, Usami T, Ohto K, Fujii K, Tsuchiya Y, Arita K, Motoyama K, Tohara M, Taijii T, Kurokawa T, Sekine M (2008) Tradeoff characteristics between resistivity and reliability for scaled-down cu-based interconnects. IEEE Trans Electron Devices 55(1):350
33. Kelly J, Nogami T, van der Straten O, Demarest J, Li J, Penny C, Vo T, Parks C, DeHaven P, Hu CK, Liniger E (2012) Electrolyte additive chemistry and feature size-dependent impurity incorporation for Cu interconnects. J Electrochem Soc 159(10):D563
34. Moffat TP, Wheeler D, Josell D (2004) Electrodeposition of copper in the SPS -PEG-Cl additive system. I. Kinetic measurements: influence of SPS. J Electrochem Soc 151:C262
35. Hayase M, Taketani M, Aizawa K, Hatsuzawa T, Hayabusa K (2002) Copper bottom-up deposition by breakdown of PEG-Cl inhibition. Electrochem Solid-State Lett 5(10):C98
36. Hebert KR (2005) Role of chloride ions in suppression of copper electrodeposition by polyethylene glycol. J Electrochem Soc 152(5):C283
37. Hirsch PB (1997) Electron microscopy of thin crystals. R. E. Krieger Pub Co, USA
38. Fukai Y, Mizutani M, Yokota S, Kanazawa M, Miura Y, Watanabe T (2003) Superabundant vacancy-hydrogen clusters in electrodeposited Ni and Cu. J Alloy Compd 356–357:270
39. Uedono A, Suzuki T, Nakamura T (2004) Vacancy-type defects in electroplated Cu films probed by using a monoenergetic positron beam. J Appl Phys 95:913
40. Kitaoka Y, Tono T, Yoshimoto S, Hirahara T, Hasegawa S, Ohba T (2009) Direct detection of grain boundary scattering in damascene Cu wires by nanoscale four-point probe resistance measurements. Appl Phys Lett 95:052110
41. Kim TH, Zhang XG, Nicholson DM, Evans BM, Kulkarni NS, Radhakrishnan B, Kenik EA, Li A-P (2010) Large discrete resistance jump at grain boundary in copper nanowire. Nanoletters 10(8):3096
42. Reed-Hill RE, Abbaschian R (1994) Physical metallurgy principles, 3rd edn. PWS Publishing Company, USA
43. Humphreys FJ, Hatherly M (2004) Recrystallization and related annealing phenomena. Elsevier Ltd, The Netherlands
44. Cullity BD (1978) Elements of X-ray diffraction, 2nd edn. Addison Wesley Publishing Co, USA

Chapter 7
Direct Copper Plating

Aleksandar Radisic and Philippe M. Vereecken

7.1 Introduction

Direct plating is the term used in the damascene interconnect technology when copper (Cu) is plated on a substrate without a copper seed. The conductive copper seed is replaced by a nobler metal such as ruthenium (Ru) or metal compounds such as RuTa or RuTiN alloys in an effort to combine seed and barrier properties into one as the lining thin film material [1]. Copper electrodeposition on top of a foreign substrate by itself is of course not that unusual, copper plated on a platinum rotating disk electrode is quite standard in the lab, but there are many technological complications when bringing it to the wafer scale. In contrast to the conductive platinum disk in the lab, the thin barrier and seed lining layers are resistive which implies a significant potential drop from the wafer edge to the wafer center. The fact that the cost scaling trends demand for denser packing of transistors (i.e., smaller features with thinner lining) and larger wafer size (currently 300 and going to 450 mm soon), only worsens this so-called *terminal effect*. Of course, this is true for both thin copper seed plating and direct plating, and both will be discussed in Sect. 7.4.

Copper electrodeposition on foreign substrates proceeds through an electrochemical nucleation and growth process. This has serious implications for the copper damascene plating process as a continuous copper thin film needs to be formed before the inlaid trench and blind hole features start to fill up with copper [2]. Hence, the coalescence thickness needs to be at least 1/3 of the effectively open feature size. This means that higher island densities will be required for each generation of feature scaling or node. This obviously sets limits to the extendibility of the direct plating process. The nucleation island density is a function of the

A. Radisic · P. M. Vereecken (✉)
IMEC, Kapeldreef 75, B-3001 Leuven, Belgium
e-mail: vereeck@imec.be

K. Kondo et al. (eds.), *Copper Electrodeposition for Nanofabrication of Electronics Devices*, Nanostructure Science and Technology 171, DOI: 10.1007/978-1-4614-9176-7_7,

© Springer Science+Business Media New York 2014

overpotential and substrate. The growth and thus shape of the islands is affected by the bath additives and by the condition of the substrate surface. Nucleation and growth phenomena will be extensively treated in Sect. 7.3.

The real challenge of direct plating, however, lays in the combination of the terminal effect and the nucleation and growth of copper into a coalesced or closed film; i.e., to make it work all over the wafer. As the substrate potential and thus overpotential changes with wafer radius, also the nucleation island density is dependent on wafer radius. Fortunately, a more severe terminal effect and thus a sharper potential drop helps the direct plating process as the nucleation is confined within a small ring area on the wafer only. Indeed, the sheet resistance of the thin barrier and non-copper seed lining combo (typically $> 50\ \Omega$/sq) is such that a high enough overpotential for copper nucleation and growth only exists in the direct proximity of the terminal (~ 1 cm). As soon as the islands in that area coalesce together, the in situ formed seed takes the role of conductive copper film and the terminal is effectively moved closer the wafer center. As such, a copper ring with a nucleation front sweeps over the surface from the wafer edge to wafer center. Importantly, as the effective area for copper electrodeposition is changing over time also the current needs to be adjusted accordingly in order to keep the current density constant. The implications of the time-dependent wafer coverage are discussed in Sect. 7.4.3.

The foremost purpose of damascene plating is to fill up the inlaid trench and blind hole features to fabricate the copper lines and vias in the back-end of line (BEOL) dielectric stack which make up the metal interconnect network on the chip. Acid cupric sulfate electrolytes with a combination of inorganic and organic additives provide subconformal or so-called superfilling of the copper for void-free fill of the trench and via features. In conventional copper plating with copper seed, the additives can interact with the copper seed as soon as the wafer is immersed and the plating continues from the "seed" which is already present [3]. In the case of direct copper plating, we need to make a distinction between one-step and two-step copper plating to fill the features with copper in the absence of a copper seed. When a thin conformal copper seed is plated on the barrier/non-copper lining from one specific bath and subsequently the wafer is plated in the conventional way from the acid cupric sulfate bath with additives for filling the features, we will use the term "*wet seed plating*" to indicate this first step [4]. When the plating is done in one step; i.e., in situ formation of the seed and fill of the features from the same acid bath, we will use the term "*direct plating.*" In the case of wet seed plating the bath needs to only provide high nucleation island density to assure low enough coalescence film thickness and typically an alkaline bath with low copper content is used (bath with large polarization resistance). In the case of direct plating the bath must provide low coalescence thickness (in situ seed) and fill of the features. Fortunately, the PEG-like suppressor additives required for subconformal feature fill also provide enhanced nucleation island density and thus thin coalescence thickness (Sect. 7.4.4.2). Focus of this chapter is on the direct plating process. The limits of wet seed plating will be discussed at the end of Sect. 7.4.2.

7.2 Direct Plating Interconnect Technology and Requirements

7.2.1 Current Copper Interconnect Technology

In the early 1990s, IBM began developing integrated circuit technology with copper interconnects [3]. Copper had lower resistivity and higher maximum current density for electromigration than aluminum; properties that were critical for improved device performance and reliability. By the end of the decade IBM produced and shipped hundreds of thousands of 6-level "copper-chip" modules. Copper interconnects were fabricated using electrodeposition, primarily due to its ability to fill high aspect ratio features with complex geometries at high deposition rates, leading to high throughput and lower manufacturing costs. Important processing steps prior to electroplating involved the deposition of a thin diffusion barrier layer, to prevent copper diffusion into silicon, and the deposition of a copper seed layer by means of physical vapor deposition (PVD) (Fig. 7.1) [3]. This PVD copper seed layer provided electrical contact and improved adhesion to the diffusion barrier layer. Once coated with PVD diffusion barrier and Cu seed layer, wafers were loaded in electrochemical cell filled with acidic Cu-sulfate bath containing proprietary organic additives. It is mainly thanks to these additives that, after applying a given current waveform, different plating rates at the bottom and top of the feature ensue, and with Cu deposition rate at the bottom being higher, void-free fill of complex features is achieved.

Ever since the 1990s, we are testing the limits of this technology by continuously reducing the size of building blocks of the integrated circuits. Every time we decrease the feature size, the number of challenges in fabricating defect-free copper interconnects increases. For example, PVD techniques typically provide nonuniform coverage along the sidewalls of a trench or a via. With trenches and vias getting narrower, PVD Cu seed must be thinner, too, in order to prevent the pinch-off at the top, and allow enough volume for Cu plating. For certain feature size and aspect ratio, this will result in incomplete PVD Cu seed coverage. After all PVD hardware and deposition tricks are exhausted, and discontinuity in the Cu seed layer persists, we can still 'repair' it by electrochemically depositing Cu from

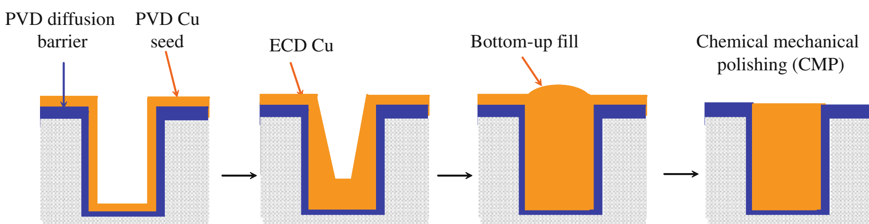

Fig. 7.1 Current copper interconnect technology

specially designed alkaline plating baths. However, Cu alkaline plating baths have limited use due to the fact that they do not have superfilling or true bottom-up Cu fill capability. Thus, we have introduced an additional step in the process, requiring additional plating cell in our plating tool, quality control instruments, etc. In addition, such a continuous thin Cu seed does not guarantee defect-free plating from a typical acidic Cu bath, since its resistivity causes initially highly nonuniform current distribution across the wafer, and possible corrosion issues in the wafer center. Anticipating these and other future challenges, researchers have started looking for alternative solutions long before the end of the twentieth century.

7.2.2 Alternative Pathways: Challenges

Deposition techniques such as chemical vapor deposition (CVD) or atomic layer deposition (ALD) typically provide smooth thin films with better conformality than PVD. Since that is not the case with Cu, once the PVD Cu seed fails to meet the processing requirements, an alternative is to electrodeposit Cu directly on the diffusion barrier or some alternative seed layer. However, it is not a priori clear which growth mode will Cu films deposited on alternative barrier/seed layers follow, and whether it will be possible to achieve the "superfilling" effects without the PVD Cu seed layer. The mode of growth of copper on a foreign substrate is dependent on the interaction energy between the adsorbed copper atom and the substrate, and the difference in interatomic spacing between the bulk copper and the substrate. In general, three different growth modes [5] can be identified (Fig. 7.2): layer by layer (Frank–van der Merwe growth), 3D island formation (Volmer-Weber growth), and 2D layer deposition followed by the growth of 3D islands (Stranski–Krastanov growth). In many cases, deposition of copper onto foreign substrates follows a 3D island growth mechanism [6, 7]. For such systems, the structure and properties of Cu films are critically dependent on the mechanism

Fig. 7.2 Thin film growth

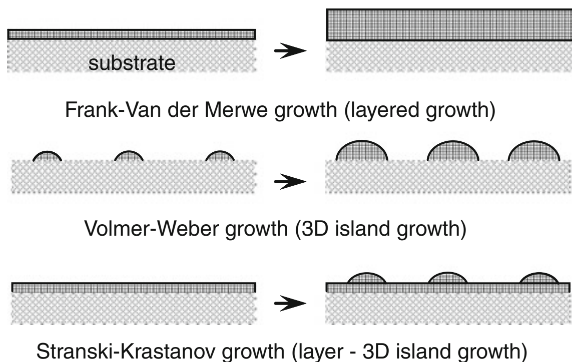

of nucleation and growth of islands. For example, let us consider a hypothetical system in which square array of identical hemispherical islands is instantaneously nucleated and growing on a foreign substrate. A critical diameter at which islands start coalescing, $d_{critical}$, is inversely proportional to the square root of the island density, $d_{critical} = (N_0)^{-0.5}$. From Fig. 7.3 we see that for $N_0 = 10^{12}$ cm^{-2}, island coalescence begins when their diameter is 10 nm. At 10 nm distance between the island centers, we are already beyond the resolution of many Scanning electron microscopes (SEM), the most commonly used tools for ex-situ studies of electrochemical nucleation and growth. And even though 10^{12} cm^{-2} of identical hemispherical islands sounds impressive, thin film coalesced from these islands will not be suitable for our damascene applications requiring 3 nm thick, continuous and uniform, layers. To meet this requirement in our hypothetical system, we must find a way to achieve island density in excess of $N_0 = 10^{13}$ cm^{-2} (i.e., they would start coalescing when their diameter is $\approx$ 3.16 nm). For coalescence to commence at $d_{critical}$ of 1 nm, we need to achieve $N_0 = 10^{14}$ cm^{-2}, which is getting very close to 1 ML (10^{15} cm^{-2}). Alternatively, we could find a way to control the growth of these islands (by modifying deposition parameters, bath composition, substrate properties, etc.) in such a way that the horizontal growth rate far exceeds the vertical one, i.e., have a quasi-layer-by-layer (or quasi-2D) growth mode, and thus relax the requirement for extremely high island density. For complex structures with small length scales, such as trenches and vias in integrated circuits, a detailed understanding of nucleation and growth phenomena, and the influence of parameters such as potential and solution chemistry on the deposition mechanism is critical in designing processes for obtaining the void-free features.

Now, let us assume for the moment that we have learned how to manipulate the islands' density and morphology, and that we can electrodeposit a continuous thin Cu seed along the sidewalls of features with complex geometries using either acidic or alkaline Cu bath. Ultimately, by continuing with the miniaturization, due to lack of free volume, Cu bath will have to play dual role; we will have to use the same bath to deposit 'wet' Cu seed layer and fill the features. Basically, as soon as

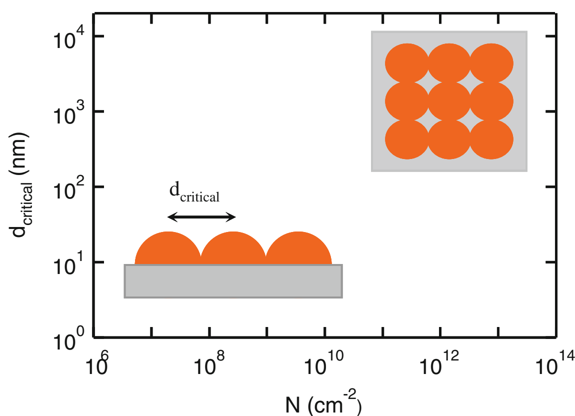

Fig. 7.3 Critical coalescence thickness as a function of island density in a square array of hemispherical islands

the 'wet' Cu seed is plated, feature fill will commence. And that is not all. Since diffusion barrier/alternative seed layers will be as thin as possible, while still functional, we will be plating Cu on a highly resistive substrate. This will result in nonuniform current distribution, and a formation of a Cu film front propagating along the wafer radius, from the edge, where the electrical contact is, toward the center; a so-called "terminal effect." Features closer to the edge will be plated first and those close to the center last (Fig. 7.4). And they all must be free of defects, which is the ultimate challenge! This means that we have to find a way to translate the same plating conditions in time, along the wafer radius, i.e., to define plating parameters in such a way that radial velocity of the Cu front is constant. Thus, we are looking for a set of deposition parameters and Cu bath formulation that would result in 'in-situ' Cu wet seed formation with almost simultaneous (closely followed) void-free fill of the features, and constant radial velocity of the Cu front propagating away from the edge of the wafer (electrical contact).

7.3 Electrochemical Nucleation and Growth

7.3.1 Introduction

In-depth theoretical analysis of electrochemical nucleation and growth phenomena can be found in specialized publications [8, 9], or in dedicated chapters of general electrochemistry textbooks [10]. All of these contain invaluable information for those interested in the field, but by far exceed the scope of this chapter. So, what

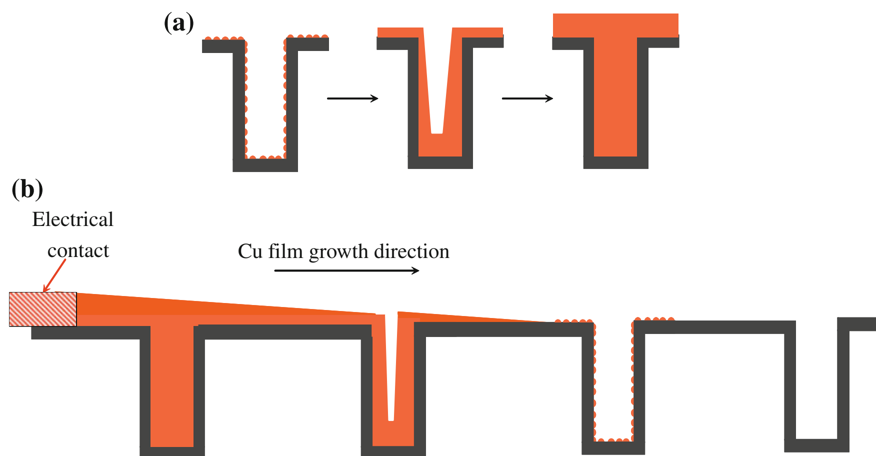

Fig. 7.4 Schematic of **a** in situ wet seed formation and Cu fill of individual features and **b** nonuniform copper plating across a wafer, i.e., Cu front propagation with simultaneous in situ wet seed formation and Cu fill of individual features

would be the most important aspects of electrochemical nucleation and growth theory that could fit in a couple of paragraphs, without overwhelming the reader with barrage of disconnected facts, and yet, not oversimplifying the matter? Classical theory of electrochemical nucleation and growth has many analogies in the classical theory of nucleation and growth of a solid from vapor or liquid phase. The main differentiator is the form of the free energy change associated with the formation of the new bulk phase, ΔG_{bulk}. In electrochemical nucleation and growth, ΔG_{bulk} is proportional to overpotential (η), a variable defined as a difference between the electrode potential (U) and equilibrium electrode potential (U_{eq}), $\eta = U - U_{eq}$. At U_{eq} the net current density is zero, i.e., forward and back reactions have the same rate, and 'electrochemical supersaturation' can be achieved by taking the system out of its equilibrium. In the case of metal film electrodeposition we apply such potentials that $U < U_{eq}$, and $\eta < 0$. The main consequence of the free energy dependence on overpotential is that nucleation and growth variables, such as nucleation rate, are overpotential dependent, too.

Another distinguishing aspect of electrochemical nucleation and growth is the size of a critical nucleus, a nucleus that has 50 % chance of becoming a stable entity, instead of dissolving back into the electrolyte, or becoming a part of nuclei growing on different electrode locations. In the case of electrodeposition of metals on metals, the number of atoms in the nucleus of critical size was typically determined to be fewer than 10 atoms [9 and references therein]. Or, at least the authors of this text are not aware of systems with larger critical nuclei sizes being described in the literature. For such small nucleus sizes, most of the atoms are on the surface, the use of macroscopic parameters such as surface free energy (γ), lacks physical sense. Milchev, Stoyanov, and Kaischev [11, 12] have used the approach of Becker and Döring [13] and Walton [14] to develop atomistic, small cluster model, for electrochemical nucleation and growth, in which no bulk properties were used. They considered phase formation on an inert electrode through different mechanisms: direct attachment from the bulk electrolyte, surface diffusion of adatoms, and nucleation at active centers, defined as the places on the electrode on which nucleation proceeds more readily due to better wetting. They demonstrated that logarithm of the steady-state nucleation rate (J) depended linearly on the overpotential, and the number of atoms in the critical nucleus can be determined from the slope of the plots of logJ versus η. Milchev, Stoyanov, and Kaischev also showed that equations for the nucleation rates based on the atomistic model turn into classical expressions at low supersaturations [12]. It has been years since Walton's original work, and progress in understanding of nucleation and growth of metals from the vapor and liquid phase has been enormous. Theoretical developments have been accompanied by improvement in experimental techniques. The advent of ultra-fast Scanning tunneling microscopy (STM) [15–17] and hermetically sealed wet cells for Transmission electron microscopy (TEM) [18–20] enabled researchers to perform in situ, real-time studies of nucleation and growth phenomena during electrodeposition of metals (Fig. 7.5), and added even more insight into processes occurring on the atomic level. And while these techniques provide direct, real-time visual observation of electrochemical nucleation

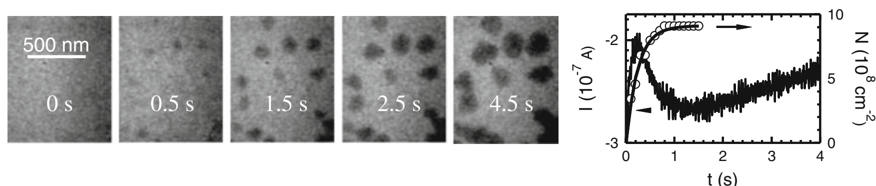

Fig. 7.5 Sequence of in situ TEM images recorded during Cu deposition on Au, together with corresponding current–time response and time evolution of island density fitted to $N(t) = N_0[1 - \exp(-k_n t)]$

and growth, they are not without limitations. Due to high speed motion of the STM tip, ultra fast STM requires specially prepared electrodes, typically single crystals with monoatomic steps only. Immediate consequence is that growth of three-dimensional (3D) islands cannot be followed in real-time, and most of the researchers focus on processes occurring close to equilibrium potential, where kinetics of deposition are slow, or special systems with underpotential deposition (UPD) region, in which two-dimensional islands form on the electrode surface (e.g., copper UPD on gold). On the other hand, in situ, real-time, TEM studies of electrochemical deposition suffer from significant loss of resolution when compared to their 'vapor' counterparts, due to a couple of micrometers thick electrolyte layer on top of the electrode/substrate. Since critical nucleus size is typically below 10 atoms, we are limited to direct observation of the later stages of islands' growth only. So, in a way, these two techniques could be complementary to each other. However, one should not forget that electrochemical techniques such as chronoamperometry (deposition under constant potential), galvanostatic deposition (under constant current deposition), or cyclic voltammetry, also enable true in situ, real-time studies of electrochemical nucleation and growth processes.

They do not provide visual images of the electrode surface, but a skilled researcher can get a pretty good idea about what to expect on the surface of the electrode based only on the current–time or potential-time responses during galvanostatic or chronoamperometry measurements, respectively. Another important difference compared to microscopy techniques is that the information is collected over the whole electrode area, and thus the measured response is an average, not a site-specific value. And while results and data presentation might not be as 'glamorous' and eye-catching as STM and TEM movies, electrochemical techniques have their own special advantages, especially when it comes to logistics, sample preparation and handling, and speed of data collection and analysis. For example, 3-electrode electrochemical cell setups are readily available in research laboratories, tests could be performed on coupons cut from actual wafers used in microelectronics industry, with a new, fresh sample for each experiment, removing doubts about electrode degradation after usage in multiple experiments, and finally, results can be quickly confirmed using ex-situ Scanning electron microscopy (SEM).

Electrochemical deposition of metal on metal involves charge-transfer, and thus the flux of atoms to the surface (current density) and supersaturation (overpotential) can be readily measured. Cyclic voltammetry (CV), chronoamperometry (CA), and galvanostatic measurements (GS) are routinely used to study electrochemical nucleation and growth phenomena [8–10]. Chronoamperometry is used most frequently due to the fact that overpotential is constant, i.e., deposition occurs under constant supersaturation conditions, and resulting current–time transients are relatively easy to interpret. Galvanostatic measurements are more difficult to interpret, since overpotential continuously changes in order to accommodate constant deposition current. However, industrial applications, where current-controlled deposition is a norm, are the driving force behind the effort to develop theories of galvanostatic nucleation and growth. Cyclic voltammetry is used mainly to determine which processes occur in which potential range, and whether charge-transfer or diffusion from the bulk is the rate-determining process during deposition in the overpotential range of interest. However, it can also be used to estimate the size of nucleation overpotential, the effects of surface pretreatment on deposited island density, etc.

7.3.2 Potential Dependence of Island Density, Critical Nucleus Size, etc. (Chronoamperometry)

In a typical chronoamperometry experiment the potential is stepped from a potential at which no deposition occurs to a potential leading to nucleation and growth of a new phase, while monitoring current response as a function of time. From the shape of the resulting current transient, one can obtain information about the mechanism of growth, nucleation rate, density of nuclei, etc. Theoretical analysis of constant-potential experiments focuses on correlations between time evolution of the shape of individual islands and corresponding current transients. The current drawn by each island is calculated based on its shape and the regime of growth: diffusion-limited, kinetically limited, or under mixed control, and then all the individual contributions summed over into a total current over the whole electrode. If, for example, the rate of appearance of supercritical nuclei follows the first-order kinetics, the island density is given by [7]:

$$N(t) = N_0[1 - \exp(-k_n t)] \tag{7.1}$$

where k_n is the first-order nucleation rate constant in units of s^{-1}, and N_0 is the saturation island density in cm^{-2}. When all of the islands are nucleated at the same time, or $k_n t \gg 1$, nucleation is designated as instantaneous, and island density is $N(t) \approx N_0$. The other extreme, when $k_n t \ll 1$, and the number of islands increases linearly with time, $N(t) \approx N_0 k_n t$, is so-called progressive nucleation. In the early stages of deposition the total current is just the sum of the individual currents. In the later stages, depending on their spatial distribution, some islands, or their

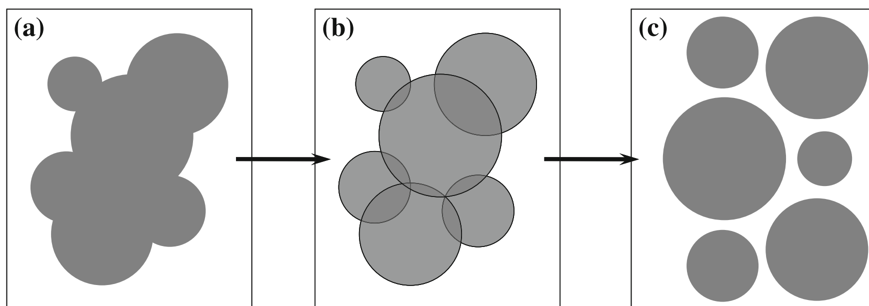

Fig. 7.6 Application of the Avrami theorem to the problem of islands' overlap: **a** true electrode area covered by the coalescing islands, and **c** extended electrode area S_{ext}

diffusion zones, depending on the growth regime, will coalesce sooner than others and the total current is not a simple summation over growth centers any more. If islands have not nucleated at the same time, the situation becomes complex enough that analytical expressions for current transients exist for special cases only. A common approach to dealing with the problem of coalescence is to use the Avrami theorem [21–23]. This theorem correlates the actual normalized area, S, covered by overlapping islands, with so-called extended area S_{ext} (Fig. 7.6); the normalized area that islands would have occupied if they were not overlapping:

$$S = 1 - \exp(-S_{ext}) \tag{7.2}$$

By using Avrami theorem we can calculate the analytical expressions for time dependence of current density in case of instantaneous and progressive nucleation. For easier comparison with experimental data these expressions can be written in the reduced form using the maximum in current density, i_{max}, and time of the maximum, t_{max} (Fig. 7.7). Once the match between normalized experimental data and normalized theoretical transients is established we can extract the nucleation and growth parameters from the given rate laws. A detailed review of examples ranging from quasi 2D nucleation and growth of monolayer thick discs (with attachment of atoms to the edge of the growing disc the rate-determining step), to nucleation followed by 3D kinetically limited growth of right cone-shaped islands, or diffusion-limited growth of 3D islands, etc., is presented in Ref. [10].

Kinetically limited growth of hemispherical islands is studied in [24–26], and diffusion to a truncated sphere in [27]. The rate laws for 3D nucleation followed by diffusion-limited growth of hemispheres are often referred to as Scharifker-Hills model [28–30]. What differentiates their work from the others is the way in which they solved the very complex problem of the overlap of the three-dimensional diffusion zones. In the approach of Scharifker and co-workers [28–30], the hemispherical diffusion zones are transformed into linear diffusion zones of radius r_d (Fig. 7.8), which would provide the same amount of material to a growing hemispherical island. By doing so, they reduced the 3D problem to a 2D problem, which can be solved using Avrami's theorem. This approach has been analyzed,

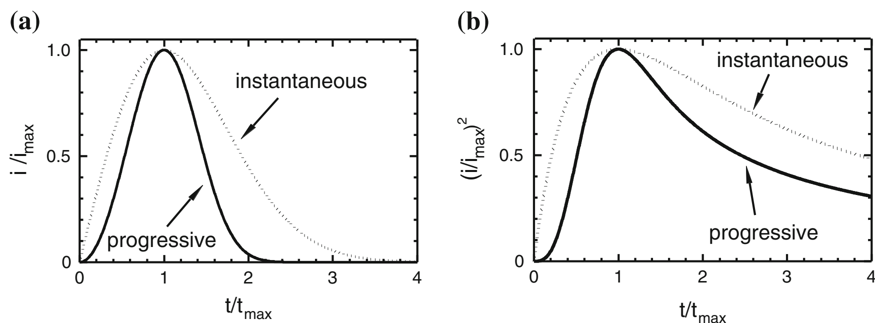

Fig. 7.7 Normalized current–time responses for **a** 2D nucleation and growth of monolayer thick discs with attachment of atoms to the edge of the growing disk the rate-determining step) [10], and **b** 3D island nucleation followed by diffusion-limited growth of hemispheres [28–30]. Instantaneous (*dotted line*) and progressive nucleation (*solid line*) cases are shown for both models

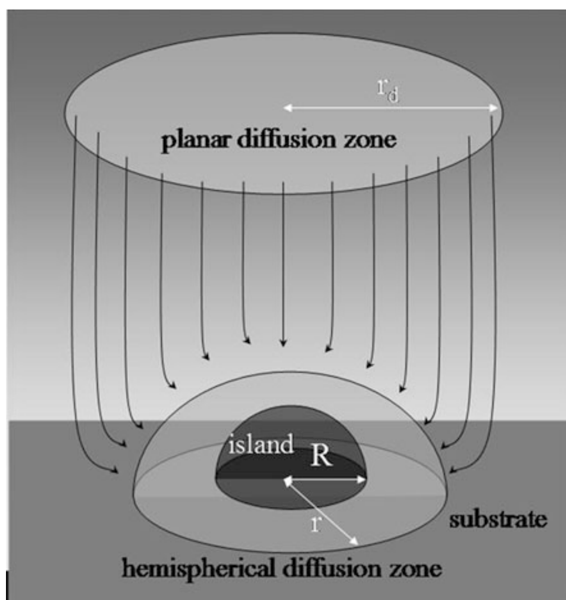

Fig. 7.8 Schematic representation of the hemispherical diffusion zone (r) around hemispherical island of radius R growing under diffusion control, and its equivalent planar diffusion zone (r_d) far from the surface of the electrode

scrutinized, and modified by authors themselves and by other researchers, but to this day their original work remains one of the most cited and compared/used models in the field.

Copper electrochemical nucleation and growth processes were studied during plating from different solution on various substrates. Cu was deposited on Si, Au, TiN, Ta, TaN, Ru, etc., from both acidic and alkaline baths [6, 7, 18, 31–36], and in all cases continuous Cu film was in the end formed by coalescence of 3D

islands. It is interesting to note that application of chronoamperometry in combination ex-situ imaging techniques (AFM, SEM) was more successful on ‘model’ substrates, such as Si, than on microelectronics relevant materials such as TaN. Cu was deposited on Si(111) from alkaline pyrophosphate solutions as well as sulfate-based acidic solutions [31, 33]. Additive-free and solutions with additives were tested. For lower copper concentrations, deposition from both alkaline and acidic baths on Si could be described using model for progressive nucleation followed by 3D diffusion-limited growth of hemispherical islands. Nucleation rate was found to depend exponentially on potential, with the inverse slope of 89 mV per decade (on a log-linear plot) for pyrophosphate, and 45 mV per decade for acidic sulfate solutions, with or without additives. The island density in acidic copper sulfate solution was exponentially dependent on potential with an inverse slope of 99 mV per decade, regardless of whether additives were present or not. The mechanism of deposition was determined to be direct attachment of ions to the nucleus with simultaneous charge-transfer with critical nucleus size of 0 or 1 atom.

Studies of Cu deposition from acidic sulfate solution on Au were done by coupling chronoamperometry with in situ, real-time TEM [18–20]. The time evolution of the island density, extracted from the TEM movies, followed first-order nucleation kinetics, as postulated in chronoamperometric models. The critical nucleus size was determined to be 3 copper atoms. Reduced parameter plots of experimental current transients showed excellent agreement with the theoretical rate laws for 3D diffusion-limited growth of hemispheres. Analysis of the first several tenths of a second in a current–time transients showed that deposition does not occur through direct attachment of ions to the growing island simultaneously with charge-transfer only, but possibly also through multiple other parallel processes, such as adsorption and surface diffusion. This might be a cause for a large discrepancy in island densities obtained from TEM movies and theoretical rate laws.

Cu deposition on PVD TiN from alkaline pyrophosphate solution showed excellent agreement with the rate laws for instantaneous nucleation followed by 3D diffusion-limited growth of hemispheres [32]. However, there was a huge discrepancy in island densities obtained from ex-situ AFM images and those calculated from the equation for the rate law for instantaneous nucleation followed by 3D diffusion-limited growth. Although the origin of the discrepancy could not be determined, the fact is that similar phenomena were observed for copper deposition from complexing solutions [37–39]. Chronoamperometric studies of direct Cu deposition on TaN proved to be even greater challenge [34]. Cu electrodeposition from sulfate, fluoroborate, EDTA, and citrate solutions on TaN diffusion barrier layers was characterized by Volmer–Webber (3D) island growth, and large nucleation overpotentials, typically between 0.65 to 1 V larger on Pt. Experimental data could not be matched with any rate laws for deposition under kinetic or diffusion control, and island densities of approximately 10^{10} cm^{-2} were obtained by applying potentials close to the onset of hydrogen evolution, which was still a couple of orders of magnitude lower than needed for interconnect applications. However, it is important to note that ex-situ SEM and AFM studies

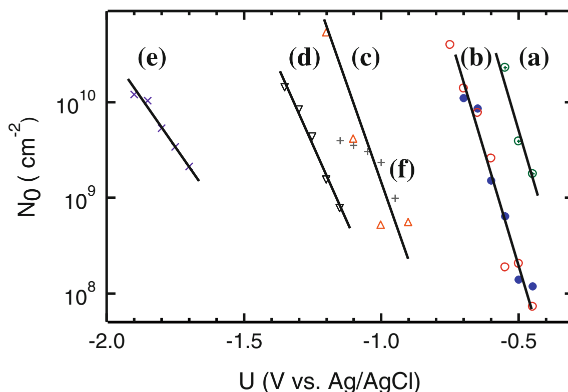

Fig. 7.9 Potential dependence of Cu island density for Cu deposition on Si(111) from an acidic sulfate bath with **a** no additives (⊕) and **b** PEG only (•) and PEG, SPS, JGB (o) [33], on **c** TiN from pyrophosphate bath (Δ) [32], on TaN from **d** citrate bath (∇) [31], **e** EDTA bath (×) [34], and from **f** fluoroborate bath (+) [34]

showed that for citrate and EDTA solutions the island density increased exponentially with more negative potentials. For fluoroborate solutions the island density increased and then saturated at more negative potentials. Potential dependence of island density for system described above is shown in Fig. 7.9.

Since Ruthenium (Ru) is considered a potential alternative seed layer to replace PVD Cu, it is not surprising that a number of studies on electrochemical Cu nucleation and growth on Ru exist in the literature [40–44]. Current–time responses to potential-step deposition from various baths were recorded on different Ru substrates, ranging from Ru shots to PVD Ru, ALD Ru, and Ru alloys [40–44]. Experimental transients in normalized form agreed to a varying degree to the transients obtained from the rate laws for nucleation followed by 3D diffusion-limited growth, depending on the bath and substrate properties. Variables such as nucleation rate and saturation island density showed overpotential dependence similar to those observed in other systems. Typically, experimental data did not fit well any of the theoretical rate laws when Cu-sulfate baths and Ru substrates with composition/properties relevant to interconnect applications were used (Fig. 7.10). Cu baths for fabrication of complex interconnect architectures typically contain open source or proprietary inorganic and organic additives. Thanks to these additives, differential plating rates at the bottom and top of the feature exist, and with Cu deposition rate at the bottom being higher, void-free, bottom-up fill is achieved. One of the keys to a successful application of direct Cu plating technology is to understand how these additives affect nucleation and growth phenomena, and how they can be used to manipulate Cu island density on Ru, for example. However, various studies showed no significant difference in normalized transients obtained for deposition from the additive-free bath and the bath with all the additives, forcing researchers to look for methods other than chronoamperometry, capable of tackling different aspects of nucleation and growth phenomena in more complicated systems.

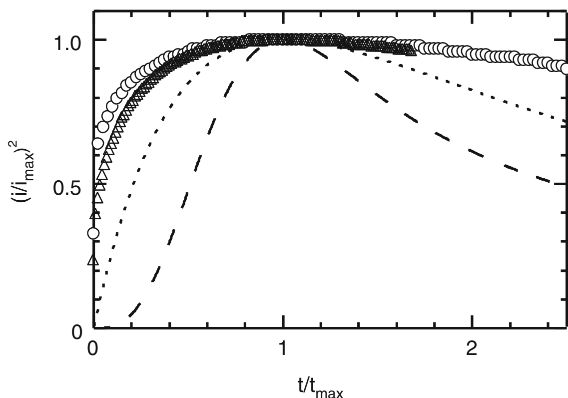

Fig. 7.10 Reduced parameter plots for instantaneous (*dotted line*) and progressive (*dashed line*) nucleation followed by diffusion-limited growth of hemispherical islands, and normalized experimental data for Cu deposition on Ru from the bath without (Δ) and with additives (o)

7.3.3 The Effect of Additives (Galvanostatic Deposition)

It is much easier to interpret the results of a potentiostatic (chronoamperometry) experiment than a galvanostatic one, due to a simple fact that in the later overpotential, and thus supersaturation, changes with time. Under galvanostatic conditions nucleation could proceed entirely under nonsteady-state conditions, and the very early stages of metal deposition are convolution of overpotential-dependent charging, nucleation, and growth processes, which makes derivation of exact analytical formulas for time evolution of island density (N(t)) and overpotential (η(t)) extremely challenging. Therefore, it is not surprising that potentiostatic studies of nucleation kinetics outnumber galvanostatic ones. However, current-controlled deposition is a norm in industrial applications, and galvanostatic deposition might offer advantages in studying the effects of additives and growth of supercritical islands.

Milchev and co-workers [45] have studied the early stages of galvanostatic deposition by performing so-called P-G-P experiments, where P-G-P stands for potential step, galvanostatic (current) step, and potential step. In this method, working electrode is initially kept at a potential where no nucleation (deposition) occurs (P). This step is followed by a galvanostatic pulse (G) to form nuclei on the working electrode surface. The galvanostatic pulse is interrupted by a potential step (P) at which no new nucleation events occur, and only the nuclei formed during the galvanostatic pulse grow. The duration of the last step is determined by the resolution of the imaging technique/instrument used to count the islands. P-G-P method enabled Milchev and co-workers [45] to study (i) the time dependence N(t) of the number of nuclei by changing the duration of the galvanostatic pulse, (ii) the time dependence of the overpotential, (iii) the time dependence of the nucleation rate, and (iv) the overpotential dependence of nucleation rate. Based on these experiments, qualitative description of a typical experimental η(t) transient is given schematically in Fig. 7.11. In the time interval [0, t_1], there is a steep change in overpotential η, due to charging of the electric double layer, and formation and

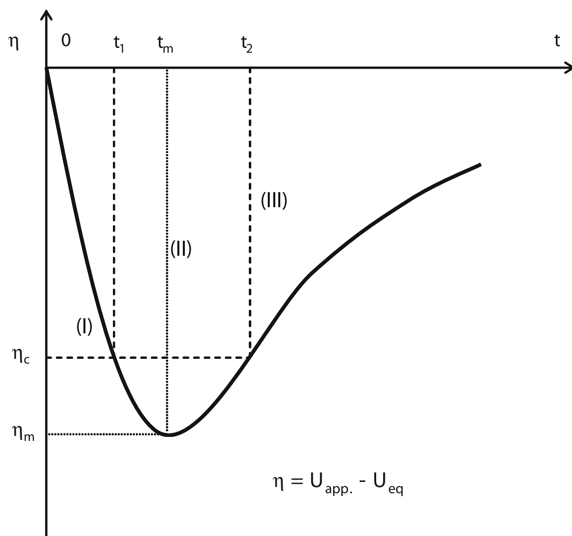

Fig. 7.11 Schematic of a typical experimental η(t) transient obtained using galvanostatic step method [45]

increase in number of subcritical clusters. At time $t = t_1$, the overpotential reaches a value η_c, and the formation and growth of supercritical clusters commences. Overpotential η reaches a peak at $t = t_m$, and then its absolute value decreases. The critical value of the overpotential, η_c, is attained again at $t = t_2$, and from t_2 onwards the current is almost entirely consumed by the growing stable islands.

Galvanostatic deposition of Cu from acidic sulfate baths on Ru-based substrates follows the qualitative model described above [43]. Cu islands were deposited on Ru from a bath with and without suppressor additive using -2 mA cm^{-2} galvanostatic pulse of different duration (please, note that this current density is chosen for ease of observation). After each deposition experiment (Fig. 7.12a), samples were examined using SEM, and islands counted. Island density was higher when suppressor additive was present in the bath for all samples. And even though duration of the longest pulse was 100 s, there was no significant change in island density when compared to 6 s long pulses, i.e., the major part of the charge was consumed to grow islands nucleated in the very short time span around the potential peak in the early stages of deposition (Fig. 7.12b). Another interesting observation is made when time evolution of the projected island surface area was analyzed [43] (Fig. 7.12c). Individual islands and total Cu-Ru interface (A_I) were determined for each deposition time, and then normalized by the total Ru electrode area (A_{Ru}). After 100 s of deposition, the fraction of Ru electrode covered by Cu islands, i.e., the ratio A_I/A_{Ru}, is more than 3 times larger when Cu was plated from the bath with suppressor additive than from the additive-free bath. Also, time evolution of the surface coverage when suppressor was present resembles Avrami theorem for phase transformations. The exponential fit to data obtained with additive-free bath reveals that Ru surface will not be completely covered by Cu even at very long times, mathematically speaking even when $t \rightarrow \infty$:

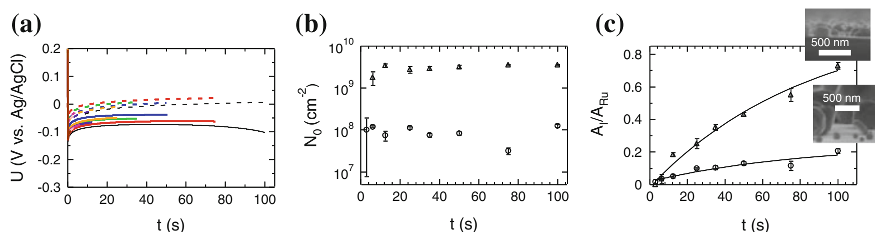

Fig. 7.12 **a** U-t responses for additive-free (*solid line*) and bath with suppressor (*dashed line*), **b** time evolution of island density, and **c** time evolution of normalized surface coverage (A_I/A_{Ru}) for bath without (o) and with suppressor (Δ). Inserts in **c** are cross-sectional SEM images of Cu islands after 100 s of deposition

$$(A_I/A_{Ru})_{SUPPRESSOR} = 1.0156 - 1.0292 \times \exp(-0.011813^{*}t), \quad (7.3)$$

for the bath with suppressor additive, and

$$(A_I/A_{Ru})_{NOADDITIVES} = 0.25 - 0.2332 \times \exp(-0.012048^{*}t) \quad (7.4)$$

for the additive-free bath.

This seemingly odd result is easily explained using cross-sectional SEM images of Cu islands (Fig. 7.12c). In the absence of additives, Cu islands were facetted, elongated, and even 'vertical,' showing strong nonwetting properties. In the presence of suppressor, Cu islands assumed mostly hemispherical shape. Both increase in island density and lowering of the island's aspect ratio (height/effective base radius) are key to successful implementation of direct plating of Cu for interconnect applications.

In their studies, Milchev and co-workers [45] have focused on nucleation phenomena in the very early stages of deposition. And this is probably the best approach when experimenting with additive-free Cu plating baths, since potential is a monotonous function of time after the initial peak at short times (Fig. 7.12). In the presence of additives, the shape of potential-time response changes significantly at later stages of deposition [43]. After initial charging nucleation peak, and island-growth plateau, potential becomes more negative, initially slowly, but then steeply. The steep increase in the absolute value of the potential is followed by an inflection point, and then the potential levels off again (Fig. 7.13a). Extensive tests and data analysis lead to conclusion that the inflection point is due to coalescence of Cu islands, after which Cu ions in the electrolyte do not 'sense' Ru surface any more. The second plateau, after the inflection point, corresponds to Cu deposition on Cu substrate from the bath with suppressor additive. The same potential should be obtained for Cu deposition on Cu working electrode of the same surface area using the same current density. Please note that this second plateau should not be confused with hydrogen evolution which can be observed if deposition is driven into diffusion-limited regime [46].

Several parameters can be defined to describe the idealized step-function response. For example, the step height, the potential difference between potentials of the second and first plateaus, can be designated as ΔU_{21}, contains information

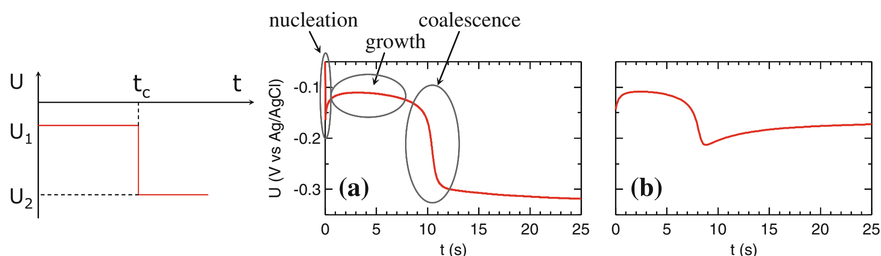

Fig. 7.13 U-t response in the presence of suppressor (**a**) and all the additives (**b**). Insert on the left shows idealized step-function response with parameter definition

about suppressor's inhibition strength. The significance of the step height is in suppressor's ability to inhibit Cu deposition on the parts of the sample already covered by Cu, and thus promoting faster Cu front propagation over RuTa areas further from the electrical contact. Stronger inhibition will also help achieve better uniformity across the resistive wafer. The time needed to reach the inflection point can be defined as the characteristic time and designated by the symbol t_c. t_c can be used to get the rough estimate of island density or the effective Cu film thickness, and examine the effects of suppressor concentration and other deposition parameters. By using the same galvanostatic pulse for different samples, while adding suppressor to the plating bath, we can increase the island density, and reduce t_c [43]. Similarly, by using the same plating bath, and delivering the same charge, but applying different deposition current density, we can explore the relationship between island and current density [43]. As expected, with increase in the (absolute value of) current density, the island density increases, and t_c decreases. Why is this important? This could be used as a selection criterion for the choice of suppressor to be used in the Cu direct plating.

The effect of inorganic components, copper sulfate ($CuSO_4$), sulfuric acid (H_2SO_4) , and chloride ions (Cl^-), on electrochemical nucleation and growth of Cu on RuTa alloy substrate was reported in the absence and the presence of a suppressor additive, polyethylene glycol (PEG) [47]. In the absence of suppressor, decrease in Cu^{2+} and Cl^- concentration and increase in concentration of H_2SO_4 lead to increase in saturation island density. The effect of each component remained unchanged when all components were mixed together. After addition of PEG suppressor molecule, the trends for Cu^{2+} and H_2SO_4 concentration and Cu island density remained the same, but Cl^- concentration had to be optimized for a maximum saturation island density to be obtained [47]. The results suggested that Cu island density increased when introducing into the solution species whose growth-suppressing species (PEG + Cl^-) were introduced into the bath and, decreased in the presence of growth-promoting species (Cu^{2+} and Cl^-). The effect of the molecular weight of polyethylene glycol (PEG) and its derivatives on Cu island density were also explored using galvanostatic step method combined with ex-situ SEM [48]. However, suppressor alone is not enough to achieve void-free fill of the trenches and vias. The presence of both suppressor and accelerator

additive in Cu plating bath is required for void-free fill of trenches and vias. The potential-time response changes again when other accelerator is added to the bath; the step is followed by a peak (Fig. 7.13b), and the step height is smaller than when suppressor only is present in the bath [43]. This is due to the fact that accelerator additive promotes Cu deposition on Cu. This is of great significance for growth of Cu islands and uniformity of direct Cu plating on wafer scale. The third additive, the leveler, which is not easily displaced from the Cu surface by the accelerator, can be added to increase the step height again, and improve suppression of Cu island growth and uniformity of the wafer scale current distribution [49]. Therefore, Cu bath composition has to be optimized to serve a threefold purpose: provide in situ deposition of Cu seed on resistive substrate, enable void-free fill of patterned features, and constant velocity of Cu front propagation (together with proper selection of deposition parameters).

And finally, galvanostatic step method can be even used to explore the overpotential dependence of Cu island density [46]. In a detailed study of the effect of Cu^{2+} concentration, authors determined that decrease in Cu^{2+} concentration resulted in increase of Cu island density for all current densities under investigation. The overpotential was defined as a difference between the potential in the first plateau, where island density is saturated and transient is growth-dominated, and equilibrium potential. The overpotential value was also corrected for IR drop in the solution. By doing so, the authors were able to demonstrate an exponential relationship between copper island density and overpotential, with concentration dependence built-in through its effect on overpotential:

$$N_0(\eta_{IR}) = N_{pre} \exp[aF(-\eta_{IR})/RT] \tag{7.5}$$

N_0 values can now be estimated for a given substrate from the copper deposition overpotential found during the galvanostatic deposition. In Eq. (7.5), the preexponential factor, N_{pre} is a system characteristic. It can be changed, for example, by removing the oxide film from the surface of the substrate. α, F, and R are constants, while T is temperature.

7.3.4 Surface Pretreatment

Together with electrochemical deposition parameters and bath composition, the state of the substrate is also an important parameter to consider when manipulating the island density. Alternative barrier/seed layers are typically polycrystalline thin films, far from perfect substrates considered in computer simulations or even single crystal substrates used in STM studies of nucleation and growth. Researchers typically postulate saturation island density, number of nucleation sites, and their distribution by activation energy in their derivation of rate laws. But these cannot be known in advance for a given polycrystalline substrate, and some of them might not be even possible to determine experimentally. And while defining, numbering, and having ultimate control over nucleation sites can prove

very challenging, there are also other, macroscopic, parameters which could affect island density. For example, thin oxide on top of alternative seed/barrier layers is detrimental to achieving both high island density and good adhesion of electrodeposited Cu. In case of Ru substrates, this thin oxide layer can be removed by electrochemical methods [50], or annealing at high temperatures in forming gas atmosphere [44]. The effect of oxide removal on island density can be easily observed using galvanostatic step method. Upon anneal in forming gas, recorded U-t responses show much shorter time to step, t_c, and ex-situ SEM confirms increase in island density [44, 45]. Oxide removal methods might vary for different types of Ru substrates. Anneal in forming gas is actually countereffective for alloy substrate containing Ru and Ta (RuTa) [44]. In this case we are limited to electrochemical methods of surface pretreatment. The effect of surface pretreatment can be confirmed again by using galvanostatic methods, but we can also use cyclic voltammetry (CV).

Current–voltage curves for Cu plating on Cu and RuTa alloy substrates from the Cu bath with/without suppressor additive are shown in Fig. 7.14. The curves for Cu deposition on Cu from the bath with and without suppressor are similar in shape, but shifted with respect to each other due to the inhibiting role of the suppressor. Current–voltage curve for Cu deposition on the RuTa from the bath with suppressor shows a peak positioned between the onsets for Cu deposition on other two curves. This is due to the fact that suppressor impedes growth of existing Cu islands and promotes Cu deposition on RuTa. After most of the RuTa surface is covered with Cu, the deposition current starts decreasing at the rate dependent on suppressor strength and adsorption rate, and at some point Cu-on-RuTa curve starts overlapping with the curve for Cu deposition on Cu when suppressor additive is present in the Cu bath. Similar to Cu on Cu deposition, suppressor cannot block Cu efficiently beyond critical potential and current steeply increases again. The total charge under the peak in the CV curve for Cu on RuTa deposition can be used to compare different RuTa substrates and estimate the effective Cu film thickness and island density. The smaller the charge under the peak, the

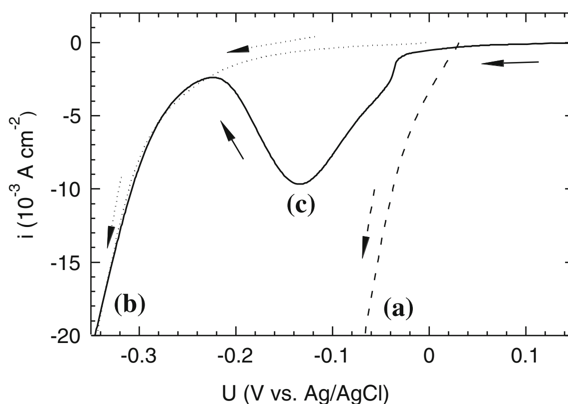

Fig. 7.14 Current–Voltage curves for Cu plating on Cu substrate from **a** additive-free bath (*dashed line*) and **b** bath with suppressor additive (*dotted line*). **c** is CV curve for Cu deposition on RuTa alloy substrate from the bath with suppressor (*solid line*)

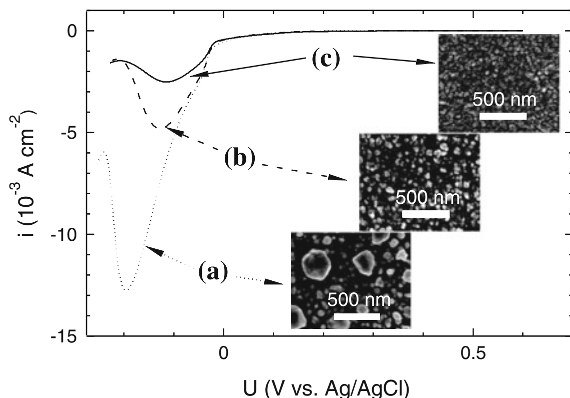

Fig. 7.15 CV peaks as a function of surface pretreatment the samples received prior to measurements. *Dotted curve* (**a**) is recorded on as received 2 nm RuTa film, while the *dashed* (**b**) and *solid curve* (**c**) corresponds to the 2 nm RuTa sample electrochemically pretreated in 10 % vol. sulfuric acid and proprietary chemistry, respectively. Inserts are top-down SEM images of Cu islands for corresponding CV and surface pretreatment

smaller the effective Cu film thickness is, i.e., higher Cu island density. An example of such a comparison is given in Fig. 7.15. CV curves recorded using the same scan rate of 20 mV/s, and the same Cu bath, show peaks of different areas depending on the surface pretreatment the sample received prior to voltammetric measurements. Dotted curve (Fig. 7.15) is recorded on as received 2 nm RuTa film, while the dashed and solid curves correspond to the 2 nm RuTa sample electrochemically pretreated in 10 % vol. sulfuric acid [50] and proprietary chemistry [51], respectively. Inserts in Fig. 7.15 also show top-down SEM images of Cu islands deposited on as received and electrochemically pretreated RuTa substrates. As predicted, the smallest charge under the peak corresponds to the highest Cu island density (7.0×10^{10} cm^{-2} for the sample pretreated with proprietary chemistry > 4.6×10^{10} cm^{-2} for 10 % vol. sulfuric acid pretreated sample > 2.6×10^{10} cm^{-2} for as received sample). Surface pretreatment could be used as the additional tool in controlling Cu island density in case varying bath composition and deposition parameters does not yield satisfactory Cu film thickness and front propagation rates.

7.3.5 Summary

Electrochemical nucleation and growth of Cu on foreign substrates typically proceeds through coalescence of 3D islands into a continuous film. When Cu is deposited from acidic sulfate baths on alternative barrier/seed layers, Cu island density depends exponentially on potential/overpotential. Similar results are obtained for other acidic and alkaline solutions with a few exceptions (e.g., Cu

deposition from fluoroborate solution on TaN). Critical nucleus size for Cu deposition is typically determined to be below five atoms, suggesting fast nucleation processes for typical deposition current densities (around -10 mA cm^{-2}) used, and a very challenging phenomena to study using current in situ imaging techniques. To increase the island density and improve Cu wetting of foreign resistive substrate, i.e., reduce the island height to effective base radius aspect ratio, and deposit thinner films with smaller island density, one can use suppressor additives. Ideal suppressor should have high adsorption rate, and strongly inhibit Cu deposition on Cu. Suppressor should affect nucleation by reducing the growth rate of Cu islands, which at constant deposition current increases overpotential, and thus increases nucleation rate. On the other hand, it should not interact with substrate by blocking nucleation sites, because that would decrease the nucleation rate. Since void-free Cu fill requires presence of accelerator additive, Cu bath composition has to be optimized to serve a threefold purpose: provide in situ deposition of Cu seed on resistive substrate, enable void-free fill of patterned features, and constant velocity of Cu front propagation (together with proper selection of deposition parameters).

7.4 Direct Plating at the Wafer Scale

7.4.1 Terminal Effect

7.4.1.1 Potential Drop Over One-Dimensional Conductor

The resistance, R (Ω), along a metal wire increases with its length, L, according to:

$$R = \frac{\rho \times L}{S} \tag{7.6}$$

with ρ (Ω cm), the electrical resistivity of the metal and S (cm^2) its cross-sectional surface area. The voltage difference between two terminals placed on the wire is simply given by Ohms law with R from Eq. (7.6). When the terminal where the current, I, is introduced into the wire has a fixed voltage, V_{TERMINAL}, the voltage along the wire (measured with a second terminal) decreases linearly with distance, L, as shown schematically in Fig. 7.16. The voltage drop from the terminal is generally indicated as the IR drop or the terminal effect:

$$V(L) = V_{\text{TERMINAL}} - I(L)R(L) \tag{7.7}$$

In this simple case of a dry wire with two terminals, the same amount of current that enters the wire at terminal 1 (I_{in}) also leaves it at terminal 2 (I_{out}), and only R is a function of distance, L, from the terminal.

When the wire is placed in an electrolyte solution, the situation becomes somewhat different as now the current can escape all along the length of the wire into the solution through electrochemical reactions and is collected at the opposite

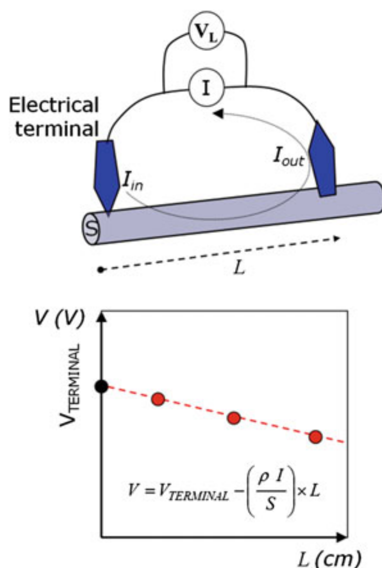

Fig. 7.16 The resistance along a wire increases with the distance between the terminals. The ohmic potential drop over this resistance when a current flows causes a linear decrease in potential relative to that of the terminal of the incoming current

current collector or counter electrode ($I_{in} = I_{out}$) as shown schematically in Fig. 7.17. In this case, also the current, I_L, going through the wire is a function of distance, L, and the potential drop is obtained by the integral of I(L) and R(L) along the length of the wire. In the case of a uniform current distribution, the current is evenly distributed along the length of the wire ($i = I/(d\pi L_0)$ *with d (cm) the wire diameter*) and an analytical solution for potential drop can be easily calculated; the opposite effects of I_L and R_L on the voltage drop give rise to the mirrored S-shaped curve in Fig. 7.17. The example uses a value for $\rho/S = 0.01$ which, for example, corresponds to a copper wire with diameter of 0.2 mm. Note that a similar behavior is expected for a strip of metal, e.g., a thin barrier film on strip of silicon wafer.

7.4.1.2 Potential Drop Over Two-Dimensional Wafer

In the case of thin metal film coated on top of a circular wafer, the potential distribution over the metal film can be described by the Poison-type relationship for Ohm's law [52–56]:

$$\nabla^2 V_m(r) = -R_s i_m(\eta(r)) \tag{7.8}$$

with R_s, the sheet resistance of the film and i_m, the current density in the film. Since electrical contact for wafer plating is typically made by a ring around the wafer periphery, it can be assumed that the potential variation for a wafer is mainly a function of the radius, r, from center to edge, and that the angular variation is negligible. Equation (7.8) then reduces to its one-dimensional form:

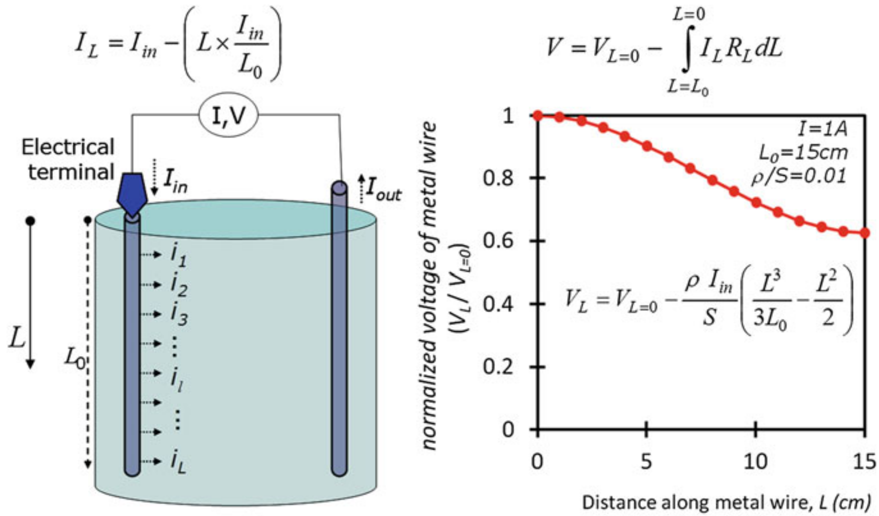

Fig. 7.17 Schematic representation of current flow through a wire in an electrolyte solution and the normalized potential variation from the terminal toward the end of the wire with a length, $L_0 = 15$ cm

$$\frac{d^2V_m(r)}{dr^2} + \frac{1}{r}\frac{dV_m(r)}{dr} + R_s i_m(\eta(r)) = 0 \tag{7.9}$$

or

$$\frac{1}{r}\frac{d}{dr}\left(r\frac{dV_m(r)}{dr}\right) = \frac{d^2V_m(r)}{dr^2} + \frac{1}{r}\frac{dV_m(r)}{dr} = -R_s i_m(\eta(r)) \tag{7.10}$$

with boundary conditions:

$$\mathrm{V_m(r) = V_{m,edge}} \text{ for r = } \mathrm{r_0} \text{ and } \frac{dV_m(r)}{dr} = 0 \text{ for r = 0} \tag{7.11}$$

with r (cm), the radius of the wafer from the center, and r_0 the radius toward the edge of the wafer where the seal contact is made. Note that we deliberately do not connote it as $V_{m,\ TERMINAL}$ as the contact with the wafer is made under a sealed ring and the solution reaches to the edge of the wafer seal only.

For constant current density, i_m, the differential Eq. (7.9) yields the simple quadratic solution:

$$V_m(r) = V_{m,\text{edge}} - \tfrac{1}{4}R_s i_m(r^2 - r_0^2) \tag{7.12}$$

showing a decrease in the potential for the metal resistive film from edge to center.

In reality the current density is a function of overpotential and as such also a function of V_m(r) (see Sect. 7.4.2). For thick copper seed (~100 nm) where the current distribution at the wafer is reasonably uniform, this assumption can be

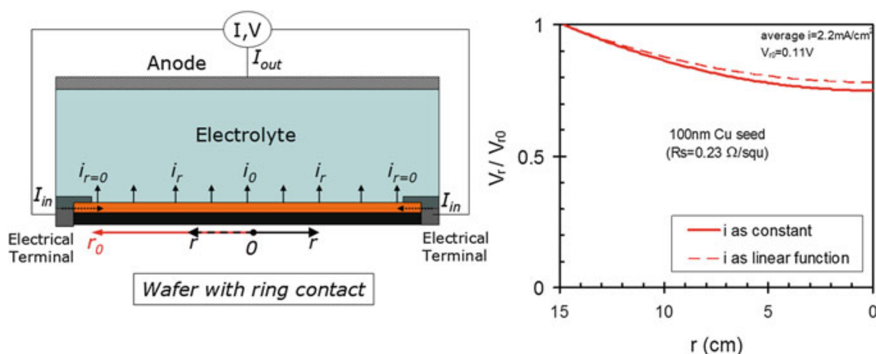

Fig. 7.18 On the left-hand side: Schematic representation of current flow through a disk-shaped thin metal film (wafer) in an electrolyte solution with a sealed ring at the edge of wafer as electrical contact (terminal). On the right-hand side: the normalized potential variation as a function of radius, r, from the center of the wafer toward the edge of wafer with a radius, r_0 = 14.8 cm for the case of 100 nm Cu thin film (Rs = 0.23□/sq), and average current density of 2.2 mA/cm^2 and V_{edge} ≈ $□_{Cu,\ edge}$ = 0.11 V; calculated assuming a constant current density (full line, Eq. (7.12)) and calculated by a sequence of linear approximation with a zero-order Bessel function as a solution. The specific case has a cathodic current density-overpotential curve described by i = 0.0014(exp(8.5□)−1) with linearization i_m = (di/d□)$□_m$ or specifically i_m = = R_sx8.5 × 0.0014[EXP(8.5 × □)) as the input for the Bessel function (note that input and result are linked through overpotential) [55]

made as illustrated in Fig. 7.18. For more resistive films such as RuX, Eq. (7.12) can give an indication of the trend for V_m and will later be used to estimate the region of the potential drop Δr_{drop} (Fig. 7.19, Sect. 7.4.4.2).

7.4.2 Overpotential Distribution

7.4.2.1 Voltage Contributions in a Plating Cell

In a plating cell, a voltage difference, ΔV, exists across the electrodes, typically as a result of an applied current [57]. For conductive electrodes, this difference consists of the sum of the overpotentials at the anode and cathode, the potential drop over the solution, and possibly a contribution of a contact or series resistance, R_c:

$$\Delta V_{cell} = (V_{m,A} - V_{m,C}) + IR_c = \eta_A(r) + \Delta V'_{SOL}(r) + (-\eta_C(r)) + (U_{eq,A} - U_{eq,C}) \quad (7.13)$$

with $V_{m,\ A}$ and $V_{m,\ C}$ the potentials of the conducting anode and cathode, respectively (and equal to that of the electrical terminals after correction of an

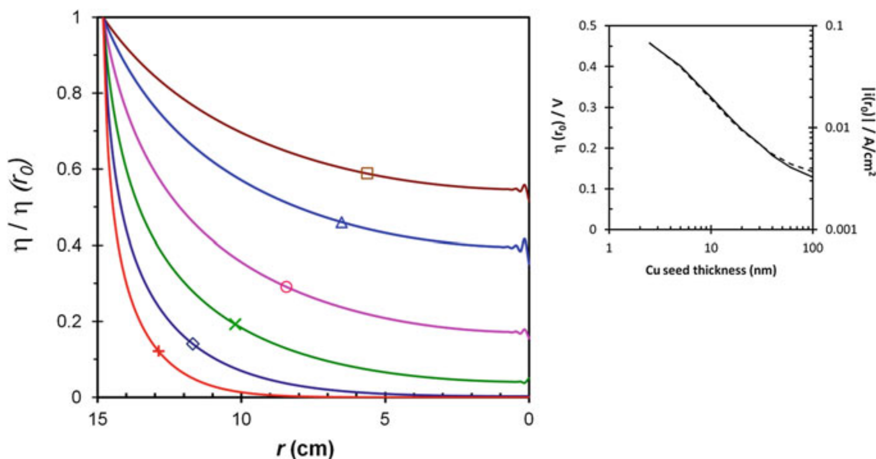

Fig. 7.19 The normalized potential variation as a function of radius, r, from the center of the wafer toward the edge of wafer with a radius, $r_0 = 14.8$ cm for the cases of (□) 60 nm (0.23 Ω/sq.), (△)+◇40 nm (1 Ω/sq.), (◯) 20 nm (3 Ω/sq.), (×) 10 nm (2.8 Ω/sq.), 5 nm (24 Ω/sq.), and 2.5 nm (70 Ω/sq.) copper thin film, and average current density of -2.5 mA/cm^2. Simulation was done by a sequence of linear approximations ($\Delta r = 0.15$ cm) with a zero-order Bessel function fitted to the empirical i-η curve (500 rpm) described by $i = 0.0014(\exp(8.5\eta) - 1)$ [55]. The inset shows the overpotentials (full line, left axis) and currents densities (striped line, right axis) at $r_0 = 14.8$, the edge of the 300 mm wafer, as a function of Cu film thickness for an average current density of − 2.5 mA/cm^2

eventual contact resistance; e.g., between the pins of the ring contact and the seed on the wafer). In the case of an inert anode or the use of different catholyte and anolyte, also at the term for the difference in equilibrium potential for the different reactions at cathode and anode needs to be taken into account. The radial dependence of the overpotentials are in this case entirely related to the variation of ΔV_{SOL} in the cell due to the finite shape of anode and cathode, the distance between anode and cathode, and the presence of resistive elements such as diffusers and shields placed between the anode and cathode. The latter are usually added to compensate ΔV_{SOL} so that the variation in the overpotential at the wafer (i.e., η_C (r) for copper plating) is minimal for a uniform current distribution. The contact resistance has no effect on the overpotential distribution but when approaching a few ohms (as for resistive substrates) can quickly challenge compliance of the power supply.

For plating on resistive substrates, also $V_{m,C}$ is now also a function of the radius, r, from the wafer center as governed by the differential Eq. (7.9) whereas $V_{m,A}$ for the conductive anode counter electrode remains constant. Equation (7.13) can be rewritten as follows:

$$V_{m,C}(r) + (-\eta_C(r)) + \Delta V'_{SOL}(r) + \eta_A(r) = V_{m,A} + IR_c + (U_{eq,A} - U_{eq,C}) \quad (7.14)$$

7.4.2.2 Overpotential Distribution at Resistive Substrates

All constants (for certain applied current) on the right of Eq. (7.14) become zero in the differential form:

$$\frac{d\left(V_{m,C}(r)\right)}{dr}+\frac{d\left(\Delta V'_{SOL}(r)+\eta_A(r)\right)}{dr}=\frac{d(\eta_C(r))}{dr} \tag{7.15}$$

For resistive substrates with sheet resistance Rs > 10 Ω/sq the potential drop over the metal thin film is much larger than the potential drop over the solution (including the change in overpotential at anode) and thus variation is $V_m(r)$ is the same as the variation in the overpotential:

$$\frac{d\left(V_{m,C}(r)\right)}{dr}\approx\frac{d(\eta_C(r))}{dr} \tag{7.16}$$

The variation of the overpotential is in analogy with Eq. (7.9) described by the differential equation:

$$\frac{d^2\eta(r)}{dr^2}+\frac{1}{r}\frac{d\eta(r)}{dr}+R_s i_m(\eta(r))=0 \tag{7.17}$$

To obtain the overpotential from Eq. (7.17), the current density is needed which is in its turn a function of the overpotential. On thin copper seed, an exponential variation between current density and overpotential may be expected in accordance with the Butler–Volmer equation. On non-copper seed such as Ru or RuX, the local current density is governed by an overpotential-dependent nucleation and growth process (current peak). In both cases, only numerical methods and computer simulation can give an exact solution [56]. However, in many cases a linear variation of current density with overpotential is a sufficient approximation which allows an analytical solution with a zero-order Bessel function [55].

Linear approximation:

We consider the case in which $i_m(\eta)$ varies linearly with overpotential η:

$$i_m(\eta)=\left(\frac{i(r_0)}{\eta(r_0)}\right)\times\eta, \tag{7.18}$$

with $i(r_0)$ and $\eta(r_0)$, the local current density and overpotential at the edge of the wafer, then the governing differential equation for the overpotential has the following form:

$$\frac{d^2\eta(r)}{dr^2}+\frac{1}{r}\frac{d\eta(r)}{dr}+\left(\frac{R_s i(r_0)}{\eta(r_0)}\right)\eta(r)=0, \tag{7.19}$$

with boundary conditions:

$$\eta(r_0) = \eta_{Cu,\text{edge}} \qquad \text{and} \qquad \frac{d\eta(0)}{dr} = 0 \tag{7.20}$$

The solution for the overpotential has the following form:

$$\eta(r) = \eta_{\text{edge}} \frac{I_0\left(r\sqrt{\frac{R_s i(r_0)}{\eta(r_0)}}\right)}{I_0\left(r_0\sqrt{\frac{R_s i(r_0)}{\eta(r_0)}}\right)}, \tag{7.21}$$

where $I_0\left(r\sqrt{\frac{R_s i(r_0)}{\eta(r_0)}}\right)$ represents the modified zero-order Bessel function.

Sequence of linear approximations:

To achieve a more accurate simulation, the linear approximation can be split up into several linear segments which construct the actual (experimental) i-η relationship [55]. When the segments are made small (e.g., steps in Δr of 0.1–0.3 cm, i.e., sufficiently smaller than Δr_{drop}, see Sect. 6.1), the linearization (or input of Eq. (7.18) for each Δr segment) can be given as

$$i_m(\eta) = \left(\frac{di}{d\eta}\right) \times \eta \tag{7.22}$$

where the value for di/dη as the input for the Bessel function is calculated for each interval. Note that input is linked to the output, namely the overpotential. Such calculation can be done with spread sheets; i.e., without the use of specialized modeling codes.

Example for copper plating on resistive thin copper seed:

Figure 7.19 shows the variation of the normalized overpotential, $\eta/\eta_{\text{Cu,edge}}$, for copper thin films. The simulation was made based on an experimentally obtained i-η curve for copper plating on copper from a commercial high copper—low acid plating bath [55]. In this case the input for the zero-order Bessel function was obtained from Eq. (7.22) whereby $\eta_{\text{Cu,edge}}$ was adjusted such that the average current density was 2.5 mA/cm^2 in all cases. Note that in this simulation the potential drop over the solution in Eq. (7.15) was neglected. For the copper seed layers thicker than 10 nm (Rs < 10 Ω/sq) the potential and consequently the current distribution can be optimized by compensation through the potential drop over the solution by use of resistive elements such as shields and diffusers placed in the plating cell as well as by the use of segmented anodes and thieves in the plating tools [58]. For very resistive seeds, the compensation will be little effective and in the initial stage of plating a large difference in overpotential and current density exists over the wafer surface [55]. Whereas the initial nonuniformity in the copper thickness can be corrected by overcompensation at later stages; i.e., higher effective current density in the center of the wafer during plating of the copper overburden, the feature fill will be obviously affected by this severe nonuniformity

in the current distribution. However, more problematic is the fact that there is not sufficient current in the center of the wafer to protect the copper seed from corrosion by dissolved oxygen or Cu^{2+} itself through the copper comproportionation reaction [55]. This means that the copper seed cannot be scaled down in thickness indefinitely due to the terminal effect. At this point, the technology needs to switch to direct copper plating on non-copper seed/barrier stack or alloy such as RuTiN [1, 59–61]. Note that the non-copper seed has to be nobler than copper itself so that no galvanic corrosion or displacement can occur [44]. For this reason, cobalt and CuMn seeds cannot be used [61]. The copper seed corrosion phenomenon also limits the use of two-step copper plating where first a *wet seed* is plated typically from alkaline baths with low cupric ion concentration (i.e., large polarization of overpotential). When the wet seed is introduced into the acid damascene plating chemistry, it will be prone to center seed corrosion as a result of the terminal effect and thus will still need to have a certain thickness (low enough Rs value). Hence, for narrow features, one-step direct plating is preferred as in this case the seed is plated in situ followed by the fill. Due to the terminal effect the in situ seed plating is confined within a small region (ring) which progresses over the wafer [43, 44, 61]. In this case, higher Rs values are actually beneficial for the process as the process is confined within a smaller region as discussed in the next section.

Example for direct copper plating on resistive none-copper seed:

Plating on foreign substrates proceeds initially through a nucleation and growth process. Hence, in this case, the i-η relationship for copper deposition on copper cannot be used. The steep increase in the nucleation peak can be fairly good simulated by a linear variation from the nucleation overpotential to the copper overpotential at the edge (or the copper front, see Sect. 6 on copper front progression). For a more accurate simulation, cyclic voltammograms can be used as empirical input, where the scan rate for the measurement corresponds to that of polarization rate due to the progression of the copper front over the wafer (see Sect. 6.1). Figure 7.20 shows the overpotential variation assuming a linear change in current density with overpotential from 0.025 V as nucleation overpotential to a copper overpotential of 0.22 V at the edge ($r = r_0$), with a current density of –10 mA/cm^2 at the edge. For direct plating purposes it is important to keep the copper deposition current on copper and thus at the edge constant (see also Sect. 7.4.3). In case of resistive substrates such as Ru and RuX, the potential drops rapidly from the edge. Nucleation occurs at an overpotential equal or larger than the nucleation overpotential, which is indicated in Fig. 7.20 as the dotted line. The inset shows the distance, Δr_{drop}, over which the potential drops from the copper overpotential at the edge to the value of the nucleation overpotential (taken here at 0.025 V). For sheet resistance values larger than 100 Ω/sq, the overpotential drop for copper plating occurs over less than 1 cm from the edge. Within this area copper nucleation will occur. The inset also shows the value for $(r_0 - r)$ at the nucleation overpotential estimated from Eq. (7.12) for the simplified case of

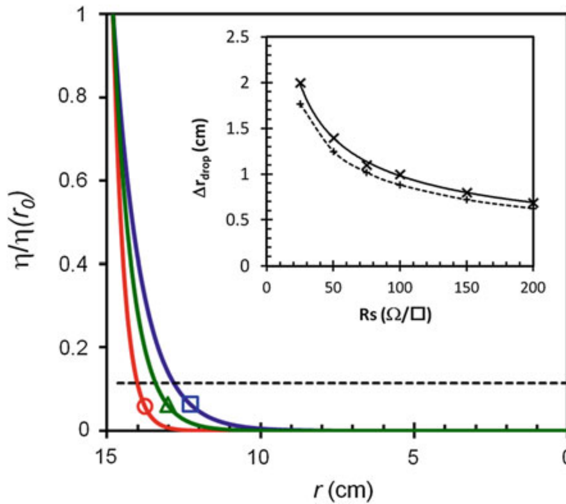

Fig. 7.20 The normalized overpotential variation as a function of radius, r, from the center of the wafer toward the edge of wafer with a radius, $r_0 = 14.8$ cm for none-copper thin film such as Ru or RuX alloys with sheet resistances of (□) 25Ω/sq.), (△) 50 Ω/sq., and (◯) 150 Ω/sq.), (×) 10 nm (2.8 Ω/sq.), 5 nm (24 Ω/sq. simulated with a zero-order Bessel function for a linear variation of current with overpotential: $i = 0.01$ A/cm^2/(0.22–0.025 V)η. The dotted line gives the normalized value of the nucleation overpotential ($\eta_{nucl}/\eta(r_0)$). The inset shows the radians difference, Δr_{drop}, over which the overpotential drops from the copper deposition overpotential at the edge, $\eta(r_0)$ to the nucleation overpotential, η_{nucl} in the plots of normalized overpotential variation (×, full line) and that estimated from Eq. (7.12) with assumption of constant current density. The difference between the simulated and estimated values is 10 %

constant current density. The difference between the estimated value and the simulated value is 10 %. Hence, Eq. (7.12) can be used to have a reliable estimate of the potential drop region in direct plating.

7.4.3 Time-Dependent Wafer Coverage

7.4.3.1 Copper Front Progression Rate

At the initial stage of direct plating, only copper nucleation will occur within a ring close to the wafer edge or terminal. When the islands coalesce they provide a conductive film (initially even a network of connected islands or porous film) on the resistive surface, effectively moving the “terminal” inward and copper nucleation will now proceed in a next region next to the first copper ring. This is a continuous process whereby the copper front thus moves radial from the edge toward the center as also the nucleation front sweeps over the surface. This process is presented schematically in Fig. 7.21 where the overpotential distribution is now shown at different times during the dynamic direct plating process. Note that the

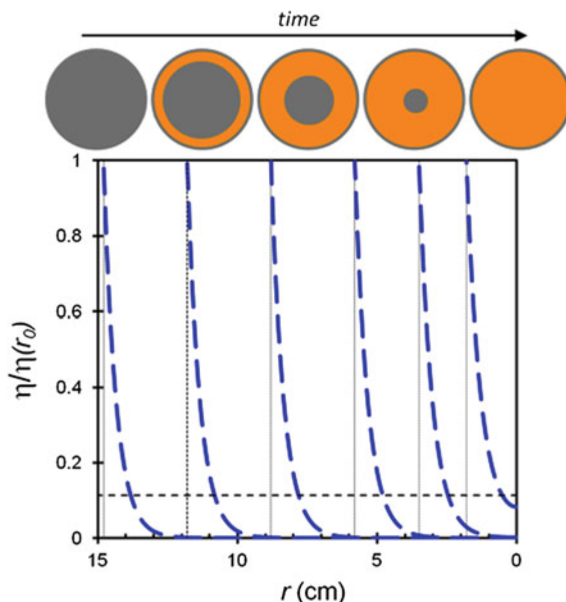

Fig. 7.21 (*top*) Schematic showing the sequential copper coverage of the wafer with time. (*bottom*) The normalized potential variation as a function of radius, r, from the center of the wafer toward the edge at different stages of copper plating with copper plated up to a distance (r–r0) of 0, 3, 6, 9, 11.3 and 13 cm (with $r_0 = 14.8$ cm) in the case of direct plating on resistive non-copper thin film such as Ru or RuX alloys with sheet resistance of 100 Ω/sq.) as simulated with a zero-order Bessel function for a linear variation of current with overpotential: $i = 0.01$ A/cm^2/(0.22–0.025 V)η. A constant overpotential of 0.22 V is assumed for the plated copper ring. The vertical dotted lines give the position of the copper front edge. The horizontal striped lines gives the normalized value of the nucleation overpotential ($\eta_{nucl}/\eta(r_0)$)

feature fill does not wait until the whole wafer is covered with copper first and thus the seed layer has to be formed in the nucleation and growth stage at the non-copper seed followed immediately by fill. Hence the current density at the already formed copper film (front) determines the fill characteristics and is the one that needs to be controlled. To keep the current density at the copper constant, the applied current needs to be adjusted according to the time-dependent plated copper area. Hence, the current is a function of the rate at which the copper front sweeps over the wafer; the copper front progression rate.

In practice, the copper front progression rate can be determined by performing time-interrupted plating experiments to measure the progress of the copper. Exact determination of the copper front can be done by Rs mapping (measurements of Rs across the wafer) but in many cases the copper front is clearly visible and can be even measured with a ruler. This type of measurements can be used to calibrate the current wave form needed to maintain constant current density throughout the plating process. Figure 7.22 shows an example of copper front progression on 300 mm blanket wafers with 4 nm RuTa film which has a sheet resistance of

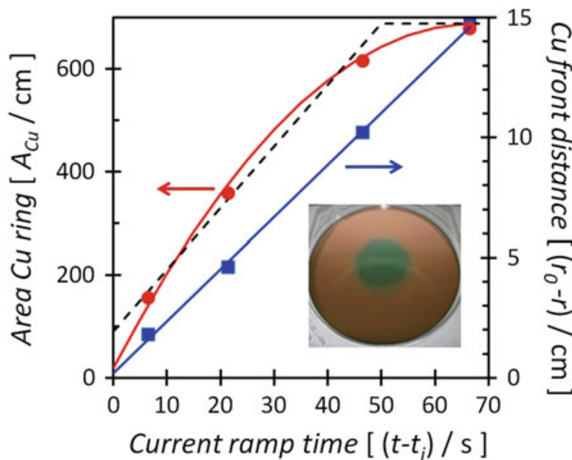

Fig. 7.22 Calibration of the current waveform for direct plating of 300 mm blanket Si/SiO_2 wafers coated with 4 nm RuTa (Rs of 130 W/sq.). Measured distance, (r_0 − r), of copper front from the wafer edge (•, *right* axis) and respective area of the plated copper ring (■, *left* axis) obtained from an interrupted linear current ramp after 15, 30, 55, and 70 s for ramp up in plating current at a rate of 0.133 A/s (i.e., from 0 to 10 A at 70 s). Before start of the ramp a cell voltage of −1.2 V was applied for 2 s which resulted in an initial ring of 2 mm. The initiation time, t_i = 8.5 s, was obtained by extrapolation of the linear (r_0 − r) relation and represents the latent time during which the current was too low to move the front forward (i.e., between 0 and 1.1A in this case). The striped line shows the linear area (current) ramp proposed from this calibration for direct plating at current density of 14.5 mA/cm^2. The inset shows the plated copper ring after a 30 s ramp. NanoPlate^{TM} 3200 copper plating chemistry: 40 g/L Cu, 100 g/L H_2SO_4, 50 ppm Cl with accelerator, suppressor, and leveler additives. The RuTa was electrochemically pretreated in HBF_4 solution. With thanks to Dr. Silvia Armini and Mr. Zaid El- *Mekki. from imec*

130 Ω/sq. First, a narrow ring of about 2 mm was made by applying a constant cell voltage of 1.2 V. This ring is used as starting point for the copper front to migrate over the wafer surface. Then, a linear current ramp from 0 to 10A over 70 s (full coverage, 14.5 mA/cm^2) is applied and subsequently the ramp is stopped at different times (15, 30, and 55 s in Fig. 7.22). The copper front progresses linearly with time after a certain latent period where the current is too low for copper front progression (nucleation). This initiation current and time are obtained from extrapolation of the linear part in the curve (8.5 s and 1.1A in this case). The slope gives the constant copper front progression rate, v_{Cu} (cm/s), which is 0.22 cm/s for Fig. 7.22. The area of the plated copper ring is then a quadratic function of time:

$$A_{Cu} = \pi\left(2v_{Cu}t - v_{Cu}^2t^2\right) \quad (7.23)$$

where t is the plating or ramp time (corrected for t_i in the case of the calibration experiment where it was started from 0A). When the current density at copper needs to be kept constant a current wave form of this shape should be applied. However, at small copper coverage (small times) also the current for nucleation on Ru in the Δr_{drop} region needs to be taken into account for the total current (is negligible at

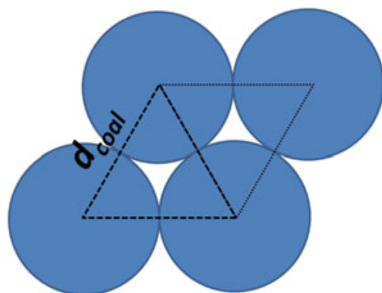

Fig. 7.23 Copper island diameter at coalescence in the ideal case of hexagonal

larger coverage). When the copper ring almost closes (r < 2 cm, see Fig. 7.21) also the center is covered with copper islands already growing out to a coalesced film. Hence, at small and large times, the current should be taken somewhat higher than just proportional to A_{Cu} (Eq. 7.23) and the desired current density (14.5 mA/cm^2 in this case). The current waveform can then be approached by a linear ramp as that shown by the dotted line in Fig. 7.22: (I = 1.3A + 0.6A/s × time) for 50 s after which the current remains at 10A. In this simulation the copper fill should occur at a current density between 14 and 15 mA/cm^2.

7.4.4 Relationship Between Electrochemical Measurements and Copper Front Progression Rate

7.4.4.1 Coalescence Thickness

The rate at which the copper front progresses over the wafer is dependent on the rate of film coalescence [62]. The film coalescence time and thickness are in their turn determined by the nucleation rate and thus the island density, as well as by the shape of the particle during subsequent growth. Flattened particles (i.e., toward 2D growth) will give faster coalescence and thus a thinner coalesce thickness (see Fig. 7.23).

The *coalescence charge density*, q_{coal} ($C\ cm^{-2}$), is related to the *copper island density*, N_p (C.m^{-2}), through:

$$q_{\text{coal}} = \frac{n\pi F\rho}{xMw} N_p d_{\text{coal}}^3 \tag{7.24}$$

with d_{coal} the average diameter of the copper islands at coalescence and x is a shape factor where x = 6 for spherical particles, x = 12 for hemispherical particles, and x > 12 for flattened particles (toward 2D or pancake-shaped particles). For Eq. (7.24) the ideal case for the hexagonal stacking of copper islands is assumed (Fig. 7.24). This can be seen as the lower limit for coalesce. In reality the stacking will be more random and q_{coal} will be higher. For the case of the flattened particle, we can take the volume of a hemisphere segment as shown in Fig. 7.25, where the height of the particle, h, is a fraction y of its diameter:

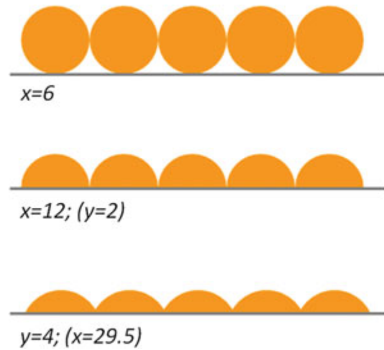

Fig. 7.24 Modes of island coalescence: spherical particles, hemispherical particles, and "flattened" particles, represented by their shape factors x and y defined in Eq. (7.25)

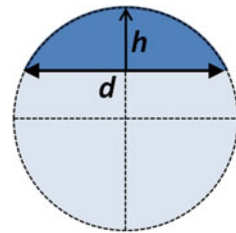

Fig. 7.25 For simulation of the "flattened" island a segment of a hemisphere is assumed with height h and island diameter, d

$$x = \frac{24y^3}{3y^2 + 4} \quad \text{for} \quad h = \frac{d_{\text{coal}}}{y} \tag{7.25}$$

When we assume a hexagonal closed packed stacking of the particles then:

$$N_p^{-1} = \frac{\sqrt{3}}{2}(d_{\text{coal}})^2 \tag{7.26}$$

Substitution of Eq. (7.26) into (7.24) gives:

$$q_{coal} = \frac{n\pi F\rho}{xMw\sqrt{N_p}} \tag{7.27}$$

The coalescence charge is directly proportional to the coalescence time when the current density is kept constant. Note that the current density is a function of the applied current and the effective surface area where copper plating takes place. As the latter changes as the copper front moves over the surface, the current needs to be adjusted accordingly if we want the current density and thus coalescence charge (and coalescence time and thickness as well as the island density) to be constant throughout the direct plating process.

7.4.4.2 Relationship Between Coalescence Thickness and Overpotential

In Sect. 7.3.2 an exponential relationship between copper island density, N(η) and copper deposition overpotential, η_{Cu}, was determined (Eq. (7.5)). As nucleation only starts when a sufficient overpotential for nucleation is applied, $\eta_{Cu} \geq \eta_{nucl,}$ a more accurate description for island density, $N_p(\eta)$, with overpotential is given as

$$N_p(\eta) = N_{\eta,\text{nucl}} \exp\left[-\frac{\alpha F}{RT}(\eta - \eta_{\text{nucl}})\right] \tag{7.28}$$

with η_{nucl} the nucleation overpotential (typically around −25 mV) and $N_{\eta,nucl}$, the island density at η_{nucl} (also in short indicated as N_0) which depends mostly on the substrate and its surface condition (see also Sects. 7.3.2 and 7.3.3).

Figure 7.26 shows the island density, N_p, as a function of copper deposition overpotential for different cases of cupric ion concentration, in the presence and absence of polyether suppressor additives, showing the universal character of Eq. (7.28). The island density was measured after galvanostatic deposition at different current densities from H_2SO_4 solutions with $CuSO_4$ concentrations ranging between 0.01 and 0.6 M. When the island density is plotted as a function of the copper deposition overpotential, the exact same exponential relationship is found in all cases. When suppressor additives are added to the solution, the island density increases as expected but follows the same exponential relationship (compare 1, 2 with 3, 4 and 4, 5). The preexponential factor includes an intrinsic nucleation density which is a function of substrate material as well as its surface condition. The preexponential $N_{\eta, nucl}$ is equal to the smallest island density obtained at the nucleation overpotential. For example, copper nucleation on RuTa alloy has a $N_{\eta,\ nucl} = 1 \times 10^7\ cm^{-2}$. After electrochemical of chemical pretreatment to remove the native oxide and carbon contamination, $N_{\eta,\ nucl}$ increases to $1 \times 10^7\ cm^{-2}$. Figure 7.26 thus proves that additives and surface treatments do affect the island density through their respective effects on the deposition overpotential and the inherent island density (preexponential factor $N_{\eta,\ nucl}$ in Eq. (7.28)).

The coalescence charge density can now be written as a function of the copper deposition overpotential at the copper front:

$$q_{\text{coal}} = \frac{n\pi F\rho}{xMw\sqrt{N_{\eta,\text{nucl}}}} \exp\left[\frac{\alpha F}{RT}(\eta - \eta_{\text{nucl}})\right] \tag{7.29}$$

Note that q_{coal} is easily converted into an equivalent copper thickness (coalescence thickness, b_{coal}) by dividing it by 2.72 mC/cm^2, which is the equivalent charge density for a 1 nm copper film. Figure 7.27 shows the coalescence thickness or in situ copper seed thickness based on Eq. (7.29). The coalescence thickness can be tuned by overpotential (but limited by the maximum allowed current density for copper fill), by $N_{,nucl}$ through choice of substrate (limited by barrier properties) and surface pretreatment and the shape factor, x, which can be tuned by additives. Next to polarization of the overpotential, the addition of

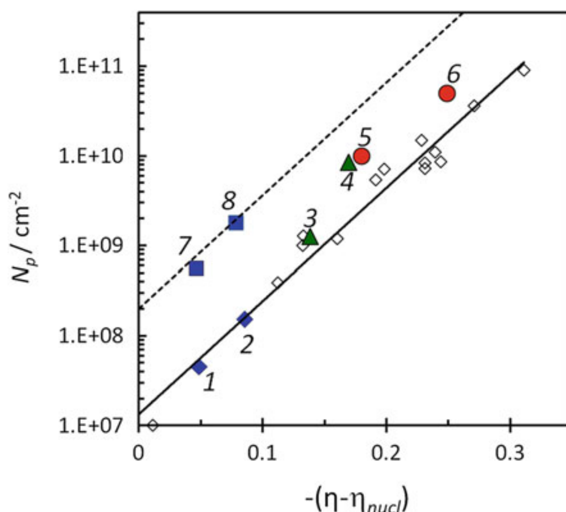

Fig. 7.26 Copper island density, N_p, as a function of (□-□$_{nuc}$) with, □, the copper deposition overpotential (for normalized copper island area of 0.19, and corrected for IR drop) and □$_{nucl}$ = −0.025 V, for galvanostatic deposition on 2 nm RuTa from (◇) solutions of 1.8 mol dm^{-3} H_2SO_4, 1.4 mmol dm^{-3} HCl and 10, 50, 100, and 600 mmol dm^{-3} $CuSO_4$; current densities between (−2.5 and −10 mA cm^{-2} for the 10, 50, and 100 mmol dm^{-3} solutions and −1−−200 mA cm^{-2} for the 600 mmol dm^{-3} solution); indicated cases are **1** 600 mM $CuSO_4$, −2.5 mA/cm^2, **2** 600 mM $CuSO_4$,−5 mA/cm^2. All data points fit to Eq. (7.28) irrespective of cupric ion concentration, with N$_{□,\ nucl}$ = 1×10^7 cm^{-2} and(□F/RT = 29 V^{-1}); the highest overpotentials are obtained for lowest $CuSO_4$ concentrations[43, 44]. Island density for 600 mM solution with the addition of the suppressors (△) PEG4000 and (◯) PPG725 for deposition at −2.5 mA/cm^2 (3, 5) and −5 mA/cm^2 (5, 6). Island density for the case of electrochemically pretreated RuTa surface in HBF_4 solution [45]; (7) 600 mM $CuSO_4$, −2.5 mA/cm^2 and (8) 100 mM $CuSO_4$, −2.5 mA/cm^2. With thanks to Drs. Magi Nagar from imec

suppressor additives typically results in flattening of the particle shape as well [48]. The overpotential can be tuned by inorganic chemistry as well. Lower $CuSO_4$ concentration results in polarization of the i-U curves (Fig. 7.26), but cupric ion depletion can be an issue. Also, the addition of suppressor and leveler additives polarize the i-V characterictics, but is limited by the requirment of void-free filling or superfilling of the features after the formation of the in situ seed. From Fig. 7.27, it follows that formation of 10 nm of in situ seed is easily attainable even for the rather low $N_{,nucl}$ of 10^7 islands per cm^2 (case of nontreated RuTa) and definitely for $N_{,nucl}$ of 10^8 cm^{-2} (case of pretreated RuTa surface), especially when the islands are somewhat flattened. To extend direct plating to technologies below 10 nm, not more than 1 nm of in situ copper seed would be allowed when a barrier/layer combo (e.g., RuTiN) of about 1 nm can be made [2]. The effective aspect ratio in this case would be already a factor 1.7 larger than the targeted aspect ratio of the 10 nm trench or via features, making void-free fill more

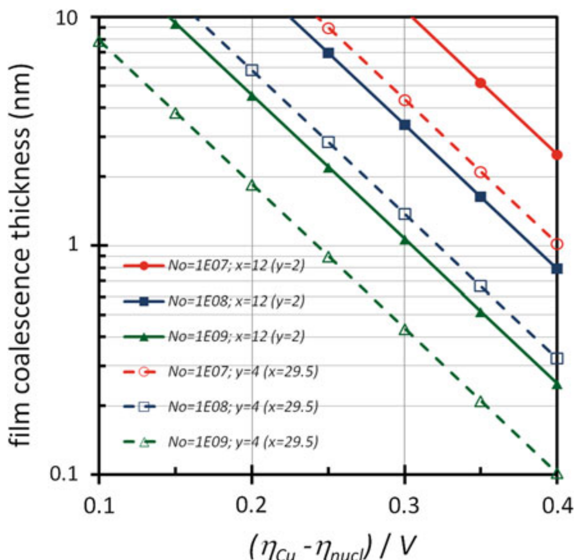

Fig. 7.27 Simulation of the film coalescence thickness as a function of copper overpotential based on Eq. (7.29) for different values of preexponential factor, $N_{\square,nuc,}$ (indicated as No in legend)and for hemisperical (x = 12) and half hemispheres (y = 4)

difficult. Hence, the selection of substrates and surface pretreatments or functionalisation that allow higher $N_{,nucl}$ are desired.

7.4.4.3 Relationship Between Copper Progression of Overpotential Polarization for Nucleation

The copper front progression rate, v_{Cu}, is linked to the electrochemical response as the peak in the cyclic voltammogram and the step in the potential transients are linked to the coalescence of the copper islands [62]. As shown below, we can make estimative predictions on the rate of copper rate progression, from the coalescence charge and time obtained from electrochemical measurements. However, only quantitative modeling of the microscopic nucleation process in combination with the macroscopic current distribution and terminal effect can give a full picture of wafer scale direct plating process [52, 55] see Fig. 7.28.

The copper front progression rate is given as

$$v_{Cu} = \frac{d(r_0 - r_{Cu(t)})}{dt} \tag{7.30}$$

with $r_{Cu(t)}$, the time-dependent radius of the copper front from the wafer center and r_0, the wafer radius (i.e., 14.8 cm in case of a 300 mm wafer with 2 mm edge exclusion of the sealed ring contact).

As the copper front moves over the wafer surface, the potential drop over the resistive non-copper substrate preceding the copper at radius $(r_0 – r_{Cu(t)})$ also sweeps over the wafer. The overpotential for copper plating, η_{cu}, is below the

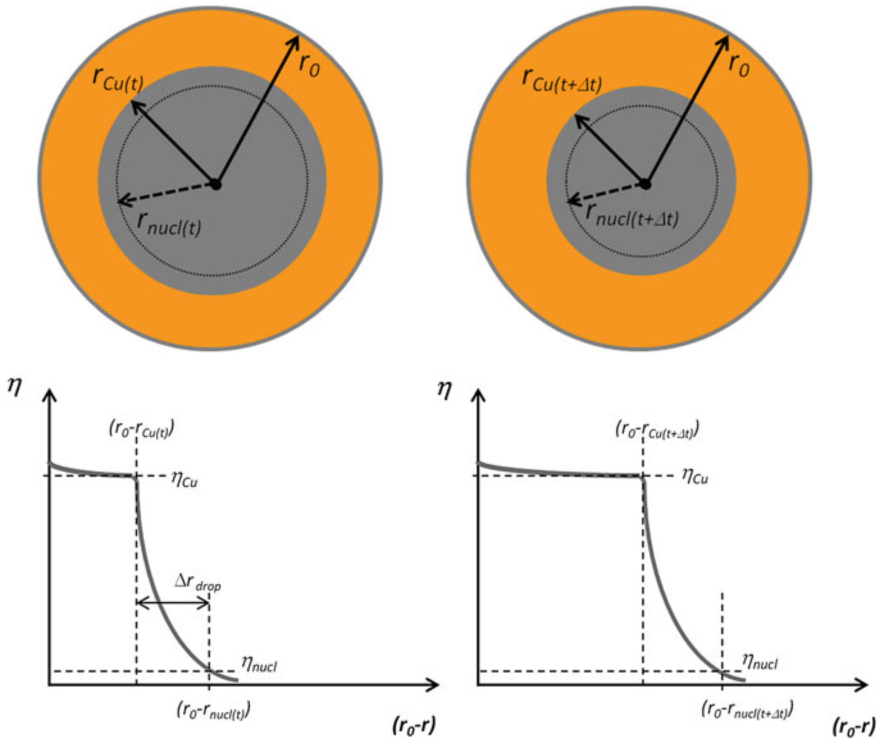

Fig. 7.28 Schematic representation of position on the wafer of copper front and nucleation fronts at time t and t + dt (*top*) and the corresponding overpotential profiles

nucleation overpotential, $0 < \eta < \eta_{\mathrm{nucl}}$, for most of the noncovered resistive substrate surface, except for the region close to the copper front, Δr_{drop}, where the overpotential drops from the overpotential of copper deposition, η_{cu}, at the copper film position $(r_0 - r_{Cu(t)})$ to the nucleation overpotential, η_{nucl}, at position $(r_0 - r_{nucl(t)})$ on the wafer. Thus, at time, t, the overpotential at position $(r_0 - r_{nucl(t)})$ reaches η_{nucl} at which point nucleation will start at this position. The overpotential in this spot increases now to η_{cu} over the time period Δt. Hence, this particular position goes through a change in overpotential with a polarization rate, v_p *(V/s)*, given as

$$v_p = \frac{d\eta}{dt} \approx \frac{(\eta_{Cu} - \eta_{\mathrm{nucl}})}{\Delta t} \tag{7.31}$$

for a quasi linear variation of the overpotential (in correspondence with linear potential variation in cyclic voltammetry). Coalescence of copper islands occurs within this time period and we can assume $\Delta t = \Delta t_{\mathrm{coal}}$ and the copper progression is given as

$$v_{Cu} = \frac{\Delta r_{\mathrm{drop}}}{\Delta t_{\mathrm{coal}}} \tag{7.32}$$

whereby Δr_{drop} can be calculated from the Bessel function. A higher sheet resistance gives rise to smaller Δr_{drop} indicating that the progression rate would be faster for more resistive substrates. However, a smaller Δr_{drop} will also give a faster polarization rate which may affect Δt_{coal}. The relationship between polarization rate and copper progression rate is found by the combination of Eqs. (7.31) and (7.32):

$$v_p \approx \frac{(\eta_{Cu} - \eta_{\mathrm{nucl}})}{\Delta r_{\mathrm{drop}}} \times v_{Cu}. \tag{7.33}$$

Fast copper progression rates thus correspond to fast polarization rates. This is intuitively understood as fast polarization rates corresponding to faster nucleation rates, higher island densities, and thus faster film coalescence. *In the wafer scale plating experiments of* Fig. 7.22*, the experimental copper progression rate was 0.22 cm/s for an average effective current density of 15* mA/cm^2 where $(\eta - \eta_{\mathrm{nucl}}) = 0.22$ V and $\Delta r_{\mathrm{drop}} = 1$ cm for *Rs* of 130 Ω/sq (Fig. 7.20) *or thus nucleation of copper islands in* Δr_{drop} *region occurred at a polarization rate of 50* mV/s. For simulation of overpotential distribution as in Fig. 7.20, a cyclic voltammogram at 50 mV/s could then be used as imperial input (as was done for the case of thin copper seed in Fig. 7.19).

The coalescence charge, q_{coal}, is obtained by integration of the current in the Δr_{drop} region:

$$q_{\mathrm{coal}} = \Delta t_{\mathrm{coal}} \int_{r_{Cu(t)}}^{r_{Cu(t+\Delta t)}} di_r \tag{7.34}$$

with i_r the local current density at position r. Assuming a linear variation of the current from 0 at $r_{\mathrm{nucl}(t)}$ to i_{Cu}, the copper plating current at the copper film, q_{coal} simplifies to

$$q_{\mathrm{coal}} \approx \frac{i_{Cu}}{2} \Delta t_{\mathrm{coal}} \tag{7.35}$$

Insertion of Eq. (7.35) into (7.32) gives the relationship between copper progression rate over the wafer, $\boldsymbol{v_{Cu}}$, the coalescence charge, q_{coal}, the effective current density at the copper film, i_{Cu}, and the width of the potential drop, Δr_{drop}:

$$v_{Cu} \approx \frac{i_{Cu} \Delta r_{\mathrm{drop}}}{2 q_{\mathrm{coal}}} \tag{7.36}$$

Smaller coalescence thickness and higher current density give rise to faster progression rates. Or, vice versa, when slower progression rates are observed, the in situ seed layer will be thicker. *In the wafer scale plating experiments of Fig. 7.22, the experimental copper progression rate was 0.22 cm/s for an average effective*

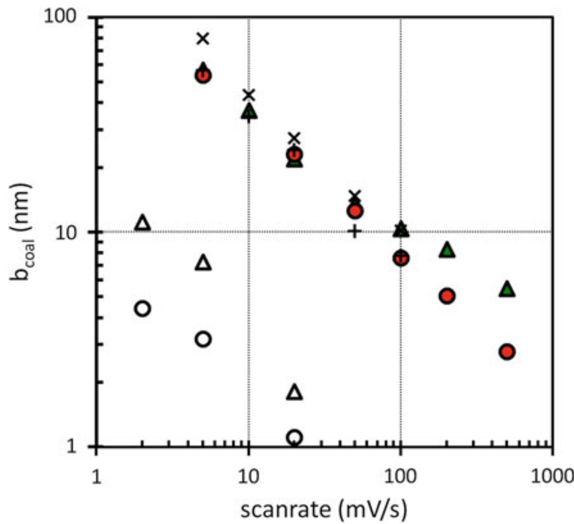

Fig. 7.29 The coalescence thickness, b_{coal}, determined from the charge under the suppression peak in cyclic voltammograms recorded at as received 2 nm PVD RuTa (▲, ×, +), as received ALD Ru (●), EC-pretreated RuTa (△) and EC-pretreated Ru (◯). Nanoplate™ NP3200 copper chemistry with suppressor additive only (15ml/l S)(▲, △, •, ◯), with suppressor and accelerator additives (15ml/l S, 10ml/l A) (×) and suppressor, accelerator, and leveler additives (15ml/l S, 10ml/l A, L); electrochemically pretreatment in 10 % vol. sulfuric at − 10mA/cm^2, sample area 0.071cm^2

current density of 15 mA/cm^2. For an Rs value of 130 Ω/sq, Δr_{drop} = 1 cm (*Fig.* 7.20), *that means an in situ copper seed of about 12.5 nm which is suitable for features down to 65 nm, as verified experimentally* [60, 61]. *Conversely, for a coalescence thickness of 1 nm if direct plating was to be extended to feature sizes below 10 nm, copper progression rates larger than 1.8 cm/s are required, i.e., full wafer coverage in less than 8 s.*

Insertion of Eq. (7.35) into (7.31) similarly gives the relationship between polarization rate and coalescence charge:

$$v_p \approx \frac{i_{Cu}(\eta_{Cu} - \eta_{\text{nucl}})}{2q_{\text{coal}}} \tag{7.37}$$

indicating an inverse relationship between coalescence thickness and polarization rate as a result of the passing by of the nucleation front with width of Δr_{drop}. *For a coalescence thickness of 1 nm, a polarization rate larger than 350 mV/s is required to provide the necessary island density.*

An important consequence from the above exercise is that the nucleation and growth process during direct plating occurs during a potential sweep and not a potential step. As such cyclic voltammetry experiments may give a more realistic view on attainable particle densities and film coalescence thickness. Thus, where potential and current step experiments can give information about maximum or

steady-state island density as discussed in Sect. 7.3, cyclic voltammograms can give potentiodynamic information and relate to the copper progression rates needed to achieve desired coalescence thickness.

In Figs. 7.14 and 7.15, cyclic voltammograms were shown for copper deposition on RuTa in the presence of chloride and suppressor additives. The suppression peak in the CV is the result of nucleation and growth, coalescence of the film and inhibition of the copper deposition rate on copper by additive adsorption. The area under the peak is a measure for the coalescent charge and equivalent film thickness (see Sect. 7.3.4). Figure 7.29 shows the coalescence thickness estimated from the charge under the suppression peaks in cyclic voltammograms measured on Ru and RuTa substrates at different polarization rates. The effect of surface pretreatment is also included. The coalescence thickness decreases with scan rate as predicted by Eq. (7.37), even though with a power between −0.6 and −0.8, i.e., lower than −1. Electrochemical pretreatment does lower the coalescence thickness considerably, in accordance with the increase in $N_{\eta,\ \mathrm{nucl}}$ in Fig. 7.26. The effect of additives is small; the addition of accelerator gives slightly thicker coalesced films, and the subsequent addition of lever again lowers it, as expected from their respective effects on the overpotential (and thus island density, see Eq. (7.29). *To achieve a coalescence thickness of 1 nm on EC-pretreated RuTa, a polarization rate of more than 100 mV/s is needed in reasonable agreement with the assessment for wafer scale plating above.*

7.5 Conclusions

To make direct plating work, a profound electrochemical understanding of the direct plating process is needed, which indicates that specialists are needed from the concept to production stages. Further, it requires a close synergy between the developments in the electrochemical process, the non-copper seed layer and the hardware. In many cases, researchers and engineers do not have control over at least one of these. These complications have in my opinion held back the introduction of direct plating in a manufacturing environment. In this chapter, we have tried to give an overview of most of the factors involved in the direct plating process with a good background on the fundamentals for better understanding. Unfortunately, we could not provide all details and for that we refer to the many references. The main focus was placed on the formation of an initial continuous copper film or in situ seed layer as this step is essential for defect-free plating process. The fill of the features itself was not treated extensively as, once the in situ process is in place, the superfill follows suit and optimization is done similar to the conventional damascene plating process. Important for wafer scale uniform fill is that the local current density is the same after the in situ seed is formed for each feature. Methods to control the local current density were treated in this chapter. It needs mention that recently superconformal fill has been demonstrated also from low cupric ion containing baths, both acidic and alkaline [63, 64]. In this

way, the advantage of high overpotential in low cupric ion baths (thin coalesced copper film) can be combined with fill.

References

1. Volders H, Carbonell L, Heylen N, Kellens K, Zhao C, Marrant K, Faelens G, Conard T, Parmentier B, Steenbergen J, Van de Peer M, Wilson CJ, Sleeckx E, Beyer GP, Tokei Z, Gravey V, Shah K, Cockburn A (2011) Barrier and seed repair performance of thin RuTa films for Cu interconnects. Microelectron Eng 88(5):690–693
2. Armini Silvia, Tokei Zsolt, Volders Henny, El-Mekki Zaid, Radisic Aleksandar, Beyer Gerald, Ruythooren Wouter, Vereecken PM (2011) Impact of "terminal effect" on Cu electrochemical deposition: filling capability for different metallization options. Microelectron Eng 88:754–759
3. Andricacos PC, Uzoh C, Dukovic JO, Horkans J, Deligianni H (1998) Damascene copper electroplating for chip interconnections. IBM J Res Devel 42:567
4. Lantasov Y, Palmans R, Maex K (2000) Direct copper electroplating. In: Edelstein D, Dixit G, Yasuda Y, Ohba T (eds) Advanced metallization conference 2000 (AMC 2000), proceedings of the conference pp 145–151
5. Venables JA (2000) Introduction to surface and thin film processes. University Press, Cambridge
6. Oskam G, Long JG, Natarajan A, Searson PC (1998) Electrochemical deposition of metals on silicon. J Phys D Appl Phys 31:1
7. Oskam G, Vereecken PM, Searson PC (1999) Electrochemical deposition of copper on n-Si/TiN. J Electrochem Soc 146:1436
8. Milchev A (2002) Electrocrystallization: fundamentals of nucleation and growth. Kluwer Academic Publishers, Norwell
9. Budevski E, Staikov G, Lorentz WJ (1996) Electrochemical phase formation and growth. VCH, New York
10. Southampton Electrochemistry Group (1985) Instrumental methods in electrochemistry. Ellis Horwood Limited, New York
11. Milchev A, Stoyanov S, Kaischev R (1974) Atomistic theory of electrolytic nucleation: I. Thin Solid Films 22:255
12. Milchev A, Stoyanov S, Kaischev R (1974) Atomistic theory of electrolytic nucleation: II. Thin Solid Films 22:267
13. Becker R, Doring W (1935) Ann Phys 24:719
14. Walton D (1962) Nucleation of vapor deposits. J Chem Phys 37:2182
15. Polewska W, Behm RJ, Magnussen OM (2003) In-situ video-STM studies of Cu electrodeposition on Cu(100) in HCl solution. Electrochim Acta 48:2915
16. Magnussen OM, Zitzler L, Gleich B, Vogt MR, Behm RJ (2001) In-situ atomic-scale studies of the mechanisms and dynamics of metal dissolution by high-speed STM. Electrochim Acta 46:3725
17. Yanson Y (2012) How additives affect Cu electrodeposition: an electrochemical STM study. PhD Thesis, Universiteit Leiden, 2012
18. Radisic A, Vereecken PM, Hannon JB, Searson PC, Ross FM (2006) Quantifying electrochemical nucleation and growth of nanoscale clusters using real-time kinetic data. Nano Lett 6:238
19. Radisic A, Ross FM, Searson PC (2006) In situ study of the growth kinetics of individual Island electrodeposition of copper. J Phys Chem B 110:7862
20. Radisic A, Vereecken PM, Searson PC, Ross FM (2006) The morphology and nucleation kinetics of copper islands during electrodeposition. Surf Sci 600:1817

21. Avrami M (1939) Kinetics of phase change. I. General theory. J Chem Phys 7:1103
22. Avrami M (1940) Kinetics of phase change. II. Transformation-time relations for random distribution of nuclei. J Chem Phys 8:212
23. Avrami M (1941) Kinetics of phase change. II. Granulation, phase change, and microstructure. J Chem Phys 9:177
24. Abayaneh MY (1982) Calculation of overlap for nucleation and three-dimensional growth of centers. Electrochim Acta 27:1329
25. Bosco E, Rangarajan SK (1982) Electrochemical phase formation (ECPF) and macrogrowth. part I. Hemispherical models. J Electroanal Chem 134:213
26. Bosco E, Rangarajan SK (1982) Electrochemical phase formation (ECPF) and macrogrowth. part II. Two-rate models. J Electroanal Chem 134:225
27. Bobbert PA, Wind MM, Vlieger J (1987) Diffusion to a slowly growing truncated sphere on a substrate. Phys A 141:58
28. Gunawardena G, Hills GJ, Montenegro I, Scharifker BR (1982) Electrochemical nucleation. Part 1. General consideration. J Electroanal Chem 138:225
29. Scharifker BR, Hills GJ (1983) Theoretical and experimental studies of multiple nucleation. Electrochim Acta 28:879
30. Scharifker BR, Mostany J (1984) Three-dimensional nucleation with diffusion controlled growth. Part 1. Number density of active sites and nucleation rates per site. J Electroanal Chem 177:13
31. Hoffmann PM, Radisic A, Searson PC (2000) Growth kinetics for copper deposition on Si (100) from pyrophosphate solution. J Electrochem Soc 147:2576
32. Radisic A, Long JG, Hoffmann PM, Searson PC (2001) Nucleation and growth of copper on TiN from pyrophosphate solution. J Electrochem Soc 148:C41
33. Radisic A, West AC, Searson PC (2002) Influence of additives on nucleation and growth of copper on n-Si.111. from acidic sulfate solutions. J Electrochem Soc 149:C94
34. Radisic A, Cao Y, Taephaisitphongse P, West AC, Searson PC (2003) Direct copper electrodeposition on TaN barrier layers. J Electrochem Soc 150:C362
35. Radisic A, Oskam G, Searson PC (2004) Influence of oxide thickness on nucleation and growth of copper on tantalum. J Electrochem Soc 151:C369
36. Guo L, Radisic A, Searson PC (2006) Electrodeposition of copper on oxidized ruthenium. J Electrochem Soc 153:C840
37. Palmisano F, Desimoni E, Sabbatini L, Torsi G (1979) Nucleation phenomena in the electrodeposition of lead onto glassy-carbon electrodes. J Appl Electrochem 9:517
38. Jacobs JWM (1988) J Electroanal Chem 247:135
39. Oskam G, Searson PC (2000) Electrochemistry of gold deposition on n-Si(100). J Electrochem Soc 147(6):2199–2205
40. Chyan O, Arunagiri TN, Ponnuswamy T (2003) Electrodeposition of copper thin film on ruthenium : a potential diffusion barrier for Cu interconnects. J Electrochem Soc 150:C347
41. Emekli U, West AC (2009) Effect of additives and pulse plating on copper nucleation onto Ru. Electrochimica Acta 54:1177
42. Guo L, Thompson A, Searson PC (2010) The kinetics of copper island growth on ruthenium oxide in perchlorate solutions. Electrochim Acta 55:8416
43. Radisic A, Boelen P, Rosenfeld A, Hernandez JL, Beyer GP, Vereecken PM (2008) Electrochemical nucleation and growth of copper on resistive substrates. ECS Trans 11:25
44. Radisic A, Nagar M, Strubbe K, Armini S, El-Mekki Z, Volders H, Ruythooren W, Vereecken PM (2010) Copper plating on resistive substrates, diffusion barrier and alternative seed layers. ECS Trans 25:175
45. Milchev A, Montenegro MI (1992) A galvanostatic study of electrochemical nucleation. J Electroanal Chem 333:93
46. Nagar M, Radisic A, Strubbe K, Vereecken PM (2013) The effect of cupric ion concentration on the nucleation and growth of copper on RuTa seeded substrates. Electrochim Acta 92:474–483

47. Nagar M, Radisic A, Strubbe K, Vereecken PM (2012) Nucleation and growth of copper on Ru-based substrates: I. The effect of the inorganic components. ECS Trans 41:75
48. Nagar M, Radisic A, Strubbe K, Vereecken PM (2012) Nucleation and growth of copper on Ru-based substrates: II. The effect of the suppressor additive. ECS Trans 41:99
49. Andricacos P, Deligianni H, Horkans WJ, Kwietniak KT, Lane M, Malhotra SG, Mc Feely FR, Murray C, Rodbell KP, Vereecken PM (2005) Method for electroplating on resistive substrates. U.S. Patent Application Pub. No US2004069648 A1, (2004), U.S. Patent. No.US 6,974,531 B2 (2005)
50. Moffat TP, Walker M, Chen PJ, Bonevich JE, Egelhoff WF, Richter L, Witt C, Aaltonen T, Ritala M, Leskelä M, Josell D (2006) Electrodeposition of Cu on Ru Barrier layers for damascene processing. J Electrochem Soc 153:C37–C50
51. Vereecken PM, Radisic A A pre-treatment method to increase Cu island density of Cu on barrier layers", U.S. Patent Application Pub. No. US2010/0273323 A1
52. Desprez P, Matlosz M, Yang JDL, West AC (1998) Estimation of front velocity in electrodeposition onto highly resistive substrates. J Electrochem Soc 145(1):165–171
53. Takahashi KM (2000) Electroplating copper onto resistive barrier films. J Electrochem Soc 147:1414
54. Purcar M, Van den Bossche B, Bortels L, Dekoninck J, Nelissen G (2004) Three-dimensional current density distribution simulations for a resistive patterned wafer. J Electrochem Soc 151:D78
55. Armini S, Vereecken PM (2010) Impact of "Terminal Effect" on Cu plating: theory and experimental evidence. ECS Tran. 25(27):185
56. Yang L, Radisic A, Nagar M, Deconinck J, Vereecken PM, West A (2012) Multi-scale modeling of direct copper plating on resistive non-copper substrates. Electrochim Acta 78:524–531. doi:10.1016/j.electacta.2012.06.076
57. Deligianni H, Dukovic JO, Andricacos PC, Walton EG (1999) Electrochemical processing in ULSI fabrication and semiconductor/metal deposition II. In: Andricacos PC, Searson PC, Reidsema-Simpson C, Allongue P, Stickney JL, Oleszek GM (eds) Electrochemical society proceedings. The electrochemical society, Pennington, NJ, vol 99-9, p 83
58. Fang R, Namiki K, Vereecken PM, Kwietniak K, Baker BC, Ide K, Suzuki H, Kanda H, Mishima K, Musaka K, Deligianni H (2005) Uniform copper electroplating on resistive substrates. In: Electrochemical processing in ULSI fabrication I, (ECS meeting 2004) The electrochemical society, Pennington, NJ
59. Lane MW, Murray CE, McFeely FR, Vereecken PM, Rosenberg R (2003) Liner materials for direct electrodeposition of Cu. Appl Phys Lett 83:2330
60. Malhotra SG, Canaperi D, Chiras S, Deligianni L, Johnson G, Krishnan M, Lane M, McFeely F, Murray C, Ponoth S, Simon A, Spooner T, Vereecken P, Yurkas J (2005) Integration of direct plating of Cu onto a CVD Ru liner. In: Erb D, Ramm P, Masu K, Osaki A, Warrendale MRS (eds) Conference Proceedings of AMC 2004, PA, p 525
61. Armini Silvia, Demuynck Steven, El-mekki Zaid, Swerts Johan, Nagar Magi, Radisic Alex, Heylen Nancy, Beyer Gerald, Leunissen Leonardus, Vereecken Philippe (2011) Direct copper electrochemical deposition on Ru-based substrates for advanced interconnects target 30 nm and 1/2 pitch lines: from coupon to full-wafer experiments. ECS Trans 35(2):117
62. Willey Mark J, Emekli Ugur, West Alan C (2008) Uniformity effects when electrodepositing Cu onto resistive substrates in the presence of organic additives. J Electrochem Soc 155(4):D302–D307
63. Atanasova TA, Carbonell L, Caluwaerts R, Tokei Z, Strubbe K, Vereecken PM (2012) Ultra-low copper baths for sub-35 nm copper interconnects. ECS Trans 41(35):83–97
64. Joi A, Landau U (2011) An alkaline copper plating process providing high nucleation density on Ru and bottom-up fill. In: Abstract #1944, 220th ECS meeting

Part III
Through Silicon Via and Other Methods

Chapter 8
Through Silicon Via

Kazuo Kondo

8.1 Introduction

The development of semiconductor devices is clearly represented by Moor's law. Moor's law, formulated by Gordon Moor at Intel, predicts that the semiconductor transistor number is doubled every 1.5 years, and this trend has held since the birth of the Intel microprocessor 4004 in 1965. Because of the limits of miniaturization in transistor fabrication, deviation from Moor's law in recent years has become an obstacle to the development of semiconductor devices. Based on a completely different concept of miniaturization—stacking of chips in the z-direction—a drastic increase in transistor number has been achieved [1]. This chip stacking technology is called "three dimensional packaging" (Fig. 8.1). The upper graph shows four chips mounted on a printed circuit board (PCB). If four chips are stacked in z-direction as shown in Fig. 8.1 , the chip size is reduced by a factor of four. Since the transistor depth is less than 1 μm and silicon chips are a few 10 μms in thickness after thinning by chemical mechanical polishing (CMP), vias are necessary to connect upper transistors to lower transistors. Hence, these are through silicon vias, TSV (Fig. 8.1 arrow). Suppose the size of chip is 1.0 cm sq and four chips are mounted on a PCB (Fig. 8.1), the signal length is 4 cm from the left solder bump to the right solder bump. With three-dimensional packaging (Fig. 8.1), the signal lengths are several tens of μms, and they are interconnected by TSVs. These shorter signal lengths are well suited for high frequency digital signal transmission.

Typical methods and materials for the TSV fabrication process are shown in Fig. 8.2:

1. High aspect ratio via etching by reactive ion etching (RIE).
2. Insulator layer formation by thermal SiO_2 or chemical vapor deposition (CVD).
3. Barrier metal layer formation by sputter or CVD.

K. Kondo (✉)
Department of Chemical Engineering, Osaka Prefecture University, Osaka, Japan
e-mail: kkondo@chemeng.osakafu-u.ac.jp

K. Kondo et al. (eds.), *Copper Electrodeposition for Nanofabrication of Electronics Devices*, Nanostructure Science and Technology 171, DOI: 10.1007/978-1-4614-9176-7_8,

© Springer Science+Business Media New York 2014

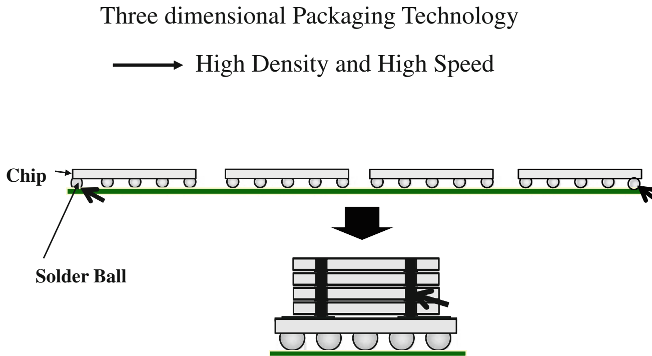

Fig. 8.1 Three-dimensional packaging technology enables high density and high speed digital signal transmission. The packaging area shrinks to ¼ size if the four chips are stacked. A shorter signal length of several 10 μm is realized. The shorter signal length enables high speed digital signal transmission

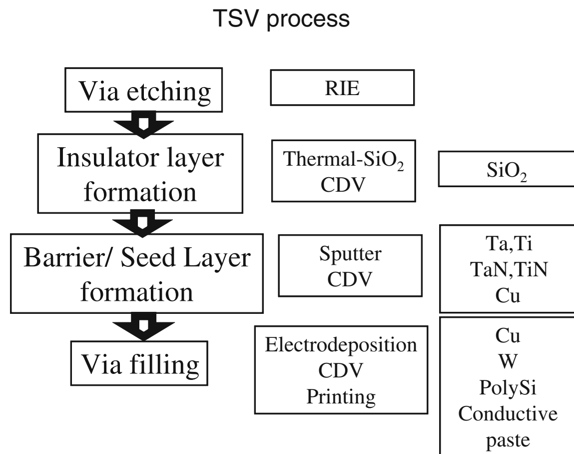

Fig. 8.2 Typical methods and materials for the TSV formation process

4. Copper seed layer by sputter or CVD.
5. Aspect ratio via filling by electrodeposition, CVD or printing.

Several methods are proposed in order to fill TSVs. They are electrodeposition, CVD, and printing. CVD is expensive and high aspect ratio vias are impossible to fill by printing. Electrodeposition is therefore the most suitable process for TSV filling. Several candidate materials have also been proposed for TSV filling. They are copper, tungsten, poly silicon, and conductive paste. Of these, copper has the lowest resistivity and is most suited for the TSV filling materials.

There are three alternative sequences for TSV fabrication: via-first process, via-middle process or via-last process (Fig. 8.3) depending on when the TSV is formed. TSV fabrication consists of via formation (etching, and insulator, barrier

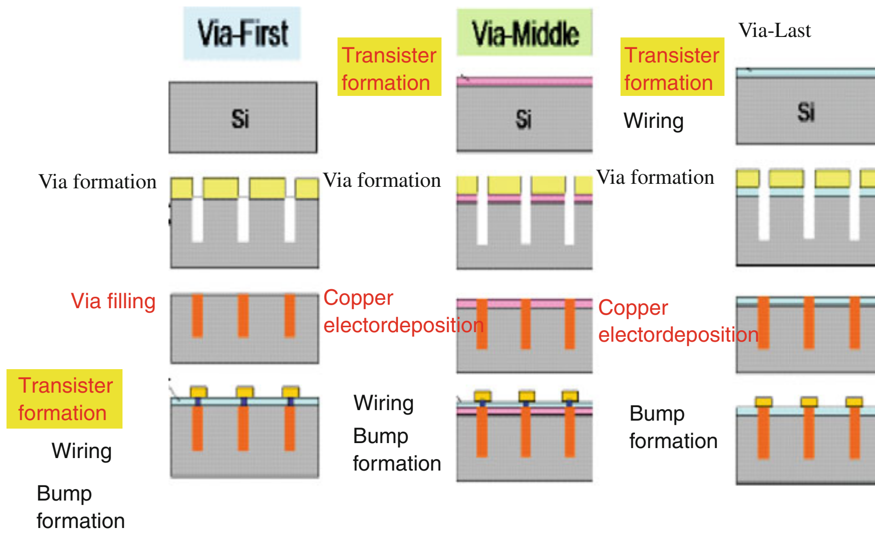

Fig. 8.3 Sequences for the via-first, via-middle, and via-last TSV processes

and seed layer formation) and via filling. In the via-first process, via formation and via filling are performed before transistor formation and wiring. In the via-middle process, via formation and copper electrodeposition are performed after transistor formation and before wiring. For the via-last process, via formation and copper electrodeposition are performed after transistor formation and wiring (Fig. 8.3).

Typical TSV structures are shown in Fig. 8.4. Processing temperatures in transistor formation are 600–1,000 °C. At these high temperatures, copper and silicon migrate and form silicide resulting in transistor deterioration. Hence, in the via-first process, the TSV is filled with polysilicon rather than copper. Once the transistors have been formed the process temperature for subsequent processing is 400–600 °C. Because of these lower process temperatures, copper can be deposited into the TSV. This copper is mostly filled by electrodeposition, since this is least expensive and is compatible with higher aspect ratios.

Fig. 8.4 Two typical structures of TSV. The structures are classified by via-first, via-middle, and via-last processes

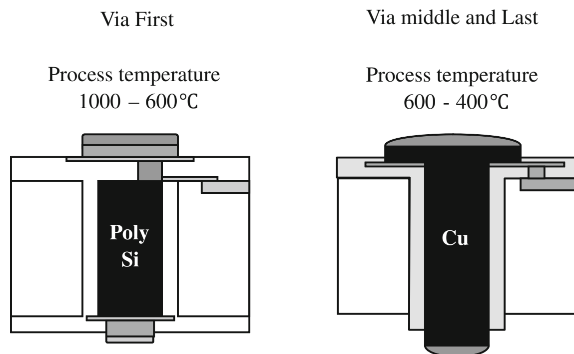

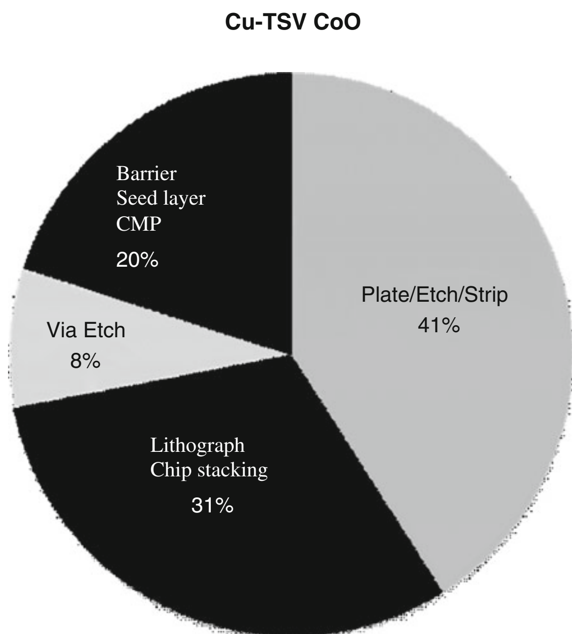

Fig. 8.5 Comparison of the process cost percentage of components of TSV fabrication

Figure 8.5 shows a comparison of processing cost percentage for the steps in TSV fabrication [2]. A large portion, 41 %, is represented by copper electrodeposition. For this reason, TSV cost reduction is mainly governed by reduction in the cost of copper electrodeposition. High speed copper electrodeposition is the most promising route for this cost reduction. However, the rate increase cannot be achieved by a simple increase in current density due to void formation. Figure 8.6

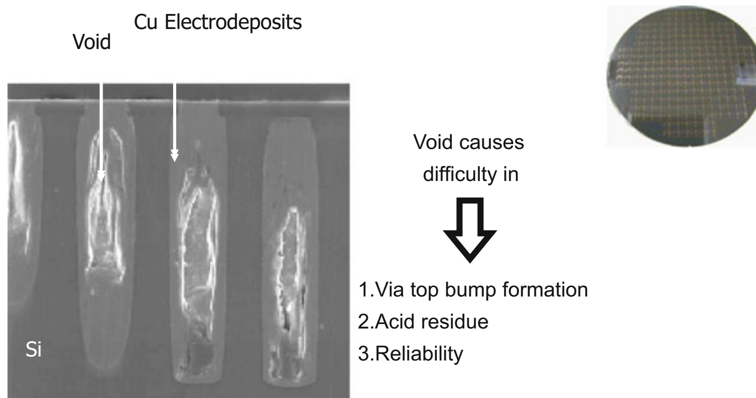

Fig. 8.6 Importance of void-free filling in copper electrodeposition

shows voids in the TSV cross-sections. Once voids are formed, they cause difficulty in via top bump formation. Also, the strong acid residue remaining inside the voids reduces the TSV reliability. Void elimination for high speed copper electrodeposition is the most critical problem in TSV filling.

The size of TSVs is a thousand times larger than that of vias or trenches used in on-chip metallization. The through-via diameter is several μms to tens of μms and the aspect ratio is more than five. Hence, TSVs are extremely deep and very challenging to fill. This is why the optimization and role of additives are important.

8.2 Three-Dimensional Packaging Developments

Development of three-dimensional packaging in Japan was initiated by a project of the Association of Super Advanced Electronics Technology (ASAET) supported by the Japanese Ministry of Trading and Economy in 1998. They report that high aspect large diameter via high speed etching and high speed copper electrodepositions into TSVs are critical issues. The author, Kondo, was a member of this project and developed the ASAET high speed electrodeposition process.

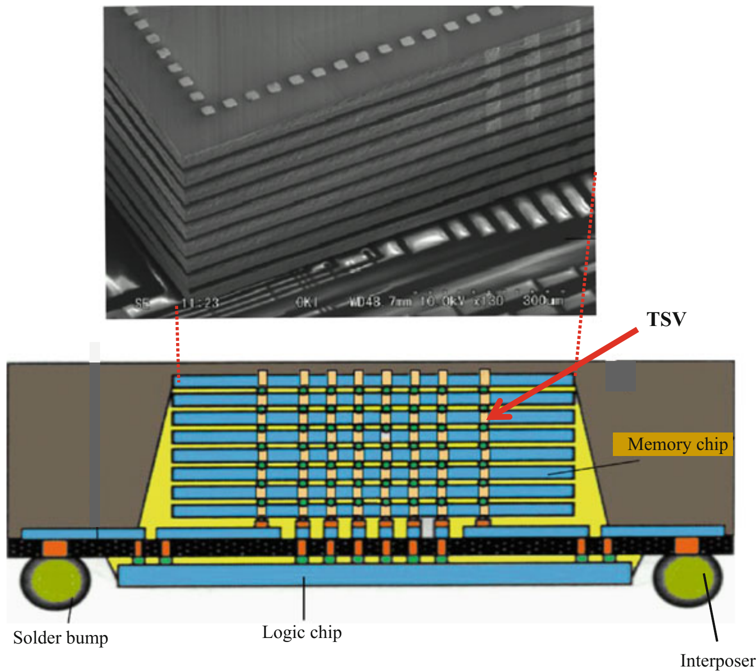

Fig. 8.7 SEM micrograph of the three-dimensional package of association of super advanced electronics technology (Elpida, Oki, and NEC) and its cross section

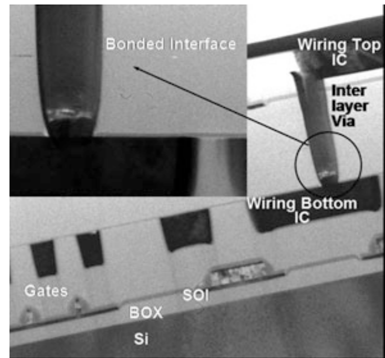

Fig. 8.8 Three-dimensional packaging by IBM with sub-μm size TSV

Worldwide, three-dimensional packaging developments date to around 2004. There are more than 40 institutions involved in this development. Arkansas University, M.I.T., Georgia Institute of Technology, and Rensselaer Institute of Technology are involved in the project in the U.S. CEA-LETI, IMEC, Fraunhofer in Europe and Tohoku University, and IME, ITRI in Asia. Many private companies such as INTEL, Toshiba, IBM, Renaissance, and Samson are also involved in the three-dimensional packaging projects.

Figure 8.7 shows an SEM micrograph of a three-dimensional package produced by ASAET (Elpida, Oki and NEC). Eight memory chips are stacked and connected

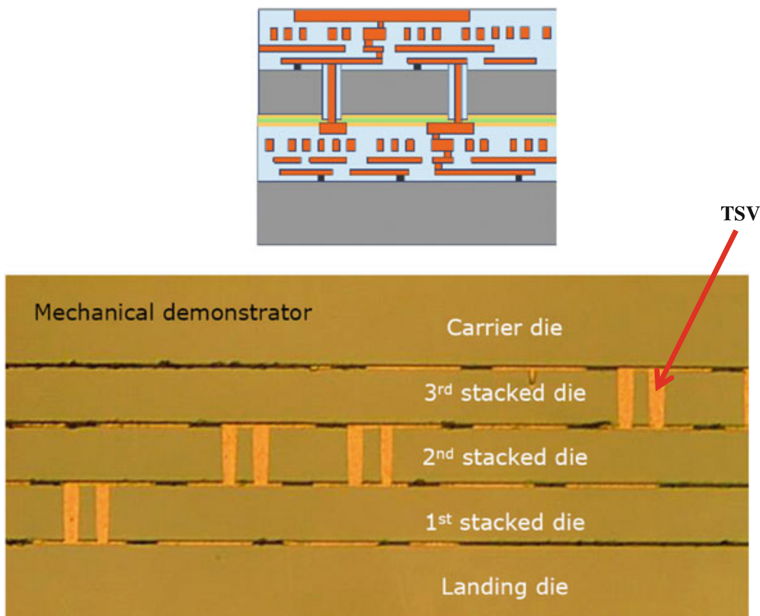

Fig. 8.9 Three-dimensional packaging by IMEC with copper nails

through TSVs. At the bottom is the logic chip. IBM developed a three-dimensional packaging process with a TSV size in the sub-μm scale (Fig. 8.8). They attached the silicon onto a glass substrate and applied CMP to the backside of the silicon. The TSVs were formed after CMP by the via-last process. IMEC employed the via-first process and they adopt 1–5 μm fine TSV called copper nail (Fig. 8.9).

8.3 High Speed Copper Electrodeposition of TSV by Kondo

The author, Kondo, started a research project on TSV filling by copper electrodeposition in 1999. ASAET had found that it is extremely difficult to fill TSVs by modification of existing copper on-chip metallization or printed circuit board copper electrodeposition baths. They asked Kondo to join the project to fill TSVs of height 70 μm and diameter 10 μm. With an aspect ratio of seven, these were very deep, narrow vias.

Two different types of additives were used in the project, namely open-literature additives and proprietary additives. The basic bath consists of $CuSO_4$ and H_2SO_4. The open-literature additives employed were Cl, (Polyethylene glycol (PEG), Inhibitor), SPS (Bis(3-sulfopropyl, Accelerator)) disulfide, and (Janus green B (JGB), Leveler). The proprietary additives, identified as SPR B and LEV A, were supplied by electroplating engineers, Japan (EEJA). The group employed periodic reverse pulse current wave-trains consisting of on time, reverse time, and off time. A silicon chip containing TSVs was attached to a rotating disk electrode (RDE), and the RDE was rotated in the electrolyte at a speed of 1,000 rpm. The anode was a plate positioned parallel to the silicon chip.

Beginning with the open-literature additives, Fig. 8.10 shows the first achievement of the project. The TSVs were filled without voids by a periodic reverse current wave-train consisting of an on time of 10 ms, a reverse time of 0.5 ms, and an off time of 10 ms. However, the on-time current density was 1 mA/cm^2, a very small current density that required 12 h to fill the via. Reduction of filling time by increase of the current density has become the main practical issue for cost reduction in filling by copper electrodeposition.

Figure 8.11 shows the leveler of JGB optimization by cyclic voltammetric stripping (CVS). The x-axis is the JGB concentration and the y-axis is the normalized Ar-value. Two different rotation speeds of RDE were applied: 100 and 2,500 rpm. The right-hand side of the figure shows the flow velocity profile close to the via. Since the chips are rotating at 1,000 rpm, the flow velocity outside of the via is rapid. Because the via is very deep and narrow, the flow velocity at the via bottom is slow. If the Ar-value at lower rotation speed (100 rpm) is larger than that at higher rotation speed (2,500 rpm), the predicted current density at the via bottom is larger and bottom up filling is expected. At a JGB concentration of 30 mg/L, the difference in the Ar-value is largest, and bottom up filling is expected. At the higher JGB concentration of 30 mg/L and current density of

Fig. 8.10 Via cross-sections of ASAET's first successful filling process with 1 mA/ cm^2

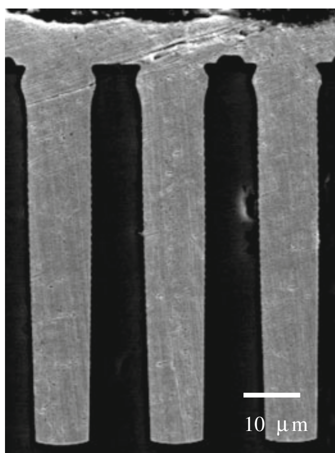

On/rev/off

10 ms/0.5 ms/10 ms

720 min

2.0 mA/cm^2, a perfect via fill was achieved within 6 h. At 3.0 mA/cm^2, voids were formed at the via bottoms. By application of two current steps, 2 mA/cm^2 for 120 min and of 3 mA/cm^2 from 120 to 210 min, perfect filling was achieved within 3.5 h [3].

Now we proceed to the proprietary additives. By CVS measurements (Similar to those shown in Fig. 8.11), the SPRB concentration was optimized at 5.0 mg/L.

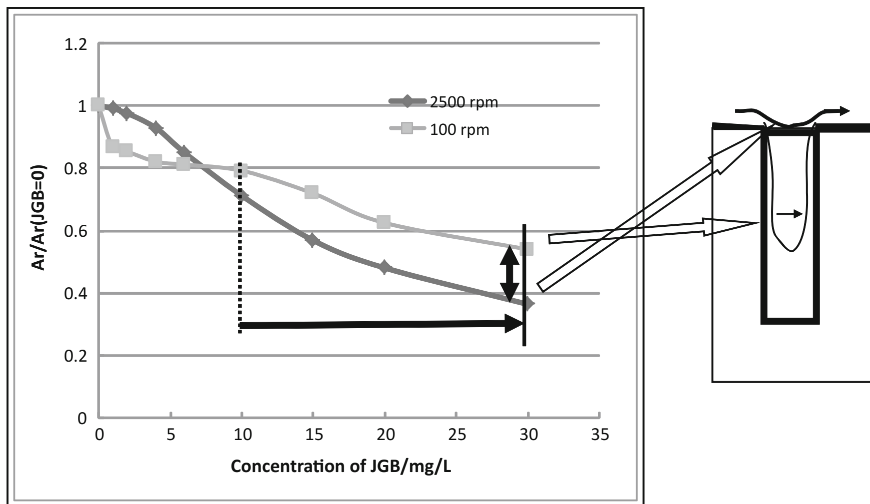

10 mg/L → 30 mg/L

Fig. 8.11 Cyclic voltammetry stripping (CVS) results. The *red curve* was taken at a RDE rotation speed of 100 rpm and the *blue curve* at 2,500 rpm

The LEVA concentration was also optimized by via cross-section examination at 0.2 mg/L at a current density of 4 mA/cm^2. Perfect via filling has been achieved at 5 mA/cm^2 within 90 min with the following parameters: SPRB = 5 mg/L, LEVA = 0.2 mg/L and SPS = 2 mg/L, on time = 200 ms, reverse time = 10 ms, and off time = 200 ms. With optimization, 90 min has been our shortest result and by applying 6 mA/cm^2, seems always form at the via center. Saturation of the electrodeposition solution with oxygen has a substantial effect on filling. Figure 8.12 shows cross sections of vias filled halfway after 50 min electrodeposition time. Without oxygen gas purge, deep and narrow seams appear at the via center, and filling is conformal. With oxygen gas purge, v-shapes develop, and filling is bottom up. With a two-step current density consisting of 6 mA/cm^2 for 50 min and 10 mA/cm^2 for 10 min, the vias were perfectly filled under oxygen gas purge with a filling time of 60 min (Fig. 8.13). Figure 8.14 shows the effect of oxygen gas purge. The x-axis is time, and the y-axis is potential. A large negative value indicates inhibition. At the via bottom, there is no difference in potential between deposition with oxygen gas purge and deposition without oxygen gas purge. At the via outside, however, a marked difference in potential exists, and the potential shifts to more negative values with oxygen gas purge. This large negative potential indicates an inhibition effect at the via outside. The mechanism by which oxygen affects the additives is shown in Fig. 8.15. The bulk electrolyte is saturated with oxygen. In the copper damascene process, electrodeposition occurs outside the via and along the via side wall and bottom. Oxygen gas is transported from the bulk electrolyte and approaches the via exterior. Oxygen oxidizes the cuprous ion to cupric ion. Since the accelerant complex consists of cuprous ion or Cu(I) thiolate, deposition outside the via is inhibited. However, the via is very deep and narrow so that oxygen is not transported to the via bottom and the cuprous ion or Cu(I) thiolate accumulates there [4].

Since the end of the ASAET project, we have continued to work on the time shortening of TSV filling. We have reduced the off time of periodical reverse

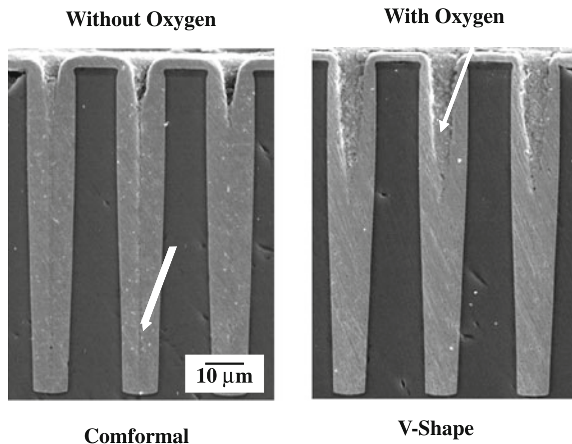

Fig. 8.12 Cross sections of half-filled vias after filling for 50 min at 6 mA/cm^2. Two cross sections without oxygen bubbling and with oxygen bubbling

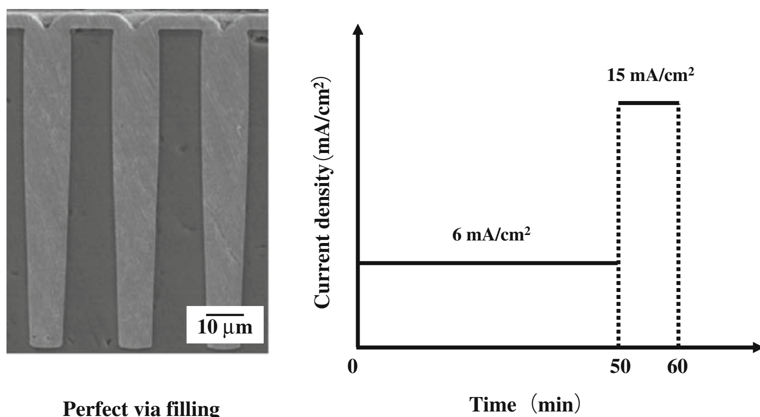

Fig. 8.13 Cross section of via with 60 min by oxygen gas bubbling. Two-step current densities are applied, initially 6 mA/cm^2 for 50 min and secondly 15 mA/cm^2 for 10 min

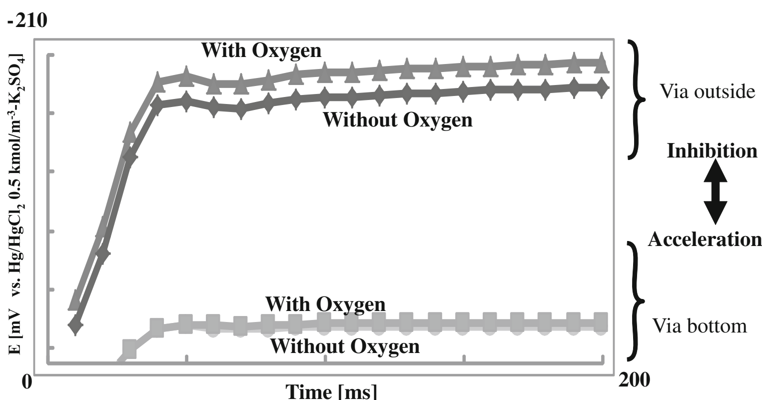

Fig. 8.14 Potential-time responses with and without oxygen gas bubbling. Note that a difference in potential exists at the via outside and potential shift to negative side with oxygen gas bubbling

Fig. 8.15 Illustration of the oxygen-assisted filling mechanism. Oxygen is transported from the bulk electrolyte and approaches the via outside

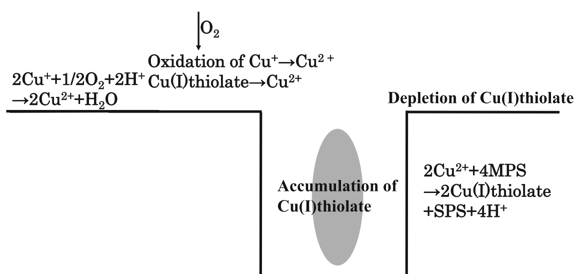

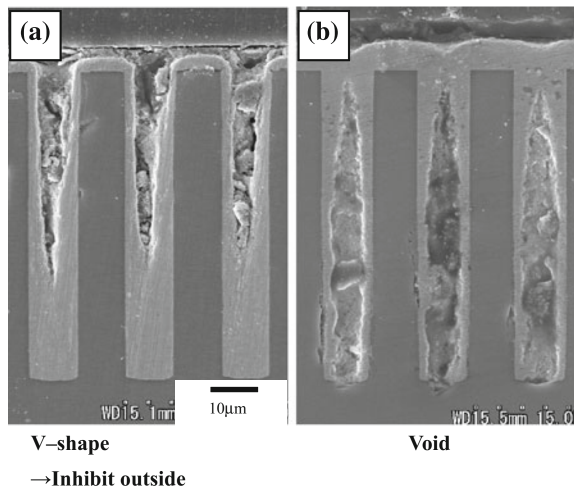

Fig. 8.16 Cross section of via with 25 min by OCT. **a** with SDDACC and **b** without SDDACC

current from 200 to 100 ms. The Diallylamine of SDDACC is chosen as the leveler. Figure 8.16 shows the effect of SDDACC. Without SDDACC, large voids form at the via centers (Fig. 8.16b). V-shape bottom up fillings are obtained with 1 mg/L of SDDACC (Fig. 8.16a). These V-shape bottom up fillings are due to inhibition effect at the via mouths.

As an alternative, Octadecanthiol microcontact printing has been applied to achieve an electrodeposition time of 37 min [5]. By optimizing the Diallylamine leveler, concentration by CVS we achieved another new time shortening [6]. Periodic reverse pulse current conditions are shown in Table 8.1. The bath composition is shown in Table 8.2. From CVS, the Ar-values at 10 rpm are larger than those of 1,000 rpm for SDDACC concentrations of 0.5–1.5 mg/L. Figure 8.17 shows cross sections of a via plated in 20 min. With SDDACC of 0 mg/L, huge voids form at via centers. Also, the via mouths are almost closed with an SDDACC

Table 8.1 Periodic reverse pulse condition

Periodical reverse pulse

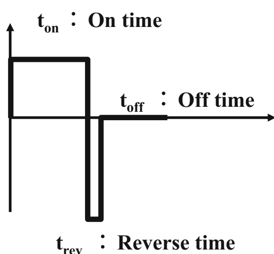

Current density and pulse condition.

I_{on}	-6 mA/cm^2
I_{rev}	12 mA/cm^2
On time	200 ms
Reverse time	10 ms
Off time	100ms

Table 8.2 Bath composition

Basic bath composition	
$CuSO_4 \cdot 5H_2O$	200 g/L
H_2SO_4	25 g/L
Additives	
Cl^-	70 ppm
SPS	2 ppm
PEG(M.W. 10,000)	25 ppm
Diallylamine	0 ~ 4 ppm

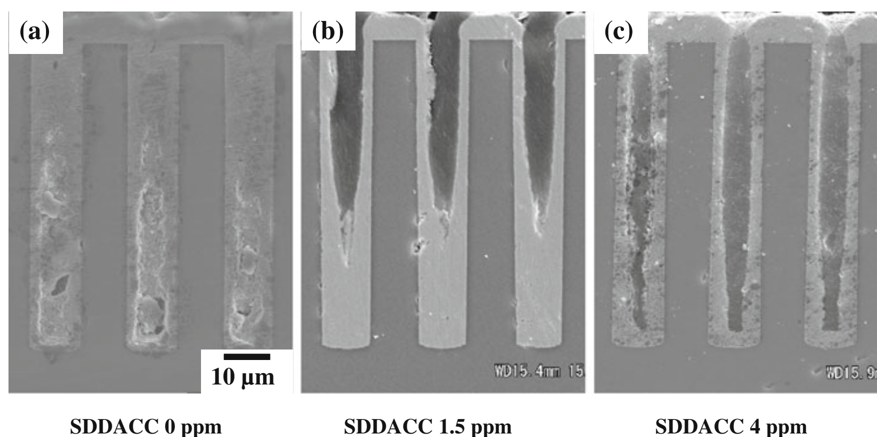

Fig. 8.17 Cross section of via after a 20 min fill. **a** SDDACC 0 ppm, **b** SDDACC 1.5 ppm, **c** SDDACC 4 ppm

concentration of 4 mg/L. V-shaped bottom up fillings are obtained with SDDACC of 1.5 mg/L. These V-shaped bottom up fillings are due to inhibition outside the via mouths. This process produces perfect filling in 35 min.

8.4 High Speed Copper Electrodeposition of TSV by Other Organizations

O. Lhun, A. A Radisic, and P. M. Verecken at IMEC (Interuniversity Microelectronics Center) have done considerable work on TSV copper electrodeposition [7, 8]. Their initial work addressed filling of 5 µm diameter and 25 µm depth vias. Additives PEG, SPS, JGB, and Cl were used. Figure 8.18 illustrates their invention. In Fig. 8.18a, the silicon surface is fully covered by a Ta barrier and Cu seed layer. In Fig. 8.18b, after the silicon surface is fully covered by Ta and Cu layers, a thin Ta cap layer is partially covered just on the top surface of the Cu seed layer.

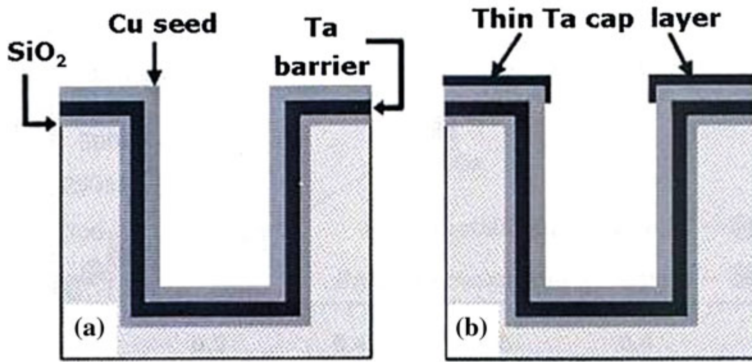

Fig. 8.18 Illustration of cross section of Ta barrier, copper seed, and thin Ta cap layers. **a** The silicon surface is fully covered by Ta barrier and Cu seed layer. **b** After the silicon surface is fully covered by Ta and Cu layers, a thin Ta cap layer is applied on the top surface of the Cu seed layer

This partially covered Ta cap layer is their invention. Figure 8.19 shows the filled copper center height and filling time. With fully covered substrate, the copper center height increase rapidly at the initial time, and 2,800 s was required to fill the via. On the other hand, with the partially covered substrate, the center height growth has an incubation period, and from 450 s the center height increased rapidly. It required 865 s to fill the via, which is 1/3 of the fully covered substrate.

JGB was used as leveler in combination with the additives above. With a larger amount of JGB, more inhibition was observed in current–voltage curves. At the bottom and outside of the via, electrodeposition is inhibited due to a higher JGB concentration. This inhibition may be related to the bottom-up mechanism, however, a detailed mechanism has not been clearly described [8]. A refinement in the crystal size at the via mouth has been observed by FIB (Field ion beam)

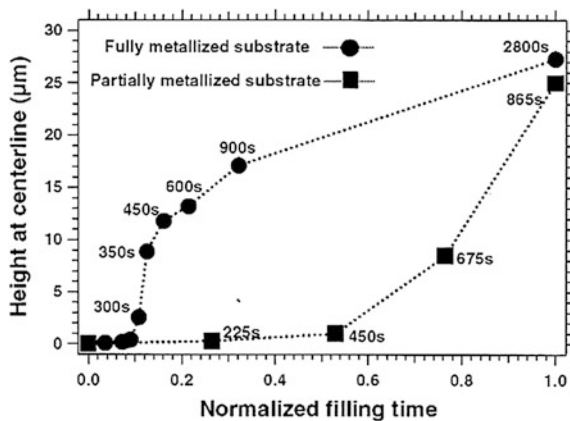

Fig. 8.19 Filled copper center height and filling time. Fully covered and partially covered substrates' center heights are shown

examination of cross sections. By use of the same commercial additives, 2–8 aspect ratio vias were filled successfully [9]. Both coupon level and wafer level have been tested. The 5 μm diameter and 40 μm depth via was filled in 1.5 h.

H. Kadota in Hitachi Kyowa [10] invented a vertically configured electrodeposition cell with a high electrolyte flow velocity of 5 m/s. Pulse current was applied with a long off time of 1.0 s at a current density of 10 mA/cm^2. It took 90 min to fill the 10 μm diameter and 70 μm depth via (Fig. 8.20). The additives used were not reported. T. P. Moffat filled donut-shaped vias using Cl and poloxamine additives at a potential of −0.650 V SSE [11]. It required 17 min to fill the via. The via cross-section top was flat and had no V-shapes.

R. Beica, T. Ritzdorf et al. [12] filled vias of 30 μm diameter and 110 μm depth, and 12 μm diameter and 100 μm depth. Unfortunately the electrodeposition conditions and additives are not described in the article. R. Baskaran et al. [13] filled 8 μm diameter and 100 μm depth vias. The exchange current densities and electron transfer coefficients for their plating bath have been measured. From the current–voltage curve, the inhibition effect increases with increasing leveler concentration. A. Flugel et al. [14] measured an oscillatory deposition potential during galvanostatic deposition. SIMS measurements showed oscillatory incorporation of contaminants. M. Arnolf et al. [15] showed that a type-I suppressor produces a temporary suppression effect. On the other hand, a type-III suppressor shows a sustained suppression effect.

J. D. Adolf and U. Landau have used numerical computation of current distribution to assess the effect of additive transport and adsorption on TSV filling

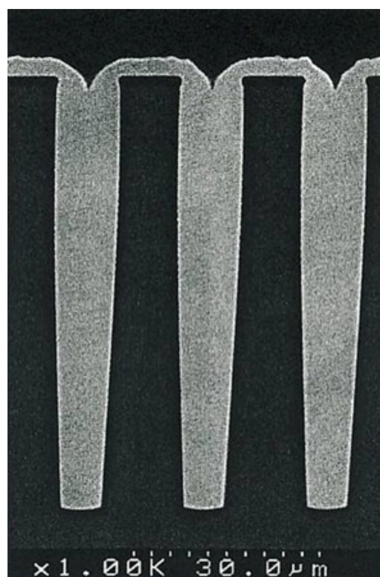

Fig. 8.20 Cross section of 10 μm diameter and 70 μm depth via by Hitachi Kyowa

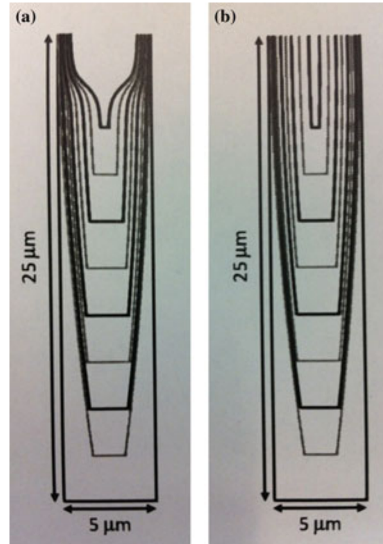

Fig. 8.21 Illustration of the effect of the leveler. The leveler reduces pinching at the top of the TSV in **a**. Pinching occurs without leveler in **b**

[16]. They recognized that the strongly bound leveler displaces both PEG and SPS [17]. The role of leveler is analyzed [18]. In the model, the leveler concentration profile is determined as a function of TSV penetration depth, and it is shown that the leveler reaches a stagnation depth due to the balance of diffusion and incorporation. Figure 8.21a shows the effect of the leveler as it significantly reduces pinching at the top of the TSV [19]. This pinching simulation at the top of the TSV is very important from a practical viewpoint.

8.5 Future Trends in TSV

One major application of TSV is the interconnection of memory and logic chip for the smartphone. This is because the TSV interconnection realizes a wide I/O and low electric power consumption.

The TSV processes will narrow down to via-middle and via-last back side. The TSVs are exposed to about 400 °C annealing temperature in the wiring stage of the via-middle process. TSV formation becomes difficult with thin wafers in the via-last back side process. The 400 °C annealing temperature of the via-middle process causes copper contamination from the TSV. Also, the annealing temperature causes pop-up of TSVs. The pop-up destroys the fragile wiring low-k materials and this causes a serious reliability problem.

References

1. Denda S (2007) Hyoumen-gijitsu 58(12):712–718 (in Japanese)
2. Setiagung C (2009) Advanced copper electrodeposition corresponding to TSV process. Paper presented at the three dimensional packaging-TSV electrodeposition tool, University of Tokyo, 31 Aug 2009
3. Sun J–J, Kondo K et al (2003) J Electrochem Soc 150(6):G355–G358
4. Kondo K, Yonezawa T et al (2005) J Electrochem Soc 152(11):H173–H177
5. Kondo K, Suzuki Y et al (2010) Electrochem S–S Lett 13(5):D26–D28
6. Hayashi T, Kondo K et al (2011) J Electrochem Soc 158(12):D715–D718
7. Lun O, Radisc A et al (2009) Electrochem S–S Lett 12(5):D39–D41
8. Lun O, Van Hoof C et al (2009) Electrochim Acta 54:2504–2508
9. Radisic A, Luhn O et al (2011) Microelectron Eng. 88:701–704
10. Kadota H et al (2010) JIEP 13(3):213–219 (in Japanese)
11. Moffat TP, Josell D (2012) J Electrochem Soc 159(4):D208–D216
12. Beica R, Sharbono C (2008) Through silicon via copper electrodeposition for 3D integration. In: Proceedings of ECTC conference, Orlando, 2008
13. Baskaran R, McHugh P (2011) Characterization of the organic components in a commercial TSV filling chemistry. Paper presented at the 220th meeting of the electorochemical society, Oct 2011
14. Flugel A, Amold M (2011) Tailored design of suppressor ensembles for damascene and 3D-TSV copper plating. Paper presented at the 220th meeting of the electrochemical society, Oct 2011
15. Arnold M, Emnet C (2010) New concept for advanced 3D TSV copper plating additives. Paper presented at the 218th meeting of the electrochemical society, Oct 2010
16. Adolf JD, Landau U (2009) Scaling analysis of bottom up fill with application to through silicon via. Paper presented at the 216th meeting of the electrochemical society, Oct 2009
17. Landau U (2010) Electroplating of interconnects—scaling from nanoscale dual-damascene to micron-scale through silicon vias. Paper presented at the 218th meeting of the electrochemical society, Oct 2010
18. Adolf JD, Landau U (2010) Additive adsorption and transport effects on the void-free metallization of through silicon vias. Paper presented at the 218th meeting of the electrochemical society, Oct 2010
19. Adolf JD, Landau U (2011) Leveler effects on filling of through silicon vias. Paper presented at the 220th meeting of the electrochemical society, Oct 2011

Chapter 9
Build-up Printed Wiring Boards (Build-up PWBs)

Kiyoshi Takagi and Toshikazu Okubo

9.1 Features and Historical Aspects of Build-up Printed Wiring Boards (Build-up PWBs)

9.1.1 Features of Build-up PWBs

Build-up printed wiring boards (build-up PWBs) are advanced forms of plated through hole printed wiring boards (PTH PWBs) [1]. Not only build-up PWBs but also PTH PWBs are based on the technologies used to achieve high density and multilayer PWBs, which are currently demanded. Build-up PWBs are considered to improve on the weak points of PTH PWBs. In order to achieve more advanced high density PWBs, progressive manufacturing technologies have been introduced. One of the most important technologies is filled via copper deposition, as mentioned in the previous chapters. The filled vias can be stacked on the vias in the lower layer, resulting in better electrical performance and greater wiring density than those achieved with conformal vias. Therefore the application of via filling is expanding. The details are described later in 9.7.3.

Regarding PTH PWBs, the conductive circuit patterns in the inner or outer layers are connected by the through holes. As the holes pass through all layers, from front to back planes, not only the portions to be connected but also the whole through hole walls are metalized. Some of the unnecessary metal patterns produce defects in the electrical properties, because such metal patterns, so-called stubs,

K. Takagi (✉)
Takagi Associates, 4-12-10 Hongodai, Sakae-Ku, Yokohama-shi 247-0008, Japan
e-mail: PBA03243@nifty.com

T. Okubo
Packaging Lab, Toppan Printing Co, 4-2-3 Takanodaiminami, Sugito-Cho, Kitakatushika-Gun, Saitama 345-8508, Japan
e-mail: toshikazu.ookubo@toppan.co.jp

K. Kondo et al. (eds.), *Copper Electrodeposition for Nanofabrication of Electronics Devices*, Nanostructure Science and Technology 171, DOI: 10.1007/978-1-4614-9176-7_9,
© Springer Science+Business Media New York 2014

sometimes act as antennae and receive noise. Moreover, the spaces that through holes occupy within the boards are not small enough to restrict the area of circuit wiring. On the other hand, build-up PWBs are fabricated in such a way that insulation and conduction layers are formed one by one, therefore conduction layers can be connected by small via holes. Then the layers are built up sequentially. These processes are similar to that used for the circuit formation in semiconductor devices and thin layer hybrid substrates. This practice can improve the weak points of PTH PWBs to realize fine pattern circuit formation.

9.1.2 Historical Aspects of Build-up PWBs

It seems that the first description of build-up PWBs was published under the name "Plated-up Technology" in 1967 [2]. Lassen reported the results of a production trial in 1979 [3]. Takagi also noticed and tried the technology [4], but did not release his results for practical use. In 1988, BrÎsamle et al. developed build-up PWBs with 10 and more layers, named "Microwiring," and applied to large-scale computers [5]. In 1991, Tsukada and his group developed Surface Laminar Circuit (SLC), build-up PWBs as the substrates for flip chip connection with semiconductor devices [6]. After that, the materials, equipment, and process technologies for manufacturing were improved and widely spread for about one decade. The production of build-up PWBs has been expanding since about 1998. At present, build-up PWBs are necessary elements for high performance electronic equipment as the package substrates for semiconductor devices, mother boards for mobile equipment, and so on.

9.2 The Evolution of PWBs with the Progression of Electronic Equipment

The fundamental roles of the PWBs are:

(1) To compose modules which realize the aimed electronic function by means of assembling and connecting electronic parts.
(2) To have the required electrical properties to make up electronic circuits.
(3) To hold and fix the assembled parts.
(4) To have long-term reliability.

The functions of electronic equipment have been improving over time. Also, semiconductor devices and electronic parts have been upgrading and downsizing. To follow these trends, the PWBs required to assemble these parts have been getting high density wiring and upgrading. The trends of characters of semiconductor chips and PWBs indicated in the International Technology Roadmap for

Table 9.1 Trends of semiconductors and PWBs forecast in the roadmap of ITRS (2010)

	Year	2011	2016
In chip	Integration(SRAM/LOGIC)	4,365/798 M_{tr}/cm^2	17,459/3,193 M_{tr}/cm^2
	Line width	38 nm	18.9 nm
	Chip size	140 mm^2	140 mm^2
	I/O pin #	5,094 pins	6,501 pins
	Performance		
	Clock frequency in chip	6.33 GHz	9.18 GHz
	Clock frequency to board	12 Gb/s	30 Gb/s
In package substrate (high performance)	Line width/space	15/15 μm	8/8 μm
	Conductor thickness	25 μm	12 μm
	Via hole diameter	60 μm	50 μm
	Via land diameter	130 μm	100 μm
	PTH diameter	100 μm	70 μm
	PTH land diameter	250 μm	150 μm
	Bump pitch	120 μm	100 μm
	Core substrate		
	Glass transition temp (Tg)	180 °C	210 °C
	Dielectric constant	2.8	2.8
	Dielectric loss	0.007	0.007
	Build-up layer		
	Glass transition temp (Tg)	200 °C	210 °C
	Dielectric constant	3	3
	Dielectric loss	0.013	0.013

M_{tr}: mega-transistor

Table 9.2 Rent's empirical law

$P = kG^V$
P: signal I/Opin#
G: total gate #
k, V: constant
Where
V for gate array: 0.5
Microprocessor: 0.45
Printed wiring boards: 0.25
System: 0.25
Memory: 0.12
k: 0.25–2

Semiconductors (2010) are summarized in Table 9.1. Table 9.2 shows Rent's empirical law about the relationship between the total gate numbers and the I/O pin numbers in electronic circuits, that indicates that increase of integration brings an increase in I/O numbers. This law is still effective. Some dimensional features of recent PWBs are shown in Table 9.3. The super high density level realizing very small lines width and, spaces, via diameters and additional high qualities are in demand. The build-up PWBs have been increasing the volume for super high density boards.

Table 9.3 Some features of the recent PWBs

Items	General level	High density level	Super high density level
Line width	150 ~ 100 μm	70 ~ 49 μm	10(5) ~ 30 μm
Line space	150 ~ 100 μm	80 ~ 50 μm	40 ~ 15 μm
Conductor thickness	25 ~ 15 μm	25 ~ 15 μm	20 ~ 10 μm
Via diameter	200 ~ 100 μm	120 ~ 60 μm	40 ~ 20 μm
Land diameter	400 ~ 200 μm	300 ~ 150 μm	100 ~ 60 μm
Layer distance	200 ~ 40 μm	80 ~ 30 μm	50 ~ 15 μm
Board thickness	2,000 ~ 400 μm	1,200 ~ 300 μm	800 ~ 80 μm
Layer #	4 ~ 10	6 ~ 20	6 ~ 40

9.3 Classification and Structure of Build-up PWBs

The build-up processes consist of a few elemental steps. They are formation of an insulation layer on the core board, formation of a conductive circuit on the insulation layer, and formation of via connections between the upper and lower conductive layers. By repetition of these steps, build-up layer (conductive and insulation layers) formation and via connection, high density multilayer PWBs are produced. These methods can bring the following merits:

(1) Vias and circuits can be designed without positioning restrictions because the vias can be positioned for each conductive layer.
(2) The circuit density can be increased, because smaller via diameters and smaller line width/space sizes are possible.
(3) Because few through holes are used, the space occupation of some through holes, which do not connect layers, can be neglected.

However, in order to realize these merits, many types of technologies must be developed, such as adequate insulation materials for build-up processes, fine via fabrication, patterning for fine circuit formation, plating for conductive layer formation, and so on.

9.3.1 Basic Build-up PWBs Processes with Cu Plating Methods

Figure 9.1 shows a cross-sectional view of a typical build-up PWB, which is fabricated in such a way that the build-up layers are formed on the PTH PWB as the core substrate having a few layers. The process steps are as follows: (The detail will be described later in Sect. 9.5.)

(a) Preparation of pattern data file and artwork—Based on the design specification of the electronic equipment, the pattern data by CAD (computer aided design system), and artwork masks are prepared.

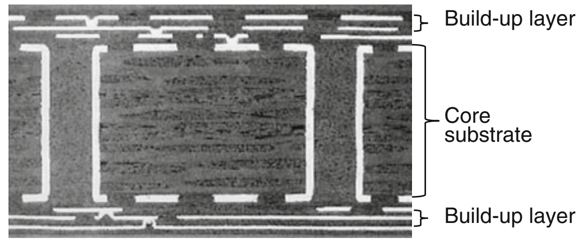

Fig. 9.1 Cross-section of typical build-up PWB

(b) PTH PWB—The PTH PWB is used as the core substrate. Then the build-up layers are built on it.
(c) Lamination of insulation layers—Insulating resin formulated for the build-up process is laminated.
(d) Fine diameter hole formation—The fine diameter holes to connect the conductive layers are made using a laser.
(e) Electroless copper plating—Electroless copper plating is applied to the insulating resin surface.
(f) Electrolytic copper plating—Electrolytic copper plating is applied to enhance the copper thickness.
(g) Etching—Unnecessary copper is etched off to form conductive circuit pattern.

The number of layers are increased by means of repeating the process steps from (a) to (g) for each layer. This build-up process can be recognized that the fabricated surface pattern in a step will become the inner pattern after the upper layer is made in the next step.

The most considerable problem of this type of build-up PWBs is that the core board must be thick enough to keep the whole board strong despite the lack of strength of the insulation resin. Because such thick core boards must have large through holes that restrict the number of connections, they cause some problems that restrict high density wiring and lower transmission characteristics. The following improved types have been developed to solve these problems.

9.3.2 All Layer IVH Build-up PWBs, Process with Cu Plating Method

(1) All Layer IVH Build-up PWBs Using Thin Copper Clad Laminate.

Interstitial Via Hole (IVH) is the via hole existing in all inner insulation layers and connecting between the specific layers. All layer IVH means that use of IVH is extended to all layers in the build-up PWB. In order to solve the problems of thick core substrate, a core material having almost the same thickness as the build-up layers is used, then the layers are built up. Figure 9.2 shows the cross-sectional view of this type of build-up PWB, indicating that the core substrate is as thin as

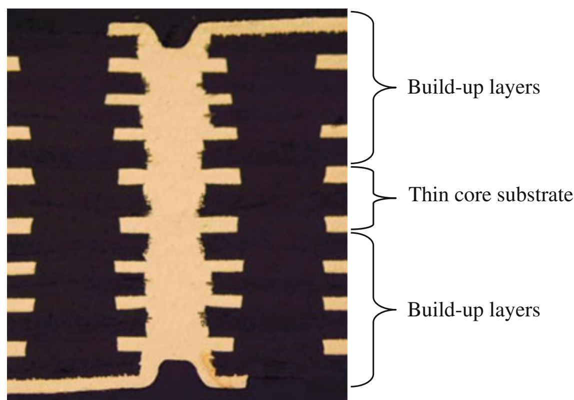

Fig. 9.2 All layer IVH build-up PWB using thin copper clad laminate

the other layers. The strength of the whole board is maintained by an increase in the number of layers.

(2) All Layer IVH Build-up PWBs Using Only Build-up Resin.

Figure 9.3 shows a cross-sectional view of an all layer IVH build-up PWB using only the build-up resin and the insulation material formulated for build-up process. This type can improve some properties but supporting plates must be used in the production process. Due to the lack of the strength of the board even in completed form, this type of board in actual use must be accompanied with many layers and supported by a stiffener in assembly process.

(3) Bumpless Connection Build-up PWBs.

Figure 9.4 shows this type of build-up PWB, which has the characteristics that the parts are directly connected to it. This is the advanced form of Bumpless Build-Up Layer (BBUL) package [7], which was disclosed by Intel in 2001. Some various parts such as LSI chips are buried in the resin-molded board.

It is produced through the following way: the parts are placed at the proper position on the board, fixed using resin, and then molded to form a supporting

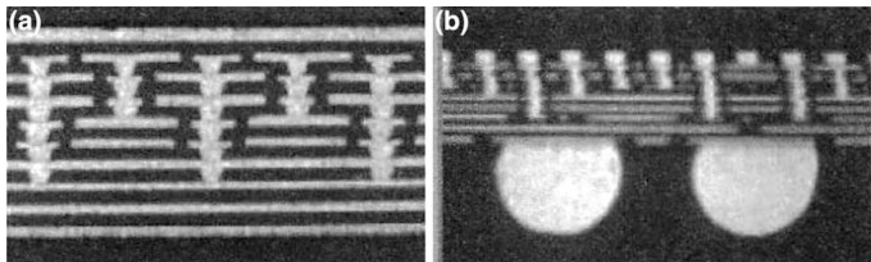

Fig. 9.3 All layer IVH build-up PWB using only the build-up resin **a** 10-layered all layer IVH build-up PWB using only the build-up resin **b** Package substrate composed with all layer IVH build-up PWB

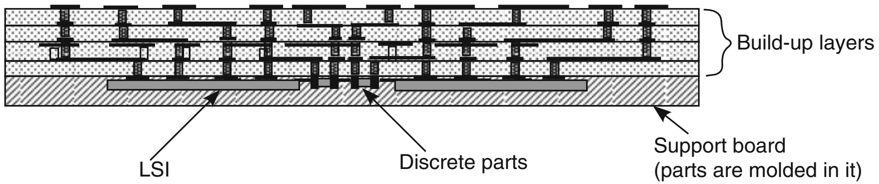

Fig. 9.4 Bumpless connection build-up PWB

board. Scrubbing is done to expose the electrodes of the parts. The build-up layers are formed making direct connection with the buried parts in the supporting layer. The supporting molded board plays as the stiffener and circuit layers are built up on it. The connection between I/O pads and circuit patterns can be made by plating small Cu pillars directly on I/O pads. It seems that this is a promising method to produce the parts embedded type PWB.

9.3.3 Build-up PWBs with Via Connection Using Conductive Paste

(1) ALIVH (All IVH) [8].

Figure 9.5 illustrates the build-up PWB made by means of ALIVH method. The insulation layer is composed of the laminate reinforced with aramid fiber sheet or with thin glass cloth. Thin glass cloth is modified to match with the hole fabrication by laser. The holes are filled with conductive copper paste to make connection between the layers. This type seldom uses plating techniques.

(2) B^2it (Buried Bump Interconnection Technology)[9].

Figure 9.6 illustrates a build-up PWB made by means of the B^2it method. The conductive pillars to connect between the layers are made of conductive paste and formed using printing techniques. The pillars penetrate the adhesive insulation sheets to make connection between layers when the pattern layers are compressed. This type also seldom uses plating techniques.

Fig. 9.5 Build-up PWB made by means of ALIVH method

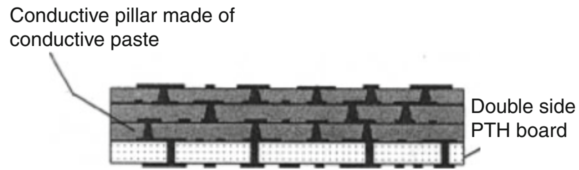

Fig. 9.6 Build-up PWB made by means of B²it method

9.4 Required Characteristics of the PWBs

PWB is one of the electronic parts. Build-up PWB is the one kind of multilayer PWBs. It is required that the electrical, mechanical, and chemical properties are satisfied. Moreover, these properties are getting upgraded to fit with the recent trend of high density, high quality, and high speed transmission.

The electrical resistance of the conductors and the insulation resistance between the conductors are important as the basic electrical properties. Moreover, characteristic impedance matching and improvement of the transmission speed are required.

These properties are strongly affected by the materials and the manufacturing technologies of the PWBs. Furthermore, because the PWBs connect and assemble many parts, the mechanical properties such as the bent strength, warpage, twist, dimensional stability, and adhesion of the conductors to the resin must be considered. Durability in high temperature environments is also required. Because many kinds of chemicals may cause attack during manufacturing procedures, also the chemical stabilities of the materials must be considered. Furthermore, stability against corrosion and electrochemical migration, which sometimes occur in actual operating circumstances, must be considered.

9.4.1 Electrical Properties

The following electrical properties are required for the PWBs:

– As the properties for direct current, conductive resistance, insulation resistance.
– As the properties for alternating current, characteristic impedance, signal transmission speed, cross-talk, other high frequency properties and electromagnetic shielding capability, and so on.

These properties are intimately correlated with the composing materials, the conformation, and the manufacturing processes.

(1) The conductive resistance.

The conductive circuit patterns formed on the surface and inside the PWBs connect the electronic parts, hence the resistance of the conductors must be as small as possible. As the circuit patterns are becoming thinner, the resistance tends

to increase. Therefore, the cross-sectional shape, the length of the circuit patterns, and the materials of the conductors are properly chosen considering the conductive resistance. Copper is commonly used material for the PWBs because the specific resistivity of copper is second smallest following silver.

(2) Insulation resistance.

When the insulation resistance between the conductors falls too low, the PWBs do not work well, so the insulation resistivity is one of the most important properties. The insulation depends on the characters of the insulating materials and the operation of the manufacturing processes. The insulation properties are evaluated from the tests performed in highly humid circumstances. It is considered that more than $5 \times 10^6\ \Omega$ in humid environments is the guideline level. The insulation is degraded by the defects of the insulating materials and faults in manufacturing processes such as the absorption of water and contamination by the residue of solutions containing ionic contents. The trend of finer patterns, giving rise to narrower pattern space, sometimes makes the insulation resistance decrease. Therefore, the developments of more highly insulating materials and more reliable operative processes have been progressing.

(3) Characteristic impedance.

Because the electric signal passing through the lines on the PWBs is pulsed wave, we must consider the signal as alternating current. Pulsed signals with square wave are composed by the combination of basic sine waves with several higher harmonic waves. The frequency must be considered to be higher than the indicated one. To follow the improvement of electronic equipment, the adaptability to high speed processing in the LSI chips is necessary. Therefore, more accurate matching of characteristic impedance (Z_0) is required. As shown in Fig. 9.7, the conductive circuit lines for a high frequency signal can be considered as the equivalent circuit composed by resistance (R), inductance (L), capacitance (C), and conductance (G), and the characteristic impedance is expressed in Eq. (9.1).

$$Z_0 = \sqrt{\frac{R + j\omega L}{G + j\omega C}}\,(\Omega/\mathrm{m}) \tag{9.1}$$

The characteristic impedance of conductive lines is determined by the factors of width and thickness of the line, distance from the ground and dielectric constant

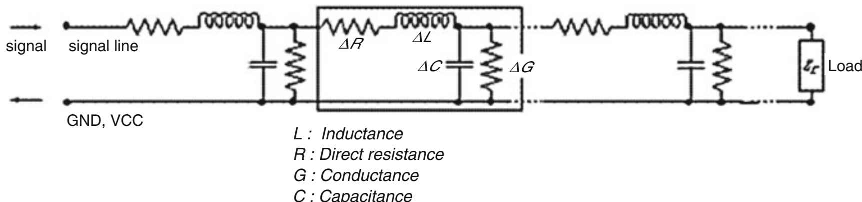

Fig. 9.7 Equivalent circuit of the lines for high frequency signal

between the signal and ground lines. The characteristic impedance matching is influenced by these factors, namely the signal reflection takes place at the point where the values of the factors vary. This causes noise that disturbs signal transmission. The deviation of the conductor size affects the noise generation, so accurate control in the manufacturing processes is very important.

(4) Skin effects.

When the pulse current is in the high frequency region, the signal current passes only in the narrow region along the surface of the conductive patterns, a phenomenon called skin effect. The higher frequency the signal is, the smaller the thickness of the current passing region becomes. The thickness of the region is expressed in Eq. (9.2),

$$\delta = \sqrt{2/\sigma\omega\mu} \quad (9.2)$$

where δ is the thickness, σ is the conductivity, ω is the frequency (= $2\pi f$), and μ is the magnetic permeability. The relationship of the signal frequency to the skin thickness is shown in Table 9.4. The roughness of the interface between the conductors and the insulator influences this effect. Therefore, developments to form smooth but strongly adhesive interfaces are required.

9.4.2 Mechanical Properties

The principal mechanical properties required for the PWBs are as follows:

(1) Bending strength.

PWBs assemble many parts to connect with them. Because of differences between the assembled parts, for example weight and size, connections sometimes

Table 9.4 Relationship of the signal frequency with the skin effect thickness (Eq. (9.2))

Frequency	Thickness (mm)
1 kHz	2.14
10 kHz	0.68
100 kHz	0.21
1 MHz	0.06
10 MHz	0.02
100 MHz	0.0066
1 GHz	0.0021
3 GHz	0.0012
5 GHz	0.00093
10 GHz	0.00066
12 GHz	0.0006

The skin effect thickness indicating the thickness at which current density decreases to 1/e of that near the surface

cause deformation of the boards. Hence, they require the strength to support the parts without deformation.

(2) Warpage, twist.

If the PWBs are not flat but warped or twisted, the connecting electrodes do not make contact with the soldered pads, and the connection fails. In order to inhibit warpage or twisting as much as possible, the materials and process conditions have to be properly selected.

(3) Peel strength.

The PWBs encounter high temperature conditions several times during assembling processes such as soldering. The conductors must not be detached at the high temperature, so stable adhesive properties of the conductors are required.

(4) Dimensional stability.

Because a position mismatch of the I/O pins with the pads on the PWBs causes the connection between the electrodes to fail, high-dimensional stability of the insulation boards is important.

(5) Thermal stability against soldering.

In the case of Sn–Pb eutectic solder, soldering is performed at about 230°. But, due to recent aggressive shift to lead-free solder materials such as Sn–Ag–Cu, the operating temperature has become higher than that of Sn–Pb solder. Because such higher soldering temperature tends to cause more damage to the organic board materials, more thermal stabilities of the materials are demanded.

(6) Coefficient of thermal expansion.

The coefficient of thermal expansion of copper is different from that of resins. The difference is compensated with the structures and the mechanical properties of copper and the board materials. The glass fiber reinforced boards has the character of expansion that the expansion along the plane direction is reduced and that in thickness direction enhanced. This character influences the connection reliability of the plated vias. Not only the materials but the structural balance of the package and the mother boards has to be considered to decrease the influence of the expansion difference.

(7) Solderability.

Usually, parts connection is made by soldering on the pads of the PWBs. The surface of the parts and the pads on the PWBs should be cleaned to make the solder joint reliable.

9.4.3 Chemical Properties

The chemical properties required for PWBs are as follows:

(1) Resistance to chemical reagents.

Many kinds of chemical reagents are used for manufacturing PWBs. Furthermore, the PWBs make contact with some chemical atmosphere in the assembly processes and even in the operating circumstances in the equipment. If residues of these chemicals remain on the PWB, the insulators and conductors are sometimes damaged. It is necessary that the insulators and conductors are sufficiently stable against these chemicals.

(2) Stability in plating operation.

Electrolytic and electroless plating are the principal processes for PWB manufacturing. The qualities of the produced PWBs are affected by the adaptability of the plating chemicals with the insulation and/or conducting materials. For example, some plating chemicals attack insulation resin and/or penetrate into the boards, then severe defects are caused on the boards. When some insulating materials contaminate the plating baths during the plating operation, the plating qualities sometimes become degraded.

(3) Stability in etching operation.

To form the conductor patterns, the copper foils are etched using etchant, a corrosive solution. The insulation materials must be stable during etching and not corroded in the etchant.

(4) Stability in organic solvent.

Many kinds of organic solvent are used for processing PWBs. Stability of the materials in such solvents is also necessary.

(5) Prevention from ion migration.

The degradation of insulation in PWBs is caused by the migration of ions in the insulation materials. These ions are derived from the residue of processing solutions and the impurities in the insulation materials. Because these damage the insulation reliabilities so much, sufficient methods to solve them must be applied [10].

9.5 Manufacturing Processes of the Build-up PWBs

9.5.1 Basic Build-up Process Using Plating Methods

Figure 9.8 indicates the basic process to form the build-up layers on the core substrate [11]. The core substrate is the ordinary PTH PWB, of which typical feature is double-sided or four-layered PWB. The build-up layers are formed on

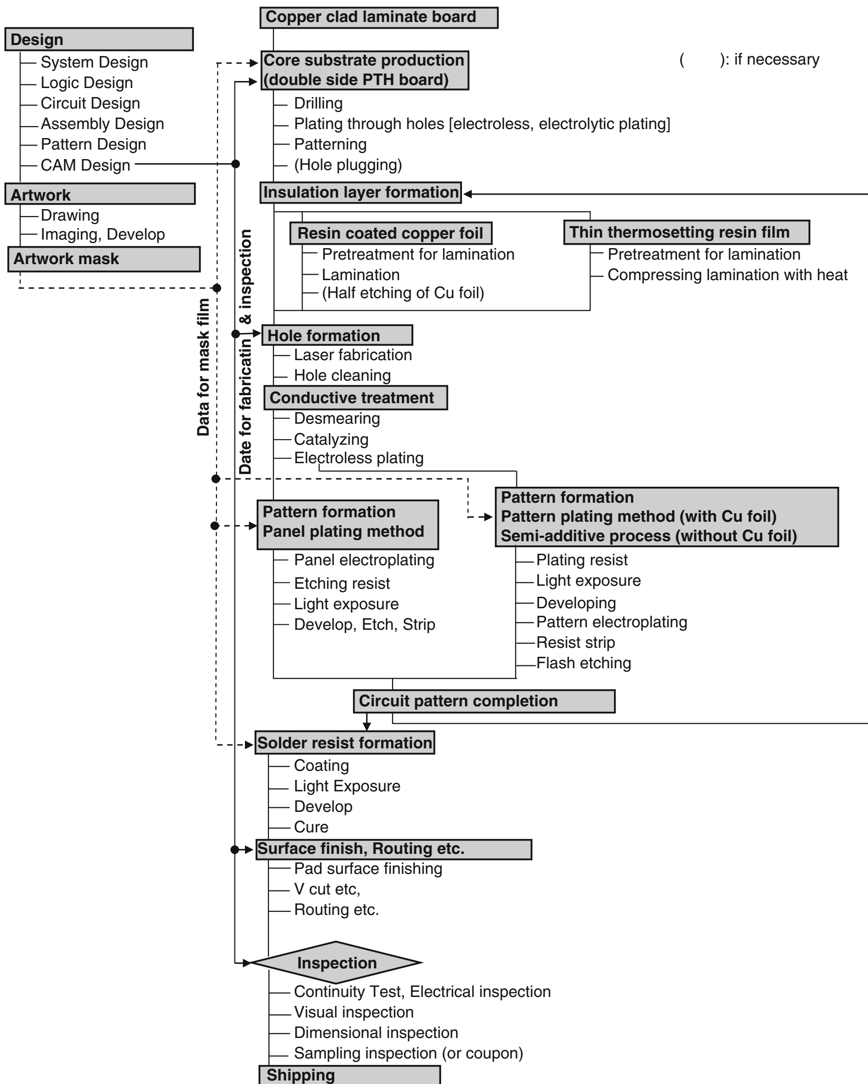

Fig. 9.8 Basic build-up process to form the build-up layers on the core substrate

the core substrate. The insulation materials used for the build-up layers are as follows:

(a) Resin-coated copper foil. Resin is coated on thin copper then cured in B stage (not completely cured) and used as the adhesive.
(b) Material combined thin copper foil with prepreg consisting of thin glass cloth.
(c) Thin thermosetting resin film used by means of compression in heated condition.

These materials are laminated on the layer where the conductive patterns have been formed. After that, holes to connect between the layers are fabricated using a laser. The laser types commonly used for such hole fabrication are CO_2 laser (wavelength 9 ~ 11 μm) and YAG laser (wavelength 355 nm). Direct laser shot on the resin layer without a mask is applied, whether copper foil exists or not on the resin surface. After hole fabrication, desmear treatment is performed to remove the smear at the bottom of holes covering the conductor. A catalytic pretreatment using Pd containing solution is necessary prior to electroless plating to initiate the electroless plating reaction. Then, electroless copper plating to make the insulating surface conductive follows. Then electrolytic copper plating deposits to make the connection of conductor completely. Plating can produce pattern formation on the surface and via connection simultaneously. The copper patterns are formed by etching after plating. There are a few types of plating/etching methods as follows:

(a) Panel plating method: Electrolytic copper plating is applied to the whole panel surface. This is mainly used in the case of copper clad laminate. After the electrolytic plating process, photosensitive dry film for etching is laminated on the panel. Then a resist pattern is formed by light exposure and developed. A conductor pattern is formed by etching, followed by removal of the resist. It is easily possible to make the plated copper thickness uniform, but the etching amount is so much that finer pattern formation becomes difficult, due to excess side etching of the pattern.
(b) Pattern plating method, semi-additive method: Electrolytic copper plating is applied only on the opening of the plating resist pattern. After electroless copper plating, photosensitive plating resist film is laminated on the electroless copper surface, then a plating resist pattern is formed by light exposure and development. Electrolytic copper plating is applied only on the opening parts to form the plated copper pattern. After that, the plating resist is removed, and the unnecessary copper layer (electroless and/or thin copper foil) is eliminated by flash etching to form the copper pattern. Pattern plating is better for fine patterns than panel plating, due to the control of the pattern shape and lower etching amount requirements. In order to make much finer conductor patterns, semi-additive method, in which direct electroless copper plating on the resin surface is made without copper foil, is recommended because etching can be reduced to prevent pattern side etching.
(c) Full additive method: The conductive pattern is formed only by electroless copper plating on the laminated resin surface, where a circuit pattern is made by special plating resist. Many developments were conducted previously, but only few applications remain at present because there are many difficulties to control the processes.

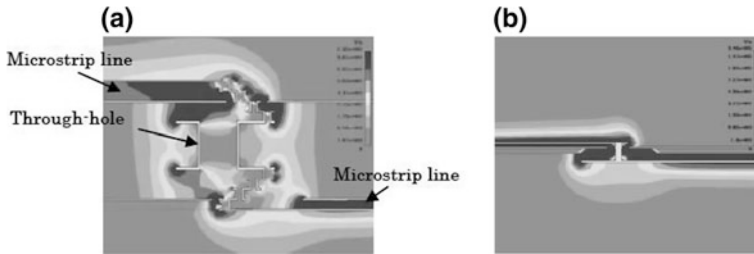

Fig. 9.9 Analysis of signal transmission characteristics in the PWBs **a** Transmission in the thick core (Conventional build-up PWB) **b** Transmission in the thin core (Multilayer thin substrate)

9.5.2 All Layer IVH Build-up PWBs Using Plating Methods

The basic build-up processes described in Sect. 9.5.1 have the features that the core substrate exists and the layers are built up on it. However, because the core substrate is thick and with large-sized through holes, high density wiring is restricted and the transmission property is poor as shown in Fig. 9.9a of [12]. In the case of thin core substrates as shown in Fig. 9.9b, this property can be improved. Therefore, build-up PWBs having only thin core substrate or those without core substrate have been developed. These kinds of build-up PWBs are called "Coreless build-up PWBs" or "build-up PWBs with any layer vias." The PWB illustrated in Fig. 9.2 consists of the thin glass fiber cloth laminates. The core substrate has the same thickness as the other layers, then the build-up layers consisting of the same laminated materials are formed on the both sides repeatedly for multilayer formation.

Figure 9.3 shows the build-up PWB without core substrate. The supporting plate is required for manufacturing and the build-up layers are formed on the plate because of the small strength of the material. The process flow is illustrated in Fig. 9.10. At first, the separable layers are formed on the supporting plate, then the layers are built up on both sides. After completion of the build-up layers, the supporting plate is separated, and the separable layers are removed by etching. The supporting plate is usually copper-laminated insulating board or stainless steel plate.

9.5.3 Bumpless Connection Build-up PWBs

The connection of the semiconductor components to the PWBs such as the packaging substrates (or so called interposer) or the mother boards is made by bumps, generally. But these bumps are larger than wiring patterns and obstructive to high density wiring. The bumpless connection build-up PWB, shown in Fig. 9.4 and applying the build-up process, can make the connection size smaller than usual

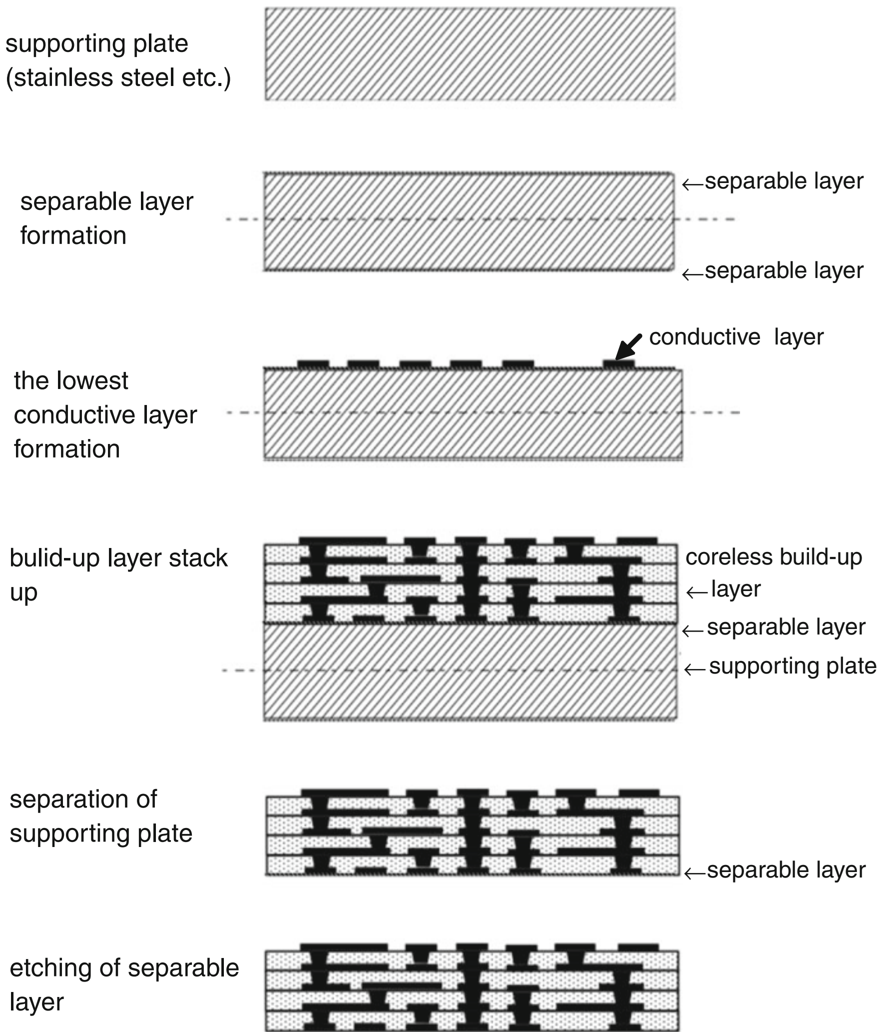

Fig. 9.10 Typical process flow of all layer IVH build-up PWB

bump. First, the semiconductor chips and the other parts are fixed on the flat plate using molding resin and scrubbed to make the upper plane flat. Then, the build-up layers are formed repeatedly as shown in Fig. 9.8. The build-up PWB, which is connected with small-plated Cu pillar to the parts without larger bumps, is produced in this way. This method is also applicable to the part-embedded PWBs.

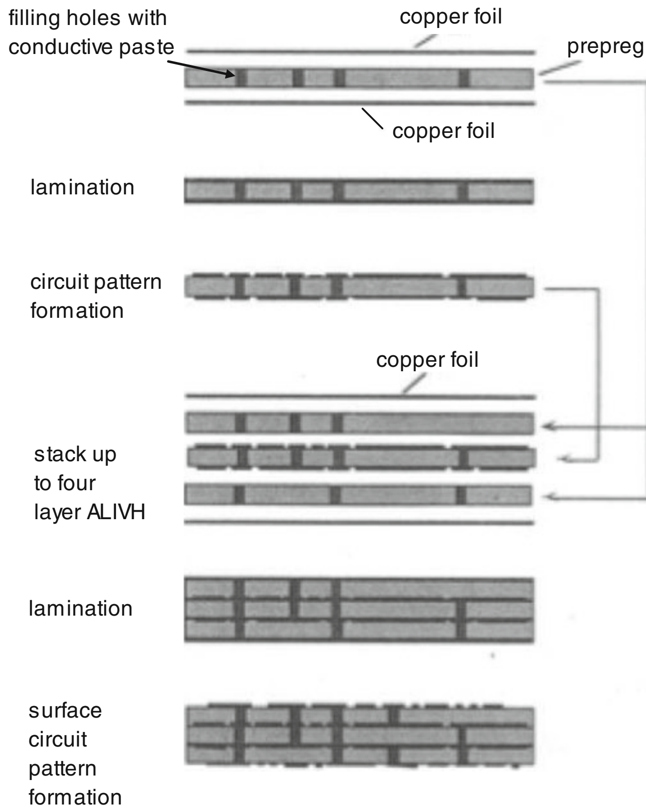

Fig. 9.11 Process flow of ALIVH

9.5.4 Build-up PWBs with Via Connection Using Conductive Paste

(1) All Layer Interstitial Via Hole (ALIVH).

Conductive paste is used for connection in the vertical direction of the board instead of plated copper metal. The fabrication process is illustrated in Fig. 9.11. First, the thin prepreg with drilled holes for via is prepared. The via holes are made by laser and filled with copper conductive paste. Then, the copper foil is laminated on both sides of the prepreg with paste-filled holes, followed by etching the copper foil to form wiring patterns. By laminating with another similar prepreg having via holes filled with conductive paste and copper foils on the double-sided board, four layer wiring board can be made. Repeating these procedures, multilayer board can be fabricated. High density patterning is associated with the technologies for fine line etching of copper foils.

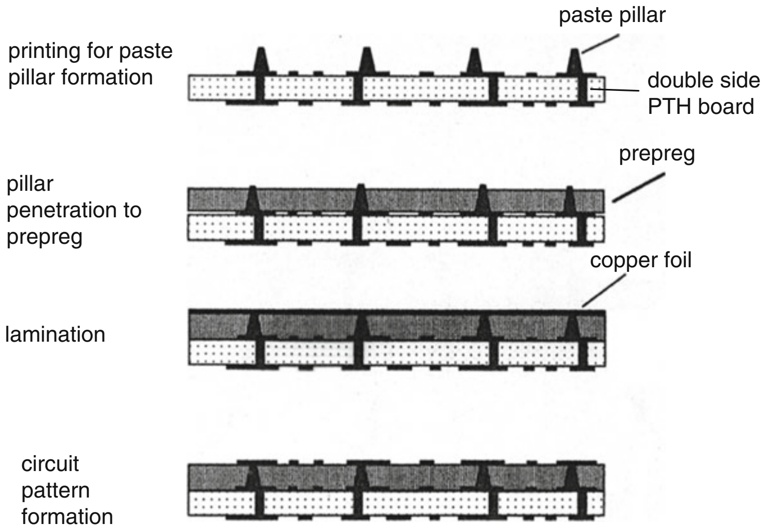

Fig. 9.12 Process flow of B^2IT

(2) Buried Bump Interconnection Technology (B^2it) [9].

As shown in Fig. 9.12, the silver conductive pillars made of silver paste are formed on the conductive patterns by means of screen printing. The pillars are high enough to make connection in the following steps. The prepreg sheet is compressed to penetrate the pillars through the sheet. Next, copper foils are laminated to make the connection with the pillars, then wiring patterns are formed by etching of the copper foil. By repeating these procedures, a multilayer board can be fabricated. To obtain high density wiring by this method, the technologies of highly fine line etching and the refined conductive pillar formation are important.

9.6 The Insulation Materials for the Build-up PWBs

There are three types of insulation materials for the build-up PWBs as follows [13]:

(1) The insulation film, which is laminated before conductive patterns are made using a semi-additive process.
(2) The resin-coated copper foil, which is laminated then conductive patterns are made by etching of copper foil.
(3) Laminating the thin prepreg including glass cloth with copper foil. The conductive patterns are made by etching of copper foil same as in the case of resin-coated copper foil.

The resin films for the insulation layer of the build-up are not strong enough to endure mechanically in the fabrication processes, so improved methods in the processes for coreless boards are necessary. When the prepreg including glass cloth is used instead, the PWBs with high mechanical strength can be made.

The insulation material is considered as the basis of the PWBs, and it is necessary for it to have sufficiently high insulating resistance even in the small layer gap and be proven in the accelerated insulation test circumstances with high temperature and high humidity.

9.6.1 The Thermosetting Resin Insulation Film for Build-up PWBs

The most common resins used for PWBs are thermosetting. The five types of thermosetting resin insulation films are listed in Table 9.5. These are classified as epoxy resins. The films are semi-cured and sandwiched between the polyethylene and polyester films. In order to give isotropic properties, inorganic fillers are involved, which are adapted to hole fabrication by laser. Most of the films have high thermal stability and low dielectric constant. The pattern fabrication on the film is performed in the semi-additive method. The other types of the resins are BT and PPE resins.

9.6.2 The Resin-Coated Copper Foil

The resin-coated copper foil is made by means of coating thermosetting resin on the one side of the copper foil then curing it partially. It is used for insulation material of build-up layer by laminating in hot press. To make wiring patterns, the panel plating method is general, but finer pattern formation is difficult due to etching of very thick copper layers, namely foil plus plated copper. To make relatively finer patterns, a pattern plating method is applied after reducing thickness of the copper foil by half through etching. The kinds of resin-coated copper foils are listed in Table 9.6. Epoxy resin is mainly used and the high thermally stable types are being developed.

9.6.3 Combination of Copper Foils with Prepreg

A hot press is applied to form the build-up layer with the copper foils and prepreg. This method is similar to the stacking process of the normal multilayer PWBs. However, the prepreg used in this case has the special feature that it is sufficiently

Table 9.5 Thermosetting epoxy resin for insulation layer of build-up PWBs

Resin	Feature	Glass transition temperature (°C)	Soldering endurability (seconds at 260 °C)	Coefficient of thermal expansion		Coefficient of water absorption (D-24/23 %)	Dielectric constant (1 MHz/1 GHz)	Dielectric loss tangent (1 MHz/1 GHz)
				α_1(ppm/°C)	α_2(ppm/°C)			
General	Non-photosensitive liquid	125–130 (DMA)		70–80	145–160		3.9/3.5	0.034/0.022
Heat resistive	Non-photosensitive film	165–185 (TMA)	>60	95	150	1.3	3.8/3.4	0.027/0.022
Halogen free	Non-photosensitive film	155–165 (TMA)	>60	45–75	120–135	1.8 (D-1/100)	3.8/3.4	0.017/0.023
Heat resistive, low dielectric constant, and halogen free	Non-photosensitive film	150 (TMA)	>60	75	150	0.8	–/2.8	–/0.014

Table 9.6 Epoxy resins used for resin-coated copper foil

Type	Resin	Thickness (mm)	Glass transition temperature (°C)	Soldering endurability (seconds at 260 °C)	Coefficient of thermal expansion		Dielectric constant (1 MHz/1 GHz)
					α_1(ppm/°C)	α_2(ppm/°C)	
General	General epoxy	0.035–0.080	125–130 (TMA)	>120	40–60	150–180	3.6–3.2/3.1–3.2
Heat resistive	Heat resistive epoxy	0.040–0.080	160–170 (TMA)	>60	20–30 (30–120 °C)	135	3.6–3.8/3.3–3.7
Halogen free	Halogen free epoxy	0.040–0.080	120–160 (TMA)	>120	35–40	140	3.6–3.8/2.8–3.7
Heat resistive, halogen free	Heat resistive, halogen free epoxy	0.035–0.080	200 (TMA)		30	100	–/3.2
High heat resistive type	Heat resistive resin-1		185–190 (TMA)	>120	40–60	90–130	–/3.4–3.9
	Heat resistive resin-2		215 (DMA)	>120	40–60		2.9–3.1/–

thin and suitable for laser fabrication, to keep the balance of small thickness with the strength of the layer reinforced by the glass cloth.

Table 9.7 lists the features of the prepregs used for the build-up layer. Table 9.8 indicates the standard thickness of the glass fiber cloth compatible with laser fabrication.

9.7 The Advanced Materials and the Manufacturing Process Technologies Developed for Build-up PWBs

The elemental process technologies applied to build-up PWBs are almost the same as those for PTH PWBs. The difference is that the patterning for the build-up processes is mainly semi-additive, however, that used for the PTH is mainly subtractive, namely panel plating methods, because semi-additive processes are more promising to obtain finer lines as above-mentioned in Sect. 9.5.1. The characteristics of the insulation materials for build-up PWBs must be thin and compatible for laser fabrication, because drilling is no longer possible for such fine vias. Many developments have been made to adapt to these requirements. Several advanced technologies for build-up PWBs are described, as follows.

9.7.1 The Glass Fiber Opening Technologies and the Glass Cloth Compatible for Laser

The build-up PWBs using glass cloth have been widely spread because the similar fabrication processes and the facilities for the conventional PTH PWBs can be used for manufacturing. The glass fibers used for such cloths consist of bunches of 100–200 filaments. Because each filament must penetrate and bond with the resin to prevent degradation of insulating properties and to improve the fabrication efficiency, the glass fiber bunches should be specially treated to be filaments. This treatment is called “fiber opening.” The bunches of treated filaments are woven into cloth, and the resin is impregnated into the cloth. In these cloths, the fibers include no pores and are uniformly coated with resin. Figure 9.13 illustrates a bunch of glass filaments treated by fiber opening and impregnated with resin [14]. Figure 9.14a shows the woven glass cloth with fiber opening treatment and Fig. 9.14b shows a cross-sectional view of glass cloth [14]. This results in the improvement of the capability of via formation by laser and the insulation properties. The nonuniformity of the glass filament distribution in the glass cloth leads to nonuniform via hole formation by laser. To avoid such nonuniformity, not only opening the fibers to be thin filaments but also fabricating the bunch of the filaments to be flattened, the glass filament distribution becomes uniform and the 30 μm of cloth thickness is achieved.

Table 9.7 Prepregs used for build-up PWB

Features			Properties after insulation layer is formed						
Types	Resin	Typical thickness (mm)	Peel strength of Cu foil (kN/m)	Peel strength of inner layer Cu foil (kN/m)	Glass transition temperature (°C)	Coefficient of thermal expansion (ppm/°C)	Elastic modulus (GPa)	Dielectric constant (1 MHz/ 1 GHz)	Dielectric loss tangent (1 MHz/1 GHz)
Prepreg containing inorganic non-woven prepreg containing inorganic non-woven filler	Epoxy hologen free	0.08		1.5–1.6	170–180 (DMA)		5–4		
For laser applicability[a]	Epoxy	0.05 0.078			160–170 (TMA) 190–200 (DMA)		30–32		
For laser applicability[a]	Epoxy hologen free	0.056 0.061			140–150 (TMA) 150–220 (DMA)		23–25		
Non-woven glass cloth	BT resin	0.03 0.05	1.0		225(DMA)	z:45–55 (< Tg)	10.0	4.3/4.1	0.0090/0.0120
Non-woven organic fiber	BT resin	0.03 0.04 0.065	1.0		210(DMA)	z:60–70 (< Tg)	7.0	3.5/3.3 (20 GHz)	0.0120/0.0034(20 GHz)

[a] Including glass cloth woven with filaments treated by fiber opening

Table 9.8 Thickness of the glass fiber cloth compatible with laser fabrication

Features	Typical thickness (mm)
General laser compatible glass fiber cloth	0.10–0.015
Highly uniform laser compatible glass fiber cloth	0.09, 0.045

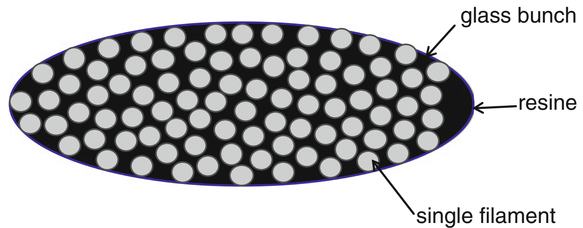

Fig. 9.13 Bunch of glass filaments treated by fiber opening (Resin is uniformly impregnated into the bunch)

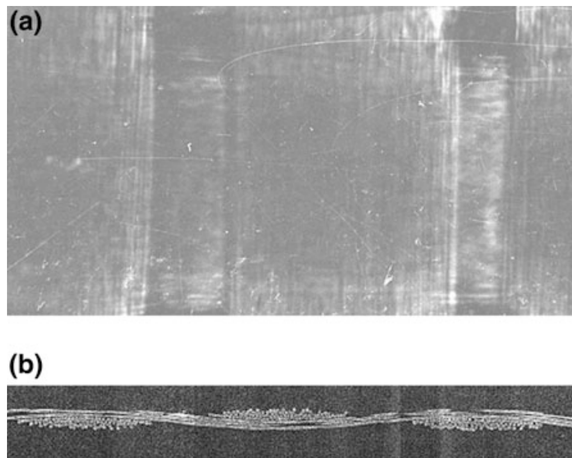

Fig. 9.14 Woven glass fiber cloth compatible with laser fabrication **a** Woven glass cloth after fiber opening **b** Cross-sectional view. Bunch of filaments becomes flattened

9.7.2 Plating Techniques to Realize Fine Circuit Pattern Wiring

The two types of plating methods to form the conductive patterns, panel plating and pattern plating (semi-additive) methods, are described in Sect. 9.5.1 and illustrated in the middle part of Fig. 9.8. The more detailed steps are shown in Figs. 9.15 and 9.16. As described in Sect. 9.5.1, the semi-additive method is recommended to make much finer conductor patterns, because etched amount can be decreased to prevent side etching of copper patterns. Figure 9.15a indicates the panel plating method. Electrolytic copper plating is applied to the whole panel surface. After the etching resist pattern is formed by photosensitive dry film, copper circuit pattern is fabricated by etching, followed by removal of the resist. Figure 9.15b indicates the pattern plating method. Photosensitive plating resist film is laminated on the electroless copper surface, then the plating resist pattern is

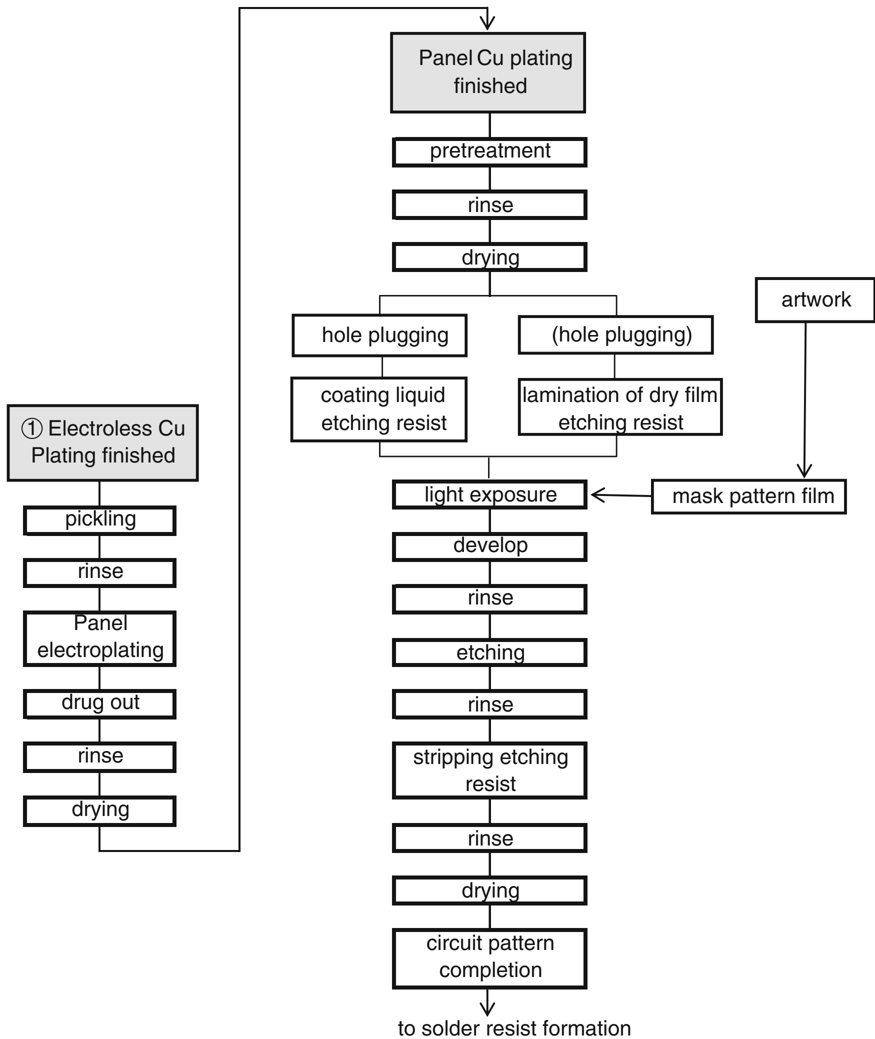

Fig. 9.15 **a**Process flow of the panel plating method**b**Process flow of the pattern plating method

formed by light exposure and developed. Electrolytic copper plating is made only on the opening parts to form the plated pattern. After that, the plating resist is removed, and the unnecessary copper layer is eliminated by quick etching to form copper patterns. The comparison between these methods is illustrated in Fig. 9.16. The thickness distribution of plated copper of panel plating is uniform because the plating is applied to the whole panel surface. However, the conductive patterns are made by etching which is associated with side etching of the patterns resulting in large distribution of pattern width and decrease of pattern accuracy. On the other

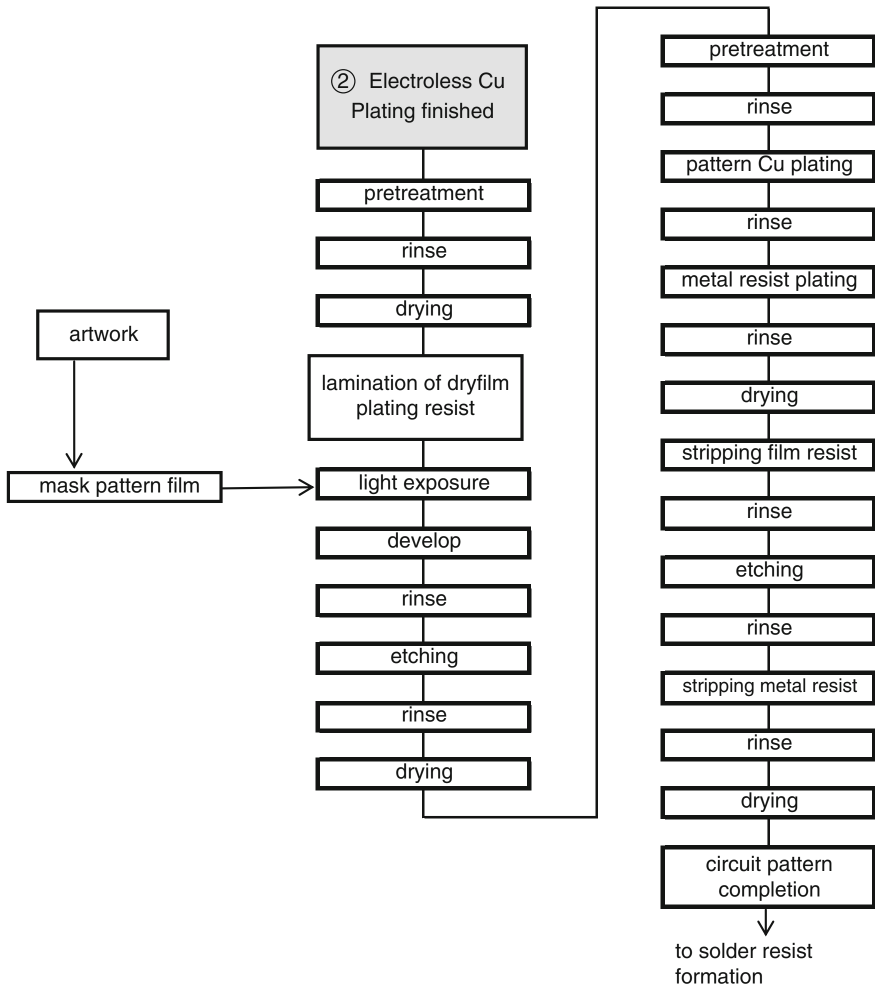

Fig. 9.15 continued

hand, in the pattern plating method, the pattern width can be controlled by the opening width of the plating resist and the etched amount is much smaller than that in panel plating because the amount is only for the electroless plating and the thin copper foil. By thinning the copper foil as much as possible and/or eliminating the copper foil, the etching time can be shortened to lead to accurate pattern width due to inhibiting of pattern side etching. So semi-additive processes, which eliminate use of copper foil and can minimize side etching, are widely used for formation of very fine patterns for high density wiring.

The thickness distribution of electrolytic copper plating is one of the most important issues. To make the thickness distribution more uniform, the current density distribution in the electroplating cell must be controlled by setting some

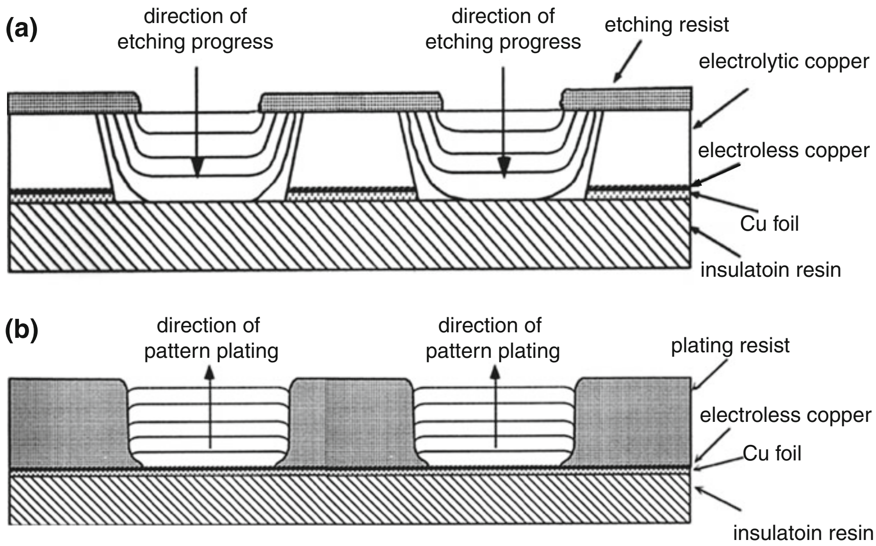

Fig. 9.16 Comparison between the panel and the pattern plating methods. **a** Panel plating **b** Pattern plating

shields and/or dummy electrodes and adjusting them. There is a reported method in which convex electrodes are set in the neighborhood of the plating area [15]. In this case, the convex electrodes work as the dummy electrodes and the current density distribution can be controlled by adjusting some factors such as height, size, area, and so on. Figure 9.17 indicates how such convex electrodes set at the side of the cathode can control the current distribution: (a) when the convex surface is conductive, current tends to go to it preferentially, and the current density on the cathode becomes lower. (b) When the partially masked convex electrode is set at the side of the cathode, the current density can be controlled to be uniform by means of adjusting the masked amount, and so on. (c) When the convex surface is insulated, all current goes to the cathode and the current density at the edge becomes higher. In case of pattern plating, the nonuniformity of pattern density causes the thickness distribution. The improvement to minimize the thickness distribution is also to be considered [16].

9.7.3 Via Filling and Through Hole Filling by Electroplating

The via holes with small diameter is used for connecting the layers in the build-up PWBs. Figure 9.18 shows the two types of stacking via structures. The conformal vias in Fig. 9.18a cannot be stacked on the vias in the lower layer, so the vias must be located in staggered way. This structure lowers the electrical performance and the wiring density. However, the filled vias in Fig. 9.18b, in which the inside is

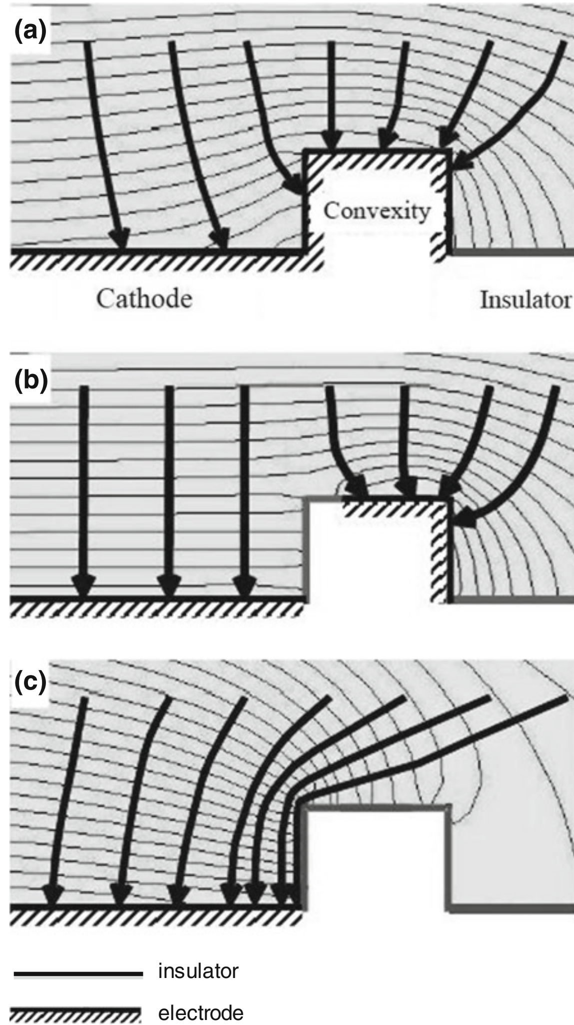

Fig. 9.17 Current distribution changes by means of the convexity electrodes set at the side of the cathode (see text)

filled with plated copper metal, can be stacked on the vias in the lower layer, resulting in better electrical performance and larger wiring density than those for the conformal vias. Therefore the application of filled vias is expanding. The example of wiring structure using a lot of the stacking filled vias is illustrated in Fig. 9.19, which is difficult to be substituted by conformal vias. The adequate control of the additives and the plating conditions in the copper plating is very important to achieve the successive and continuous filling performance. The mechanisms of copper filling should be recognized, as described previously in this book.

For making the plated through holes of the core substrate, the control of additives and plating conditions can result in filling of the small through holes as long as the substrate is not so thick, which can improve the electrical performance

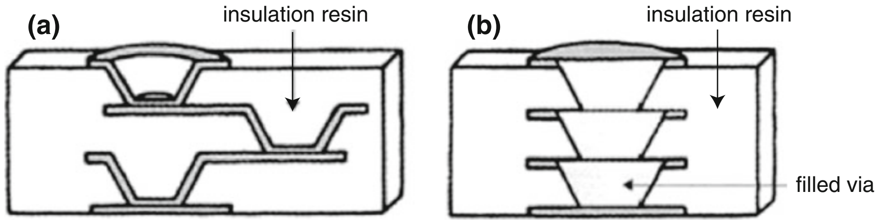

Fig. 9.18 Comparison of two types of stacking via structures **a** Staggered connection (*conformal vias*) inductance: 190 pH hole diameter (*bottom*): 65 μm thickness between layers: 30 μm via pitch :150 μm **b** Stacked connection (*filled vias*) inductance: 46 pH hole diameter(*bottom*): 65 μm thickness between layers: 30 μm

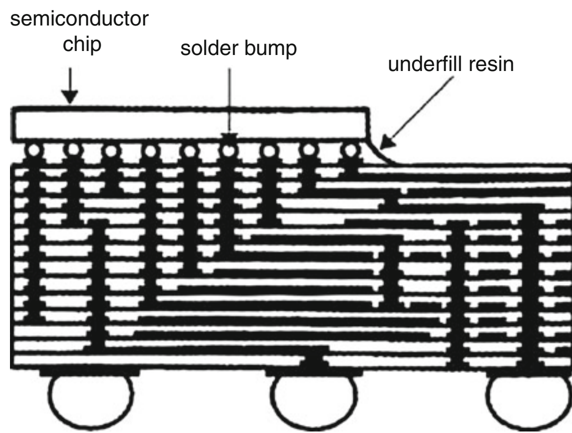

Fig. 9.19 Example of wiring structure using a lot of the stacking filled vias

and wiring density. Figure 9.20 shows the filled through hole by means of copper electroplating. This filled through hole can increase the fine-sized holes and their density in the core substrate, leading to high density wiring of the core substrate.

9.7.4 The High Adhesion Strength of Copper Circuit on the Flat Resin Surface

Not only high density wiring but also high signal transmission properties are required for build-up PWBs. As indicated in Table 9.4, due to the skin effect, most of the signal transfers within about 2 μm of the surface in case of 1 GHz signal. Therefore, the interface between the conductors and the insulators must be flat. Otherwise the signal transfer route becomes longer. On the other hand, a flat interface tends to have lower adhesion strength. A surface treatment compatible with a flat interface with high adhesion strength should be developed. When the resin adheres on the copper surface, surface treatment of the copper can enhance

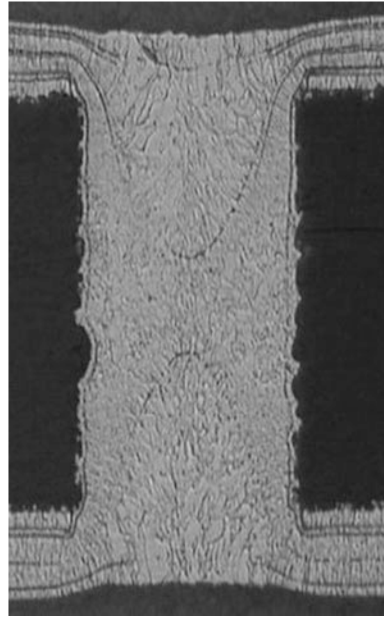

Fig. 9.20 Example of filled through hole

the adhesion. When the electroless copper plating has to be applied to a flat resin surface, additional treatment of the resin is important, because usual electroless plating does not normally adhere to the surface. The several methods are described as follows:

(1) Adhesion of resin on low profile copper foil
Usual copper foils have rough surfaces to which resins adhere by means of anchor effects. The roughness affects the transmission properties, so low profile copper foils with small roughness have been wide-spread. As shown in Fig. 9.21, a cross-sectional view of copper foils, the conventional copper foil (a) has 7 ~ 9 μm of roughness (Rz) and the low profile one (b) has 2.7 ~ 3.3 μm. Recently copper foil with the lower profile, 1.3 ~ 1.7 μm or less, has been developed. Figure 9.22 indicates that the transmission loss depends on the copper foil profile, and it shows that low profile foil is better. On the other hand, the low profile may bring lower adhesion with the resin, but this is not yet a practical issue. A recent research result shows improvement of the adhesion with resin by means of coating the silane coupling agent on the copper foil [17]. In this method, the coated silane coupling agent was heated on the flat copper foil at the high temperature to enhance the adhesion. The combination of silane coupling agent and resin is important.
(2) The Adhesion of electroless copper plating on the cured resin surface. In the semi-additive processes, electroless plating is applied to the resin surface to make it conductive. The adhesion strength between the electroless plating and the resin is important. Usually, by means of optimizing resin composition and

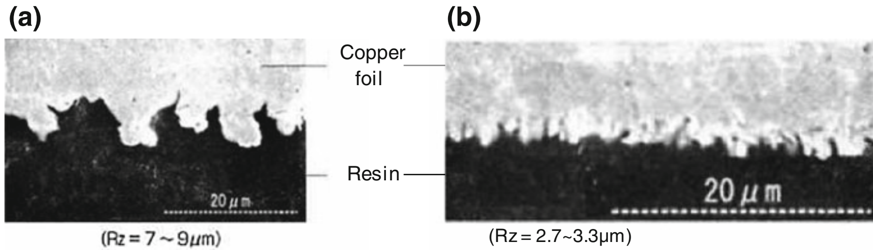

Fig. 9.21 Cross-sectional views of copper foils **a** Conventional copper foil **b** Low profile copper foil

Fig. 9.22 Dependence of the transmission loss on the profile of copper foils

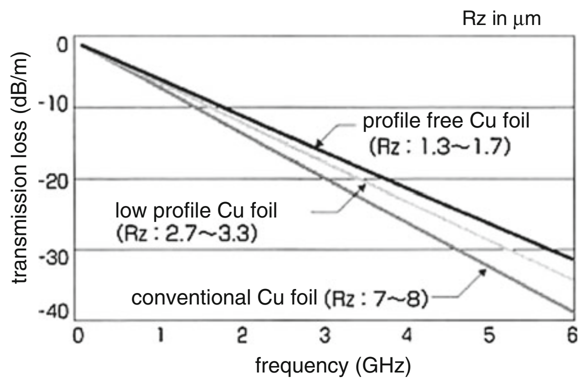

making 2 ~ 3 μm of roughness by desmearing (resin chemical etching), the resin has anchors to provide adhesion. As the roughness enlarges the transmission loss, the adhesive electroless plating made on the flat resin surface is an important subject. Many researches have been conducted and some typical methods are indicated as follows:

(a) Modification of the resin surface by irradiation with ultraviolet.
(b) Generation of active groups to connect with copper surface by chemical treatment of the polyimide resin surface.
(c) Introduction of dispersed nanoparticles in the resin followed by dissolution of the particles to form fine roughness.
(d) Coating the organic layer with a porphyrin structure compound which can stick to both resin and plated copper.
(e) Formation of an organic thin layer on resin and reactive group to acquire the affinity to plated copper.
(f) Introduction of compounds containing nitrogen, sulfur and silicon between the resin and the electroless copper plating to form a molecular bond.

There have been many other proposed methods. These may be effective for the single side and double side laminate boards. However, for the build-up PWBs, in

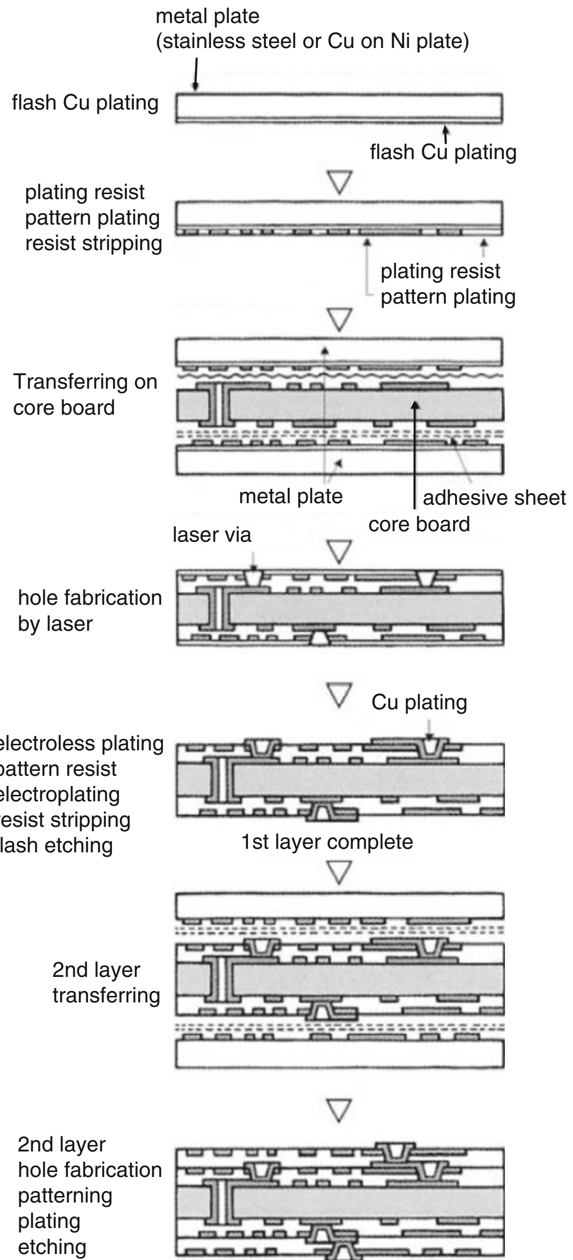

Fig. 9.23 Pattern transferring process

which the steps of flattened resin coating and desmearing are repeated for each layer, it seems that these are neither compatible with the current processes nor sure to replace them in practical use.

(3) The Pattern Transferring Processes on Smooth Resin Surface [18, 19].

The methods by which the formed conductor patterns are transferred on the uncured resin have been proposed for fabricating build-up PWBs. The methods have not been practiced yet. Some attempts for development were made and some derived processes were designed. A few examples are described as follows [20]:

The basic process flow is illustrated in Fig. 9.23. At first, a flash copper plate is made on the base metal plate of which surface is finished to make the plated copper stripped easily. After the plating pattern resist is formed, the pattern plating is made, followed by a surface treatment for adhesion with the resin. Next, these plated circuit patterns are transferred on the core board with the uncured resin by means of hot press. After cooling and stripping the base metal plates, the surfaces are covered with the flash copper plating previously made on the base metal plate. Following the sequential steps, hole forming by laser, desmearing, electroless plating, plating resist formation, and pattern electroplating into the holes, the via connection between the layers is made. The via filling plating is preferable for this purpose. Then by stripping of the resist and etching of the remained flash plating by quick etching, the formation of the conductive circuit layer is completed. The surface is flat as the conductive patterns buried in the resin except for the vias. The resin also has a flat surface and adheres to the conductive patterns strongly enough because the adhesion of patterns is made with not only the bottom but also with the side edges. Repeating these procedures, the build-up layers can be added. In Fig. 9.23, the illustrated processes are incorporated with the basic ones described in Sect. 9.5.2. Also the processes described in Sects. 9.5.3 and 9.5.4 can be applied to these transferring processes. The merits of these transferring processes are as follows:

- A flat resin and copper surface can be obtained.
- The Pd catalyst for electroless copper plating used in the via formation step can be removed in flash etching step.
- No Pd catalyst residue exists between the patterns.
- Solder resist coating is easy because the surface is flat.

9.8 Closing Remarks

The various topics related to the build-up PWBs, the history, manufacturing process, materials, recent developments, and so on, are described. In the circumstances where the electronic equipment is going to the direction of requiring high operation speed and high density assembly and semiconductor devices become more integrated, the build-up PWBs have been enhancing the importance, regardless of the categories from the package substrates assembling bare chips to

the mother boards uniting whole system. In order to respond the importance, it is necessary for us to construct the optimal manufacturing processes and improve the manufacturing circumstances to achieve high reliability.

References

1. Takagi K (2006) Yoku wakaru build-up tasou purintohaisenban d-up P dekiru made; in Japanese (Comprehensive Handbook of Manufacture of Multilayer BuilWBs). Nikkan Kogyo Shinbun, Tokyo, p 10
2. Beadles, RL (1967) Interconnection and Encapsulation. ASD-IDR-63-316 14:654
3. Lassen, CL (1979) Electronics. p 27
4. Takagi K (1986) Tasou printohaisenban no seizou koutei to gijutsu; in Japanese (Manufacturing Processes and Technologies of Multilayer PWBs). Denshi Gijutsu-Supplement Edition in June 28(7):58
5. BrÎsamle H, Brabetz B, Ehrenstein VV, Bachmann F (1988) Technology for microwiring substrate. Siemens Forschugs−und Entwicklungsberichte 17(5):249
6. Tsukada Y (1991) Hyosou Purinto Haisenban To Flip Chip Jisso Gijutsu (Surface Laminar Circuit (SLC) and Flip Chip Connection Technologies). Hyomen Jisso Gijutsu. Surface Mount Technologies 1(1):28
7. Intel Press Release (2001) Development of innovative packaging technology. Oct 09 2001
8. Yoshida (1999) Zensou IVH Kouzou"ALIVH" (All Layer IVH Structure "ALIVH") Proceedings of 13th Meeting of Japan Institute of Electronics Packaging (JIEP), Aoyama Gakuin University, Tokyo, March, 1999, p 209
9. Fukuoka Y, Oguma T, Tahara Y (1998) New high density substrates with buried bump interconnection technology (B^2it). In: Proceedings of 1998 international symposium of microelectronics, San Diego, Nov 1998, p 431
10. The Report of the Workshop for Evaluation Research of Electrochemical Migration (2009) The Study of the Acceleration Test Methods for the Insulation of High Density Printed Wiring Boards. Japan Institute of Electronics Packaging (JIEP). June, 2009
11. Takagi K (2011) Yoku wakaru build-up tasou purintohaisenban no dekiru made; in Japanese (Comprehensive Handbook of Manufacture of Multilayer PWBs Third Edition). Nikkan Kogyo Shinbun, Tokyo, p 220
12. Nakase K, Sakai J, Shimoto T, Inoue H (2004) High-frequency properties of the MLTS (Multi-Layer Thin-Substrate). In: Proceedings of international conference of electronics packaging (ICEP), Tokyo, April 2004, p 109
13. Takagi K (2011) Yoku wakaru build-up tasou purinto haisenban no dekiru made; in Japanese (Comprehensive Handbook of Manufacture of Multilayer PWBs) Third Edition. Nikkan Kogyo Shinbun, Tokyo, p 196
14. Asahi Schwebel: Technical Material
15. Okubo T, Kodera T, Kondo K (2004) Uniformity formation of panel plating by using convexity modification of cathode holder (in Japanese). J Japan Inst Electronic Packaging 7 (2):141
16. Okubo T, Kodera T, Kondo K (2006) Patterned Copper Plating Layer Thickness Made Uniform by Placement of Auxiliary Grid Electrode about Ball Grid Arrays. Chem Eng Commun 193(12):1503
17. Takahashi M, Dobashi M, Yamashita T (2004) The effects of silane coupling agents on the adhesion of copper circuits with printed wiring boards (in Japanese). In: Proceedings of 110th meeting of surface finishing society of Japan, 14A-8, Matsushima, Sept 2004, p 41

18. Takagi K (1980) The manufacturing method of high density printed wiring boards. Japan Patent 999420, May 1980
19. Takagi K (2000) Build-up Tasou Haisenban Gijutsu; in Japanese (Technologies of Multilayer Build-up Printed Wiring Boards). Nikkan Kogyo Shinbun, Tokyo, p 75
20. Takagi K (2006) The manufacturing technologies of printed wiring boards. In: Japan Institute of Electronics Packaging (JIEP) (ed) Handbook of printed wiring board technologies, 3rd edn. (in Japanese), Nikkan Kogyo Shinbun, p 327

Chapter 10
Copper Foil Smooth on Both Sides for Lithium-Ion Battery

Akitoshi Suzuki and Jun Shinozaki

10.1 Introduction

An electrodeposited copper foil has been used in many areas of printed-wiring boards, such as rigid printed-wiring boards and flexible printed-wiring boards, as shown in Fig. 10.1. Even now, it is estimated that more than 90 % of all the electrodeposited copper foil production is being used for printed-wiring boards.

On the other hand, the use of electrodeposited copper foil as the negative electrode collector of lithium-ion batteries has recently been attracting attention. The time when the electrodeposited copper foil came into use in this field was comparatively recent, i.e., in the latter half of the 1990s. Many lithium-ion batteries are being used for mobile phones, smart phones, notebook personal computers, etc. In addition, major automakers around the world are currently studying its use in EV, HEV, PHEV, etc.

A “copper foil smooth on both sides,” which is an electrodeposited copper foil for lithium-ion batteries, has been developed during the optimization process because a decrease in the capacity retention rate occurred during repeated charge and discharge of the battery when the electrodeposited copper foil for a printed-wiring board was used as the lithium-ion battery negative electrode collector.

Around 1991 lithium-ion batteries began to be industrially mass-produced. At that time, a rolled copper foil was used as the negative electrode collector. In the mid-1990s, an attempt to use an electrodeposited copper foil as the negative

A. Suzuki (✉)
Development Dept. Copper Foil Division, Furukawa Electric Co., Ltd. Metal Research Center, 601-2, Otorozawa, Nikko-City, Tochgi 321-2336, Japan
e-mail: mr441466@mr.furukawa.co.jp

J. Shinozaki
Furukawa Electric Co., Ltd. Metal Research Center, Nikko-City, Japan
e-mail: mr251719@mr.furukawa.co.jp

K. Kondo et al. (eds.), *Copper Electrodeposition for Nanofabrication of Electronics Devices*, Nanostructure Science and Technology 171, DOI: 10.1007/978-1-4614-9176-7_10,
© Springer Science+Business Media New York 2014

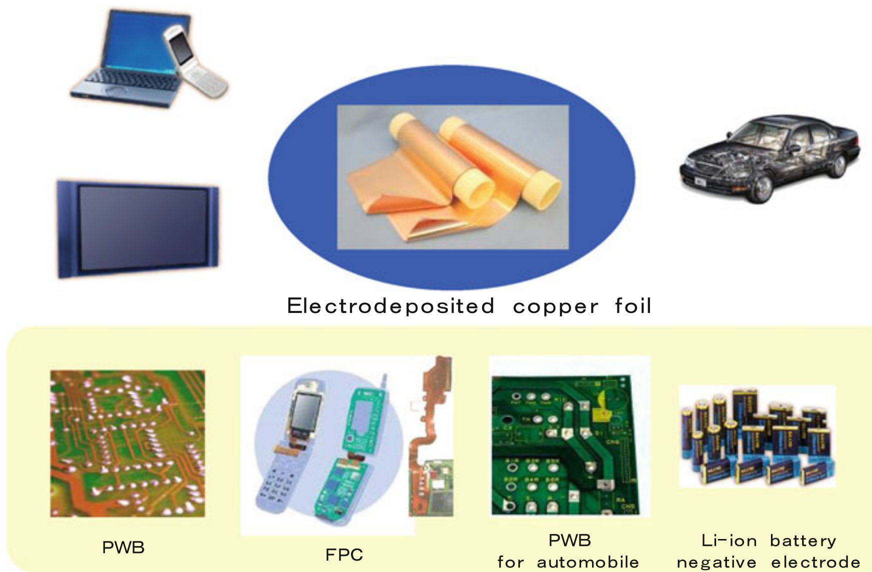

Fig. 10.1 Uses of electrodeposited foil

electrode collector instead of the rolled copper foil was performed in order to reduce costs. Because only the electrodeposited copper foil for printed-wiring boards existed as an electrodeposited copper foil at that time, the electrodeposited copper foil for printed-wiring boards was used as the negative electrode collector in manufactured batteries for charge–discharge tests.

The electrodeposited copper foil for printed-wiring boards has (a) a “matte side” with pyramidal convexities and the opposite side and (b) a “shiny side” with a smooth face as shown in Fig. 10.2.

Though the battery capacity retention rate of lithium-ion batteries gradually decreases with repeated charge and discharge, the capacity retention rate of the battery using the electrodeposited copper foil for printed-wiring boards as the negative electrode collector decreased at a rate faster than that of the battery using the rolled copper foil.

As a result of various analyses of this phenomenon, it was found that the decrease in the capacity retention rate was promoted if the copper foil having a remarkably different surface roughness of the “matte side” versus the “shiny side” like the electrodeposited copper foil for printed-wiring boards was used, and that the decrease in the capacity retention rate could be suppressed if the electrodeposited copper foil with both sides smooth and shiny was used.

An electrodeposited copper foil for use in lithium-ion batteries was developed based on such a finding of a “copper foil smooth on both sides” as shown in Figs. 10.2c, d.

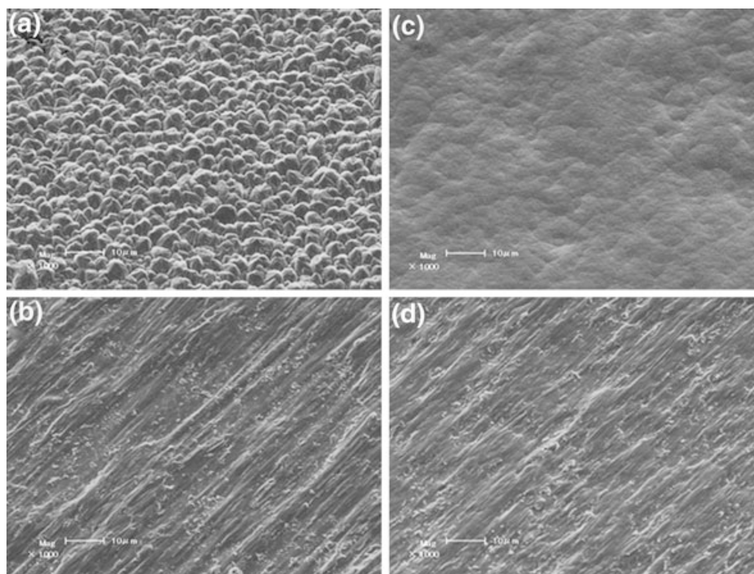

Fig. 10.2 SEM micrographs of surface morphology of 10 μm untreated copper foils **a** Matte side of copper foil for PWB **b** Shiny side of copper foil for PWB **c** Matte side of copper foil for LIB **d** Shiny side of copper foil for LIB

During the production of the “copper foil smooth on both sides,” a copper-sulfuric acid electrolyte in which organic additives and chloride ions were added was used in order to obtain a copper foil with a smooth shiny surface. The organic additives used in this study are the same types of organic additives used in the Cu damascene electroplating process.

In this paper, regarding the “copper foil smooth on both sides,” which is being used for the lithium-ion battery negative electrode collector, its manufacturing process, mechanical characteristics, characteristics as a negative electrode collector, and recent trends are described.

10.2 Manufacturing Process of Electrodeposited Copper Foil

The manufacturing process of the electrodeposited copper foil is first described. The manufacturing process of the electrodeposited copper foil consists of a dissolving process to dissolve the copper raw material, an electroforming process, a surface treatment process, a slitting process to slit the copper foil to the required width, and a sheeting process to further cut the copper foil after slitting when a sheet-shaped copper foil is required as shown in Fig. 10.3.

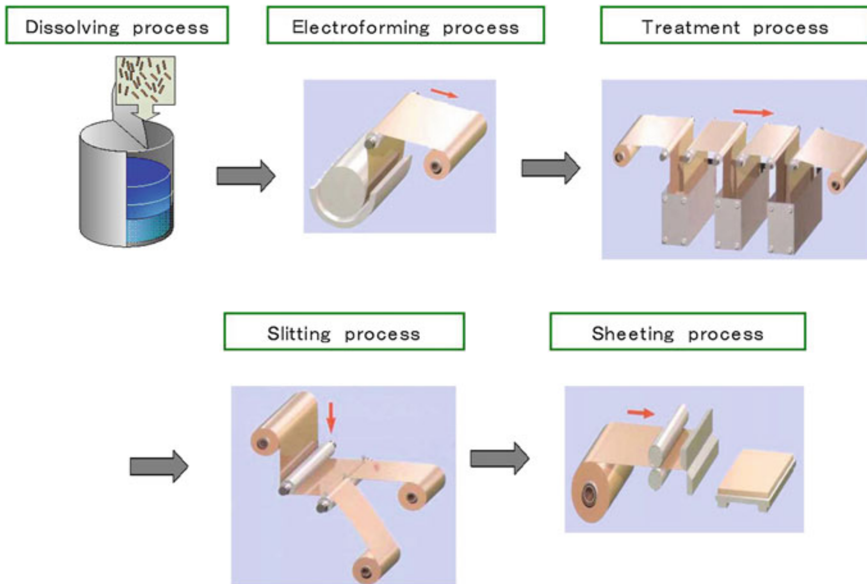

Fig. 10.3 Manufacturing process of electrodeposited copper foil

In the electrodeposited copper foil for the printed-wiring board, the product after slitting and the product after cutting are used according to the manufacturing process of the customer.

On the other hand, though the product after slitting is used for the electrodeposited copper foil for lithium-ion batteries, there are few cases in which the product after cutting is used. The reason for this is that the negative active material is applied to the coiled copper foil during the manufacturing process of the lithium-ion battery's negative electrode.

10.2.1 Dissolving Processes

This is a process to dissolve the copper raw material in a copper-sulfuric acid electrolyte. Since copper is used as the anode in a conventional copper plating process, the copper concentration in the electrolyte is unchanged because when the copper is electrodeposited on the cathode from the electrolyte, almost the same amount of copper dissolves from the anode. Consequently, this process is not required in the conventional copper plating process.

On the contrary, in the manufacturing process of the electrodeposited copper foil, the copper concentration in the copper-sulfuric acid electrolyte decreases and the sulfuric acid concentration increases when the manufacturing of the electrodeposited copper foil is continuously carried out because the manufacturing is carried out using an insoluble anode (DSE) as described in Sect. 10.2.2.

It is required to maintain a certain copper concentration in the copper-sulfuric acid electrolyte in order to continuously carry out the manufacturing of the electrodeposited copper foil. Therefore, copper is dissolved in the copper-sulfuric acid electrolyte during this process, and the copper concentration in the electrolyte remains constant.

The copper-sulfuric acid electrolyte having a concentration of about Cu = 50–100 g/l and H_2SO_4 = 50–150 g/l is used as the electrolyte.

As for the copper raw material, scrap wire, which is prepared by shredding electric wire of about 2–3 mm in diameter to the size of about 20–30 mm in length, is used. However, the scrap wire with a high purity of greater than 99.9 % of copper is used although it is called scrap wire. Moreover, the reason to use the raw material of such a shape is to promote the copper dissolution.

The dissolution of copper is carried out using a dissolution vessel made of SUS as shown in Fig. 10.2. The scrap wire is charged into the copper-sulfuric acid electrolyte at a temperature of about 40–70 °C, and air is bubbled through it. The reactions at this time are expressed as ionic Eqs. (10.1) and (10.2).

$$Cu + 1/2O_2 \rightarrow CuO \quad (10.1)$$

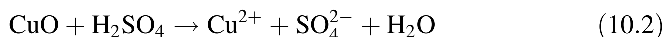

$$CuO + H_2SO_4 \rightarrow Cu^{2+} + SO_4^{2-} + H_2O \quad (10.2)$$

10.2.2 Electroforming Processes

The electroforming process is shown in Fig. 10.4. In this process, various organic additives and chloride ions are added to the copper-sulfuric acid electrolyte prepared by the preceding dissolution process. The blended electrolyte is kept at a temperature of about 40–60 °C, and supplied from the lower side of the rotating cylindrical titanium drum, then the electrolysis is carried out.

A titanium drum is used as the cathode, and an DSE is placed under the titanium drum. The copper-sulfuric acid electrolyte flows between the titanium drum and the DSE, an electric current is applied to the electrodes at the high current density of about 30–100 A/dm^2, and a copper layer is electrodeposited on the titanium drum. After the thickness of the copper layer meets the predetermined thickness requirement, the copper layer is peeled and coiled, and a raw electrodeposited copper foil is obtained.

The reaction on the titanium drum (cathode) is expressed by ionic Eq. 10.3.

$$Cu^{2+} + 2e^- \rightarrow Cu \quad (10.3)$$

On the other hand, the reaction of ionic Eq. 10.4 occurs on the DSE to produce oxygen gas. This oxygen gas agitates the electrolyte.

$$H_2O \rightarrow 2H^+ + 2e^- + 1/2O_2 \quad (10.4)$$

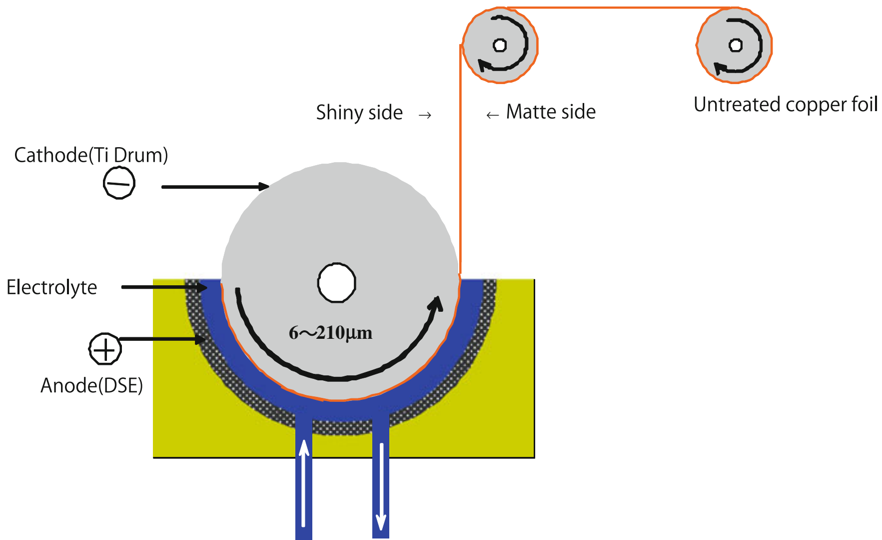

Fig. 10.4 Electroforming process

The amount of electrodeposited copper on the titanium drum is proportional to the quantity of electricity (current density × time) passed through the titanium drum and the DSE. The current density is usually kept constant, therefore, the thickness of the copper foil is adjusted by the rotation speed of the drum.

The thickness of the electrodeposited copper foil for lithium-ion batteries is from about 6 to 20 μm.

On the other hand, the thickness of the electrodeposited copper foil for printed-wiring boards is usually about 9 to 210 μm, and recently, a copper foil with a thickness of about 400 μm is also being manufactured.

The copper foil manufactured in this process is called "untreated copper foil." The "untreated copper foil" means a copper foil, which has not been subjected to any surface treatment after it was peeled from the drum. [1]

Figure 10.2 in Sect. 10.1 shows the surface profiles of the "untreated copper foil" used for printed-wiring boards and for lithium-ion batteries.

As for the electrodeposited copper foil for printed-wiring boards, the surface with pyramidal convexities shown in Fig. 10.2a is called the "matte side," and the smooth surface in Fig. 10.2b is called the "shiny side." The "matte side" is a surface which was in contact with the copper-sulfuric acid electrolyte. The reason why it is called the "matte side" is that it has a rough surface with pyramidal convexities on the electrodeposited copper foil used for printed-wiring boards as shown in Fig. 10.2a.

The "shiny side" is a face which was in contact with the titanium drum in Fig. 10.4. Though it has a smooth shiny surface in appearance, and called the "shiny side," a small streak is observed when observed by SEM as shown in

Fig. 10.2b. The reason for this is that the "shiny side" is a replica of the brush lines caused by polishing the surface of the titanium drum.

The surface of the titanium drum is polished at regular time intervals. Since the surface of the titanium drum is always exposed to the copper-sulfuric acid electrolyte at high temperature and high concentration of sulfuric acid, the surface of the titanium drum gradually becomes rough, thus it becomes difficult to peel off the copper foil when the copper foil is continuously manufactured for a long time. In order to prevent this problem, the surface is polished at regular time intervals to make it easy to peel off the copper foil.

As for the electrodeposited copper foil for lithium-ion batteries, the "shiny side" of Fig. 10.2d is no different from the electrodeposited copper foil for printed-wiring boards, however, the "matte side" of Fig. 10.2c has a shiny smooth surface. The reason for the difference in both types is that a different organic additive is added to the copper-sulfuric acid electrolyte, which is used in the electroforming process.

The use of the basic bath composition for the copper-sulfuric acid electrolyte is common in both copper foil manufacturing processes. The electrodeposition of copper is carried out after the chloride ion and organic additives are added to the electrolyte. The surface profile of the copper foil can be adjusted by selecting the type of organic additive to be added.

Organic additives to produce pyramidal convexities on the surface are added when making the electrodeposited copper foil for printed-wiring boards, and organic additives to produce a shiny smooth surface are added when making the electrodeposited copper foil for lithium-ion batteries.

In addition, the reason to make the shiny smooth surface on the electrodeposited copper foil for lithium-ion batteries is explained in Sect.10.4.

10.2.3 Surface Treatment Processes

For the electrodeposited copper foil for printed-wiring boards, the untreated copper foil, which is the raw foil produced by the electroforming process, is placed in the treater shown in Fig. 10.5. The "matte side" is subjected to a surface treatment in the following order: copper plating (called copper nodule plating) with a grain size of about 1–3 μm, nickel plating and zinc plating with a thickness of about 10–30 nm, chromate coating with a thickness of about 1–3 nm, and a silane coupling treatment.

On the other hand, the "shiny side" is subjected to zinc plating with a thickness of about 10–30 nm, and a chromate coating with a thickness of about 1–3 nm.

The copper foil before being subjected to the surface treatment process and the one after the surface treatment process are shown in Figs. 10.5a, b as the untreated copper foil and treated copper foil, respectively.

The purpose of applying such a copper nodule plating and the surface treatment is improvements in the following characteristics of (1–6) are demanded for the

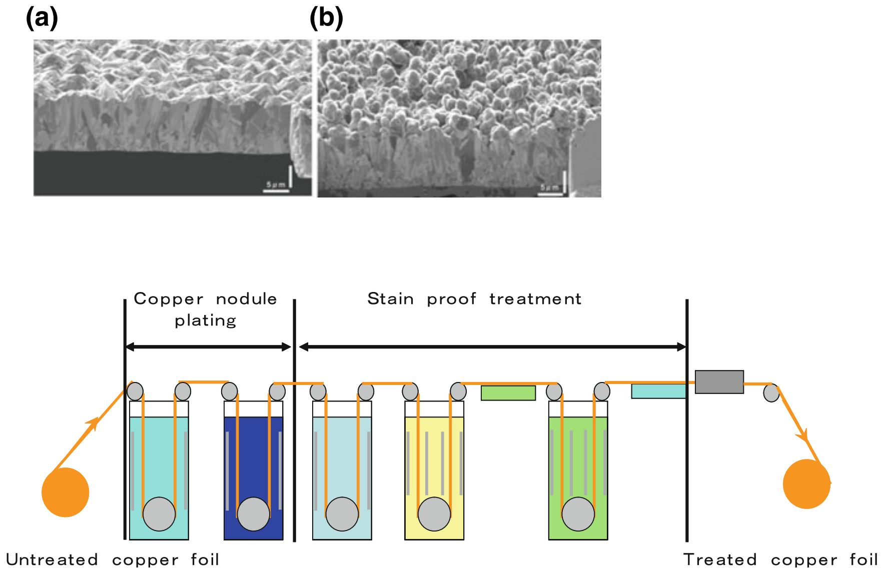

Fig. 10.5 Treatment Process **a** Untreated copper foil (12 μm raw foil) **b** Treated copper foil (12 μm)

electrodeposited copper foil for printed-wiring boards when the electrodeposited copper foil is laminated with a glass–epoxy prepreg or polyimide films, etc., by hot pressing and the wiring circuit is formed by etching.

(1) Improve the adhesive strength between the copper foils and resin substrates.
(2) Prevent discoloration of the copper foils caused by the hot pressing.
(3) Improve the etchability of the wiring circuits.
(4) Reduce the undercutting of the foil during the etching of the wiring circuits.
(5) Prevent deterioration of the adhesive strength between the copper foils and resin substrates caused by air, heat, moisture, etc., during use of the printed-wiring boards.
(6) Preventing discoloration when the copper foil is stored for a long term.

On the other hand, in the case of the electrodeposited copper foil for lithium-ion batteries, only the chromate coating is applied to the "matte side," "shiny side," and none of platings, such as the plating of copper particles called copper nodule plating, nickel plating, and zinc plating, are applied. The reason for this is as follows: when a carbon active material layer is formed on the surface of the electrodeposited copper foil to assemble a battery, and its cycling characteristics are measured by repeating the charge and discharge, the copper foil having a concavoconvex "matte side" and a smooth "shiny side" exhibits a greater decrease in the capacity retention rate compared to the copper foil having both sides smooth. This is explained in Sect.10.4.

Chromate coating is a treatment to deposit the oxide of chromium on the surface of the copper foils, and the oxide is formed by soaking the foil in a chromium containing aqueous solution or by electrolysis. It is a very thin coating with a thickness of about 1–3 nm.

Figure 10.6 shows the surface profiles of the copper foils used for printed-wiring boards and lithium-ion batteries after the surface treatment process.

The chromate coating given to the copper foil for use in lithium-ion batteries is very thin with a thickness of about 1–3 nm as previously described. Consequently, the surface profile of the chromate-treated copper foil for use in lithium-ion batteries observed by SEM, Figs. 10.6 c, d, is rarely different from that of the untreated copper foil shown in Figs. 10.2c, d in Sect. 10.1.

In addition, the purpose of applying the chromate coating is to satisfy characteristics (1)–(3).

(1) Prevent any decrease in the cycling characteristics during repeated charging and discharging of the batteries by maintaining an excellent electric contact between the copper foil and the active material.
(2) Improve the wettability when the active material slurry is coated.
(3) Prevent discoloration of the copper foil when it is stored for a long term.

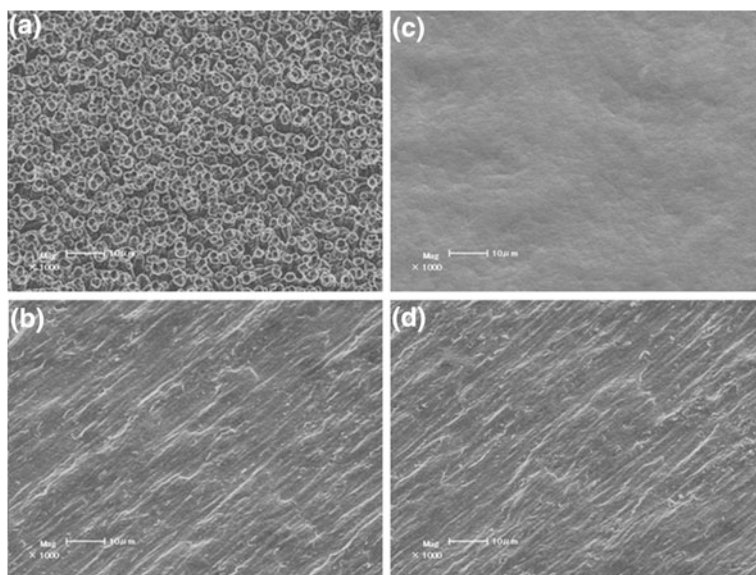

Fig. 10.6 SEM micrographs of surface morphology of treated copper foils. **a** Matte side of copper foil for PWB (12 μm) **b** Shiny side of copper foil for PWB (12 μm) **c** Matte side of copper foil for LIB (10 μm) **d** Shiny side of copper foil for LIB (10 μm)

10.2.4 Electrodeposited Copper Foil for Lithium-Ion Battery

The lithium-ion batteries currently being marketed were invented in 1985 as lightweight and high capacity batteries using $LiCoO_2$ for the positive electrode and carbon for the negative electrode. [2, 3] Studies for industrialization were then carried out, and they were put in practical use in 1991, and the industrial production started.

Figure 10.7 shows the structure of a lithium-ion battery. A material that a carbon powder is attached to the surface of a copper foil is used as the negative electrode. The raw materials of the active material layer, which is applied to the surface of the copper foil of the negative electrode collector, consists of a negative active material, conductive material, binder, and solvent.

The negative active material is a carbon powder with an average particle size of 5–30 μm. Carbon black with particles of about 0.03 μm coupled like a chain is often used as the conductive material.

Different binders and solvents are used for the solvent binder and aqueous binder. The solvent binder is polyvinylidene fluoride (PVDF) and the solvent is 1-methyl-2-pyrrolidone (NMP).

On the other hand, for the aqueous binder, the binder is the styrene-butadiene copolymer (SBR), and the solvent is water. In addition, as the aqueous binder, sodium carboxymethylcellulose (CMC) is also added as a thickener.

When lithium-ion batteries first appeared on the market, a solvent binder was used. However, aqueous binders began to be used, and they account for about 90 % of the current market.

The reasons why aqueous binders are principally used are as follows: [4]

(1) The calorific value of the thermal decomposition of the electrode is low while charging.
(2) It is easy to obtain a high capacity.

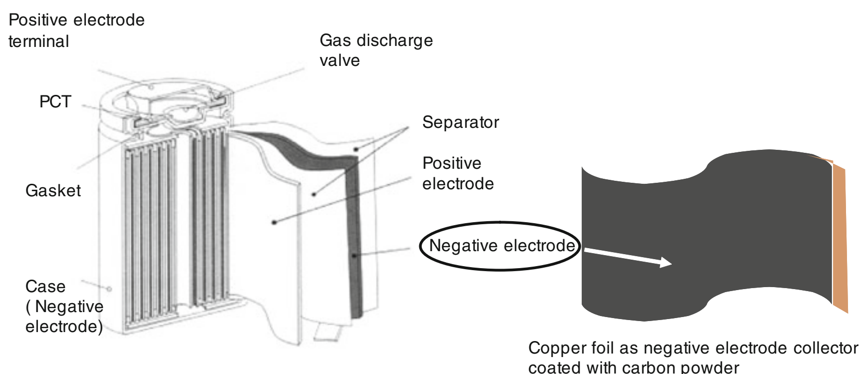

Fig. 10.7 Lithium-ion battery and negative electrode

(3) It excels in the charge/discharge cycling characteristics.
(4) Water with few environmental burdens can be used as the solvent.
(5) The cost of collecting organic solvents can be reduced.
(6) An explosion-proof type coating machine is unnecessary.

Figure 10.8 shows the manufacturing process of the negative electrode. [5] The solvent is first added to the negative active material, the conductive material, and the binder, and they are mixed to form a slurry.

As shown in Fig. 10.8, the slurry is applied to the surface of the copper foil while continuously running the coiled copper foil of 8–10 μm thickness. Usually, the thickness of the slurry layer is about 50–300 μm. The coated copper foil is then passed through the drying oven to evaporate the solvent, and it is reeled again into a coiled state. The drying condition at this time is said to be from several minutes to tens of minutes at 100–150 °C though it differs among battery manufacturers.

Furthermore, the copper foil coated with the active material is pressed by passing through the gap between the rolls. The thickness and density of the active material are equalized by the pressing. Usually, the thickness of the active material after pressing is about 10–100 μm though it differs according to the required characteristics of the battery.

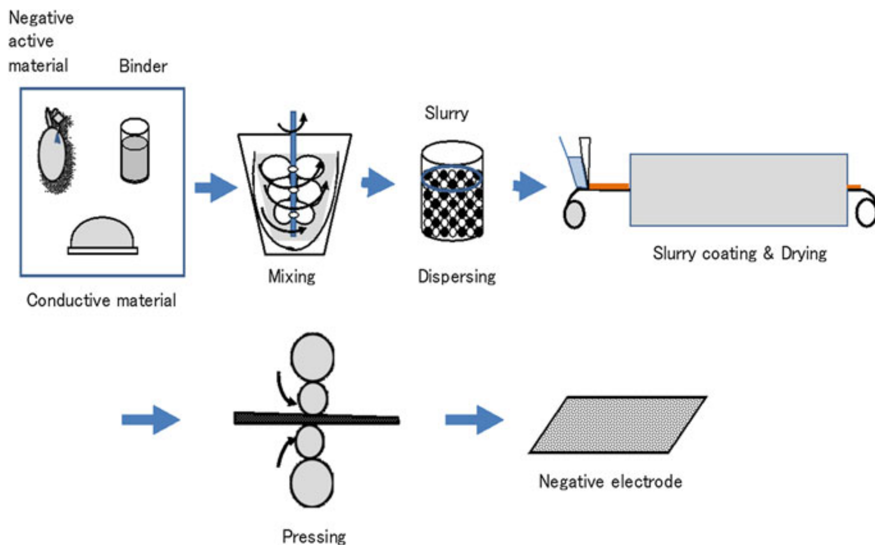

Fig. 10.8 Manufacturing process of negative electrode Ref. [5]

10.2.5 Reason for the Need of a Copper Foil Smooth on Both Sides

As for the electrodeposited copper foil for lithium-ion batteries, electrodeposited copper foils with a smooth and shiny surface on both sides are used. The magnified surface profiles of the "matte side" and the "shiny side" by SEM are slightly different as shown in Figs. 10.6c, d in Sect. 10.2.3. However, it is difficult to distinguish the "matte side" from the "shiny side" because both sides visually look smooth and shiny.

During the early development stage of lithium-ion batteries, a rolled copper foil was mainly used as the copper foil for the negative electrode collector. There are considerable differences in their characteristics between the electrodeposited copper foil and the rolled copper foil, and these differences are largely dependent on the difference in their manufacturing processes.

The rolled copper foil is manufactured by first making a square copper ingot, and repeating rolling by passing many times it through the gap between the rolls. The surface profile of the rolled copper foil is a replica of the surface profile of the mill roll as shown in Fig. 10.9. Therefore, there is no significant difference in their shapes and roughness between both sides.

In the mid-1990s, the use of electrodeposited copper foils instead of rolled copper foils was examined as a cost reduction measure of the copper foil for the negative electrode collector.

The manufacturing cost of the rolled copper foil has a tendency to increase with a decrease in thickness though the manufacturing cost of the electrodeposited copper foil does not increase very much even if its thickness decreases. In general, it is said that the manufacturing cost of the electrodeposited copper foils is less expensive than the cost of rolled copper foils when the thickness becomes less than 35 μm. At that time, copper foils with a thickness of about 10 μm were used for the negative electrode collector. It was highly expected to reduce the cost by using the electrodeposited copper foil instead of the rolled copper foil. However, the electrodeposited copper foil at that time was only the electrodeposited copper foil used for printed-wiring boards. It was a copper foil, which had a "matte side" with pyramidal convexities as shown in Figs. 10.2a, b in Sect.10.1 and a smooth surface on the "shiny side."

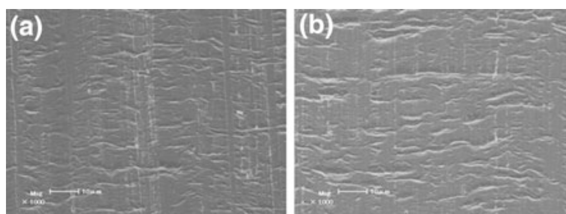

Fig. 10.9 SEM micrographs of rolled copper foil surfaces (Thickness of copper foil:10 μm). **a** Rolled copper foil A Side (10 μm) **b** Rolled copper foil B-Side (10 μm) opposite side of A side

When the electrodeposited copper foil for printed-wiring boards with such remarkably different surface profiles on both sides was used for the negative current collector of lithium-ion batteries, a problem occurred such that the decrease in the capacity retention rate was greater than when using a rolled copper foil with both side smooth. Though this reason could not be initially understood, it turned out that the decrease in the capacity retention rate due to the charge–discharge cycling of the battery occurred when the surface profile of one side of the copper foil was significantly different compared to the other side. This phenomenon is explained in detail in the following experimental results.

10.3 Experimental

10.3.1 Manufacturing Process of Negative Electrode

Three kinds of electrodeposited copper foils and electrodeposited copper foils for printed-wiring boards (STD foil) that were 12 μm thick with different surface roughnesses between the front side and the back side were used in this experiment as listed in Table 10.1. Each roughness value of the "matte side" and the "shiny side" is listed in Table 10.1.

In this experiment, test pieces having the roughness of the "matte side" Rz = 0.70–3.70 μm were prepared by changing the type and amount of the organic additives added to the copper-sulfuric acid electrolyte.

In addition, Rz denotes the 10-point average roughness defined by JIS-B-0601-1994. [6]

On the other hand, the roughness of the "shiny side" was changed by adjusting the polishing of the titanium drum. Though the roughness of the most rough one was Rz = 2.00 μm, there exists some over 2.00 μm in actual products. However, peeling the copper foil off the titanium drum becomes difficult when the surface becomes too rough. Therefore, it is difficult to manufacture one exceeding Rz = 3.00 μm.

As for the negative active material, petroleum pitch was used as the starting material. It was baked to produce a rough granular pitch coke. This rough granular pitch coke was ground into a powder with a mean particle diameter of 20 μm, and

Table 10.1 Test specimens of charge–discharge cycle test

	Matte side roughness Rz (μm)	Shiny side roughness Rz (μm)	Difference between M-side and S-side Rz (μm)
Specimen1	2.10	1.58	0.52
Specimen2	1.32	1.60	0.28
Specimen3	0.70	2.00	1.30
Specimen4 (STD foil)	3.70	1.93	1.77

the powder was baked in an inert gas at 1,000 °C to remove impurities, thus a coke material powder was obtained.

The negative electrode material contained 90 % by weight of the obtained coke material powder and 10 % by weight of polyvinylidene fluoride as a binder.

Next, this negative electrode material was dispersed in a solvent of 1-methyl-2-pyrrolidone to make a slurry.

This slurry was applied to both sides of the above-described belt-like electro-deposited copper foil of 12 μm thickness. It was compressed by the roller press after drying to make a negative electrode strip. This negative electrode strip had a 90 μm layer thickness on both sides of the negative electrode material after forming, and its width was 55.6 mm and length of 551.5 mm.

10.3.2 Manufacturing Process of Positive Electrode

A positive active material ($LiCoO_2$) was prepared by mixing 0.5 mol of Li_2CO_3 with 1 mol of cobalt carbonate. This mixture was then baked for 5 h in air at 900 °C, and $LiCoO_2$ was obtained.

The obtained positive active material ($LiCoO_2$), the graphite conductor and polyvinylidene fluoride binder in 91, 6 and 3 % by weight were mixed to prepare the positive electrode material, respectively. This material was dispersed in n-methyl-2 pyrrolidone to make a slurry.

The slurry was next uniformly applied to both sides of a belt-like aluminum positive electrode collector having a thickness of 20 μm. It was compressed by the roller press after drying to make a positive electrode with a thickness of 160 μm. This positive electrode strip has the same 70 μm thickness on both sides of the layer of the positive electrode material after forming, and its width was 53.6 mm with a length of 523.5 mm.

10.3.3 Battery Manufacturing Process

The prepared belt-like positive electrode and belt-like negative electrode were stacked along with a microporous polypropylene film separator of 25 μm thickness and 58.1 mm width to make a stacked electrode assembly.

This stacked electrode assembly was spirally wound many times in the longitudinal direction with the negative electrode inward, and the outermost end of the separator was fixed with a tape to make a spiral electrode assembly. The dimensions of this spiral electrode assembly were a 3.5 mm inside diameter and 17 mm external diameter.

The spiral electrode assembly described above was placed in a nickel-plated steel battery case with insulation plates on both the top and bottom sides of the assembly.

In order to make an electrical connection to the positive and negative electrodes with the battery case, the positive electrode collector was connected through an aluminum lead to the battery case lid, and the negative electrode collector was connected through a nickel lead to the battery case.

Five grams of a nonaqueous electrolyte, which was prepared by dissolving 1 mol/l of $LiPF_6$ in the mixed solvent comprised of equal parts of propylene carbonate and diethyl carbonate, was poured into the battery case in which the spiral wound electrode assembly had been placed.

The battery case lid was then fixed by placing a gasket coated with asphalt between the battery case lid and the battery case, and tightening the battery case.

As described above, a 18650 size cylindrical battery was prepared.

10.3.4 Test Results of Charge/Discharge Cycle of Batteries

The capacity retention rate after 100 cycles of repeated charge/discharge at the rate 0.5C of the cylindrical battery was examined, which used the electrodeposited copper foils listed in 1–4 in Table 10.1 for the negative electrode collector.

The capacity retention rate was calculated from the following formula using the discharge capacity, Q1, at the first cycle and the discharge capacity, Q100, at the 100th cycle.

$$\text{Capacity retention rate} = (\text{Q100})/(\text{Q1}) \times 100$$

Figure 10.10a, b shows the results. It is preferable that the surface roughness Rz of the matte side is less than 3 μm, because the capacity retention rate significantly decreased if the surface roughness Rz of the matte side was greater than 3 μm. Moreover, as for the shiny side, it is desirable that the surface roughness Rz is less than 3 μm.

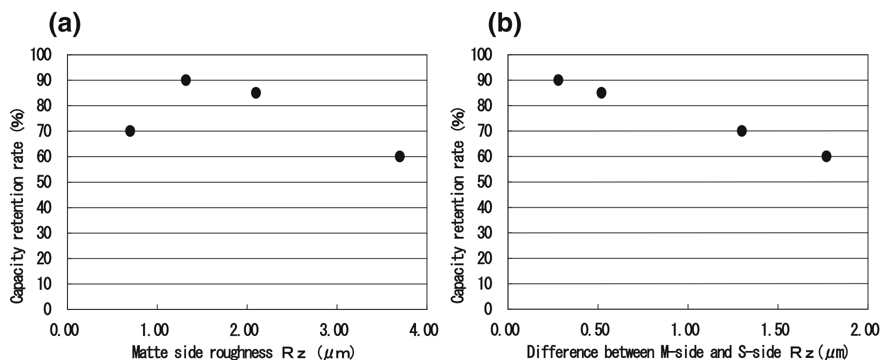

Fig. 10.10 Relation between surface roughness of copper foil and capacity retention rate. **a** Matte side roughness Rz (μm) **b** Differnce between M-side and S-side Rz (μm)

Moreover, the capacity retention rate decreases with an increase in the difference of the surface roughness Rz between the matte side and the shiny side as shown in Fig. 10.10b. As a result, it can be concluded that the desirable difference in the surface roughness between the matte side and the shiny side be less than 1.3 μm.

Based on these results, an electrodeposited copper foil, i.e., "copper foil smooth on both sides," which had a low surface roughness on the matte side and a small difference in roughness on the matte side and the shiny side, has been developed as an electrodeposited copper foil for the negative electrode collector of lithium-ion batteries.

However, the facts that the capacity retention rate decreases when the surface of the negative current collector copper foil is rough and when the difference in the surface roughness of both sides is significant are well-known phenomena. The reason for this has not yet been elucidated.

10.4 Manufacturing Process of Copper Foil Smooth on Both Sides

As already described, the "copper foil smooth on both sides" has a smooth and shiny surface on the "matte side" as well as on the "shiny side." When compared to the STD foil for printed-wiring boards, though there is no difference in the shape of the "shiny side," the shape of the "matte side" is quite different and has a smooth shiny surface.

The reason for such a difference in the surface profile is that the type of organic additives added to the copper-sulfuric acid electrolyte is different. The bath in which the organic additives, such as glue and gelatin, and chloride ions were added was used for the copper-sulfuric acid electrolysis solution, which was used for manufacturing the electrodeposited copper foil for printed-wiring boards is shown in Fig. 10.2a, b in Sect. 10.1.

When these organic additives were used, and a surface with pyramidal convexities was obtained as shown in Fig. 10.2a in Sect. 10.1.

On the other hand, the "copper foil smooth on both sides" has a smooth and shiny surface of the "matte side" as well as on the "shiny side" as shown in Figs. 10.2c, d in Sect. 10.1, and Fig. 10.6c, d in Sect. 10.2.3.

When the copper foil smooth on both sides is manufactured, a copper-sulfuric acid electrolyte, in which the components, such as 3-mercapto-1-propanesulfonic acid sodium salt (MPS) and bis (3-sulfopropyl) disulfide disodium salt (SPS), which are called brightening agents for copper plating, are added with a leveler consisting of a nitrogen-containing organic compound and an organic polymer selected from high-molecular-weight polysaccharides, is used.

Figure 10.11 shows the surface profile of the electrodeposited copper foil prepared from the copper-sulfuric acid electrolyte containing chloride ions, a brightening agent (MPS), leveler (L), and polymer (P).

When the copper-sulfuric acid electrolyte, which contained the chloride ions, MPS, leveler (L), and polymer (P), was used, the matte side with a smooth and shiny surface was obtained as shown in Fig. 10.11b, and it had a granular crystal structure as shown in Fig. 10.12.

Figure 10.13 shows the X-ray diffraction results of this copper foil. It was concluded that the electrodeposited copper foil for printed-wiring boards is formed

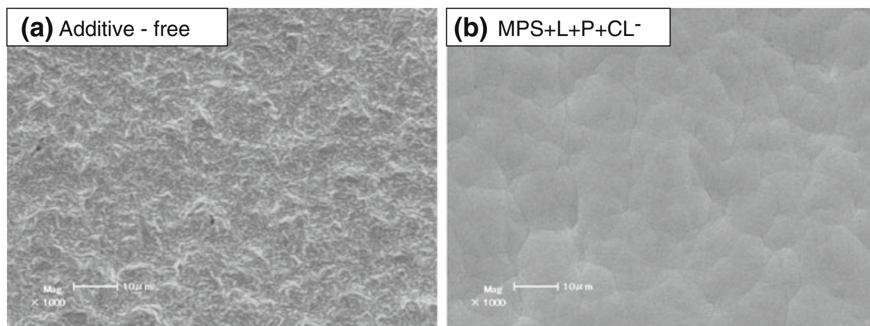

Fig. 10.11 SEM micrographs of electrodeposited copper foil surface

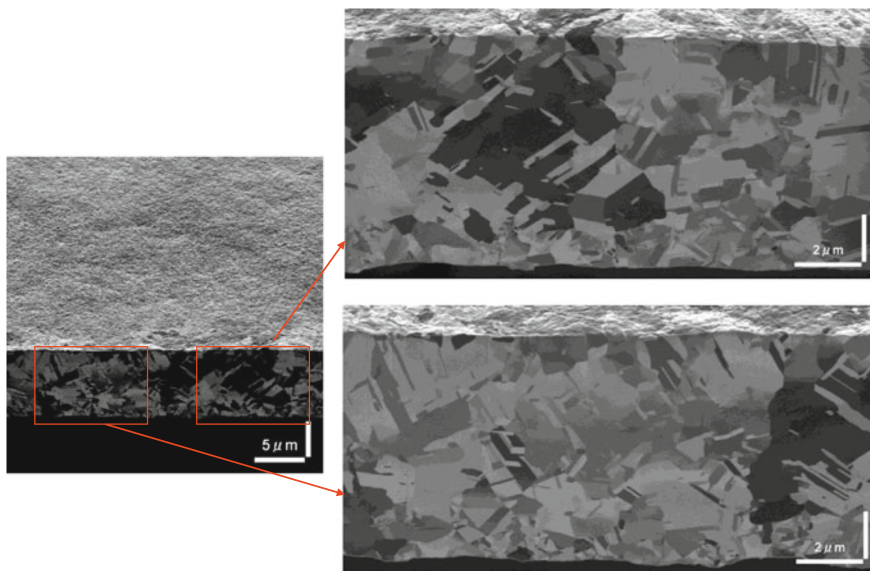

Fig. 10.12 FIB—SIM image of copper foil smooth on both sides cross-sections (10 μm)

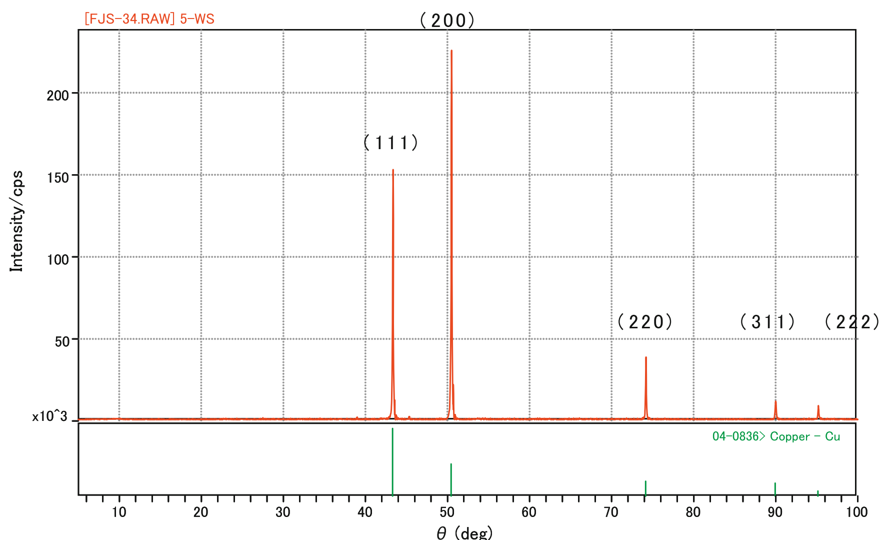

Fig. 10.13 X-ray diffraction data of copper foil smooth on both sides

with crystals having the (110) orientation [7–11] Unlike the copper foil for printed-wiring boards, this copper foil has a strong XRD peak for (200) orientation.

As for the copper electrodeposition using a copper-sulfuric acid type electrolyte, which contained the 3-mercapto-1-propanesulfonic acid sodium salt (MPS), bis (3-sulfopropyl) disulfide disodium salt (SPS), leveler (L), and polymer (P), it was carried out by panel plating during the early stage of the development of the electrodeposited copper foils. Moreover, a similar type of organic additive is being used in the current copper damascene electroplating process. However, in the case of the panel plating, the electrolysis was carried out under the conditions of a low electric current density of about 1–5 A/dm^2 using a soluble copper anode.

On the other hand, in this study, the electrodeposited copper foil has been manufactured at a high electric current density of 30–100 A/dm^2 using a DSE for the first time.

10.5 Properties of the Copper Foil Smooth on Both Sides: Mechanical Properties, Conductivity, Impurities in Copper Foil

The “copper foil smooth on both sides” has the feature that its “matte side” is smooth and shiny as well as its “shiny side.” Moreover, it has another feature; in that, it has a high electrical conductivity, high elongation, and low impurities in the copper foil compared to the conventional STD foil for printed-wiring boards (Table 10.2).

Table 10.2 Mechanical properties of copper foil smooth on both sides and STD foil

		Copper foil smooth on both sides (10 μm)	STD foil (10 μm)
Mattle side roughness	(Rz:μm)	1.50	3.70
Shiny side roughness	(Rz:μm)	1.60	1.95
Tensile Strength	(MPa)	320	330
Elongation	(%)	10.0	5.0
Conductivity	(%IACS)	98.9	96.5

It is indicated that the "copper foil smooth on both sides" contained a lower amount of organic additives compared to the STD foil. It seems that this fact is related to the properties of the higher conductivity and the higher elongation compared to the STD foils.

10.6 Properties of Copper Foil Smooth on Both Sides: Room Temperature Recrystallization Phenomenon

The "copper foil smooth on both sides" has a very high tensile strength of about 650 MPa immediately after manufacturing. However, it gradually becomes soft when it is kept at room temperature, and finally, its tensile strength becomes stable at about 320 MPa as shown in Fig. 10.14. The commercially available copper foil for lithium-ion batteries has a stabilized tensile strength after the room temperature recrystallization.

The room temperature recrystallization phenomenon, which occurred in the electrodeposited copper foil obtained from the copper-sulfuric acid electrolyte containing a certain type of organic additive, has been known a long time ago [12, 13].

It is postulated that the reasons for the recrystallization phenomenon at room temperature are that the gradual relaxation of the crystal defects due to the electrolytic deposition and deformation of the crystal lattice due to the adsorption of the additives at the grain boundary.

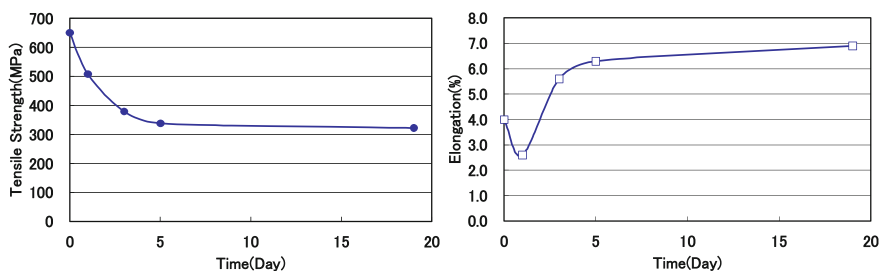

Fig. 10.14 Change in mechanical properties of copper foil smooth on both sides versus time at room temperature. (Foil thickness:10 μm)

The occurrence of the room temperature recrystallization phenomenon on the copper foil was also reported. It was electrodeposited from a copper-sulfuric acid electrolyte containing chloride ions, SPS, and polyethylene glycol, in which the same types of organic additives for the electrolyte of the "copper foil smooth on both sides" were used [14–16].

Concerning the reason why the room temperature recrystallization occurs, Hasegawa analyzed the details of the copper foil, electrically deposited from the copper-sulfuric acid electrolyte containing chloride ions, SPS, and polyethylene glycol. In this study, the X-ray diffraction, resistance and elongation were measured on the copper foil obtained from three kinds of electrolytes: (a) no-additive, (b) CL-PEG, and (c) CL-PEG-SPS [14].

Among them, the copper foil obtained from the (c) CL-PEG-SPS bath exhibited a more intensive peak of the (200) orientation versus the time after the electrolytic deposition, and the peak ratio, I200/I111, which is the peak ratio of the (200) orientation to the (111) orientation, significantly changed from immediately after the electrodeposition to 5 days, and then it equilibrated after 7 days.

Immediately after the electrodeposition, the peak ratio was I200/I111 $\approx$ 0.1. However, after 7 days later, it reached I200/I111 $\approx$ 0.8. On the other hand, the copper foils obtained from (a) no-additive bath and (b) CL-PEG bath exhibited no change from immediately after the electrodeposition until 7 days later, and the peak ratio was I200/I111 $\approx$ 0.2.

Moreover, when the crystal size was calculated using Scherrer 's formula from the peaks of the (111) orientation and (220) orientation, the crystal size increased from immediately after the electrodeposition until about 5 days later, and reached equilibrium after 7 days (Figs. 10.15, 10.16, and 10.17).

Furthermore, Abe also analyzed the room temperature recrystallization phenomenon of the electrodeposited copper foil prepared from the copper-sulfuric acid electrolyte containing chloride ions, SPS, and polyethylene glycol. In the analysis, he reported that the aging softening phenomenon of the electrodeposited copper foil was caused by the grain coarsening, and that the crystal orientation changed along with it [15, 16].

Since the "copper foil smooth on both sides" uses the chloride ion, MPS, and the same type of organic additive of polyethylene glycol for the copper-sulfuric acid electrolyte, it is considered that the room temperature recrystallization occurs due to a similar mechanism with the electrodeposited copper foil obtained from the copper-sulfuric acid electrolyte containing chloride ions, SPS, and polyethylene glycol. As shown in Fig. 10.13 in Sect. 10.4, the X-ray diffraction data of the copper foil after the room temperature recrystallization, the intensity of the (200) orientation increased.

However, this room temperature recrystallization phenomenon does not always take place in electrodeposited copper foils. No change in the tensile strength and crystal structure was observed in the STD foil for the above-described printed-wiring board even when it was stored at room temperature.

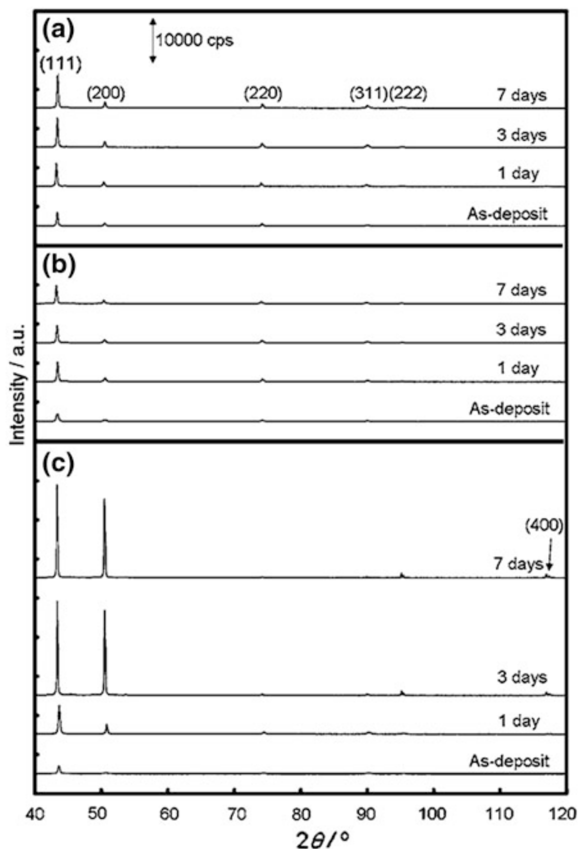

Fig. 10.15 Change in XRD profile of copper deposits with time at room temperature. The specimens were obtained from the **a** additive-free, **b** CL-PEG, **c** CL-PEG-SPS baths Ref. [14]

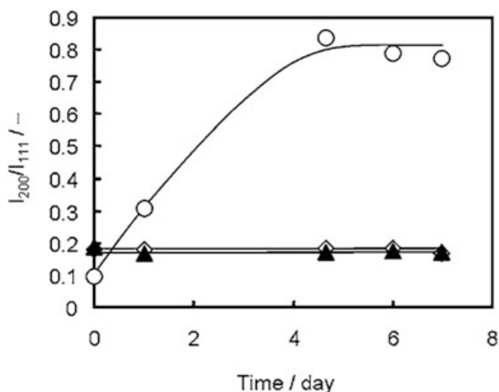

Fig. 10.16 Change in crystallographic orientation with time at room temperature. The specimen were obtained from the (◇) additve-free, (▲) CL-PEG, (°)CL-PEG-SPS baths. The grain size was calculated from XRD peaks for **a** (111) and **b** (200) orientation using Scherrer's formula [14]

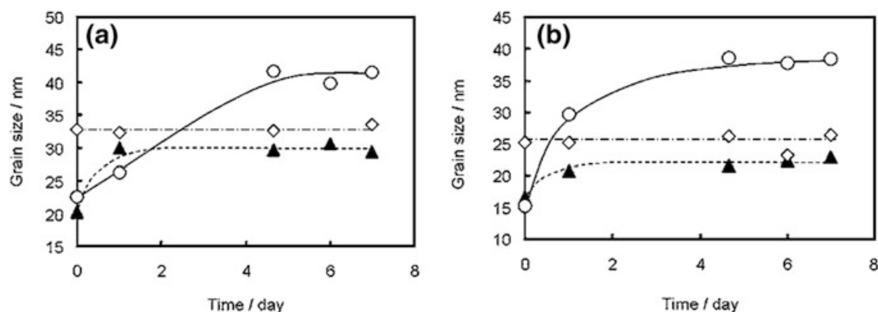

Fig. 10.17 Change in grain size of copper deposits with time at room temperature. The specimens were obtained from the(◇) additve-free, (▲) CL-PEG,(°)CL-PEG-SPS baths. The grain size was calculated from XRD peaks for **a** (111) and **b** (200) orientation using Scherrer's formula [14]

10.7 Mechanism of Action of Organic Additive Used for Manufacturing Copper Foil Smooth on Both Sides

The organic additive, which is added in minute amounts to the electrolyte in the manufacturing process of electrodeposited copper foils, has a big effect to the mechanical properties, such as crystal structure, tensile strength, elongation, and surface roughness of the copper foil. It is important to elucidate the effect of the additives, which causes the deposition behavior of the copper foils, in order to satisfy the quality assurance of the current copper foils and various characteristics of the copper foils that will be demanded in the future.

However, the mechanism of action and the mechanism of the deposition and characteristics of the copper foils on the additives used in manufacturing of the current "copper foil smooth on both sides" have not been sufficiently elucidated. An electrochemical analysis was then done concerning the effect of each additive on the deposition behavior of the "copper foil smooth on both sides."

10.7.1 Experimental

10.7.1.1 Measurement of Potentiodynamic Polarization Curve

The potentiodynamic polarization curves were measured in order to investigate the effect of additives on the copper electrodeposition. A three-electrode system potentiostat was used for the measurement, and a borosilicate glass cell was used as the electrolytic cell.

A copper foil was used as the working electrode, and it was covered with a heat-resistant and chemical-resistant masking tape except for the test area of

Table 10.3 Electrolyte composition

Cu	H_2SO_4	Chloride ion
(g/L)	(g/L)	(ppm)
50–100	50–150	10–50

3 × 3 mm. The surface of the electrode was soaked in 10 vol% sulfuric acid for 30 s to remove the oxide film immediately before the soaking in the test solution.

A Pt plate was used for the counter electrode, and a Ag/AgCl (sat. KCl) electrode was used as the reference electrode. The standard electrode potential at 298 K is 0.196 V (vs. NHE). In the following sections, all potential data are expressed versus this electrode potential as the standard.

A copper-sulfuric acid electrolyte, which was prepared in the laboratory, was used as the test solution. The electrolyte composition is listed in Table 10.3. Three kinds of additives, which were used for manufacturing the "copper foil smooth on both sides," were used.

Each additive was dissolved in deionized water at the ratio of about 1,000 mg/L, and a given amount of this aqueous solution was added to the above-described electrolyte to prepare the test solution. After the additive had been added, the air in the cell was replaced by N_2 gas for 30 min. After the open circuit potential of the working electrode had been measured for 60 s, the working electrode was cathodically polarized from that potential at the constant rate of 1 mV/s.

In addition, the test solution temperature was kept at 333 K during the measurement using a water bath.

10.7.2 CV Measurement in the Solution Without Copper Ion

In order to observe the electrochemical behavior and adsorption behavior of the additive, cyclic voltammetry (CV) was done using a solution without the copper ions. The same three-electrode system potentiostat as used in Sect. 10.7.1 was used for the measurement, and an acrylic H-shaped cell was used as the electrolytic cell.

Two pieces of Pt wire were used for the working electrode and the counter electrode, respectively, and a Ag/AgCl (sat. KCl) electrode was used as the reference electrode. The diluted sulfuric acid of 100 g/L was used as the test solution. Each additive was added to this solution, and the measurement was done after the air had been replaced with N_2 gas for 30 min.

After the open circuit potential of the working electrode had been measured for 60 s, the potential sweep was started from that potential in the direction of the cathode potential. The potential sweep rate was carried out at 200 mV/s, the potential sweep range was −0.25 to −1.5 V, and the measurement was done for 3 cycles.

In addition, the liquid temperature was kept at 333 K during the measurement using a water bath.

10.8 Results and Discussion

10.8.1 Changes in Electrochemical Characteristics of Copper-Sulfuric Acid Electrolyte Containing Additives

In order to investigate the effect of the additives on the electrodeposition of copper, the potentiodynamic polarization curve was measured, and the results are shown in Fig. 10.18.

When the curve without the additive and the one with added MPS were compared at the same potential, the electric current density of the MPS-added solution was slightly higher in the range of about −0.1 to 0.1 V. Therefore, it was confirmed that the electrodeposition of copper was promoted. Since the production of copper foil in the mass production facility is carry out at a constant current density, the potential becomes more noble by the addition of MPS. Based on the electrochemical aspect, it is expected that the grain size during the electrodeposition become larger because the over-voltage required during the electrodeposition is low. Moreover, it is expected that the hydrogen evolution reaction becomes

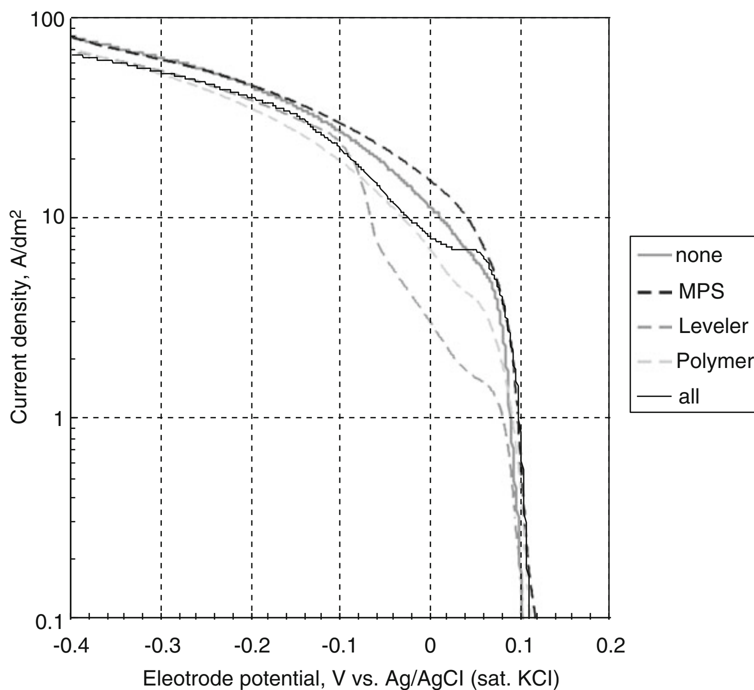

Fig. 10.18 Current dencity-potential curve of Cu-H_2SO_4 electrolyte containing various kinds of organic additives

difficult to occur. However, when the effect by the reaction between the additive and the copper ion or by the incorporation of the additive appears, it does not necessarily simply occur this way.

Similarly, it is understood from the curve with the leveler that the electrodeposition of copper was inhibited. Though the inhibition of the electrodeposition of copper is indicated for the polymer additive, its effect is smaller than the leveler.

It was found that a peak occurred at about 0.08 V when all three kinds of additives were added. Because the change in the reaction behavior was dependent on the potential in the system containing MPS, it would appear that an electrochemical effect other than the physical coating effect by simple adsorption was produced.

10.8.2 Electrochemical Behavior of Additives in the Solution Without Copper Ions

Based on the result described in Chap. 8.2.1, it was confirmed that MPS had an effect on promoting the electrodeposition of copper. In general, it is reported that the mechanism of action of MPS is similar to Eqs. (10.5) and (10.6), and that it promotes the electrodeposition of copper.

$$4\text{MPS} + 2\text{Cu}^{2+} \rightarrow 2\text{Cu(I)} - \text{thiolate} + \text{SPS} + 4\text{H}^{+} \quad (10.5)$$

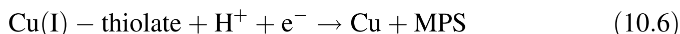

$$\text{Cu(I)} - \text{thiolate} + \text{H}^{+} + \text{e}^{-} \rightarrow \text{Cu} + \text{MPS} \quad (10.6)$$

The effect of the additive amount of MPS on the amount of plating was investigated using Cyclic Voltammetric Stripping (CVS) .

In addition, the amount of plating indicates the quantity of electricity required for dissolving the copper plating, which was plated on the Pt rotating electrode using CVS at a constant rate by cathodic polarization and then dissolved by anodic polarization.

Since the rate and range of the potential sweep were constant, the greater the dissolving electric current, the easier the plating is done at a given potential sweep. The relation between the amount of plating and the additive amount of MPS is shown in Fig. 10.19. Two kinds of solutions, the one in which only the chloride ions were added to the copper sulfate plating solution, and the other in which the chloride ion, leveler and polymer were added, were used as the test solutions.

As for the electrolytic bath containing only chloride ions, the amount of plating did not change with the addition of several ppm of MPS. On the other hand, as for the electrolytic bath containing chloride ions, leveler and polymer, the amount of plating increased along with an increase in the additive amount of MPS even for several tenths of a ppm. These results suggest that the promotion effect of MPS on the electrodeposition of copper cannot be explained only by Eqs. (10.5) and (10.6), and that there exists a significant effect by the interaction with the other additives.

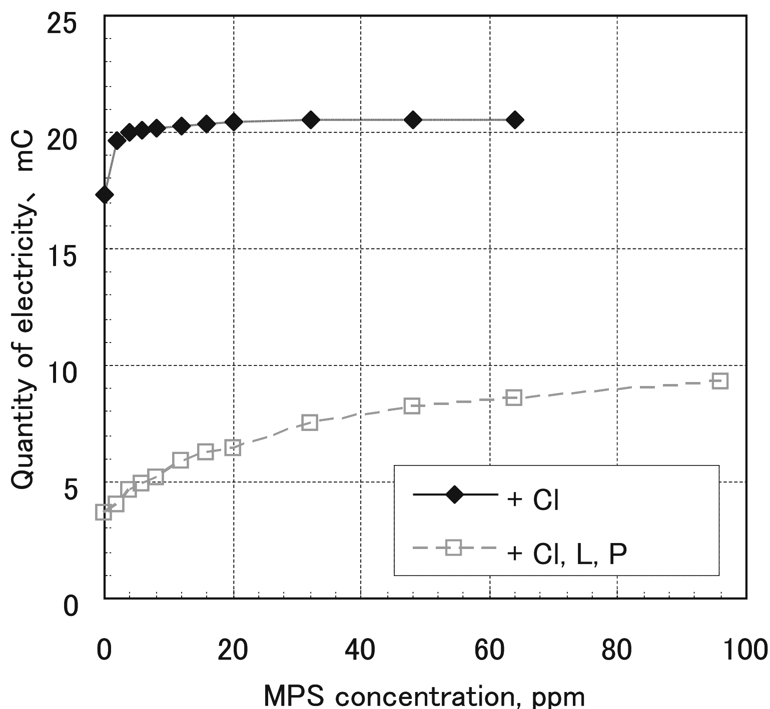

Fig. 10.19 Determination of MPS concentration by CVS

Based on the above results, the CV measurement was done in order to examine the electrochemical behavior of the additive in the solution without the copper ion. First of all, the CV behavior of the Pt wire in the bath without the additive is shown in Fig. 10.20. This graph is used as comparison data to evaluate the following results. Figure 10.21 shows the result when only MPS was added. The 200 mV/s data in Figs. 10.20 and 10.21 were used as examples for making a comparison. The adsorption peak of the hydrogen atom at about 0 to −0.2 V decreased as the additive amount of MPS increased. It is presumed that the adsorption of hydrogen atoms was prohibited by the MPS adsorbed on the electrode. The reduction peak of the Pt oxide at about 0.5 V became smaller along with an increase in the additive amount of the MPS. This is attributable to the MPS being adsorbed on the electrode and inhibited the formation of the Pt oxide during the anodic polarization. Moreover, a big oxidation current peak was observed at about 1.1 V. Therefore, it can be postulated that an oxidation reaction caused by MPS occurred. However, the cathodic current corresponding to this reaction could not be confirmed. Based on these results, it was clarified that MPS was adsorbed on the Pt electrode, and that it did not develop a direct electrochemical reaction except for the oxidation at about 1.1 V. Because it did not develop a direct electrochemical reaction, it is considered that it influenced the electrodeposition of

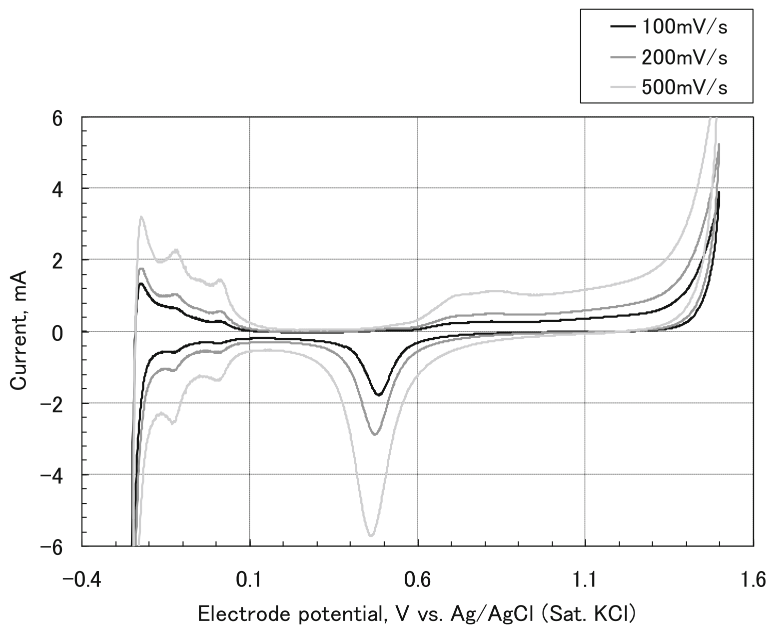

Fig. 10.20 Cyclic–voltammetry behavior of Pt surfaces in aqueous H_2SO_4 (additive-free)

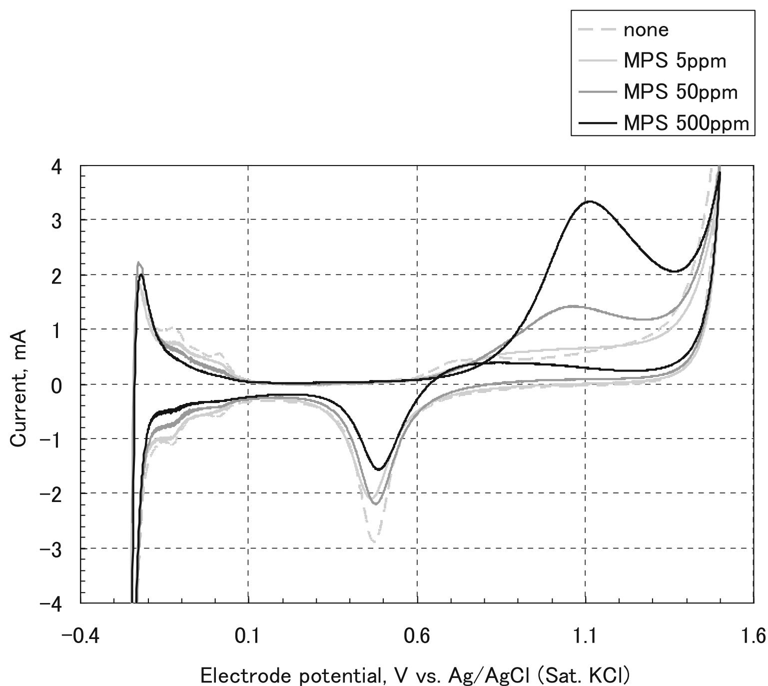

Fig. 10.21 Cyclic–voltammetry behavior of Pt surfaces in aqueous H_2SO_4 (MPS-added: 200 mV/s)

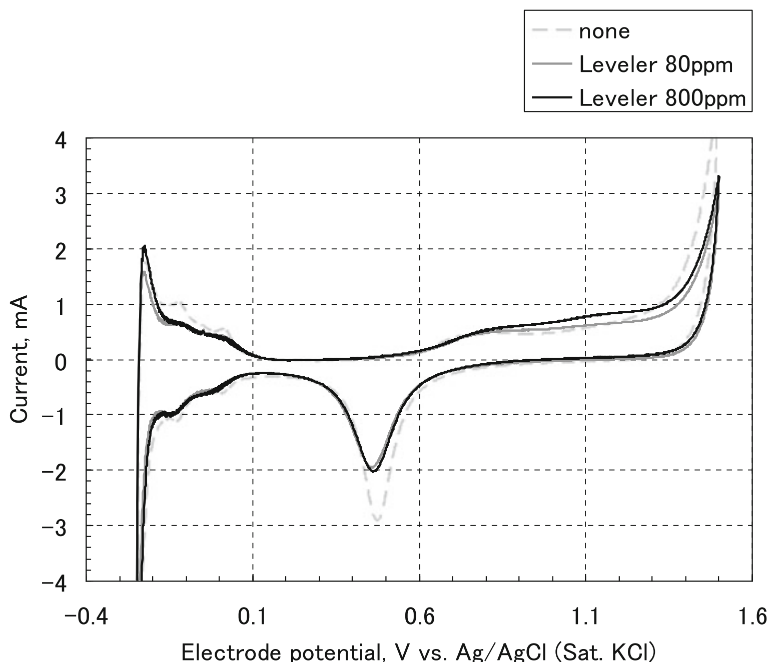

Fig. 10.22 Cyclic–voltammetry behavior of Pt surfaces in aqueous H_2SO_4 (Leveler added: 200 mV/s)

copper by either or both the MPS adsorption on the electrode surface and the reaction with the copper ions.

Next, only the leveler was added, and a similar measurement was done. These results are shown in Fig. 10.22. Because the leveler also reduced the adsorption peak of the hydrogen atom and the reduction peak of the Pt oxide as did MPS, its adsorption on the surface of the electrode is presumed. However, since the effect was independent of the concentration of the leveler and its effect was smaller than that of MPS, it is presumed that its adsorption on the surface of the electrode was weaker than that of MPS. No other electric current, which indicated an electrochemical reaction, was observed, therefore, it was clarified that the leveler did not develop a direct electrochemical reaction.

These results are summarized as follows: in the system containing no copper ions, it has been found that:

(1) MPS and the leveler were adsorbed on the Pt electrode.
(2) The adsorption of the leveler was weaker than that of MPS.
(3) Neither MPS nor the leveler developed a direct electrochemical reaction except for the oxidation of MPS at about 1.1 V.

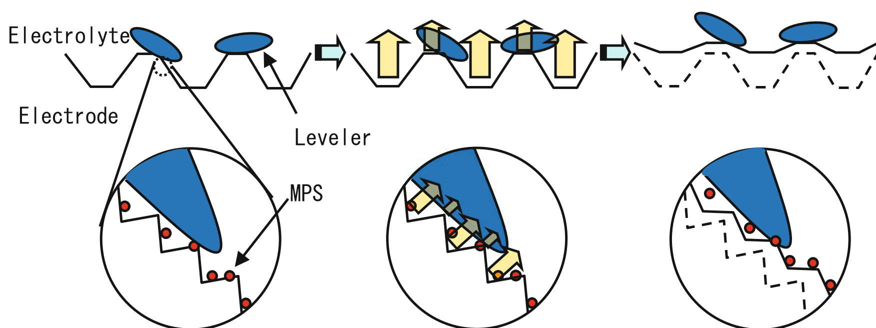

Fig. 10.23 Theory of MPS and Leveler adsorption mechanism on cathode

10.8.3 Adsorption of Additives Discussion

Figure 10.23 shows the model of the mechanism of action by the leveler and MPS that was based on the previous results. The leveler was comparatively weakly adsorbed on the electrode, and a direct electrochemical reaction was not produced. Moreover, it is known that the leveler is adsorbed by diffusion control.

The effect of the leveler to basically suppress the electrodeposition of copper increases as the adsorption frequency increases as the stirring intensity increases. Based on this, it is expected that the leveler with bigger molecular weight is adsorbed on the tip of the convex part of the electrode more often compared to MPS. It is presumed that the leveler does not produce an electrochemical reaction on Pt, and that it does not produce an electrochemical reaction even during the electrodeposition process of copper. Based on this assumption, a model of smoothing the copper surface can be proposed such that the copper surface is physically covered with the leveler to decrease the electrodeposition current density of the copper surface by adsorption. Since MPS is comparatively strongly adsorbed on the electrode, and its molecular weight is 178, it is presumed to be adsorbed on the concave parts of the electrode where the frequency of adsorption of the leveler is low and on the microregions regardless of the convexoconcave nature. Because MPS promotes the electrodeposition of copper, it is considered that it contributes to the glossiness in the microregions. Because this effect of MPS appears in the microregions, it is considered that the smoothing in the macroregions is not carried out in the environment where the leveler does not exist, and that no glossiness is obtained.

10.9 Recent Trends

As already described, the rolled copper foil was initially used as the copper foil for the negative electrode collector of lithium-ion batteries. However, at present, the ratio of using the “copper foil smooth on both sides” is much higher than that of

Table 10.4 Comparative advantages of copper foil smooth on both sides for Li⁻ion battery

	Copper foil smooth on both sides	Rolled copper foil	Comparative advantage
(1) Foil width	◯	×	Copper foil smooth on both sides: ~ 1 300 mm Rolled copper foil: ~ 650 mm
(2) Foil thickness variation	◯	Δ	Less thickness variation of C activated layer
(3) Mechanical property after annealing	◯	×	Less wrinkles during C coating
(4) Number of customers	◎	Δ	Most customers prefer both side smooth copper foil

◎ Excellent ◯ Good Δ Fair × Poor

the rolled copper foil. The reason for this is that the significance of the "copper foil smooth on both sides" regarding the mechanical properties and the yield during battery production was confirmed by the battery manufacturers. Table 10.4 shows the difference in their properties. In addition, the main characteristics are explained as follows:

10.9.1 Effect of Variation in the Foil Thickness

As shown in Table 10.5 and Fig. 10.24, the "copper foil smooth on both sides" has a feature that the variation in the foil thickness is smaller than that of the rolled copper foil.

These data show the measured values of the thickness in the transverse direction and machine direction of the 540 mm wide and 10 m long copper foil by the β-ray nondestructive thickness tester. The "copper foil smooth on both sides," has a small variation in the thickness in both the transverse direction and machine direction.

This difference in the thickness variation of the copper foil has a huge effect on the variation in the weight of the negative active material layer when the negative active material is applied.

Table 10.5 Foil thickness measurement data

	Copper foil smooth on both sides	Rolled copper foil
Number of data (n)	333	333
Average value (g/dm^2)	0.891(10 μm)	0.861(10 μm)
Minimum value (g/dm^2)	0.885	0.845
Maximum value (g/dm^2)	0.902	0.875
σ	0.0037	0.0061

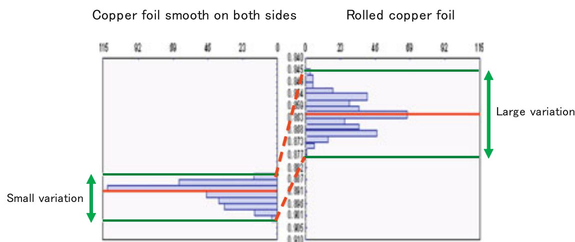

Fig. 10.24 Foil thickness variation of copper foil smooth on both sides and rolled foil

Recently, studies to use lithium-ion batteries for HEVs have been carried out. The lithium-ion batteries for HEVs have thin active material layers in order to generate high power unlike the batteries for a conventional mobile phone, smartphone or personal computer. In that case, it is said that the variation in the weight of the negative active material layer has an effect on the variation in the capacity of the batteries.

10.9.2 Mechanical Property After Heat Treatment

During the manufacturing process of the negative electrodes, they are treated at a temperature of 100–150 °C for several minutes to tens of minutes during the application and drying of the active material. Though this temperature slightly varies depending on the battery manufacturer, there is little change in the tensile strength and elongation of the "copper foil smooth on both sides" even when it is subjected to such a temperature as shown in Figs. 10.25 and 10.26.

Figures 10.27, 10.28, 10.29, and 10.30 show the crystal structures of the "copper foil smooth on both sides" and the rolled copper foil at room temperature and after the heat treatment of 200 °C × 1H. For the "copper foil smooth on both sides," the crystal structure is almost unchanged. On the other hand, for the rolled foil, it is completely annealed and the grain coarsening due to recrystallization is observed.

As described in Sect. 10.6, since the crystal defects (caused by the electrodeposition) and the deformation of the crystal lattice (caused by the adsorption of the additives to the grain boundary) of the "copper foil smooth on both sides" have been relaxed by the room temperature recrystallization, it is considered that it is stable for heating at about 100–150 °C.

On the other hand, for the rolled copper foil, the dislocations, which multiplied due to the cold working, disappear, and softening caused by the recrystallization occurs even by heating at about 100–150 °C. Such a difference in characteristics has a significant effect on the yield during the manufacturing process. When the active material is applied to the "copper foil smooth on both sides" and dried, it produces few wrinkles due to the drying temperature compared to the rolled copper foil.

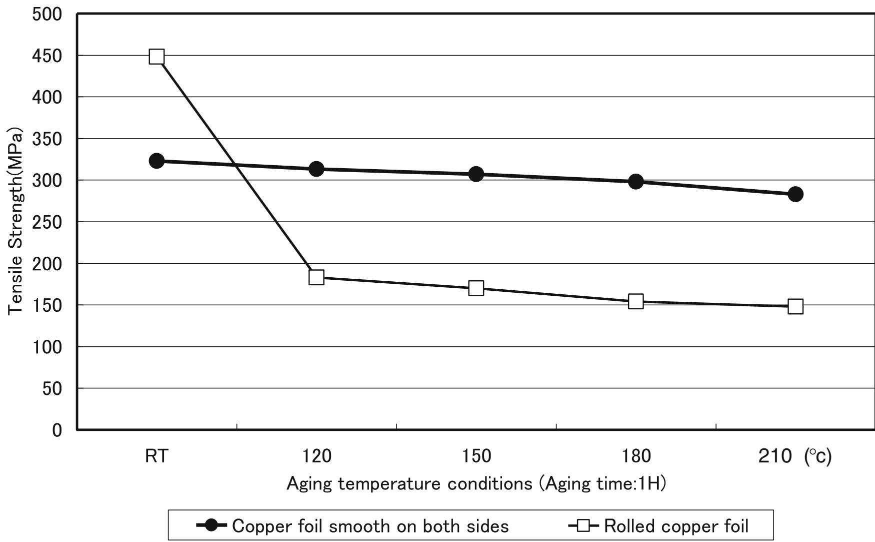

Fig. 10.25 Tensile strength after heating (foil thickness: 10 μm)

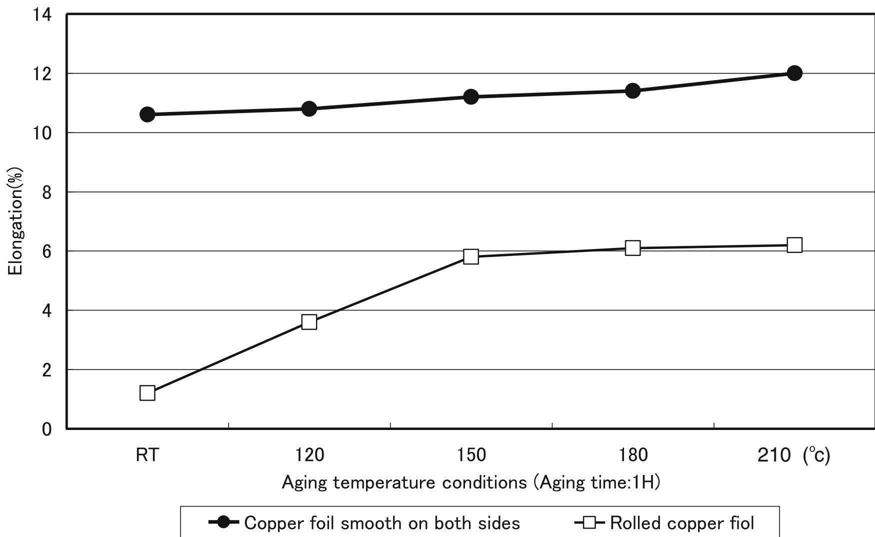

Fig. 10.26 Elongation after heating (foil thickness: 10 μm)

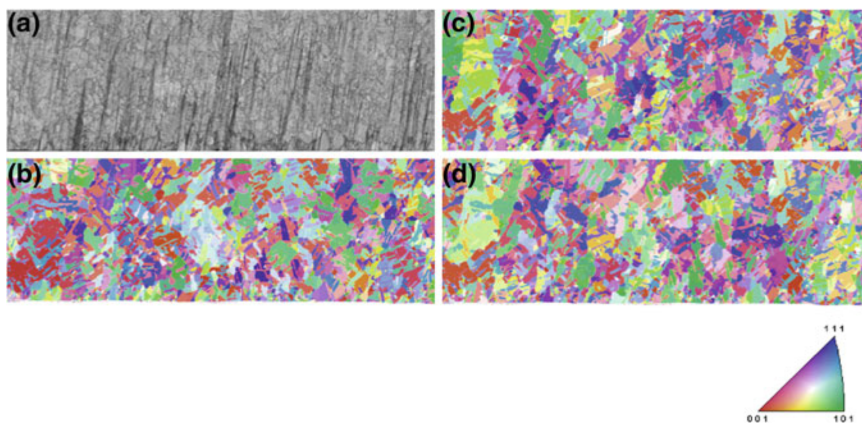

Fig. 10.27 Inverse pole figure map of 35 μm copper foil smooth on both sides (RT) **a** IQ (Image Quality) Map **b** IPF Map (ND) **c** IPF Map (TD) **d** IPF Map (RD)

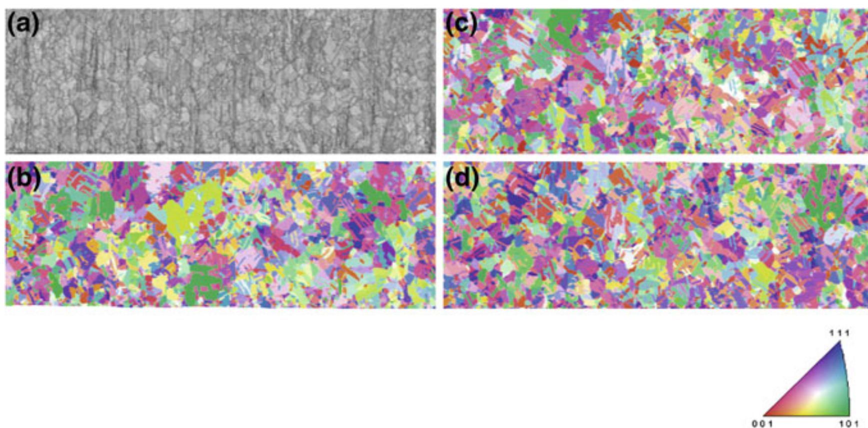

Fig. 10.28 Inverse pole figure map of 35 μm copper foil smooth on both sides (after 200 °C × 1 H) **a** IQ (Image Quality) Map **b** IPF Map (ND) **c** IPF Map (TD) **d** IPF Map (RD)

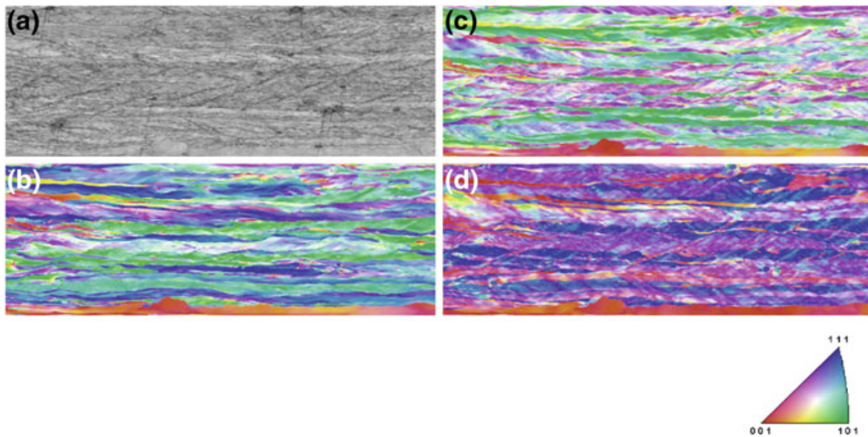

Fig. 10.29 Invese pole figure map of 35 μm rolled copper foil (RT) **a** IQ (Image Quality) Map **b** IPF Map (ND) **c** IPF Map (TD) **d** IPF Map (RD)

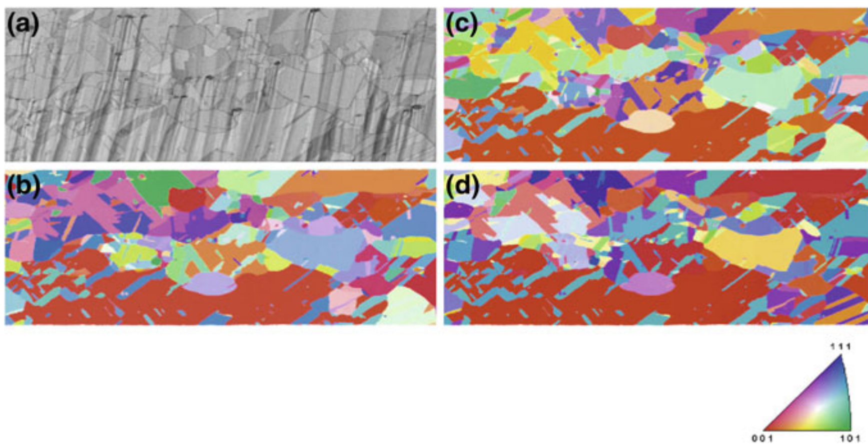

Fig. 10.30 inverse pole figure map of 35 μm rolled copper foil (after 200 °C × 1 H) **a** IQ (Image Quality) Map **b** IPF Map (ND) **c** IPF Map (TD) **d** IPF Map (RD)

10.10 Summary

(1) A decrease in the capacity retention rate was promoted when an electrodeposited copper foil for printed-wiring boards was used as the lithium-ion battery negative electrode collector. The "copper foil smooth on both sides" was developed during the process of solving this problem.
Though the battery capacity retention rate of lithium-ion batteries gradually decreases with repeated charge and discharge, the decrease in the capacity

retention rate was promoted if the copper foil having remarkably different surface roughnesses of the "matte side" and "shiny side" like the electrodeposited copper foil for printed-wiring boards was used. The decrease in the capacity retention rate could be suppressed if an electrodeposited copper foil with both sides smooth and shiny was used.

The electrodeposited copper foil for lithium-ion batteries, "copper foil smooth on both sides," was developed based on the above finding.

(2) The "copper foil smooth on both sides" is manufactured using a copper-sulfuric acid electrolyte to which 3-mercapto-1-propanesulfonic acid sodium salt (MPS) or bis (3-sulfopropyl) disulfide disodium salt (SPS), a nitrogen-containing organic leveler, and an organic polymer selected from high-molecular weight polysaccharides are added.

The copper electrodeposition using the copper-sulfuric acid type electrolyte containing such an organic compound was carried out by panel plating during the early stage of the electrodeposited copper foil development. Moreover, a similar type of organic additive is being used in the current copper damascene electroplating process. However, this example is the first time that an electrodeposited copper foil was manufactured using an DSE at a high current density.

(3) The "copper foil smooth on both sides" has a tensile strength of about 650 MPa immediately after manufacturing. However, it gradually softens during storage at room temperature, but becomes stable at the tensile strength of about 320 MPa. The copper foil for commercially available lithium-ion batteries is the one softened at room temperature and then its tensile strength has been stabilized.

(4) An electrochemical analysis was done for each additive concerning its effect on the deposition behavior of the electrolyte used in manufacturing the "copper foil smooth on both sides." It is presumed that the leveler is comparatively weakly adsorbed on the electrode, and that the adsorption is carried out under diffusion controlled conditions. Consequently, the place where the amount of agitation is higher has a greater effect on suppressing the electrodeposition of copper due to an increase in the adsorption frequency of the leveler. Moreover, it is expected that the leveler is selectively adsorbed on the convex part of the electrode compared to MPS, because of bigger molecular weight compared to the MPS molecular weight of 178. We suggest a new model in which the leveler physically coats the copper surface, and that the current density of the copper electrodeposition at the adsorbed part is suppressed in order to make the copper surface smooth.

Since MPS is comparatively strongly adsorbed on the electrode and has a molecular weight of 178, it is presumed that MPS is adsorbed on the concave part of the electrode where the adsorption frequency of the leveler is low and to more of the microregions regardless of the convexoconcavity. It is considered that MPS contributes to forming a shiny microregion because MPS promotes the electrodeposition of copper.

(5) Though, the rolled copper foil was initially used as the lithium-ion battery negative electrode collectors, a higher ratio of the “copper foil smooth on both sides” is currently being used. The reason for this is that the “copper foil smooth on both sides” excels in mechanical characteristics and in yield when used in manufacturing batteries.

5.1 There is a feature in which the variation in the foil thickness of the “copper foil smooth on both sides” is lower than that of the rolled copper foil. This difference in the variation of the copper foil thickness has a big effect on the variation in the weight of the negative active material layers when the negative active material is applied.

5.2 During the manufacturing process of negative electrodes, the negative electrodes are heated to 100–150 °C for a few minutes to tens of minutes when the coating of the active material is dried. There is little change in the tensile strength and elongation on the “copper foil smooth on both sides” even when it is heated to such a temperature. On the other hand, the rolled copper foil recrystallizes at about 100–150 °C and becomes soft.

Such a difference in characteristics has a significant effect on the production yield of negative electrodes. The “copper foil smooth on both sides” has the feature that it produces few wrinkles due to the drying temperature compared to the rolled copper foil when the active material is applied to it and dried.

References

1. CFIA (Circuit Foil Industry Associate, Japan) Standard, 0001-1999
2. Yoshino A (1986) JP Patent 1,989,293. US Patent 4,668,595. EP Patent 205,856B2
3. Yoshino A (1986) JP Patent 2,668,678
4. Kanamura K (2010) Lithium-ion batteries for vehicles. Nikkan Kogyo Shinbunsya, Tokyo, pp 163–168
5. Yada S (2006) Practical evaluation technology of lithium-ion batteries and capacitors. Gijyutsu Jyoho Kyokai, Tokyo, pp 132–140
6. JIS-B-0601-1994
7. Koura N, Watanabe K, Yamagishi T (1993) Effect of Gelatine and Cl^- on a Copper Deposition. J Surf Finish Soc Jpn 44(7):626–630
8. Osaka T, Tamura K, Sakakibara A, Okinaka Y (1996) Factors controlling the surface morphology of copper foil for printed wiring board electrodeposited at high speed. J Jpn Inst Interconnect Packag Electron Circ 11(7):487–493
9. Osaka T, Sakakibara A, Tamura K, Homma T, Okinaka Y (1996) Complex effects of additives of Cl^- and glue on surface morphology of copper foil for printed wiring boards electrodeposited at high speed. J Jpn Inst Interconnect Packag Electron Circ 11(7):494–499
10. Koura N, Ejiri Y, Mamiya M, Idemoto Y, Matsumoto F (2000) Effects of gelatine and chloride ion on copper electrodeposition. J Surf Finish Soc Jpn 51(9):938–944
11. Kondo K, Shimada K, Tanaka Z (2003) Crystal Orientation and Growth of Electrolytic Copper Foil. J Jpn Inst Interconnect Packag Electron Circ 6(1):64–67

12. Von Michael G (1978) Entwicklung eines selbstregulierenden sauren Glanzkupferbades fur Spezialzwecke. Metalloberflache 32(10):430–434
13. Stoychev DS, Tomov IV, Vitanova IB (1985) Recovery and recrystallization of electrodeposited bright copper coatings at room temperature. Microhardness in relation to coating structure. J Appl Electrochem 15:879–886
14. Hasegawa M, Nonaka Y, Negishi Y, Okinaka Y, Osaka T (2006) Enhancement of the ductility of electrodeposited copper films by room-temperature recrystallization. J Electrochem Soc 153(2):C117–C1203
15. Abe H, Nakamura K, Shimazaki H, Mogi M, Matsunaga K, Ito T, Miura Y, Watanabe T (2004) Age softening phenomenon at room temperature of electrodeposited copper plating film for gravure cylinder. J Print Sci Technol 41(1):40–47
16. Abe H, Kondo A, Watanabe T (2004) J Jpn Inst Met 68(9):844–850

Chapter 11
Through Hole Plating

Wei-Ping Dow

11.1 Introduction

Plated through hole (PTH) is an age-old process technology, especially in the fabrication of printed circuit boards (PCBs). However, PTH is still employed currently for advanced PCB fabrication. The main differences between the conventional PTHs and the current PTHs are acceptable criteria of process and reliability. For conventional PTH fabrication, a high throwing power is a basic criterion. Multilayer PCBs with a high density of interconnection (HDI) are common, and three-dimensional (3D) chip stacking packaging also employs through-silicon holes (TSHs) as well as through-silicon vias (TSVs). Therefore, the metallization process becomes more and more complex. For example, both through-holes (THs) and microvias (i.e., blind vias) may exist together on the same PCB and are simultaneously put in one plating bath for electroplating. As a result, not only the throwing power of PTHs but also the filling performance of microvias has to be taken into account. This is a big challenge because a low copper(II) ion concentration combined with a high acid concentration usually is suitable for a high throwing power of a PTH, but a high copper(II) ion concentration combined with a low acid concentration usually is suitable for filling microvias.

When the THs and microvias are completely filled with copper, it is called copper Damascene process that is carried out by electrodeposition. The copper Damascene process can significantly improve the electrical performance and reliability of PCBs. However, this process relies strongly on organic additives in the copper plating bath, which can dominate the secondary current density distribution inside the TH and correspondingly change the deposited profile of copper in the TH. For conformal deposition in a PTH, the mass transfer of copper(II) ion

W.-P. Dow (✉)
Department of Chemical Engineering, National Chung Hsing University, 250, Kuo-Kuang Road, Taichung 40227, Taiwan
e-mail: dowwp@dragon.nchu.edu.tw

K. Kondo et al. (eds.), *Copper Electrodeposition for Nanofabrication of Electronics Devices*, Nanostructure Science and Technology 171, DOI: 10.1007/978-1-4614-9176-7_11,
© Springer Science+Business Media New York 2014

and the conductivity of the plating solution are key for enhancing the throwing power of the PTH because the primary current density distribution determines the major plating outcome [1, 2]. For the copper Damascene process, organic additives play important and critical roles because they dominate the secondary current density distribution, which sometimes leads to an unbelievable plating result if someone only considers the effect of the primary current density distribution. For example, the hole mouth is a "peak" area where current density distribution is naturally concentrated based on the primary current distribution. On the other hand, the primary current density at the center position of the TH is relatively low. Accordingly, copper is preferentially deposited at the mouth rather than the center of the hole. However, when organic additives are added to the plating solution, the story is being changed. These organic additives can preferentially adsorb at the hole mouth due to their specific functional groups, such that the primary current density distribution does not dominate the copper deposition [1, 2]. Instead, copper deposition is forced to occur in the TH in galvanostatic plating. At the same time, if the coverage of the organic additive on the as-deposited copper surface is potential-dependent, a copper deposition gradient will be generated along the TH. Because the concentration of the organic additive is higher outside the TH than inside the TH, copper will be preferentially deposited at the center position of the TH rather than the mouth.

Copper Damascene process is not originally used for PCB fabrication [3–6] but for semiconductor fabrication [7–9]. At that time, blind vias rather than THs were completely filled with copper deposit. The bottom-up copper filling of blind vias is also caused by the chemical interaction of specific organic additives, which causes a specific secondary current density distribution to cause copper to be preferentially deposited at the location where the original primary current density distribution is low [10, 11]. Usually, three organic additives, a suppressor, an accelerator, and a leveler, are necessary for excellent filling of blind vias. For TH filling, however, a single organic additive is sufficient to achieve a complete filling [12–14]. A copper plating solution that is suitable to carry out bottom-up filling of a blind via and contains a single organic additive was merely proposed theoretically for explaining the mechanism of filling a blind via whose feature size falls into the nanoscale [7, 15]. A practical copper plating solution that contains a single organic additive for TH filling plating was not proposed until 2008 [12–14]. Practical TH filling by copper electroplating shows that the secondary current density distribution controlled by the organic additive is more crucial than the primary current density distribution.

In this section, two topics will be individually discussed according to their final applications and reliability criteria. Although HDI process is popular because of the requirement of smartphones, the conventional PTH with a high throwing power is still a basic component in the advanced PCBs. In addition, thick PCBs employed for Web communication stations also need PTHs with a very high aspect ratio. Therefore, the first part in the section will be focused on the conformal plating of a TH. The content of the first part will include some basic definitions of conformal plating of PTHs, throwing power measurement methods and tools, and factors that

influence throwing power. The second part in the section will be concentrated on filling plating of THs. This is a novel plating technology but many new products need the plating technology, such as HDI of PCB, connection of 3D chip stacking, and heat dissipation substrate of 3D LED. In the second part, the necessity and benefits of TH filling will be explained. How to evaluate the filling performance of a TH and how many physical and chemical factors will influence the filling performance of a TH will be discussed herein.

11.2 Conformal Plating of Through Holes

11.2.1 Definition and Criterion of Throwing Power of PTHs

For conventional PTHs of a PCB, a throwing power of 100 % is an ideal criterion. The definition of throwing power is defined by Eq. (11.1) and illustrated in Fig. 11.1.

According to the definition illustrated in Fig. 11.1a, the throwing power of a copper plating solution is as follows:

$$\text{Throwing power (TP)} = (H_c/H_a) \times 100\,\%, \tag{11.1}$$

where H_a is the copper thickness plated on the board surface and H_c is the copper thickness plated at the center position of the PTH. If the TP is equal to 100 %, it means that the copper thickness plated at the center position equals that on the board surface. However, the corner around the hole mouth is regarded as a "peak", such that its local current density is always higher than anywhere else during plating [16–25]. After electroplating, the local high current density results in

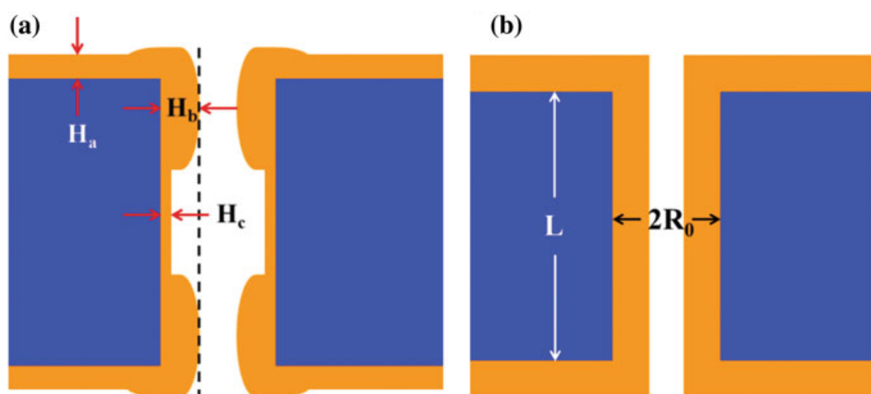

Fig. 11.1 Definition of throwing power on a PTH after copper electroplating. **a** Throwing power is $(H_c/H_a) \times 100\,\%$, the uniformity inside the PTH is $H_c/H_b \times 100\,\%$, **b** Both the throwing power and the uniformity are 100 %

copper overhang, as illustrated in Fig. 11.1a. The top thickness of the copper overhang is defined as H_b. Sometimes, the TP approaches 100 % but a copper overhang still occurs, meaning that the uniformity inside the PTH is smaller than 100 %. A perfect PTH is illustrated in Fig. 11.1b, in which both TP and uniformity are 100 %.

$$\text{Uniformity inside a PTH} = (H_c/H_b) \times 100\,\% \tag{11.2}$$

As to the aspect ratio of a PTH, it is usually defined as $L/2R_0$. However, this definition does not reflect practical difficulty in achieving uniform plating of PTHs. Instead, the term, L^2/R_0, can reflect the difficulty in achieving uniform plating of PTHs [16, 19, 25, 26].

11.2.2 Measurement Tools and Methods

Regarding the throwing power on a PTH, it can be estimated in advance using the Hull cell, as illustrated in Fig. 11.2. The Hull cell is a miniature electroplating tank. The cathode is angled with respect to the anode. As a result, when a voltage is applied across the anode and cathode, the resulting current density varies along the length of the cathode, being highest at the point where it is closest to the anode.

The corresponding current density distribution on the cathode is calculated according to the applied current, as shown in Fig. 11.3. For example, when the applied current is 2 A, the corresponding current density distribution varies from 80 $A{\cdot}ft^{-2}$ (ASF) (the left side) to 1 ASF (the right side) on the cathode. In this way, one is able to assess the effect of varying current density by means of a single test run.

At the highest current density, the deposit may be burned to form a dendritic structure due to a limiting current. At the lowest current density, no deposition may be observed. Figure 11.4 shows two cathode pictures after a Hull cell test

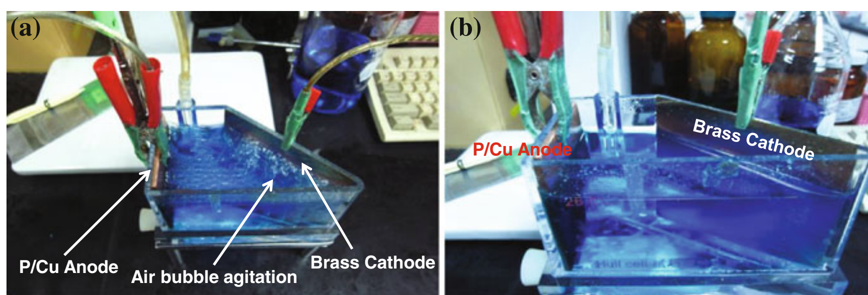

Fig. 11.2 Pictures of a Hull Cell with a volume is 267 mL. The anode is a P-containing Cu plate and the cathode is a brass plate. Air bubbles jet out at the cell bottom near the cathode for agitation. **a** *top view*, **b** *side view*

	PANEL EDGE													
1 AMP	40	30	25	20	15	12	10	8	6	4	3	2	1	0.5
2 AMPS.	80	60	50	40	30	24	20	16	12	8	6	4	2	1
3 AMPS.	120	90	75	60	45	36	30	24	18	12	9	6	3	1.5
5 AMPS.	200	150	125	100	75	60	50	40	30	20	15	10	5	2.5

AMPS./SQ. FT. — 267 ML or 534 HULL CELL

TOTAL CURRENT

7.5 GM/1000 ML. OR 7.8 ML/1000 ML.

2 GM/267 ML. HULL CELL = 1OZ./GAL = 6.25 LBS./100 GAL.
2 ML/267 ML. HULL CELL = 0.96 FL. OZ./GAL. = 8 PTS./100 GAL.
4 GM/534 ML. HULL CELL = 1OZ./GAL. = 6.25 LBS./100 GAL.
4 ML/534 ML. HULL CELL = 0.96 FL. OZ./GAL = 8 PTS./GAL.

AMPS./SQ. FT.—1000 ML. HULL CELL

	PANEL EDGE												
3 AMPS.	90	60	45	36	30	24	18	15	12	9	6	3	0.6
5 AMPS.	150	100	75	60	50	40	30	25	20	15	10	5	1

CU.FT.×7.48 = GAL.
GM./L.×0.134 = OZ./GAL.
OZ./GAL.×7.5 = GM./LITRE
GAL.×3785 = ML.
LB.×453.6 = GM.
A/SQ.FT×0.108 = A/SQ.DM

Fig. 11.3 The corresponding current density distribution from the *left side* (highest current density) to the *right side* (lowest current density) on the brass cathode

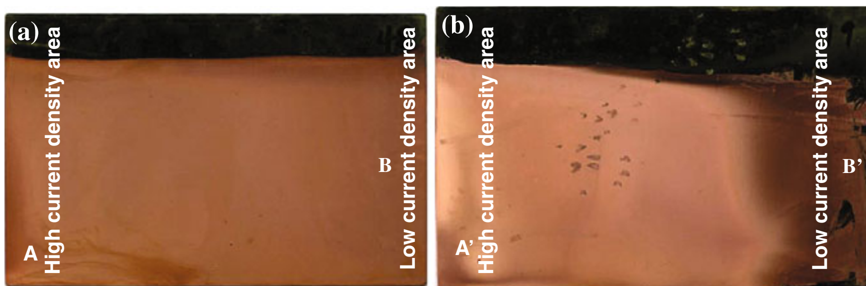

Fig. 11.4 Pictures of brass cathodes after copper plating at 2 A for 5 min using two copper plating formulas in the Hull Cell. **a** Formula I, containing suppressor, accelerator, and leveler, **b** Formula II, containing accelerator only

using two copper plating formulas. Figure 11.4a shows that the copper plating formula composed of $CuSO_4$, H_2SO_4, suppressor, accelerator, and leveler can perform copper deposition from 80 ASF to 1 SAF. Slightly rough copper deposit appears at the area A with a dark-brown color. Also, copper can be deposited at the area B in a good coverage shown in Fig. 11.4a. On the other hand, rough copper deposit is obtained at the area A by using formula II, composed of $CuSO_4$, H_2SO_4, and accelerator, as shown in Fig. 11.4b, no copper is deposited at the area B. This indicates that formula I exhibits a higher throwing power than formula II if there is no mass transfer limitation in the plating bath.

11.2.3 Physical Factors

Several physical factors, such as forced convection, electrolyte conductivity, geometric shape, and so on [19, 25], must be considered in order to obtain a high

throwing power within a PTH. One important physical factor that significantly dominates the plating uniformity is the aspect ratio (AR, $L/2R_0$) of the PTH, which is defined in the Sect. 2.1. A high AR means the plating solution does not easily pass through the PTH, which leads to a low metallic cation concentration and a high ohmic resistance at the hole center [27]. Therefore, the throwing power of the PTH is low. Regarding the physical factor, a simulation model was proposed to obtain Eqs. (11.3) and (11.4) [25, 27].

$$\bar{I}_{L,\,\mathrm{avg}} = \frac{FD_iC_b}{R_0}\left(1.15A^{1/3} - 1.2 - 0.65A^{-1/3}\right) \tag{11.3}$$

$$I_{c,\Omega} = \pi^2 RTR_0\kappa / \alpha_c FL^2, \tag{11.4}$$

where A is $R_0^4\rho V_0^2/2\mu D_i L^2 f_b^2$; ρ is the electrolyte density in g/cm^3; V_0 is the maximum PCB moving speed in cm/s; μ is viscosity in g/cm·s; D_i is diffusivity in cm^2/s; f_b is the fraction of the plating bath cross-section not occupied by the PCB area; and κ is the electrolyte conductivity in mho/cm.

$\bar{I}_{L,\,\mathrm{avg}}$ is the average current density at the limiting mass transfer rate in mA/cm^2. $I_{c,\,\Omega}$ is the ohmic critical current density at the center of the PTH imposed by the ohmic resistance. By comparing Eq. (11.3) with Eq. (11.4), both current densities are functions of L^2/R_0. However, $I_{c,\,\Omega}$ is much more sensitive to the L^2/R_0 ratio, meaning that $I_{c,\,\Omega}$ decreases more rapidly than $\bar{I}_{L,\,\mathrm{avg}}$ as the L^2/R_0 ratio of the PTH becomes large. In other words, when the ohmic limitation takes place, its current density value is still well below that at which mass transfer becomes a significant limitation. Therefore, the ohmic rather than the mass transfer resistance imposes the critical limitation on the current density at which a high AR PTH may be uniformly plated.

Unless the plating process is entirely mass transfer controlled, increasing $\bar{I}_{L,\,\mathrm{avg}}$ by strong agitation or jet impingement produces limited improvement in uniform plating for a high AR PTH [18]. On the contrary, increasing $I_{c,\Omega}$ by increasing the electrolyte conductivity (κ) or by reducing the board thickness (L) can effectively reduce the ohmic resistance inside the PTH.

At the same average plating current density, two dimensionless groups, represented by Eqs. (11.5) and (11.6), are useful for judging the final throwing power after all plating parameters are given [18, 19].

$$I^* = \frac{4FL^2 i}{RTR_0\kappa} \tag{11.5}$$

$$\xi = \frac{4FL^2 i_0}{RTR_0\kappa}, \tag{11.6}$$

where i is the average plating current density in mA/cm^2; i_0 is the exchange current density in mA/cm^2. Equation (11.5) represents a dimensionless deposition rate; Eq. (11.6) represents a dimensionless ratio of ohmic resistance to charge transfer resistance. According to Eq. (11.5), a board with PTHs of 200 µm diameter and

3 mm thickness will have more uniform copper deposited inside than a board of holes 400 μm in diameter and 6 mm in thickness due to the smaller I^* value for the thinner board, although both have the same aspect ratio of 15. However, their L^2/R_0 ratios are different, whereas the former is 9 cm, the latter is 18 cm. A higher L^2/R_0 ratio leads to a higher I^* and ξ, which causes lower uniformity inside the PTH [18, 19]. This comparison also shows that the aspect ratio (i.e., $L/2R_0$) cannot reflect the difficulty in plating a uniform PTH but L^2/R_0 can do so. Also, increasing the electrolyte conductivity (κ) can decrease both I^* and ξ, which will result in high copper uniformity inside the PTH. In addition, decreasing i_0 by adding an organic additive also can decrease ξ, which can improve the plated copper uniformity of a PTH. However, this belongs to the effect of chemical factors.

11.2.4 Chemical Factors

The throwing power and uniformity of a PTH are not only influenced by physical factors but also by chemical factors. Chemical factors mean plating additives. For a high throwing power, an organic additive, namely a leveler, is significantly effective. Those levelers which are able to enhance the throwing power of a PTH have a specific functional group, namely quaternary ammonium cation. Five typical levelers are illustrated in Fig. 11.5 [28]. Usually, one leveler molecule bears one quaternary ammonium cation, such as JGB, DB, MV, and SO. However, the leveler AB has four quaternary ammonium cations.

Since the leveler is an organic cation, it prefers to adsorb onto the cathode during plating, especially at the area of high current density. They either physically inhibit copper deposition at a peak position or electrochemically share the charge for copper deposition at the peak position. Consequently, they exhibit a leveling effect on copper deposition. The physical inhibition on copper deposition by a leveler is caused by the selective adsorption of nitrogen cations at the peak position. The electrochemical charge share is due to the electrochemical reducibility of these levelers [29, 30]. Both amine and quaternary ammonium cation are electrochemical reducible. Therefore, when the leveler preferentially adsorbs at the peak position, the local charges will be donated to the leveler rather than copper ions. Hence, copper ions will be forced to deposit elsewhere, leading to a leveling effect.

The reducibility of these levelers means that they are consumed during plating. Therefore, a concentration gradient of a leveler will be established from the hole mouth to the hole center. This is the root cause of enhancement in throwing power as the leveler is added in the plating solution. Since the electrochemical reduction reaction of the leveler is associated with the pH value of the plating solution [29, 30], and its adsorption is dependent of chloride ion concentration [31, 32], the leveling mechanism is complex.

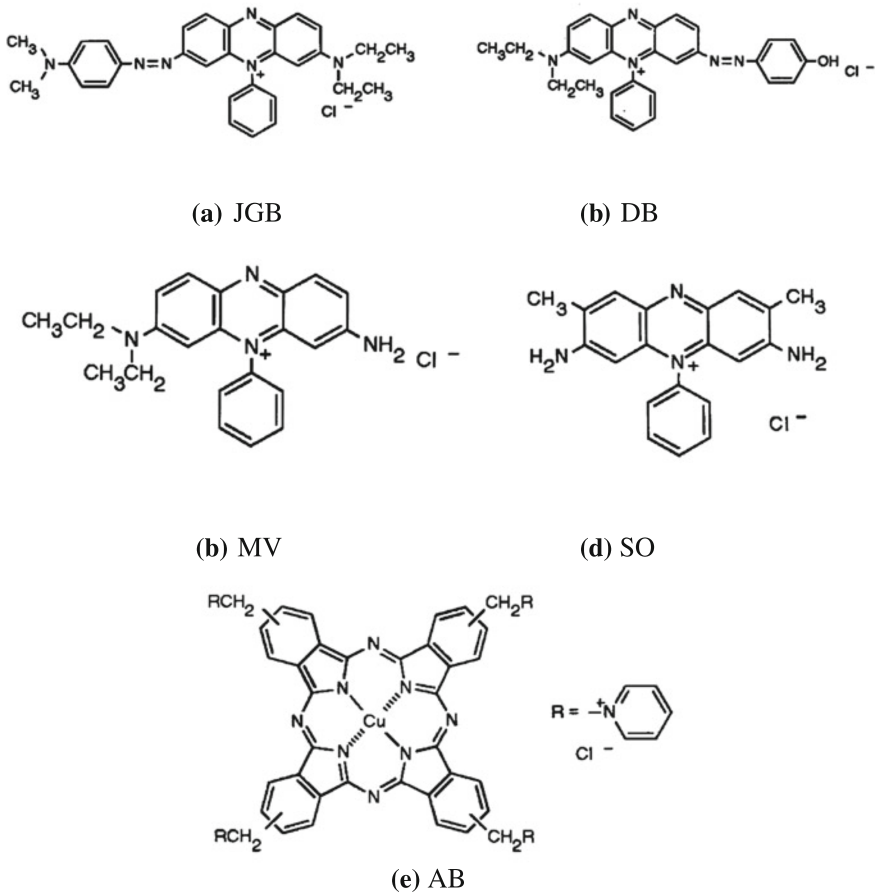

Fig. 11.5 Molecular structures of various levelers. **a** Janus Green B (JGB); **b** Diazine Black (DB); **c** Methylene violet 3RAX (MV); **d** Safranine O (SO); **e** Alcian blue (AB)

11.3 Filling Plating of Through Holes

11.3.1 Necessity and Benefit

HDI of PCBs [33, 34] and 3Dchip stacking packaging [35–37] have become two of the most important topics in the field of advanced electronic product fabrication. To meet the interconnect requirements of high-frequency transmission applications, i.e., a low electrical resistance and low thermal resistance, THs designed for PCBs and interposers have become necessary components. However, the traditional PTH process only metalizes the sidewalls of the THs, which cannot meet the current reliability specifications. Instead, TH filling by copper electroplating has been developed to meet the critical reliability requirement [38]. According to the

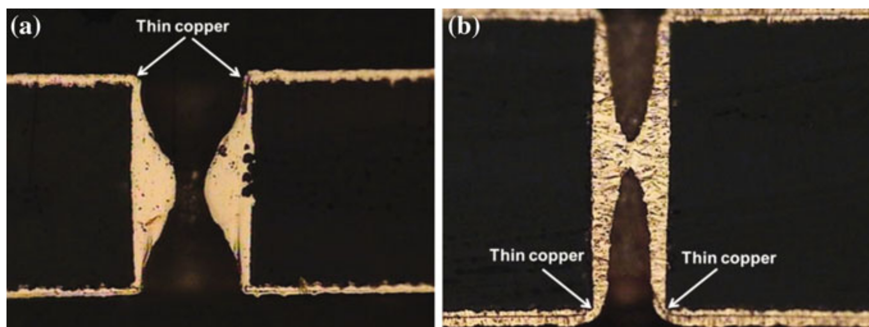

Fig. 11.6 Cross sections of THs at early plating stage. **a** Hole diameter is 85 μm and hole depth is 150 μm (AR = 1.76, $L^2/R_0 = 0.53$ mm); **b** Hole diameter is 60 μm and hole depth is 250 μm (AR = 4.17, $L^2/R_0 = 2.08$ mm) [12]

definition of the throwing power of a PTH in Sect. 11.2.1, the throwing power of the fully filled TH is larger than 100 %. Evidently, the deposited result does not follow the primary current density distribution, because the current density distribution from the hole mouth to the hole center is reversed due to the addition of an organic additive in the plating bath. The reversed current density distribution is the secondary current density distribution [1, 2], which leads to the fastest copper deposition occurring at the center position of the TH and results in a butterfly shaped deposition profile of the filled TH cross-section at the early plating stage, as shown in Fig. 11.6 [12]. Accordingly, the TH filling technology by copper electroplating is called butterfly technology (BFT) [12–14, 39].

The root cause of the secondary current density distribution is the concentration gradient of an organic additive. Usually, the plating formula is composed of a single additive [12–14, 39]. The basic composition for filling TH is a high copper(II) ion concentration and a low acid concentration, which is opposite to that for the uniform plating of a PTH mentioned in the previous section. Basically, the mass transfer of copper ions for the TH filling relies on diffusion and migration rather than convection. Hence, once the forced convection is strong, conformal deposition (i.e., a high throwing power) will be obtained [14]. Figure 11.6 also shows that the butterfly shaped deposit profile is independent of the AR of the TH, meaning that the filling electroplating is not sensitive to the ohmic resistance inside the TH, as shown by Eqs. (11.4) and (11.6).

11.3.2 Evaluation Methods

The concentration gradient of the organic additive inside the TH is key for the butterfly shaped deposition profile. Therefore, forced convection is an important physical factor in control of the concentration gradient of the additive. Cyclic

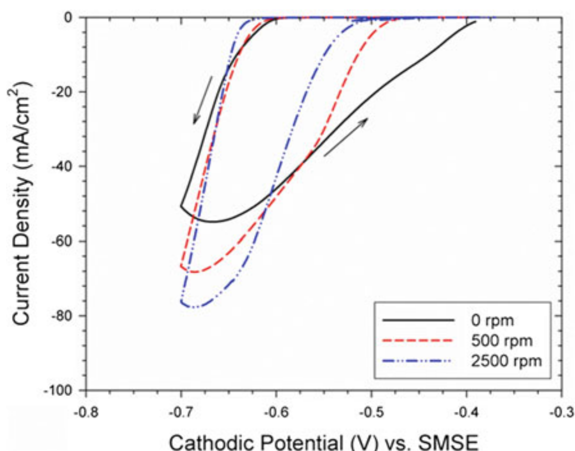

Fig. 11.7 Cyclic voltammogram of Cu deposition in plating bath that contains no accelerator but an inhibitor only. The plating solution is composed of 0.88 M $CuSO_4$, 0.18 M H_2SO_4, 40 ppm NTBC, and 20 ppm Cl^-. The temperature of the plating solution is maintained at 25 °C. The scan rate is 1 mV/s. The molecular structure of NTBC is shown in Fig. 11.8 [12]

voltammetry (CV) [12] and galvanostatic measurements [13] on a rotating disk electrode can be used to evaluate the filling performance. Commonly, the stronger the forced convection, the lower the copper deposition rate will be, as shown in Fig. 11.7 [12]. Figure 11.7 shows that copper electrodeposition is strongly inhibited when the cathode potential is swept toward more negative potentials. Once the cathodic potential returns and shifts toward a more positive potential, the corresponding current density and peak current density of copper deposition is dependent on the rotation speed of the working electrode.

The faster the rotation speed is, the higher the peak current density will be. This indicates that the copper electrodeposition is mass transfer-limited. Hence, strong forced convection is beneficial to the mass transfer of copper (II) ion onto the cathode when the inhibitor has been electrochemically desorbed from the cathodic surface. However, when the cathodic potential is more positive than −0.6 V, the higher the rotating speed is, the smaller the current density will be. This means that forced convection is beneficial for readsorption of the inhibitor if its adsorption is potential-dependent. In fact, the practical current density for the TH filling is low, so that the cathodic overpotential is relatively small. Therefore, copper will be forced to be deposited at the place where forced convection is relatively weak.

Consequently, the slowest copper deposition rate will occur on the board surface and the fastest copper deposition rate will take place at the center position of the TH. Since the organic additive is electrochemically reducible, it will share the charge provided at the hole mouth (i.e., the peak position). Therefore, a dog bone-like deposition, as illustrated in Fig. 11.1a, does not happen. Instead, a thin copper layer is obtained at the hole mouth, as shown in Fig. 11.6.

11.3.3 Chemical Factors

Figure 11.8 shows two typical organic additives for the TH filling [12–14, 39]. Both molecules have two tetrazolium salts, which are electrochemically reducible [40–43]. After the electrochemical reduction of tetrazolium salts in the presence of acid, the nitrogen-carbon ring is opened and their electrochemical properties change correspondingly [40–43].

NTBC has two nitro groups and TNBT has four nitro groups, which are also electrochemically reducible to be hydroxyl amine or amine groups in the presence of acid [41, 42, 44–47]. These hydroxyl amine and amine groups are good ligands for adsorption onto copper surface. Therefore, when NTBC and TNBT are used as copper plating additives, their inhibiting effect on copper electrodeposition is dependent on pH value, cathodic potential, and chloride ion concentration.

The concentration gradient of these additives inside the TH is caused by the overpotential gradient and by the electrochemical adsorption characteristics of chloride ion. The overpotential gradient inside the TH determines the conversion of the electrochemical reduction reaction along the TH. In addition, a high cathodic overpotential is not beneficial for the transfer and adsorption of chloride ions into the TH and onto the hole wall, especially at the center position of the TH. Figure 11.9 shows that copper is preferentially deposited at the hole mouth in the absence of NTBC. This result is in agreement with that of a common PTH. Since chloride ion is the only additive, it facilitates copper deposition at the peak position, resulting in a dog bone-like copper profile [48]. An extremely rough copper deposit is produced by the accelerating effect of chloride ion [49].

When the copper plating solution only contains NTBC but no chloride ion, the deposition behavior is significantly changed, as shown in Fig. 11.10. Copper is preferentially deposited at the center position of the TSH rather than at the hole

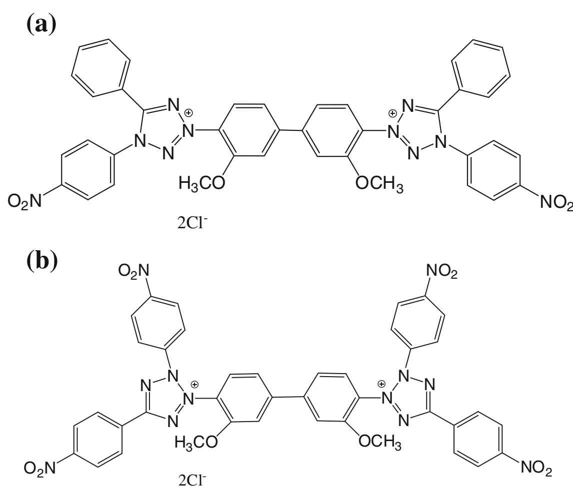

Fig. 11.8 Molecular structures of **a** Nitrotetrazolium Blue chloride monohydrate (NTBC), **b** Tetranitroblue tetrazolium chloride (TNBT)

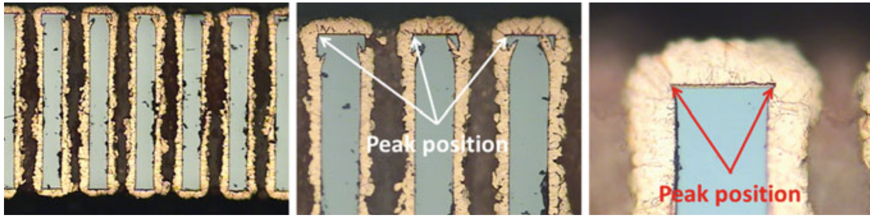

Fig. 11.9 Cross-sections of through-silicon holes (TSHs) after copper electroplating. The plating solution is composed of 0.88 M $CuSO_4$, 0.54 M H_2SO_4, and 20 ppm Cl^-. The current density is 1.5 $A{\cdot}ft^{-2}$. The depth and diameter of the TSH are 380 and 50 μm, respectively [48]

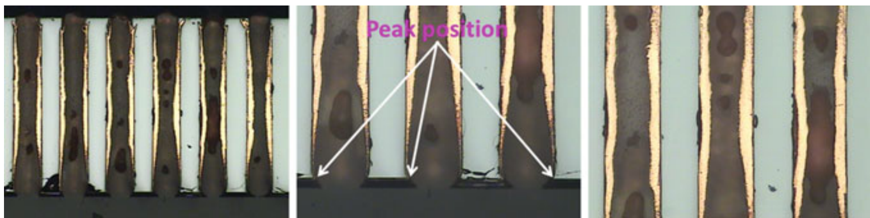

Fig. 11.10 Cross-sections of through-silicon holes (TSHs) after copper electroplating. The plating solution is composed of 0.88 M $CuSO_4$, 0.54 M H_2SO_4, and 40 ppm NTBC. The current density is 1.5 $A{\cdot}ft^{-2}$. The depth and diameter of the TSH are 380 and 50 μm, respectively [48]

mouth. Evidently, the copper deposited on the wafer surface and at the hole mouth is very thin. This result implies that the copper deposition is not dominated by the mass transfer of copper ion or the ohmic resistance of the plating solution. It is dominated by the concentration gradient of NTBC under the plating condition.

When the current density is increased from 1.5 $A{\cdot}ft^{-2}$ to 3 $A{\cdot}ft^{-2}$, mass transfer of copper ion will again be an issue, as shown in Fig. 11.11. The copper deposition rate is higher than the mass transfer rate of copper ion, such that the position of the fastest copper deposition moves from the hole center toward the hole mouth. However, little copper is deposited at the peak position (i.e., hole mouth), meaning that NTBC + chloride ions can effectively inhibit copper deposition at the peak position.

When the current density is decreased to 1.5 $A{\cdot}ft^{-2}$, the TSH can be fully filled by copper electroplating, as shown in Fig. 11.12. It is worthy to note that the overburdened copper layer on the wafer surface is very thin, implying that copper is preferentially deposited inside the TSH because there is a concentration gradient of an inhibitor (NTBC + Cl) from the outside surface of the TSH to the center of the TSH during copper plating.

When the THs are completely filled with the copper deposit and are free of voids, a metallization process and pattern design of a PCB can be accordingly changed. For traditional PTHs, only the hole wall is metallized by copper electroplating. The empty center is filled with a polymer or nonconducting material. Therefore, a ring pad must be made around the TH opening, which is used as a

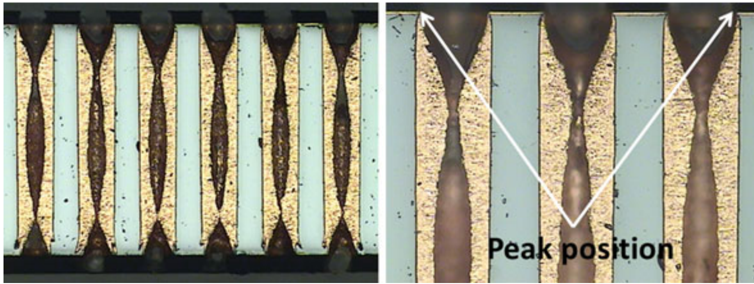

Fig. 11.11 Cross-sections of through-silicon holes (TSHs) after copper electroplating. The plating solution is composed of 0.88 M $CuSO_4$, 0.54 M H_2SO_4, 20 ppm Cl^-, and 40 ppm NTBC. The current density is 3.0 $A{\cdot}ft^{-2}$. The depth and diameter of the TSH are 380 and 50 μm, respectively [48]

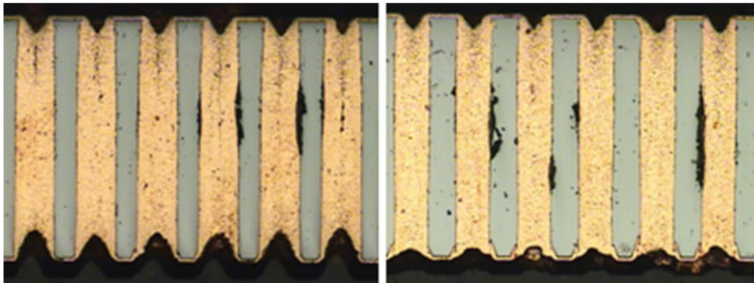

Fig. 11.12 Cross-sections of through-silicon holes (TSHs) after copper electroplating. The plating solution is composed of 0.88 M $CuSO_4$, 0.54 M H_2SO_4, 20 ppm Cl^-, and 40 ppm NTBC. The current density is 1.5 $A{\cdot}ft^{-2}$. The depth and diameter of the TSH are 380 and 50 μm, respectively [48]

terminal of a conducting line. However, these ring pads occupy a lot of pattern area; they do not meet the criterion of HDI. Alternatively, the pattern area can be saved when the THs are fully filled by copper electroplating. After electroplating, exposure, development, and etching processes, copper bumps are formed. These copper bumps are usable as the terminals, so the ring pad design is unnecessary. This is called a padless process [12].

In addition, if a microvia is stacked on the PTH, the empty center of the PTH must be filled with a polymer or a nonconducting material to act as a supporting material for the subsequent stacked microvia. Accordingly, the top surface of the polymer or the nonconducting material that is filled in the TH must be metallized again by copper electroplating. Obviously, the process is complex, and an adhesion issue exists between the filling material and the plated copper layer. Alternatively, if the THs are fully filled by copper electroplating, a process without pad design is feasible. Besides, the entire conductivity of the patterns will be greatly enhanced because the polymer-filled THs are replaced by the copper-filled THs [12].

References

1. Newman J, Thomas-Alyea KE (2004) Electrochemical systems, 3rd edn. Wiley, New Jersey
2. Kanani N (2004) Electroplating—basic principles, processes and practice, 1st edn. Elsevier Ltd., Netherlands
3. Kobayashi T, Kawasaki J, Mihara K, Honma H (2001) Via-filling using electroplating for build-up PCBs. Electrochim Acta 47:85–89
4. Kondo K, Yamakawa N, Tanaka Z, Hayashi K (2003) Copper damascene electrodeposition and additives. J Electroanal Chem 559:137–142
5. Lefebvre M, Allardyce G, Seita M, Tsuchida H, Kusaka M, Hayashi S (2003) Copper electroplating technology for microvia filling. Circuit World 29:9–14
6. Dow W-P, Huang H-S, Lin Z (2003) Interactions between brightener and chloride ions on copper electroplating for laser-drilled via-hole filling. Electrochem Solid-State Lett 6:C134–C136
7. Andricacos PC, Uzoh C, Dukovic JO, Horkans J, Deligianni H (1998) Damascene copper electroplating for chip interconnections. IBM J Res Dev 42:567–574
8. Moffat TP, Wheeler D, Huber WH, Josell D (2001) Superconformal electrodeposition of copper. Electrochem Solid-State Lett 4:C26–C29
9. West AC, Mayer S, Reid J (2001) A superfilling model that predicts bump formation. Electrochem Solid-State Lett 4:C50–C53
10. Moffat TP, Wheeler D, Edelstein MD, Josell D (2005) Superconformal film growth: mechanism and quantification. IBM J Res Dev 49:19–36
11. Vereecken PM, Binstead RA, Deligianni H, Andricacos PC (2005) The chemistry of additives in damascene copper plating. IBM J Res Dev 49:3–18
12. Dow W-P, Chen H–H, Yen M-Y, Chen W-H, Hsu K-H, Chuang P-Y, Ishizuka H, Sakagawa N, Kimizuka R (2008) Through-hole filling by copper electroplating. J Electrochem Soc 155:D750–D757
13. Chen C-H, Lu C-W, Huang S-M, Dow W-P (2011) Effects of supporting electrolytes on copper electroplating for filling through-hole. Electrochim Acta 56:5954–5960
14. Dow W-P, Liu D-H, Lu C-W, Chen C-H, Yan J–J, Huang S-M (2011) Through-hole filling by copper electroplating using a single organic additive. Electrochem Solid-State Lett 14:D13–D15
15. West AC (2000) Theory of filling of high-aspect ratio trenches and vias in presence of additives. J Electrochem Soc 147:227–232
16. Kessler T, Alkire R (1976) A model for copper electroplating of multilayer printed wiring boards. J Electrochem Soc 123:990–999
17. Engelmaier W, Kessler T (1978) Investigation of agitation effects on electroplated copper in multilayer board plated-through holes in a forced-flow plating cell. J Electrochem Soc 125:36–43
18. Alkire RC, Ju JB (1987) The effect of an impinging fluid jet on mass transfer and current distribution in a circular through-hole. J Electrochem Soc 134:1172–1180
19. Yung EK, Romankiw LT, Alkire RC (1989) Plating of copper into through-holes and vias. J Electrochem Soc 136:206–215
20. Pesco AM, Cheh HY (1989) The current distribution within plated through-holes: I the effect of electrolyte flow restriction during DC electrolysis. J Electrochem Soc 136:399–407
21. Yung EK, Romankiw LT (1989) Fundamental study of acid copper through-hole electroplating process. J Electrochem Soc 136:756–767
22. Hazlebeck DA, Talbot JB (1991) Modeling of the electroplating of a through-hole considering additive effects and convection. J Electrochem Soc 138:1985–1997
23. Chern JWE, Cheh HY (1996) Modeling of plated through-hole processes: I current distribution. J Electrochem Soc 143:3139–3144
24. Chern JWE, Cheh HY (1996) Modeling of plated through-hole processes: II effect of leveling agents on current distribution. J Electrochem Soc 143:3144–3148

25. Poon GKK, Williams DJ (1998) Modeling of acid copper electroplating: a review. J Electron Manuf 08:15–37
26. Hazlebeck DA, Talbot JB (1990) Modeling of additive effects on the electroplating of a through-hole. AIChE J 36:1145–1155
27. Lanzi O, Landau U (1988) Analysis of mass transport and ohmic limitations in through-hole plating. J Electrochem Soc 135:1922–1930
28. Dow W-P, Li C–C, Lin M-W, Su G-W, Huang C–C (2009) Copper fill of microvia using a thiol-modified Cu seed layer and various levelers. J Electrochem Soc 156:D314–D320
29. Hai NTM, Wandelt K, Broekmann P (2008) Stable anion–cation layers on Cu(111) under reactive conditions. J Phys Chem C 112:10176–10186
30. Hai NTM, Furukawa S, Vosch T, De Feyter S, Broekmann P, Wandelt K (2009) Electrochemical reactions at a porphyrin-copper interface. Phys Chem Chem Phys 11:5422–5430
31. Dow W-P, Huang H-S, Yen M-Y, Huang H-C (2005) Influence of convection-dependent adsorption of additives on microvia filling by copper electroplating. J Electrochem Soc 152:C425–C434
32. Dow W-P, Yen M-Y, Liu C-W, Huang C–C (2008) Enhancement of filling performance of a copper plating formula at low chloride concentration. Electrochim Acta 53:3610–3619
33. Takagi K, Honma H, Sasabe T (2003) Development of sequential build-up multilayer printed wiring boards in Japan. Electr Insul Mag IEEE 19:27–56
34. Sundaram V, Tummala RR, Fuhan L, Kohl PA, Jun L, Bidstrup-Allen SA, Fukuoka Y (2004) Next-generation microvia and global wiring technologies for SOP. IEEE Trans Adv Packag 27:315–325
35. Blackshear ED, Cases M, Klink E, Engle SR, Malfatt RS, de Araujo DN, Oggioni S, LaCroix LD, Wakil JA, Pham NH, Hougham GG, Russell DJ (2005) The evolution of build-up package technology and its design challenges. IBM J Res Dev 49:641–661
36. Topol AW, Tulipe DCL, Shi L, Frank DJ, Bernstein K, Steen SE, Kumar A, Singco GU, Young AM, Guarini KW, Ieong M (2006) Three-dimensional integrated circuits. IBM J Res Dev 50:491–506
37. Lau JH (2011) Overview and outlook of through-silicon via (TSV) and 3D integrations. Microelectron Int 28:8–22
38. Dow W-P, Chen H–H (2004) A novel copper electroplating formula for laser-drilled micro via and through hole filling. Circuit World 30:33–36
39. Dow W-P, Lu C-W, Lin J-Y, Hsu F-C (2011) Highly selective Cu electrodeposition for filling through silicon holes. Electrochem Solid-State Lett 14:D63–D67
40. Bielski BHJ, Shiue GG, Bajuk S (1980) Reduction of nitro blue tetrazolium by CO_2^- and O_2^- radicals. J Phys Chem 84:830–833
41. Umemoto K, Okamura N (1986) Reaction of hydroxide ion with electron acceptors in dimethyl sulfoxide. Bull Chem Soc Jpn 59:3047–3052
42. Umemoto K (1989) Electrochemical studies of the reduction mechanism of tetrazolium salts and formazans. Bull Chem Soc Jpn 62:3783–3789
43. Oritani T, Fukuhara N, Okajima T, Kitamura F, Ohsaka T (2004) Electrochemical and spectroscopic studies on electron-transfer reaction between novel water-soluble tetrazolium salts and a superoxide ion. Inorg Chim Acta 357:436–442
44. Brooksby PA, Downard AJ (2005) Multilayer nitroazobenzene films covalently attached to carbon. an AFM and electrochemical study. J Phys Chem B 109:8791–8798
45. Üstündağ Z, Solak AO (2009) EDTA modified glassy carbon electrode: preparation and characterization. Electrochim Acta 54:6426–6432
46. Nazemi Z, Shams E, Amini MK (2010) Covalent modification of glassy carbon electrode by nile blue: preparation, electrochemistry and electrocatalysis. Electrochim Acta 55:7246–7253

47. Cougnon C, Nguyen NH, Dabos-Seignon S, Mauzeroll J, Bélanger D (2011) Carbon surface derivatization by electrochemical reduction of a diazonium salt in situ produced from the nitro precursor. J Electroanal Chem 661:13–19
48. Lu C-W (2010) Development of a new formula for filling through-hole by copper electroplating. In: Chemical Engineering, Master Thesis, National Chung Hsing University, Taiwan
49. Nagy Z, Blaudeau JP, Hung NC, Curtiss LA, Zurawski DJ (1995) Chloride ion catalysis of the copper deposition reaction. J Electrochem Soc 142:L87–L89

Erratum to: Acceleration Effect

Dale P. Barkey

Erratum to:
Chapter 3 in: K. Kondo et al. (eds.), *Copper Electrodeposition for Nanofabrication of Electronics Devices*, DOI 10.1007/978-1-4614-9176-7_3

The material at the end of Chapter 3 (text on pages 56, 57, and top of 58 at the end of section 3.4) should not be regarded as part of the chapter and was inserted without the knowledge or consent of the author.

The online version of the original chapter can be found under DOI 10.1007/978-1-4614-9176-7_3

D. P. Barkey (✉)
Department of Chemical Engineering, College of Engineering and Physical Science,
Kingsbury Hall, Room W305, Durham, NH 03824, USA
e-mail: dpb@cisunix.unh.edu

K. Kondo et al. (eds.), *Copper Electrodeposition for Nanofabrication of Electronics Devices*,
Nanostructure Science and Technology 171, DOI: 10.1007/978-1-4614-9176-7_12,

© Springer Science+Business Media New York 2014